Modeling of immunogenic cell death

Andrea Checcoli

PSL UNIVERSITÉ PARIS

THÈSE DE DOCTORAT
DE L'UNIVERSITÉ PSL

Préparée à l' Institut Curie dans le cadre d'une cotutelle
avec le Centre de Recherche des Cordeliers

Modélisation de la mort cellulaire immunogène

Modeling of immunogenic cell death

Soutenue par

Andrea Checcoli

Le 20 Septembre 2024

École doctorale n°474

FIRE: Frontières de l'Innovation en Recherche et Éducation

Spécialité

Biologie des Systèmes

Préparée aux laboratoires

"Cancer et génome : Bioinformatique, biostatistiques et épidémiologie des systèmes complexes", Institut Curie, Unitè INSERM U900

"Metabolisme, Cancer et Immunitè", Centre de Recherche des Cordeliers, Unitè INSERM UMRS1138

Composition du jury :

Denis THIEFFRY Institut Curie, CNRS, PSL Université	*Président du jury* *Examinateur*
Sylvie BABAJKO Université Paris Citè, INSERM	*Rapporteur*
Elisabeth REMY Aix Marseille Université, CNRS	*Rapporteur*
Josselin NOIREL Conservatoire National des Arts et Métiers	*Examinateur*
Laurence CALZONE Institut Curie	*Directrice de thèse*
Jonathan POL Université Paris-Saclay, INSERM	*Co-Directeur de thèse*

PSL UNIVERSITÉ PARIS institut Curie

Acknowledgments

First of all, I would like to express gratitude to the jury members for participating in this thesis defense and for your careful review of my manuscript.

Next, I would like to thank my supervisors, Laurence and Jonathan for sharing the burden of my supervision. I know it has not been simple at times (my parents struggled for several years too). I want to thank you very much for the incredible opportunities you gave me and the unconditional support I received throughout this thesis and even before, during my internship.

I take the chance to thank Prof. Guido Kroemer and Dr. Emmanuel Barillot for having me in their labs throughout my Ph.D.
Thank you very much to the administrative personal of CRC, Mehdi and Linda Bennaci, and the people from Institut Curie: N Deo Kati Ba Pierozzi and Emma Kaufmann. Your help was invaluable.

A special "thank you" then goes to all my lab mates of the Equipe 11 at Centre de Recherche des Cordeliers. You made this journey a special one and supported me in every moment, joyful and sad ones.
In particular I would like to thank Maria Perez-Lanzon and Juliette Paillet for initiating me to the magical world of experimental biology. When I arrived to the lab, I did not even know how to tie my shoes and if I am now capable of any lab skill, it is because of you two.
A special thanks goes to Vincent, Fatima, Sylvie, Chiara, Mehdi, Karla, Lucille, Celeste, Sarah, Léa, Flavia, Yanbing, Maria, Marie, Mojgan, Hui Chen, Gautier, Isa, Allan, Giulia, Emily, Sijing and all the great people that have been around Kroemer lab within the last three years at Cordeliers.
I would like to say thank you very much to my fellows of the Sysbio team at Institut Curie: Sofia, Saran, Lucie, Luca, Nicola, Loic, Matthieu, Daniel, Cristobal, Ellora, Jane, Loredana, Theo, Alexei and last but not least, Marco. We have come a long way together and we have much further to go. Thank you for supporting me and for being a great friend.

To my friends, those who came here from abroad and those I met here in Paris: thank you for supporting me all the way through the last three years (or more). You've been my shelter and I love you.

To my family, for being the pillar of my life.

To Mimi, for being my home.

Résumé

Cette thèse vise à approfondir notre compréhension de la Mort Cellulaire Immunogène (ICD) et de son potentiel à améliorer l'efficacité des traitements chimiothérapeutiques. En adoptant une approche multidisciplinaire qui intègre la biologie expérimentale et computationnelle, cette recherche aborde des questions clés essentielles à l'avancement des études sur l'ICD.

Malgré les progrès réalisés dans le décryptage des mécanismes moléculaires de l'ICD, des lacunes importantes subsistent dans notre compréhension. Cette thèse s'efforce de combler ces lacunes en identifiant les facteurs et les voies critiques impliqués dans l'ICD et en développant des modèles computationnels pour prédire et renforcer l'immunogénicité des agents chimiothérapeutiques.

Un axe central de ce travail a été l'identification d'une signature moléculaire distincte de l'ICD, au-delà des marqueurs traditionnels tels que les DAMPs libérés et exposés à la surface. Une telle signature pourrait servir de biomarqueur fiable pour prédire le potentiel immunogène des chimiothérapies. De plus, la recherche a exploré les facteurs sécrétés, en particulier les cytokines, qui jouent un rôle crucial dans l'initiation du cycle immunitaire anticancéreux en recrutant et activant les cellules immunitaires. Comprendre ces facteurs est essentiel pour optimiser le potentiel immunogène des régimes chimiothérapeutiques.

En outre, la thèse s'est penchée sur les voies cellulaires qui régulent la sécrétion et la libération des DAMPs liés à l'ICD. En explorant les réseaux de signalisation et les mécanismes moléculaires impliqués, l'étude visait à découvrir des voies influençant l'immunogénicité des cellules mourantes, avec l'objectif potentiel d'identifier de nouvelles cibles pour amplifier la réponse immunitaire via l'induction de l'ICD.

Sur la base de ces résultats, la recherche a également exploré la possibilité de recréer l'ICD in silico. En intégrant à la fois les marqueurs établis et nouvellement identifiés dans des modèles computationnels, la thèse visait à simuler les processus de l'ICD, prédire les résultats des traitements et orienter les futures expérimentations.

Enfin, la thèse a évalué la capacité prédictive des modèles in silico développés pour évaluer l'immunogénicité des médicaments chimiothérapeutiques. L'objectif ultime était d'utiliser ces modèles pour optimiser les formulations médicamenteuses et les protocoles de traitement, renforçant ainsi leur efficacité immunothérapeutique et contribuant au développement de stratégies de médecine personnalisée.

En conclusion, cette thèse apporte des contributions significatives au domaine de l'ICD en combinant validation expérimentale et modélisation computationnelle innovante. Elle établit une base pour une compréhension plus intégrée de la manière dont les thérapies anticancéreuses peuvent être optimisées pour exploiter pleinement le potentiel du système immunitaire dans la lutte contre le cancer.

Mots clés : Mort Cellulaire Immunogène, Biologie des Systèmes, Cytokines, Modelisation en Silico

Abstract

This thesis aims to advance our understanding of Immunogenic Cell Death (ICD) and its potential to enhance the efficacy of chemotherapeutic treatments. By employing a multidisciplinary approach that integrates experimental and computational biology, this research addresses key questions essential for the progression of ICD research.

Despite the progress made in unraveling the molecular mechanisms of ICD, significant gaps in our knowledge remain. This thesis seeks to bridge these gaps by identifying critical factors and pathways involved in ICD and by developing computational models to predict and enhance the immunogenicity of chemotherapeutic agents.

A central focus of this work was the identification of a distinct molecular signature of ICD beyond the traditional hallmarks, such as released and surface-exposed DAMPs. Such a signature could serve as a reliable biomarker for predicting the immunogenic potential of chemotherapies. Additionally, the research investigated the secreted factors, particularly cytokines, that play a crucial role in initiating the cancer immunity cycle by recruiting and activating immune cells. Understanding these factors is key to optimizing the immunogenic potential of chemotherapeutic regimens.

Furthermore, the thesis delved into the cellular pathways that regulate the secretion and release of ICD-related DAMPs. By exploring the signaling networks and molecular mechanisms involved, the study aimed to uncover pathways that influence the immunogenicity of dying cells, potentially identifying new targets to amplify the immune response through ICD induction.

Building on these findings, the research also explored the feasibility of recapitulating ICD in silico. By integrating both established and newly identified hallmarks into computational models, the thesis aimed to simulate ICD processes, predict treatment outcomes, and guide future experimental efforts.

Finally, the thesis evaluated the predictive power of the developed in silico models in assessing the immunogenicity of chemotherapeutic drugs. The ultimate goal was to use these models to optimize drug formulations and treatment protocols, thereby enhancing their immunotherapeutic efficacy and contributing to the development of personalized medicine strategies.

In conclusion, this thesis makes significant contributions to the field of ICD by combining experimental validation with innovative computational modeling. It establishes a foundation for a more integrated understanding of how cancer therapies can be optimized to fully exploit the immune system's potential in combating cancer.

Keywords : Immunogenic Cell Death, Systems Biology, Cytokines, In silico Modeling

Contents

Liste des figures

Dedicato a Nonno Silvano
e a Zio Edo.

Chapter 1

Introduction

Aims

In this chapter I will introduce the founding principles of Immunogenic Cell Death in the context of cancer therapy. To complement the latter, general features of cancer biology and immunology will be provided.

1 Insights into the biology and epidemiology of cancer

1.1 Definition and epidemiology of cancer

The term *cancer* refers to a class of pathologies that show deregulations in cellular behavior.

A broader definition of cancer states that a cancer occurs when cells undergo uncontrolled proliferation far beyond their physiological boundaries causing the insurgence of diseases in the region where they are located and potentially, invading other tissues, and any other part of the organism.[1]

Cancer is today the second main cause of death in the world. The last report issued by the United Nations Agency for Research on Cancer estimated that in 2022 almost 20 million new cases of cancer were registered, as well as approximately 9.7 million deaths related to cancers [190]. Age-standardized estimates indicate Europe, North America, Japan, and Oceania as the world areas in which cancer has the highest rate of incidence, between 258.5 and 462.5 new cases every 100,000 individuals considering both male and female populations (Fig. 1.1 A). Worldwide, the rate of

[1] The term cancer, is a word derived from the latin term "cancĕr", which in turn is derived from the greek word *karkinós* (καρκινος) and means literally "crab". The first one to use the word in his writings was the ancient Greek physician Hippocrates (~460-370 B.C.). Even though originally indicated as a mythological monster, the word karkinós has been used by Hippocrates to indicate non-healing swelling or ulcerous formation, while the word *karkinoma* to describe non-healing "cancers" [100]. Previous testimony about diagnoses attributable to cancer also comes from Mesopotamian and Egyptian ancient civilizations, indicating the never-lasting occurrence of this phenomenon throughout history.

incidence for men and women is respectively of 238.3 and 196.4 new cases every 100,000 individuals [52]. The male population is primarily affected by lung cancer, followed by prostate and colorectal cancers, while the female population is predominantly impacted by breast cancer (Fig. 1.1 B)

In Europe, cancer incidence estimates show that Russia has the highest rate (14.2 % of total cases in Europe), followed closely by Germany (13.5 %), France (10.8 %) and the United Kingdom (10.2 %).

Breast cancer is the most common cancer affecting women in Europe (29 % of reported new cases), although the incidence rate is significantly higher than the corresponding mortality rate. For every 100,000 women, there are 147.6 new cases, while the mortality rate stands at 34.8 per 100,000. Other major cancers affecting the female population are colorectal, tracheal, bronchial, and pulmonary cancers[2]. The European male population is primarily affected by prostate cancer (22.4 % of incidence), malignancies of the trachea-bronchus-lung system (13.9 %) and colorectal cancers (13.3 %). The mortality rate for the trachea-bronchus-lung maligancies is 22.8 %, 12.4 % for colorectal cancer and 10.9 % for prostate cancer [47].

In France (Fig. 1.1 D), cancer tragically stands as the leading cause of death. According to the French National Institute for Demographic Studies (INED), in 2020, 186 out of every 100,000 men and 94 out of every 100,000 women were affected. Epidemiological studies grouping both genders indicate lung cancer as the most frequent, followed by breast and colorectal cancers.

The leading causes of cancers can be grouped into three main categories: biological (e.g., bacteria, viruses), chemical (e.g., formaldehyde, alcohol, tobacco, cadmium), and physical (e.g., ionizing and UV radiation). Additionally, aging represents a comorbidity factor as the risk of contracting cancer increases with age. Such incidence increases due to life-span accumulated genetic mutations that augment mutational burden and the concomitant decrease in the performance of DNA repair [112].

[2]https://ecis.jrc.ec.europa.eu/ Retr. 24/04/2024

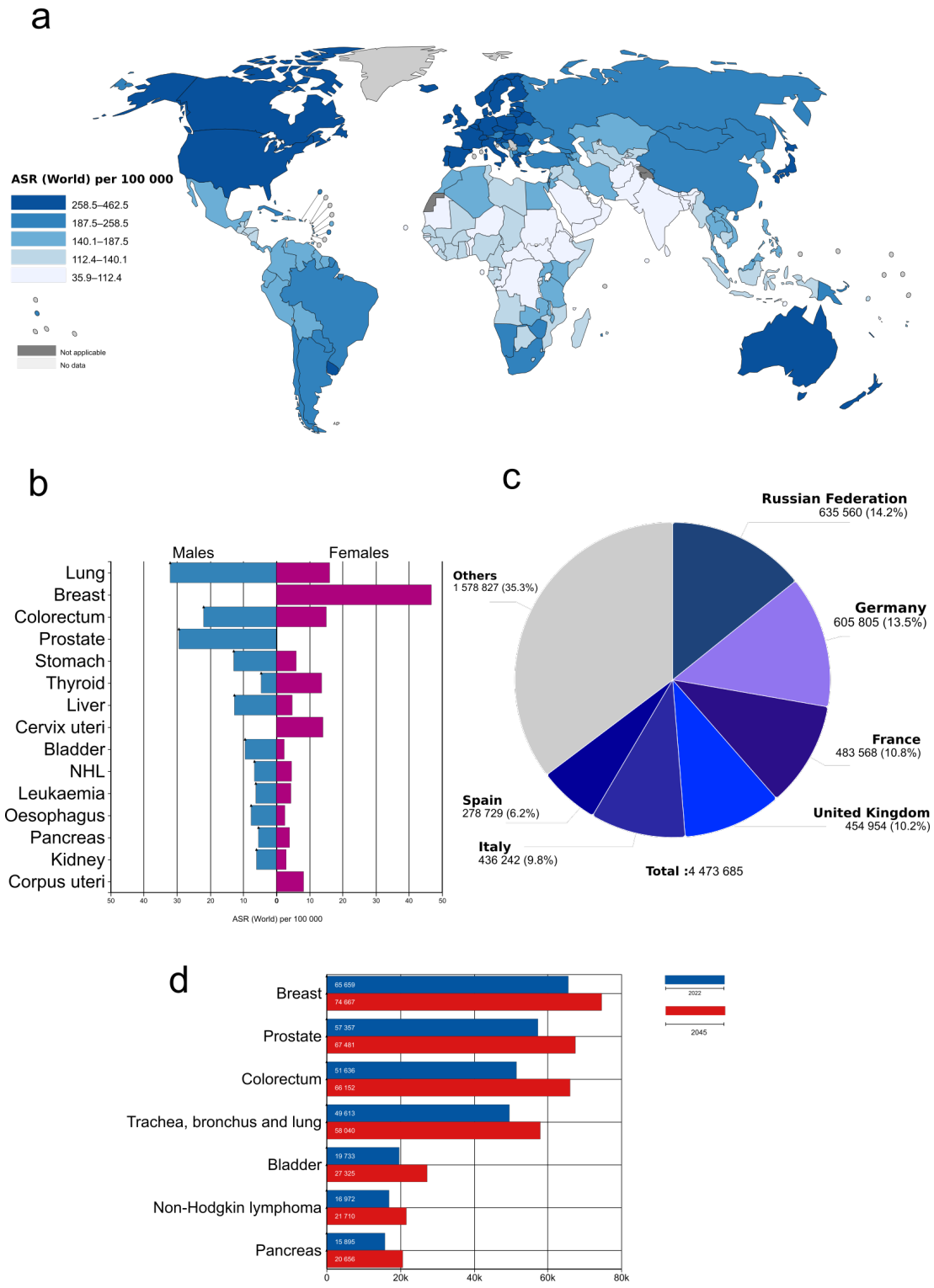

Figure 1.1: IARC - WHO 2022 report on worldwide cancer incidence: **a)** age-standardized-rate world distribution of cancer cases in 2022, **b)** male vs. female world incidence distribution, **c)** number of new cancer cases (all types, both sexes) in 2022 in Europe, **d)** number of new cancer cases in France by cancer type and 2045 projection (in red). https://gco.iarc.fr/today/en. Retrieved on 24/04/2024.

1.2 General features and mechanisms of tumorigenesis

The origin of cancers is a process known as *oncogenesis* and it is due to an incorrect process of DNA reparation, thus compromising gene functionality. Cell division may be impaired due to mutations responsible for i) the inactivation of genes identified as tumor suppressors (i.e., controlling the machinery of DNA replication), such as BRCA2, and ii) the constitutive activation of pro-oncogenic factors (i.e., genes encoding factors that drive cell proliferation), like PDGF or ERBB2. Mutations induced in those genes can be conserved because of incorrect DNA reparation and promote clonal expansion of the mutated cells, finally leading to tissue hyperplasia. The accumulation of additional genetic modifications allows pre-malignant cells to pass from a tumor promotional phase to a progression stage. As a consequence, malignant cells can invade the adjacent tissues or even migrate to other sites and form metastasis. The uniqueness of the processes leading to the accumulation of mutations within each cancer type (and each individual) helps shape the intrinsic complexity in the identification of general and effective diagnostic tools and treatment programs.

In 2000, the foundational paper titled *"The Hallmarks of Cancer*, [71] identified six common features shared by several cancer types. The authors defined the scientific paradigm for cancer as a multifaceted phenomenon characterized by a limitless replication potential, the ability to invade other tissue and induce metastasis, its capability to induce angiogenesis, to evade apoptosis, the autocrine supply of growth signals, and the insensitivity to anti-growth signals. Within the last twenty years, the set of hallmarks increased first to ten[72] including genome instability and mutational potential, deregulation in cellular energetic balance, tumor-induced and sustained by the tumor, and the avoidance of immune destruction. As a follow-up publication, the same authors updated the list to fourteen[70] hallmarks, with the addition of the non-mutational epigenetic reprogramming of cancer precursor, the pro-tumorigenic effect of senescent cells, plasticity in phenotypic differentiation and the interplay between cancer and microbiota modulating factors such as growth, inflammation and/or immune evasion.

In a recent perspective article, Swanton and colleagues [170] insisted on the need for a shift in the approach used by the scientific community to understanding cancer pathogenesis, moving from dogmatic reasoning based on the hallmarks of cancer to a broader view of cancer as a complex systemic disease (fig: 1.2). A new systemic approach to decipher cancer pathogenesis is therefore focused on dynamical properties influenced by various factors, including age, environmental exposures, and systemic changes induced by cancer. Moreover, cancer development involves a complex interplay of genetic mutations and environmental factors, with significant influence from the tumor micro- and macro-environments.

The tumor microenvironment. The tumor microenvironment, or TME, is composed of several cell populations encompassing cancer cells, tumor-associated stromal cells (i.e., cancer-associated mesenchymal stem cells (MSCs), fibroblasts, adipocytes, pericytes, and endothelial cells), as well as immune cells (fig: 1.3) e.g., macrophages, dendritic cells (DCs), neutrophils, T cells. [3].

These populations of the TME form cellular niches that interact dynamically and play crucial roles in tumor behavior, treatment response, and immune surveillance. The potential to improve therapeutic interventions relies on understanding these niches, in order to manipulate specific cell types or signaling pathways. Moreover, the significance of cellular niches becomes especially apparent in the context of metastatic colonization, where specific components within dormant niches play a crucial role in maintaining metastatic cells in a quiescent state, thereby enabling their eventual outgrowth. However, the characteristics of these dormant niches and how they evolve over time are still not well understood. Advancements in spatially-resolved omics technologies have enabled researchers to further characterize these cellular niches within the TME, revealing their complex nature and spatial organization [148]. This understanding has led to the identification of tissue-intrinsic immune-regulatory landscapes, regenerative programs, and other phenotypic states associated with some tumor niches, paving the way for new classifications of tumors.

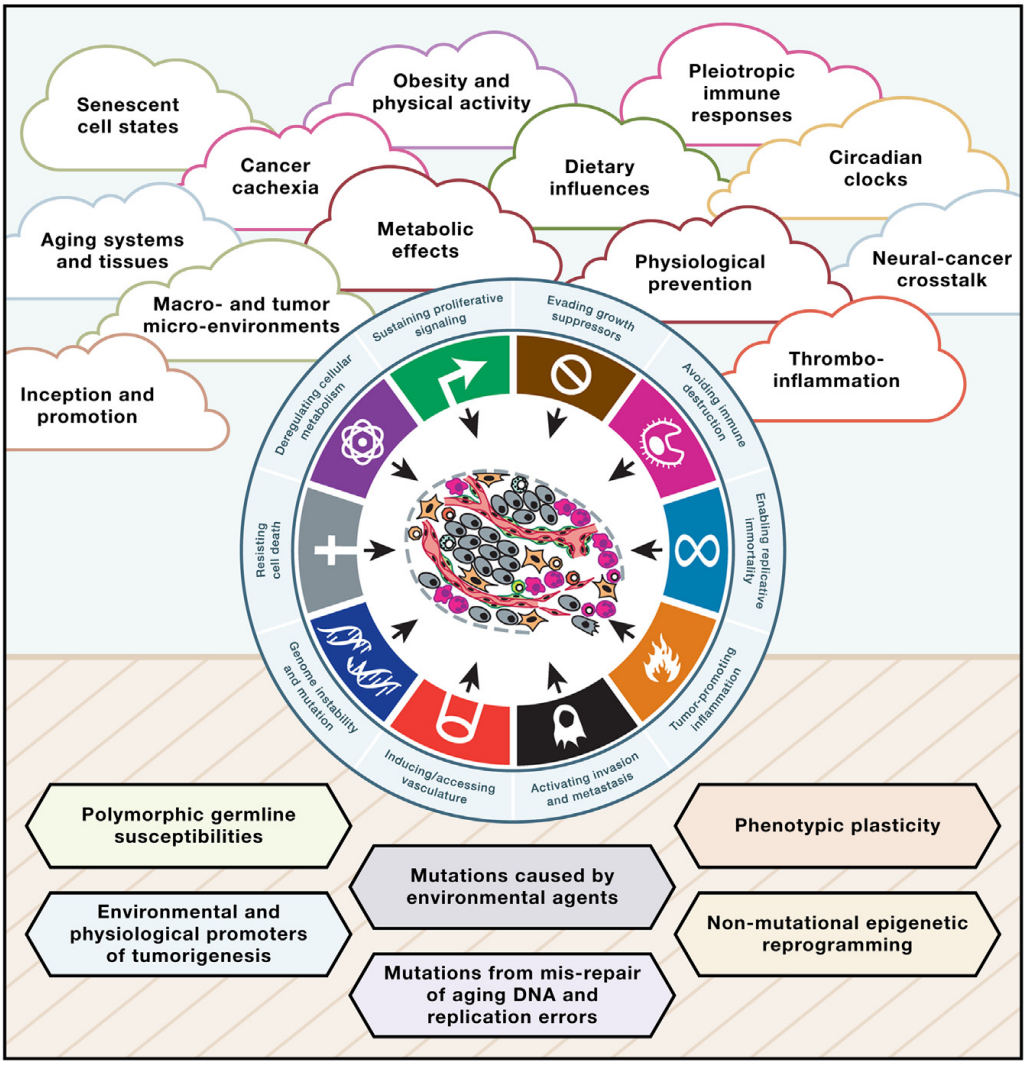

Figure 1.2: The hallmarks of Cancer and the "clouds of complexity". This image presents a holistic view of cancer pathogenesis. At the center, the hallmarks of cancer are depicted, underpinned by established mechanistic effectors that regulate and promote cancer initiation and progression, although a complete understanding of these processes remains elusive. At the top, the clouds represent factors that significantly influence cancer pathogenesis and progression, but whose impacts are not yet fully understood. *Image from Swanton C et al., Embracing cancer complexity: Hallmarks of systemic disease. Cell. 2024*

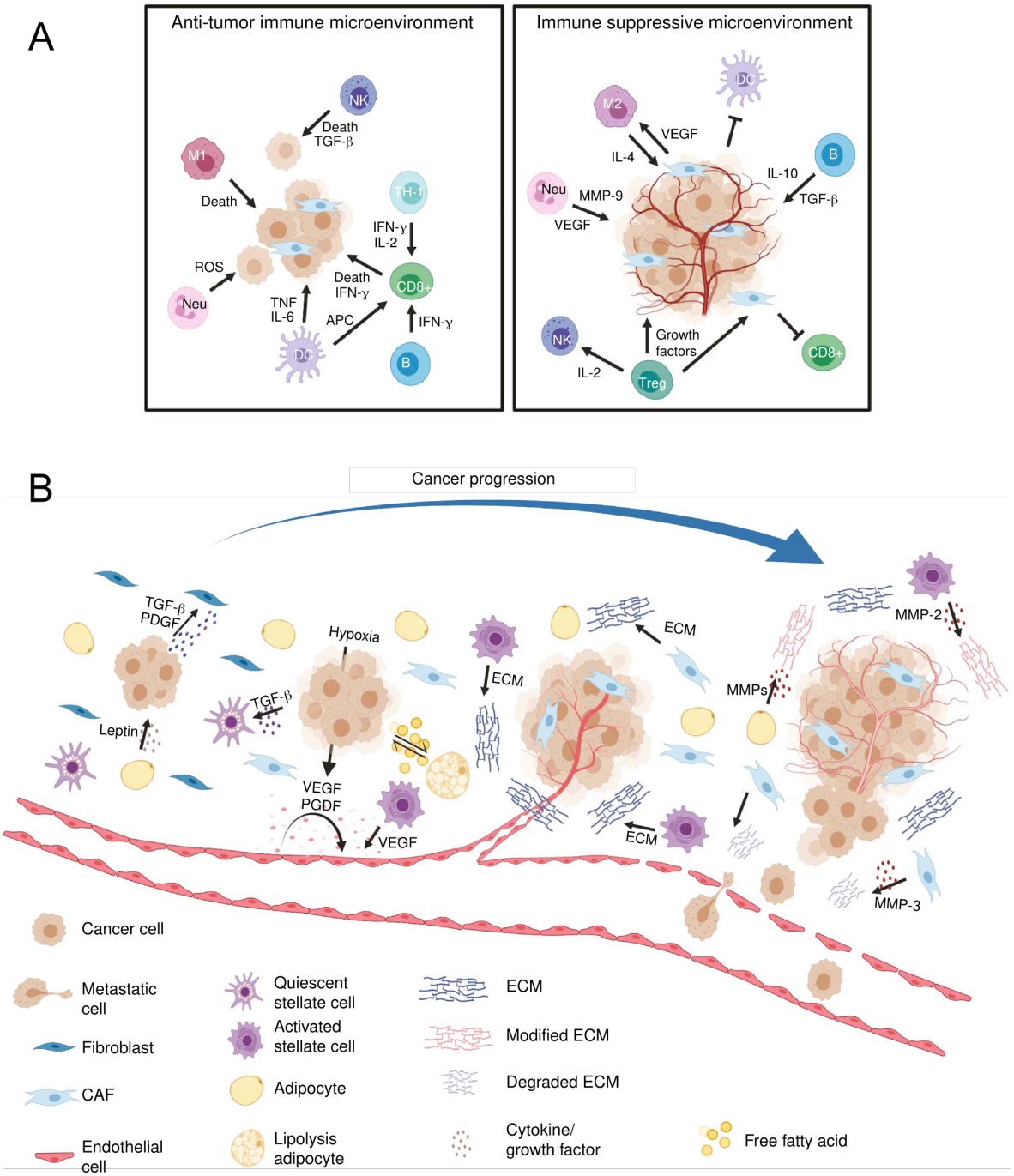

Figure 1.3: The tumor microenvironment: **A.** Left: The antitumor immune microenvironment composed of heterogeneous immune cell populations contributes to tumor surveillance and suppresses tumor formation. Right: an alternative scenario is given by other immune cell types playing pro-inflammatory and pro-tumorigenic roles. **B.** Non-immune cells populating the TME regulate angiogenesis, proliferation, invasion, and metastasis by secreting growth factors and cytokines. *Image adapted from Anderson NM, Simon MC. The tumor microenvironment. Curr Biol. 2020*

The tumor macro-environment. The term "tumor macro-environment" refers to the wide set of factors - systemic and environmental - affecting and affected by tumor development and progression. Among these factors, we can list physiological, metabolic, and immunological elements from distant organs and tissues, as well as systemic responses to tumor growth and progression (e.g., cachexia). Moreover, tumor-induced changes in the immune system extend beyond the local environment,

significantly altering the systemic immune landscape during cancer progression: molecules secreted by cancer cells, immune, and non-immune stromal cells can influence the organism globally. Key mechanisms include tumor's autocrine effects, therapy-induced secretory phenotypes[113], DNA damage responses in genetically unstable tumor cells (e.g., the secretion of type 1 interferon [IFN-I])[24], microbial influences from diet and environment, and stress-induced metabolites [49]. These factors contribute to dysregulated myelopoiesis and a pro-tumorigenic macro-environment. Furthermore, systemic immune responses are influenced by physiological changes such as circadian rhythms and, as mentioned before, stress.

In the following subsection, I will delineate the principles underlying the influence of immunity in antitumor therapy. This discussion will include the mechanisms through which the immune system identifies and attacks tumor cells, the function of immune checkpoints, and the therapeutic approaches designed to amplify antitumor immune activity.

1.3 Cancer treatments

Although surgery still constitutes most point-wise interventions in cancer treatment lines, surgical removal of malignant neoplasms is often supported by additional therapies. Until the 1960s, radiation therapy and surgery have been the primary options in the treatment of solid cancer. In the case of radiation therapy, for more than a century, ionizing radiation has been utilized in cancer treatment, exploiting the vulnerability of rapidly dividing cancer cells compared to normal cells. Its primary impact on tissues is direct cell death, largely through DNA damage, leading to reduced cell populations and impaired function. Ionizing radiation can directly damage cellular molecules or indirectly generate free radicals through the ionization or excitation of water molecules. However, the emergence of micrometastases and cancer recurrence after these treatments prompted the rise of combination chemotherapy as a significant strategy in cancer management.

Chemotherapy is a term that encompasses a class of drugs that aims to halt the proliferation of cells and the spread of tumors, thus preventing invasion and metastasis. Tumor growth inhibition occurs at various levels within the cell and its surroundings. Conventional chemotherapy agents can be categorized based on their mechanism of action. Overall, by interfering with DNA, RNA, or protein synthesis, or by affecting their activity, chemotherapies can disrupt macromolecular synthesis and impair cancerous cell functions. This interference, when sufficient, leads to cell cycle arrest and death, particularly apoptosis. Repeated doses of chemotherapy may be necessary to achieve a response. The efficacy of cytotoxic drugs is most pronounced during the S phase of the cell cycle when DNA synthesis occurs. Yet, alkaloids and taxanes act during the M phase, by blocking mitotic spindle formation.

Combination chemotherapy is often employed to elicit adequate responses and appears to hinder

the emergence of resistant cell clones by enhancing cytotoxicity in both resting and dividing cells. The cellular mechanisms governing proliferation and differentiation are complex. Numerous receptors and signal transduction pathways are at work, regulating cell differentiation, growth, and survival, as well as tumor angiogenesis and metastasis. Some of these pathways can be selectively inhibited with molecularly targeted therapies.

Chemotherapy can be administered in various modalities, including neoadjuvant[3], adjuvant[4], and combined with additional treatments. Adjuvant therapy has become standard practice for breast, lung, colorectal, and ovarian cancers. Combined modalities, including chemotherapy and radiation, are utilized to shrink tumors before surgery or with curative intent in cancers such as those affecting the head and neck, lungs, or anus.

Aside from chemotherapy, immunotherapy has emerged as a groundbreaking development in cancer treatment. The application of immunological findings to cancer therapy has steadily risen in recent decades, driven by major breakthroughs that have propelled the field of research forward. In the following section, we will outline the significant milestones that have shaped the advancement of immunology-based research in cancer therapy over the past century, and we will also delve into the current approaches in the field of immunotherapy.

[3]Neoadjuvant treatments are given as a first step to shrink a tumor before the main treatment, which is usually surgery. They include chemotherapy, radiation therapy, and hormone therapy. It is a type of induction therapy. (NIH, Dictionary of Cancer Terms https://www.cancer.gov/publications/dictionaries/cancer-terms/def/neoadjuvant-therapy. Retrieved on 24/04/24)

[4]Adjuvant therapies are given after the primary treatment to lower the risk of cancer relapse. They include chemotherapy, radiation therapy, hormone therapy, targeted therapy, or biological therapy. (NIH, Dictionary of Cancer Terms https://www.cancer.gov/publications/dictionaries/cancer-terms/def/adjuvant-therapy. Retrieved on 24/04/2024)

2 Immune system and cancer

2.1 From Immunoediting to Immunotherapy: The Evolution of Cancer Treatment

The immune system plays a dual role in the context of cancer, known as immunoediting. This process includes both the identification and elimination of cancer cells (immunosurveillance) and the selection of cancer cells that can escape immune detection, leading to tumor development. Immunoediting can be divided into three phases: elimination, equilibrium, and escape.

During the elimination phase, the immune system identifies and eradicates cancer cells. Cytotoxic CD8+ T cells recognize tumor antigens presented on major histocompatibility complexes (MHC-I, II) on the surface of tumor cells, leading to their destruction. On one hand, these tumor antigens can be self-antigens with aberrant/abnormal expression, also referred to as tumor-associated antigens (TAAs). For instance, NY-ESO1 (New York esophageal squamous cell carcinoma 1) is normally expressed in the testis but can be detected in several tumors, such as esophageal, lung, and hepatocellular carcinomas [178]. On the other hand, tumor antigens can be non-self-antigens, also referred to as tumor-specific antigens (TSAs). These latter can be derived from oncogenic viruses or result from mutations accumulated during carcinogenesis and are known as neoantigens.

In the equilibrium phase, some cancer cells that survive the initial immune response undergo genetic and epigenetic changes that enhance their resistance to immune attack. This phase represents a dynamic state where the immune system continuously exerts selective pressure on the cancer cells, leading to the survival of more resistant variants.

Finally, during the escape phase, cancer cells that have acquired resistance to immune detection proliferate uncontrollably, resulting in the emergence of tumors. This model is supported by observations that tumors from immunodeficient mice are more immunogenic than those from immunocompetent mice [155].

The discovery of the role played by cytokines such as interferon γ (IFNG) in immunosurveillance and the increasing understanding of immunoediting have laid the foundation for the development of cancer immunotherapies. These therapies aim to restore and enhance the immune system's ability to recognize and destroy cancer cells, counteracting the mechanisms that allow tumors to evade immune detection.

2.2 General features of antitumor immunity

2.2.1 Innate and adaptive immunity

The immune system orchestrates a sophisticated defense against cancer, deploying a multifaceted response to eliminate malignant cells. Comprising innate and adaptive immunity, these defense

mechanisms cooperate to detect and eradicate tumors. Innate immunity acts as the frontline, swiftly recognizing cancerous cells via diverse receptors. Both innate and adaptive immune cells secrete cytokines such as IFNs, tumor necrosis factors (TNFs), and interleukins (ILs), further modulating the immune response against cancer. Macrophages, neutrophils, DCs, and natural killer (NK) cells form the cornerstone of the innate arm, initiating inflammation, phagocytosis, and cytokine release to combat tumors (**Fig.** 1.3 A). On the other side, T lymphocytes are key adaptive mediators/effectors of antitumor activity. However, as reported in the previous sections, tumor progression reshapes the immune microenvironment by releasing proinflammatory ligands like TNF-α, IL-1, and IL-6, transforming growth factor (TGF)-β, which contribute to altering immune responses and ensure cancer survival.

Adaptive immunity tailors responses upon encountering tumor antigens. Antigen-presenting cells (APCs), predominantly DCs, capture and present tumor antigens via MHC molecules to T cells. DCs serve as crucial mediators bridging the innate and adaptive immune responses, especially in the realm of cancer. Upon the immunogenic demise of cancer cells, a cascade of damage-associated molecular patterns (DAMPs) is unleashed and constitutes the repertoire of alarm signals that trigger immune system activation. Equipped with pattern recognition receptors (PRRs), DCs discern these DAMPs, prompting their maturation and upregulation of co-stimulatory molecules and MHC molecules. Subsequently, mature DCs migrate to the lymph nodes, where they present tumor antigens to T cells, fostering the proliferation and differentiation of antigen-specific T and B cells. Crucial in this process, cytotoxic T lymphocytes (CTLs) and helper T cells coordinate cellular immunity against cancer.

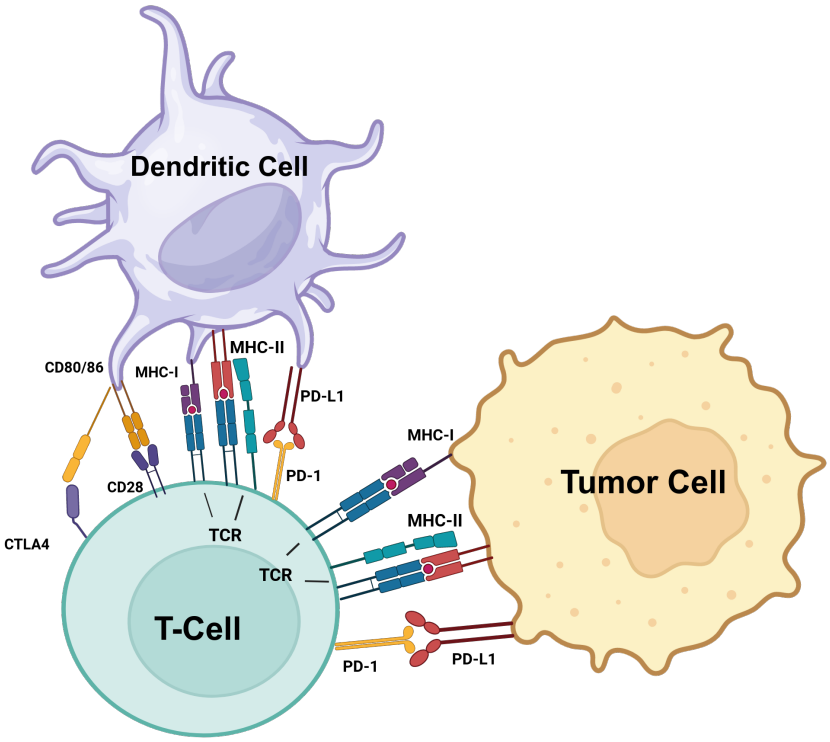

Figure 1.4: Co-stimulatory and co-inhibitory landscape: Co-stimulatory cues, like the interaction between CD28 on T cells and CD80/86 on DCs, combined with the recognition of major histocompatibility complex class I and II (MHC-I/II) molecules on cancer cells by the T cell receptor (TCR), stimulate T cell activation and proliferation, bolstering the immune response against cancer. Conversely, inhibitory signals, such as PD-1 on T cells engaging with PD-L1 on cancer cells or CTLA-4 outcompeting CD28 for CD80/86 binding, inhibit T cell activity, enabling cancer cells to evade immune surveillance.

2.3 Immunogenic Cell Death in Cancer Therapy

2.3.1 Forms of Cell Death

In response to microenvironmental challenges, mammalian cells activate signaling pathways aimed at restoring cellular homeostasis. However, if these challenges exceed cellular repair capacities, the same molecular cascades initially supporting cytoprotection, shift towards promoting regulated cell death (RCD)[171]. RCD can occur via various mechanisms, depending on factors such as the nature of the perturbation and cellular characteristics.

The classification of cell death modalities has long been a subject of debate in cell biology. Historically, it was relying onthe morphological and structural features of the dying cells. Among the classical forms of cell death, type 1 cell death - commonly referred to as apoptosis - is characterized by cell shrinkage, membrane blebbing as well as DNA fragmentation, and chromatin condensation. Type 2 cell death refers to autophagy-dependent forms of cell death. Type 3 cell death refers to

necrosis, which is characterized by a general loss of integrity of the cell membrane and a consequent spillage of subcellular components. While necrosis has been considered an unregulated form of cell death, necroptosis constitutes its regulated counterpart.

Currently, cell death modalities are separated into two main categories: accidental cell death (ACD) and RCD, based on functional aspects. ACD occurs when cellular homeostatic controls are overruled by unpredictable events that compromise cellular stability. On the other hand, regulated forms of cell death include specific signaling pathways and molecular effectors. Among RCD modalities, apoptosis, necroptosis, ferroptosis, parthanatos and autophagy-dependent cell death can be listed. Some forms of RCD are furthermore characterized by their efferocytosis-like features and immunologically silent/tolerogenic: cells degraded following the activation of one of the RCD programs are phagocytated without activating any immune response. This is a property of standard apoptosis. Conversely, some forms of RCD activate an immune response and are thus non-tolerogenic/immunogenic; this aspect will be expanded in the next section.

Efferocytosis is therefore a fundamental process in maintaining homeostasis and preventing dysfunctional inflammatory processes; dysregulations in its mechanism promote disease establishment. Efferocytosis ensures the production of anti-inflammatory cytokines while simultaneously repressing proinflammatory cytokines, therefore promoting inflammation resolution.

2.3.2 The Hallmarks of Immunogenic Cell Death

Some forms of cell death - whether they are RCD or ACD - can engage an adaptive immune response against antigens captured from deceased cells. This phenomenon has been identified as "immunogenic cell death" (ICD). In opposition to silent efferocytosis, considered to be a tolerogenic process, some RCD modalities are able - under specific circumstances - to trigger an adaptive immune reactivity. To benefit from the immunosurveillance functions exerted by actors of adaptive immunity, such as conventional T cells, three conditions need to be filled: dying cells need to provide i) adjuvanticity, as well as ii) antigenicity, to attract and activate the immune sentinels and effectors, and iii) the microenvironment needs to be permissive to the establishment of such local immune recruitment and reactivity [96].

Antigenicity arises from the capture of TSA and TAA from dying cells by APCs, and their subsequent cross-presentation on MHC molecules to T cells. These latter can achieve clearance of surviving malignant cells sharing an immunopeptidome homology (i.e. common antigen epitopes presented onto MHCs). Of note, stress conditions imposed on cancer cells via immunogenic interventions are capable of enhancing both the production of tumor antigens, notably neoantigens, and the expression of MHC molecules on tumor cells' surface [205].

To overcome peripheral tolerance or prevent T cell energy, antigenicity must be complemented by adjuvanticity. The latter property stimulates APC recruitment and activation, and their subsequent ability to provide proinflammatory and co-stimulatory signals required for T cell priming (Fig. 1.4) [154]. Adjuvanticity originates from the release of DAMPs by cancer cells stressed/dying upon cytotoxic interventions. These danger signals can be detected by PRRs, on APCs' surface [121, 66]. Within the last two decades, intensive investigation has been conducted on the release of DAMPs by cancer cells induced by several therapeutic approaches such as conventional chemotherapeutic [27], radiotherapy [136], photodynamic therapy [59], and oncolytic virotherapy [115]. Scientific community-driven initiatives have endeavored to delineate the repertoire of DAMPs, elucidating the features contributing to defining a common set of features for ICD across diverse therapeutic contexts [55].

2.3.3 Molecular features of ICD

The set of DAMPs that are considered characteristic hallmarks of ICD comprises: the chaperone protein Calreticulin (CALR), extracellular detected adenosine triphosphate (ATP), high mobility group box 1 (HMGB1), type I interferon response, and Annexin A1 (ANXA1). Although a consensus has been established for the first three, the two latter appear to be contextual to a type of ICD induced by chemotherapies [11, 183] and have been less investigated than CALR, ATP and HMGB1. In this section, we will provide a compendium on the available knowledge circa the mechanistic machinery regulating the exposure and the release of the different DAMPs constituting the molecular signature of chemotherapy-induced ICD.

CALR exposure CALR is a 60 kDa endoplasmic reticulum (ER) resident protein. Under homeostatic conditions, CALR serves as an essential molecular chaperone within the ER lumen where it operates in concert with calnexin for protein quality control and with protein disulfide-isomerase A3 (PDIA3 or ERp57) for protein folding. In contrast to calnexin, which is anchored to ER membrane, CALR can freely move within the ER lumen, and supply the Ca^{2+} needed for both proteins to exert their chaperone functions via its high capacity calcium binding C-domain [126].

Under stress conditions initiated by ICD inducers, CALR is exposed on the surface of dying cancer cells with other ER chaperone proteins, including heat shock protein 70 and 90 (HSP70, HSP90) as well as the above-mentioned PDIA3. The absence of phosphatidylserine when CALR is exposed on cell membranes indicates that apoptosis has not occurred yet and that the presence of CALR is not a consequence of membrane modifications following the apoptotic program [136].

The path to CALR exposure involves a signaling cascade originating from the ER stress caused by

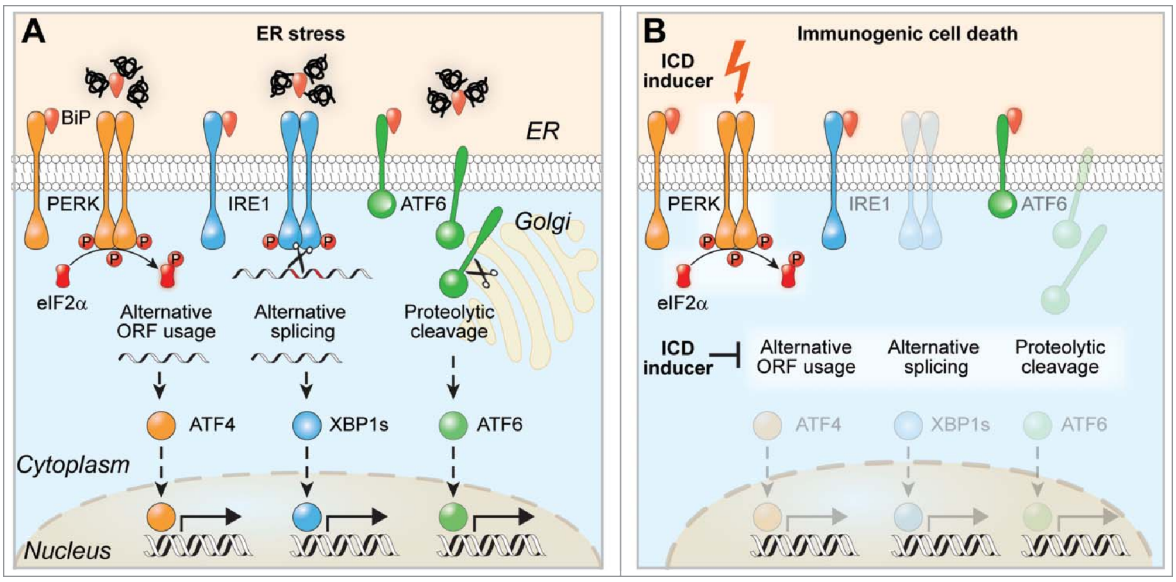

Figure 1.5: ER stress activated pathways leading to CALR exposure. A ER stress activates three pathways: **(i)** PERK-mediated eIF2α phosphorylation leading to ATF4 translation, **(ii)** IRE1 dimerization causing XBP1 alternative splicing, and **(iii)** ATF6 translocation to the Golgi for cleavage and nuclear translocation. These processes aim to eliminate or repair misfolded proteins. B. Immunogenic cell death (ICD) inducers like anthracyclines or oxaliplatin only mediate PERK-dependent eIF2α phosphorylation. Image adapted from [17]

ICD inducers resolved by the activation of the unfolded protein response pathway (UPR). Downstream, the UPR diversifies its mechanism through three different branches including the eukaryotic translation initiation factor 2-alpha kinase 3 (eIF2AK3), also known as the dsRNA activated protein kinase-like ER kinase (PERK), the activating transcription factor 6 (ATF6), and serine/threonine-protein kinase/endoribonuclease inositol-requiring enzyme 1α (IRE1α). These three molecular sensors interact with BiP/GRP78, with stress triggering BiP/GRP78 dissociation and UPR activation.

ATF6 is a type II ER transmembrane protein with a transcriptional activation domain in its cytosolic region. ATF6 has two isoforms, ATF6α and ATF6β. ATF6β regulates CALR gene expression, vital for neuronal survival and ER Ca2+ balance under stress conditions, thereby enhancing ER Ca2+ capacity. This upregulation supports augmented ER-mitochondrial contacts, enabling Ca2+ transfer to mitochondria for ATP production, crucial for energy maintenance during stress. On the other hand, upon dissociation from BiP, ATF6α moves from the ER membrane to the Golgi, where it is cleaved by site 1 and site 2 proteases (S1P and S2P). This cleavage generates an active basic leucine zipper (b-ZIP) factor, the N-terminal fragment of ATF6α, which then translocates to the nucleus to activate UPR genes, including those that promote protein folding by overexpressing chaperones, X-box binding protein 1 (XBP1), and BiP.

IRE1α, a type I ER transmembrane endoribonuclease/kinase, has a kinase domain and an endoribonuclease domain in its cytosolic N-terminal luminal domain. The activation of IRE1α occurs through dimerization and autophosphorylation and facilitates the downstream splicing of XBP1 mRNA. The spliced XBP1 encodes a b-ZIP transcription factor (TF) that upregulates UPR genes

involved in ER-associated protein degradation (ERAD) and protein folding.

The third viable UPR branch involves the dissociation of eIF2AK3 from BiP. This process induces the phosphorylation of eukaryotic initiation factor 2α (eIF2α) resulting in the attenuation of messenger RNA (mRNA) translation by inhibiting the formation of cap-dependent ribosomal initiation complexes. Moreover, phosphorylated EIF2α specifically promotes the translation of mRNA encoding ATF4, a b-ZIP TF (Fig 1.5). ATF4 induces growth arrest and enhances the expression of genes related to chaperones, antioxidants, XBP1, and DNA damage-inducible transcript 3 (DDIT3). In the context of ICD-inducing chemotherapies, the exposure of CALR is achieved through the EIF2α phosphorylation, mediated by EIF2AK3. Cell lines used for these observations included murine methylcholanthrene-induced fibrosarcoma MCA205, human osteosarcoma U2OS, and colon carcinoma CT26. However, recent studies have shown that in human melanoma cells, anthracyclines induce EIF2α phosphorylation through other kinases: EIF2AK2 or EIF2AK4. Under UPR activation, the translocation of CALR from the ER lumen to the cell's membrane occurs via the Golgi apparatus: a complex formed by CALR and PDIA3 is finally able to reach the external membrane in an exocytotic manner with N-ethylmaleimide-sensitive-factor attachment protein receptors (SNARE).

Once exposed, CALR provides an "eat-me signal" for myeloid cells. Proximal DCs (and macrophages) expressing the CALR-binding lipoprotein receptor-related protein 1 (LRP1) can uptake the antigens loaded on MHC molecules presented on the surface of dying cancer cells.

Extracellular release of ATP. Prior to an "eat-me" signal, it is crucial for APCs to receive a "find-me" signal that would play a chemotactic role and favor APC migration to dying tumor cells undergoing ICD. The ATP released by stressed cells constitutes an adjuvant signal and provides such pro-migration signaling. ATP is an essential metabolite that fuels most of the biochemical processes in eukaryote organisms. Under normal circumstances, the ATP concentration within a cell ranges between 3 and 10mM, while in the proximal extracellular space, the concentration normally shrinks to 10nM. The concentration levels (inner and outer) are preserved by the activity of ectonucleoside triphosphate diphosphohydrolase 1 (ENTPD1, also known as CD39) and 5'-nucleotidase (NT5E or CD73). These two enzymes hydrolyze ATP into adenosine diphosphate (ADP), adenosine monophosphate (AMP) with ENTPD1 and ultimately in adenosine (ADO) via NT5E [161]. The two enzymes are expressed in both tumor cells and immune cells, with a particular predominance for ENTPD1.

ATP binds to two classes of receptors, called purinergic receptors: P2XR which is an ATP-gated ion channels, and P2YR G protein-coupled receptors (Fig. 1.6. Both receptors are expressed by several cancer cell lines and primary tumors, as well as host cells such as immune cells, notably DCs. Moreover, by binding to P2X7R receptors expressed by DCs, extracellular ATP is also responsible for

the up-regulation of maturation markers such as CD80 or CD86 and, in human PBMCs for class II MHC [140].

The presence of extracellular ATP has been positively correlated with type 1 helper $CD4^+$ T cells (Th1) and $CD8^+$ T cells, as a consequence of APC activation and maturation, such as for DCs. On the other hand, extracellular ADO favors some immunosuppressive features of the TME, for instance promoting $CD4^+$ T cell differentiation into regulatory T cells (Tregs) and their immunosuppressive function by binding to their adenosine A2A receptor (A2AR)[161]. Adenosine receptors are also expressed on dendritic cells: for immature DCs, extracellular ADO increases their chemotaxis but for mature ones, adenosine receptor activation induces pro-inflammatory, angiogenic, immuno-suppressive, and tolerogenic factors, reducing de facto their cross-presentation potential [2].

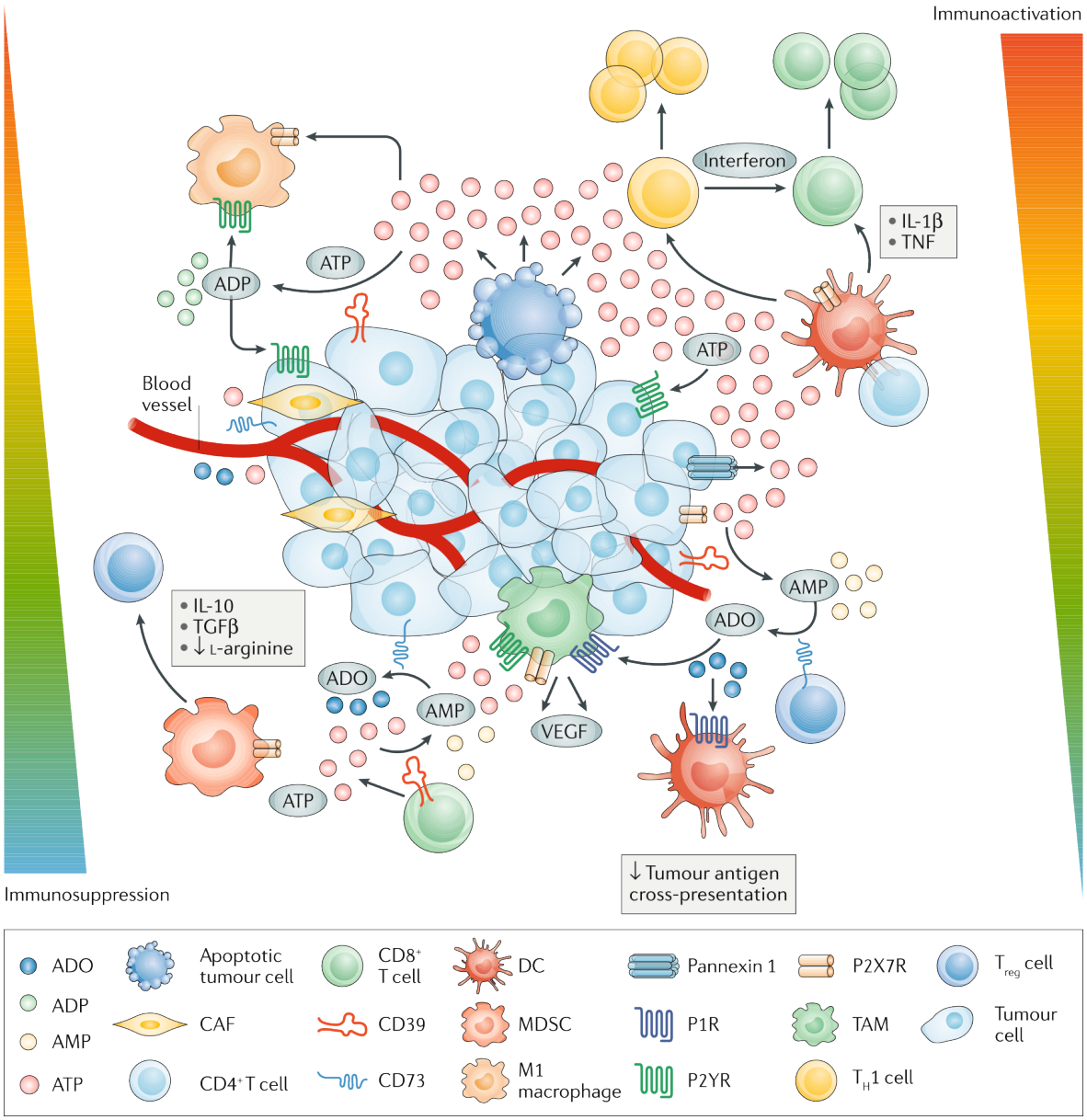

Figure 1.6: ATP release mechanisms in the TME. ATP is released into the TME through various mechanisms: cell death-induced efflux, plasma membrane transporters, exocytosis, and microvesicle shedding. In the TME, ATP can either bolster antitumor immunity or foster immunosuppression. It activates NLRP3 inflammasome in macrophages and DCs, triggering cytokine release and antigen presentation. ATP breakdown by ectonucleotidases generates ADP, AMP, and adenosine (ADO), impacting purinergic receptors on tumor and immune cells. ADO promotes immunosuppression by inhibiting DC antigen presentation, fostering M2 macrophages, and recruiting MDSCs, creating a highly immunosuppressive TME.

Moreover, in a TME characterized by a low concentration of extracellular ATP, myeloid cells such as tumor-associated macrophages (TAMs) or myeloid-derived suppressor cells (MDSCs) favor an immune-inhibitory environment. For instance, when ATP binds to the purinergic receptors expressed by MDSCs, it drives the accumulation of arginase and the following release of proinflammatory signals such as IL10, or TGFβ, thus promoting the recruitment and differentiation of Tregs within the TME.

ATP can be released due to several possible stimuli, such as inflammation, hypoxia, tissue damage, and other cell stress. Among these stimuli, ICD-inducing therapies are capable of triggering

the extracellular release of ATP. Immune cells, as well as cancer cells, express pathways that support ATP accumulation in the TME, with pannexin 1 (PANX1) being a key pathway for ATP efflux in many cell types. PANX1 plays a crucial role in purinergic signaling and features a feedback inhibition mechanism where ATP binding to its low-affinity extracellular site prevents excessive ATP accumulation. Additionally, PANX1 is activated during chemotherapeutic drug-induced apoptosis via effector CASP3. Upon ICD induction, ATP can also be released by tumor cells via autophagy. This phenomenon is a process that involves the engulfment of cytoplasmatic material into double-membrane vesicles, the autophagosomes. The latter then fusion with lysosomes to create autolysosomes, where the engulfed material is degraded. In anthracycline-induced ICD, the autophagic pathway is activated and intracellular ATP is secreted through autolysosomes that are transported to the cell membrane via lysosomal-associated membrane protein 1 (LAMP1). Under the administration of anthracyclines, the down-regulation or knock-down of autophagy factors, such as the autophagy proteins 5, 7, 10, 12 (ATG5, ATG7, ATG10, ATG12), Beclin 1 (BECN1) or LAMP1, have been associated with reduced ATP release and, consequently, with ICD failure and a diminished T cell activation [127] However, autophagy is not necessary for ICD induced by hypericin-based PDT and its inhibition can enhance immune cell activation [57].

Extracellular release of HMGB1. High mobility group box 1 (HMGB1) is a phylogenetically conserved nuclear protein (99% homology between human and mouse [53]) and highly expressed in all mammalian cells. Under normal circumstances, HMGB1 binds to chromatin, and stress conditions can activate pathways that lead to its release from the nucleus and, consequently, its shuttling to the cytoplasm. Post-translational modifications to the nuclear localization signals (NLS) of HMGB1 (NLS1 and NLS2) are responsible for its release [174]. Such modifications comprise the acetylation or deacetylation operated by histone acetyltransferases (HATs), such as acetyltransferase 2B (KAT2B), CREB-binding protein (also known as CREBBP or KAT3A) and histone acetyltransferase p300 (EP300), and by histone deacetylases (HDACs). In any case, once HMGB1 has been released from its nuclear binding site, the acetylation of lysine in the NLS prevents its return to the nucleus. Under persistent oxidative stress, HMGB1 binds to nuclear exporter exporting 1 (XPO1) and gets transferred to the cytoplasm following acetylation. Release of HMGB1 from the nucleus via its (de)acetylation can be triggered by various pathways including sirtuin 1 (SIRT1) [194], Janus kinase 1 (JAK1)/signal transducer and activator of transcription (STAT1) [114], or protein kinase C (PKC), which also phosphorylates serine residuals (Ser35,Ser39 and Ser42) in the the two NLS[137]. Release mechanisms have been divided into two categories: active and passive.

Active processes have been studied since the first observations made on HMGB1 release following lipopolysaccharide (LPS) stimulation [187]. HMGB1 is not secreted through the conventional

ER-Golgi secretory machinery. Most of the active release models indicate that in response to stimuli, HMGB1 translocates from the nucleus to the cytoplasm and its release occurs via lysosomes (or autophagosomes) and the consequent fusion with the cell membrane. Alternatively, in case of necrosis, the compromised cell membrane allows passive diffusion of HMGB1 in the extra-cellular medium. Modulators of active secretion include reactive oxygen species (ROS), calcium ions, XPO1, and Tumor Protein 53 (TP53). Oxidative stress is regulated by the NFE2-like b-ZIP transcription factor (NFE2L2 or NRF2), which enhances the transcription of antioxidant genes, including heme oxygenase-1 (HMOX1). HMOX1 plays a role in inhibiting the oxidative stress-induced translocation of HMGB1 into the cytosol, establishing a feedback loop that mitigates cellular damage triggered by oxidative stress. This feedback mechanism helps maintain cellular homeostasis by counteracting the harmful effects of oxidative stress [128].

Supporting evidence of HMGB1 active release indicates that in human colon cancer cells, in response to oxidative stress or starvation, the extra-nuclear shuttling of HMGB1 increases the autophagic flux [172]. Calcium ions behave as second messengers in many cellular processes. Regulation of calcium ions' intracellular concentration and transport is mediated by several channels and pumps; any disruption of intracellular calcium signaling may induce cell damage. HMGB1 translocation and release are mediated by calcium ions in several in vitro cancer models [50]. XPO1 is a nuclear protein involved in the recognition and export of leucine-rich nuclear export signals (NES) and plays a major role in transporting RNA or proteins from the nucleus to the cytoplasm. Heat shock protein family A member 1A (HSPA1A) inhibits the binding between XPO1 and HMGB1 in macrophages. Given that XPO1-mediated export of tumor suppressor proteins has been documented in various cancer types [186], it is plausible that HMGB1 is also translocated by XPO1 in cancer cells.

In cancer cells, TP53 and HMGB1 are mutual regulators. DNA repair is regulated by the complex formed by the two proteins [110]. TP53 activation controls neoplastic inflammation by inducing the release of HMGB1. On the other hand, passive mechanisms rely on several types of cell death. Modulators of HMGB1 passive release are constitutive of such forms of cell death, including pyroptosis, ferroptosis, necroptosis, necrosis, and apoptosis. Passive processes are regulated by several factors. The persistence of DNA damage overactivates Poly(ADP-Ribose) Polymerase 1 (PARP1) in mammalian cells, inducing a high demand for nicotinamide adenine dinucleotide (NAD+) and consequent ATP depletion. PARP1 activation induces the release of HMGB1 during necrosis caused by DNA-damaging drugs [92]. During necroptosis, which can be triggered by chemotherapy, the formation of necrosomes is regulated by members of the receptor-interacting serine-threonine kinase (RIPK) family. Among them, RIPK3 appeared involved in the release of

DAMPs, including HMGB1 [44]. Other molecular effectors of cell death control HMGB1 release. This is the case of the initiator and executor caspase signaling, whose activation is observed in multiple types of RCD. During immunogenic apoptosis, the release of cytochrome c from mitochondria activates CASP9 followed by CASP3, which, along with CASP7, leads to HMGB1 release.

Once released in the extracellular milieu, HMGB1 can bind to toll-like receptor 4 (TLR4) and glycosylation end product-specific receptor (AGER or RAGE) [5]. Additionally, HMGB1 can form a heterocomplex with CXCL12, which enhances T cell recruitment by binding to CXCR4. This binding induces a structural conformation distinct from that induced by CXCL12 alone [151].

When HMGB1 binds to TLR4 receptors expressed on innate immune cells, it can activate the NF-kB pathway via Myeloid differentiation primary response 88 protein (Myd88) and the interferon regulatory pathway 3 (IRF3) via TIR-domain-containing adapter-inducing interferon-β (TRIF). TLR4 is expressed on several type of myeloid cells such as DCs, MDSC, Tregs and macrophages (Mϕ) (Fig. 1.7).

These HMGB1-stimulated pathways trigger the production of cytokines and mediate a systemic inflammatory response. Conversely, binding of HMGB1 to CD24 or hepatitis A virus cellular receptor 2 (HAVCR2, best known as TIM3) harbor immunoinhibitory effects. In conventional DCs (cDCs) infiltrating the TME, the capture of HMGB1 (together with DNA) inhibits HAVCR2 immunosuppressive function, and restores stimulator of interferon response cGAMP interactor 1 (STING1)-dependent production of type I IFNs [40].

In pancreatic cancer, HMGB1 stimulates the expression of PDL1 via hypoxia-inducible factor 1 subunit alpha (HIF1A) after binding to AGER [104]. Despite its double-edged sword nature, HMGB1 release in the context of immunogenic cell death (ICD) is considered essential for a successful outcome. HMGB1 stimulates DC maturation and their production of the cytokine IL12 [125], thus driving the establishment of a type 1 adaptive immune response. Shreds of evidence supporting this theory come from studies on $TLR4^{-/-}$ and $MYD88^{-/-}$ mice treated with anthracyclines or the platinum salt oxaliplatin (OXA), which showed no antitumor activity. Moreover, co-culture experiments with impaired HMGB1 functionality showed a reduced ability of DCs to perform cross-presentation [4].

[5]HMGB1 protein binds to TLR4 with higher affinity than in the case with AGER8. Given the bacterial origin of recombinant HMGB1, several studies argued that HMGB1 alone would have less affinity for TLR4 and that is the contamination with bacterial LPS that confers it its affinity for TLR4

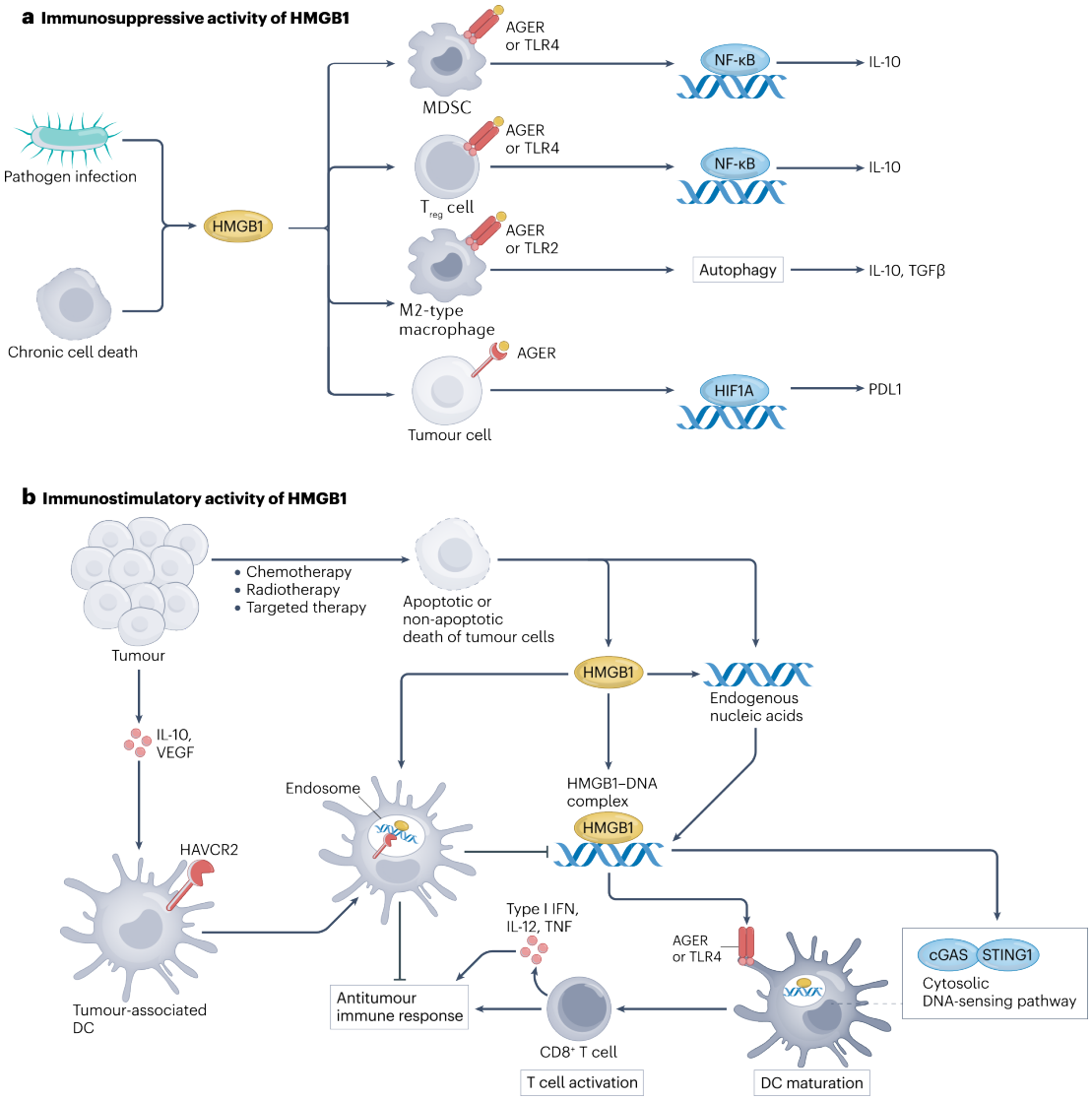

Figure 1.7: Immunosuppressive and immunostimulatory functions of HMGB1. **A** HMGB1 immunosuppressive effects: When HMGB1 binds to AGER (advanced glycosylation end product-specific receptor) receptors expressed on myeloid-derived suppressor cells (MDSCs), regulatory T cells (Tregs), or M2 macrophages, it triggers the release of pro-inflammatory cytokines such as IL-10. In the case of M2 macrophages, TGF-β is also released. Furthermore, autocrine stimulation via AGER receptors in cancer cells, particularly in pancreatic cancer, induces the expression of PD-L1, contributing to immune evasion. **B.** In the absence of treatment, tumors often release pro-inflammatory signals that contribute to immunological tolerance, effectively dampening the antitumor immune response and allowing the tumor to evade immune detection. However, cancer therapies such as chemotherapy and radiotherapy can induce the release of HMGB1 as a consequence of cancer cell death. When HMGB1 is recognized by TLR4 receptors on dendritic cells (DCs), it promotes their maturation and stimulates the production of crucial ligands necessary for robust T-cell activation, thereby enhancing the antitumor immune response. Adapted from Daolin Tang et al [173]

HMGB1 and its receptor TLR4 are targets of interest for cancer therapy. Epidemiological analysis of patient cohorts revealed that breast cancer patients harboring loss-of-function polymorphisms of TLR4 experience more frequent relapse after receiving anthracycline-based treatments [182, 4]. In the case of melanoma patients, DC-based vaccine efficacy is affected by TLR4 loss-of-function [179], as well as for colorectal cancer patients treated with OXA [177] and head-and-neck squamous cell carcinoma treated with systemic treatment [15].

Type 1 Interferon signaling. Type 1 interferons (IFN-I) are cytokines that can be produced by most cell types. Such production follows the stimulation of PRRs present on the cell surface, as well as in the cytosol or within endosomes (Fig. 1.8 A). PRRs can sense nucleic acids, freed from the nucleus of dying/dead cells. Nucleic acid receptors include RNA sensors such as melanoma differentiation-associated gene 5 (MD15 or IFIH1) as well as retinoic acid-inducible gene I (RIG-I or DDX58) or DNA sensors like DNA-dependent activator of IFN-regulatory factors (DAI or ZBP1). Moreover, IFN-I production has been associated with sensing by other intracellular receptors like DEAD-box and DEAH-box helicases as well as the nucleotide-binding oligomerization domain (NOD)-containing proteins NOD1 and NOD2. Similarly, surface receptors such as TLRs (TLR4, TLR3) are strong activators of IFN-I response [123, 36].

Downstream of these receptors, several pathways are responsible for the transcription of genes encoding IFNA/B by activating a few master regulators like interferon regulatory factors (IRFs), notably IRF3 and IRF7. The activatory phosphorylation of IRF3 and IRF7 is mainly mediated by IκB kinase-ϵ (IKKϵ) and TANK-binding kinase 1 (TBK1). Once activated, IRF3 and IRF7 stimulate the transcription of IFN-I-encoding genes, notably *IFNB* and *IFNA4*. Depending on the PRRs activated, the NF-kB pathway can be activated and further contribute to the transcription of IFN-I genes. Once secreted, IFN-I bind to ubiquitous IFNA/IFNB receptor (IFNAR) and activates the downstream JAK1 and tyrosine kinase 2 (TYK2) adapters which, in turn, phosphorylate STAT1 and STAT2 in the cytosol [123, 36]. Phospho-STAT1/2 homo/heterodimers will be able to interact with IRF9 and form the interferon-stimulated gene factor 3 (ISGF3) complex. This latter will translocate to the nucleus and control the second wave of production of IFN and an array of interferon-stimulated genes (ISGs). ISGs include activators (e.g., *IRF7* [152]) and inhibitors (e.g., *USP18* [12]) of the IFN response, as well as regulators of cell survival and immunoregulatory genes (e.g., the pro-inflammatory cytokine CXCL10 [43, 106]), among others.

In the TME, IFN-I exhibits multifaceted roles that on one side bolster antitumor immunity (Fig. 1.8 B). Locally, IFN-I can be produced by several cell types such as cancer-associated fibroblasts (CAFs), TAMs, and other innate and adaptive immune cells. In DCs, the production is triggered following the detection of DNA via the cGAS-cGAMP-STING pathway. Alternatively, binding of extracellular HMGB1 to TLR4 stimulates DCs to produce IFN-I through myeloid differentiation factor 88 (MyD88) signaling [4]. IFN-I are vital for the maturation and activation of NK cells, subsequently increasing their cytotoxicity [169]. IFN-I also promotes DC differentiation, maturation, and migration into lymph nodes, facilitating the activation of $CD8^+$ T cells and increasing intratumoral DC accumulation. In cancer cells, IFN-I upregulates tumor antigen [68] and MHC class I expression [22], facilitating antigen uptake and cross-presentation by DCs, enhancing tumor cell

visibility to the immune system. Additionally, IFN-I reduces Treg [74] infiltration and proliferation within the tumor, thereby mitigating their immunosuppressive effects. Also, they inhibit neutrophil infiltration, longevity, and chemokine production, which can otherwise support tumor progression. Lastly, IFN-I decreases the differentiation and maturation of MDSCs which prevents the downstream activity of cytotoxic $CD8^+$ T cells.

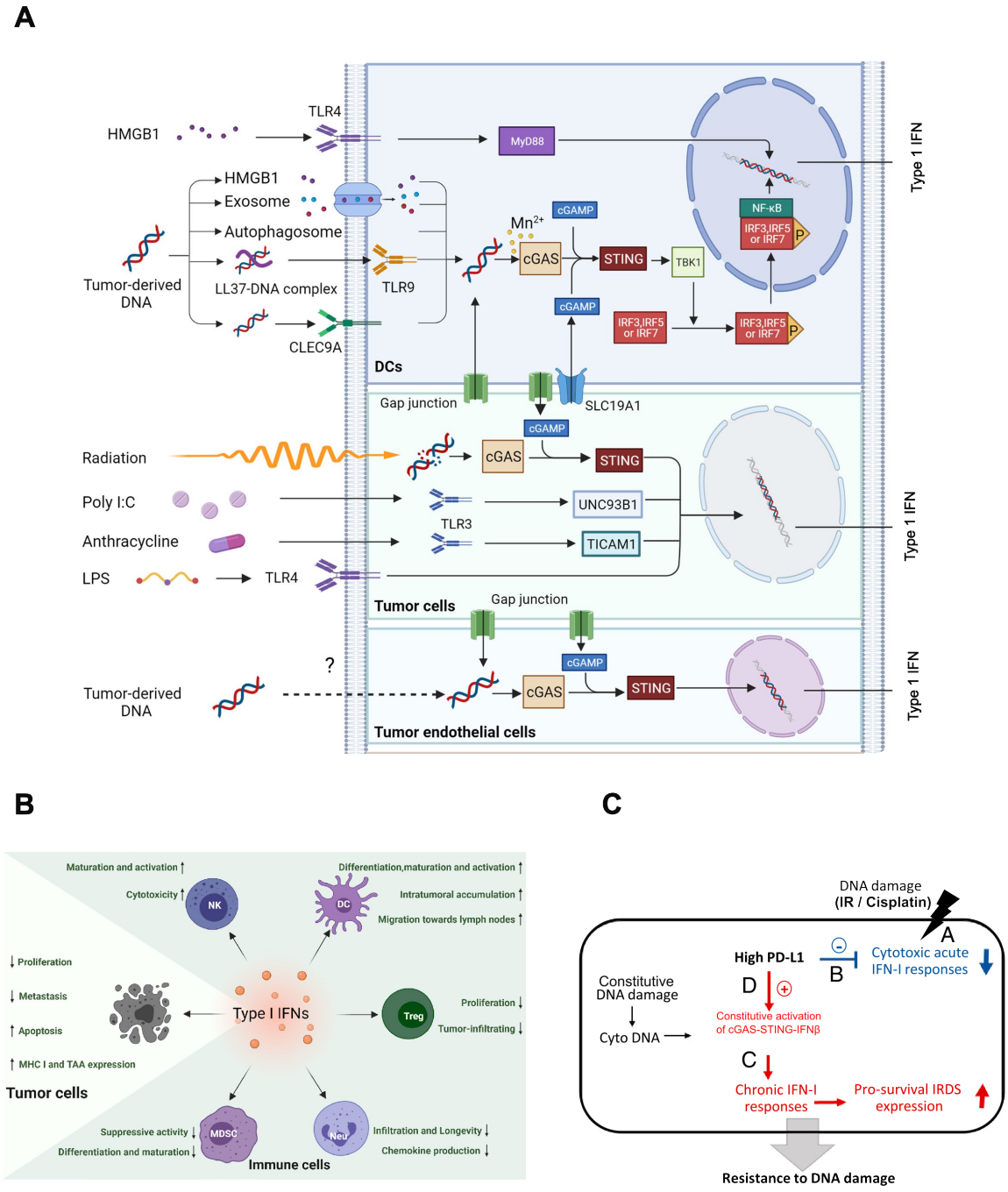

Figure 1.8: Type 1 interferon response and production in cancer cells. A Type 1 IFN production modalities and stimuli. Adapted from Yu et al. [199], B. Immunostimulatory effects of IFN-I [199] C. Pro-survival effects of IFN-I in cancer cells expressing high levels of PD-L1 [35]

In cancer cells, IFN-I can have both prosurvival and immunostimulatory effects, according to the strength and the duration of the stimulation [34]. Examples of the protumoral effects of IFN-I come from cancers harboring mutations in the Ataxia-telangiectasia mutated (*ATM*) gene [34] or in *TP53* [101]. In both cases, these mutations lead to a constitutive IFNβ expression that can compromise the efficacy of DNA-damaging agents. In addition, high constitutive levels of PD-L1 enhance the production of IFN-I by activating the STING1 pathway. Moreover, IFN-related DNA damage-resistant signature (IRDS) genes are also up-regulated in lung carcinoma [35]. On the contrary, following the administration of DNA-damaging chemotherapies, such as anthracyclines (e.g., doxorubicin [DOX]), the activation of TLR3 receptors sense RNA released by dying cancer cells. TLR3 activity, in turn, favors the release of chemokine C-X-C motif ligand 10 (CXCL10), hence boosting the chemotaxis of T-cells expressing the conjugate receptor CXCR3. The in vivo neutralization of CXCR3 compromises the efficacy of doxorubicin in mounting an antitumor response by reducing the chemotactic effects sparkled by the autocrine release of IFN-I [157]. Other DNA-damaging cancer therapeutics, such as ionizing radiation in breast cancer, also up-regulate the production of IFN-I [189].

ANXA1/FPR1-2 axis. Annexin A1 (ANXA1) is part of a protein superfamily of the annexins and its phospholipid-binding mechanism relies on $Ca2^{2+}$. The superfamily shares the same C-terminal while the N-terminal varies according to the member and is the location for most post-translational modifications. First observations on ANXA1 indicated its role in mediating anti-inflammatory response to glucocorticoids by inhibiting phospholipase A2. This process occurs through the binding of ANXA1 to formyl peptide receptor 1 and 2 (FPR1, FPR2) [141].

ANXA1 is expressed in several cell types including epithelial cells and immune cells such as neutrophils and macrophages. Recent investigations highlighted its multiple contributions in several processes: on one side ANXA1 has antitumorigenic features given by its potential to reduce inflammation and on the other hand it can promote invasion and metastasis (only for late-stage cancers) [19]. In the case of breast cancer, ANXA1 actively regulates the NF-kB pathway inducing the expression of matrix metalloproteinase 9 (MMP9), thus enhancing the invasion potential. Furthermore, ANXA1 is a caspase-dependent ligand [5], required for apoptotic cell engulfment.

The importance of ANXA1 in ICD has been assessed using $^{-/-}$ cancer cells and $Fpr1^{-/-}$ mice, proving the critical role of ANXA1 binding to formyl peptide receptor 1 (FPR1) on the surface exposure of CALR under the administration of ICD-inducing treatments such as DOX or mitoxantrone (MTX). Such genetic modifications negatively impacted ICD induction through impairment of DC activity [11]. In any case, the precise mechanisms regulating ANXA1 release and production are currently under investigation.

Epidemiological studies on breast carcinoma cohorts have revealed that the recurrence of metastasis

in patients treated with anthracyclines is frequently associated with a loss-of-function mutation in FPR1, attributed to single-nucleotide polymorphism (SNP) [182]. Similarly, colorectal cancer patients treated with the platinum-based drug OXA who carry FPR1 polymorphisms exhibit poorer overall survival and a less favorable metastasis-free prognosis [182]. Recent research on breast cancer cell lines [159] has highlighted the role of post-translational modifications of ANXA1, where serine protease 22 (PRSS22 or tryptase ε), transcriptionally initiated by E2F1, modifies ANXA1, a known substrate of PRSS22. This modification appears to facilitate breast cancer metastasis through the FPR2/ERK signaling pathway.

Inhibition of transcription. Recently, the work of Dr. Juliette Humeau in the team provided evidence of an additional hallmark of ICD, namely the inhibition of transcription [81]. Starting with an in silico screening of a large library of chemical compounds, clusters of *bona fide* ICD inducers were detected by computing a predictive ICD score taking into account the impact of these drugs on the release of the abovementioned ICD-related DAMPs. Among these compounds emerged Actinomycin D (DACT), an antibiotic commonly employed in clinical settings for the care of several cancer types such as testis, some ovarian cancers, and Ewing's Sarcoma. Preclinical investigations using DACT evidenced a correlation between the release of DAMPs and the inhibition of RNA synthesis. Furthermore, inhibition of transcription was observed for other ICD inducers such as the anthracyclines MTX and DOX, and the platinum salt OXA.

2.3.4 Cancer immunotherapies

Cancer immunotherapies encompass heterogeneous approaches aimed at reinvigorating cancer immunosurveillance. Immune checkpoint inhibitors (ICI) and other immunomodulatory monoclonal or bispecific antibodies have shown impressive transversality, with remarkable efficacy across multiple oncological indications. Other immunotherapeutic approaches currently approved in the clinics include cancer vaccines, cytokines, or again adoptive cell therapy. Furthermore, cytotoxic/lytic interventions that induce ICD and stimulate antitumor immunity also join the immunotherapeutic arsenal.

- **Immune checkpoint inhibitors.** Immune checkpoints function as regulatory elements, governing the activity of T cells and restraining their attack on cancer cells. Central to this regulatory network are programmed cell death protein 1 (PD-1) and cytotoxic T-lymphocyte-associated protein 4 (CTLA-4). PD-1, found on activated T cells, plays a critical role in suppressing immune responses to maintain tolerance and prevent autoimmune reactions. Upon interaction with its ligands, programmed death-ligand 1 (PD-L1) and PD-L2,

PD-1 transmits inhibitory signals that suppress T cell activity, enabling cancer cells to evade immune surveillance.[168] Nivolumab and Pembrolizumab are ICIs consisting of monoclonal antibodies targeting PD-1 and preventing its interaction with PD-L1. Similarly, CTLA-4 acts as a negative regulator of T cell activation, primarily during the immune response's initiation phase. By binding to CD80 and CD86 on antigen-presenting cells, CTLA-4 competes with the costimulatory molecule CD28, dampening T cell activation and proliferation (**Fig.** 1.4). The ICI Ipilimumab targets CTLA-4 and block its function, empowering T cell responses against tumor antigens and augmenting antitumor immunity. Although these mechanisms preserve the immunological potential of T cells, long-term effects related to excessive immune responses are still under investigation [86].

- **Cancer vaccines.** Cancer vaccines aim to stimulate an adaptive antitumor response by overexpressing a tumor antigen inside the tumor microenvironment and/or in peripheral tissues where APCs patrol. They can be prophylactic, such as the HPV vaccine for preventing cervical cancer, or therapeutic, designed to treat established tumors [51].

- **Cytokines.** Cytokine therapy relies on the administration of proinflammatory cytokines. In particular, IL-2 and IFN-α have been approved by the FDA for cancer treatment: IL-2 for advanced renal carcinoma and metastatic melanoma, and IFN-α for hairy cell leukemia and melanoma [16]. Systemic delivery of these cytokines remains infrequent in clinical practice due to limited response rates and severe adverse events, notably due to the short half-life of the molecules and their potent inflammatory activity [77] Current research on optimizing the clinical use of cytokines for the care of cancer is now focusing on three key aspects: i) favoring a local, rather than systemic, administration, ii) improving the pharmacokinetic, and iii) identifying synergies with other immunotherapies, notably ICIs.

- **Adoptive cell therapy.** Adoptive cell transfer (ACT) is an advanced immunotherapeutic approach that entails the isolation and ex vivo expansion of autologous or allogeneic T cells, which are subsequently reinfused into the patient to target and eradicate cancer cells. These T cells can be genetically engineered ex vivo, mostly to edit their TCR. ACT has demonstrated significant efficacy in treating blood cancers and some solid tumors like melanoma. However, challenges persist in optimizing T cell persistence and functionality, as well as managing adverse effects such as cytokine release syndrome [83]. Among the available options for ACT, CAR-T cell therapy relies on the adoptive transfer of T lymphocytes whose TCR has been genetically substituted by a chimeric antigen receptor (CAR). The latter mostly consists of a single-chain variable fragment (scFv) that is specific to a surface cancer antigen. Although intrinsically

complex and expensive, this targeted approach is clinically approved for the efficient treatment of certain leukemia, lymphoma, and myeloma.[20].

ICD inducers. A wide array of cytotoxic/cytolytic interventions can trigger cancer ICD, mediating antigen spreading together with exposure and release of DAMPs, and ultimately promoting antitumor immune response.

The gold standard assay to determine the ability of an intervention to drive cancer ICD relies on a vaccination-rechallenge experiment. In detail, murine cancer cells are first treated in vitro with the agent. Once cell mortality reaches a specific threshold (50% to 70%), these treated (dying and dead) cells are suspended and injected subcutaneously into one flank of immunocompetent mice of the same genetic background. After a 7-15-day period, these mice are injected with live, non-treated, cancer cells of the same line in the opposite flank [80]. Then, tumor growth is monitored. An absence of tumor development validates the ICD-related vaccination potential of the agent. Indeed, effective ICD inducers provide long-term immune-mediated protection against the re-injected cancer cells, a phenomenon not replicated by cells treated with cytotoxic compounds unable to induce ICD [27].

ICD-inducing agents have been classified according to their mechanism of action (Fig. 1.9). Type 1 ICD inducers act on cancer cells by inducing danger signaling via ER stress while triggering cell death through ER stress-unrelated pathways, for instance at the level of mitochondria or nuclei (e.g., by impairing DNA replication and repair mechanisms). Conversely, Type 2 ICD inducers selectively trigger both DAMP release and cell death via ER stress targets (e.g., ROS production, and altered ribosomal biosynthesis).

The first drugs recognized for their immunogenic potential were evidenced in mice and consisted of the anthracyclines DOX, daunorubicin, and idarubicin [27]. Another anthracycline, MTX [136, 138], along with the platinum derivative OXA [116, 135, 138, 150], the alkylating agent cyclophosphamide [30, 62, 150], the proteasome inhibitor bortezomib [28, 37, 41, 160], the RNA polymerase II inhibitor lurbinectedin [192], the cyclin-dependent kinase inhibitor dinaciclib [76], the topoisomerase inhibitor teniposide [188], the bromodomain inhibitor JQ1 [146], and the antibiotics bleomycin [25] , wogonin [197], and septacidin [166] exhibit similar characteristics. Additionally, some anticancer treatments involving physical signals such as radiotherapy [4, 116, 136], photodynamic therapy [59, 64, 94, 95, 93, 97], ultraviolet C (UVC) light [135, 138, 150, 195], electrical pulses [133, 134], high hydrostatic pressure [54], microwave thermal ablation [200], and photochemotherapy [175] have demonstrated immunogenic properties. Similarly, some targeted therapies, such as the epidermal growth factor receptor (EGFR) antibody [144, 60], certain

oncolytic peptides [203], oncolytic viruses [21, 91, 201], and specific bacterial toxins [167] also exhibit these properties. (see Table 2.3.4).

Some chemotherapies like etoposide, mitomycin C, and cis-dichlorodiammineplatinum(II) (cisplatin, CIS) fail to trigger ICD as they do not trigger CALR exposure [120, 136]. However, these agents can gain immunogenic properties when combined with agents that target the endoplasmic reticulum (ER) and activate CALR translocation, such as the ER stressor thapsigargin or the eIF2α phosphatase inhibitor salubrinal [136]. Although crizotinib [108] and cardiac glycosides [124] exhibit all the hallmarks of ICD in vitro, they only effectively induce ICD when complemented with cytotoxic agents like CIS or mitomycin C.

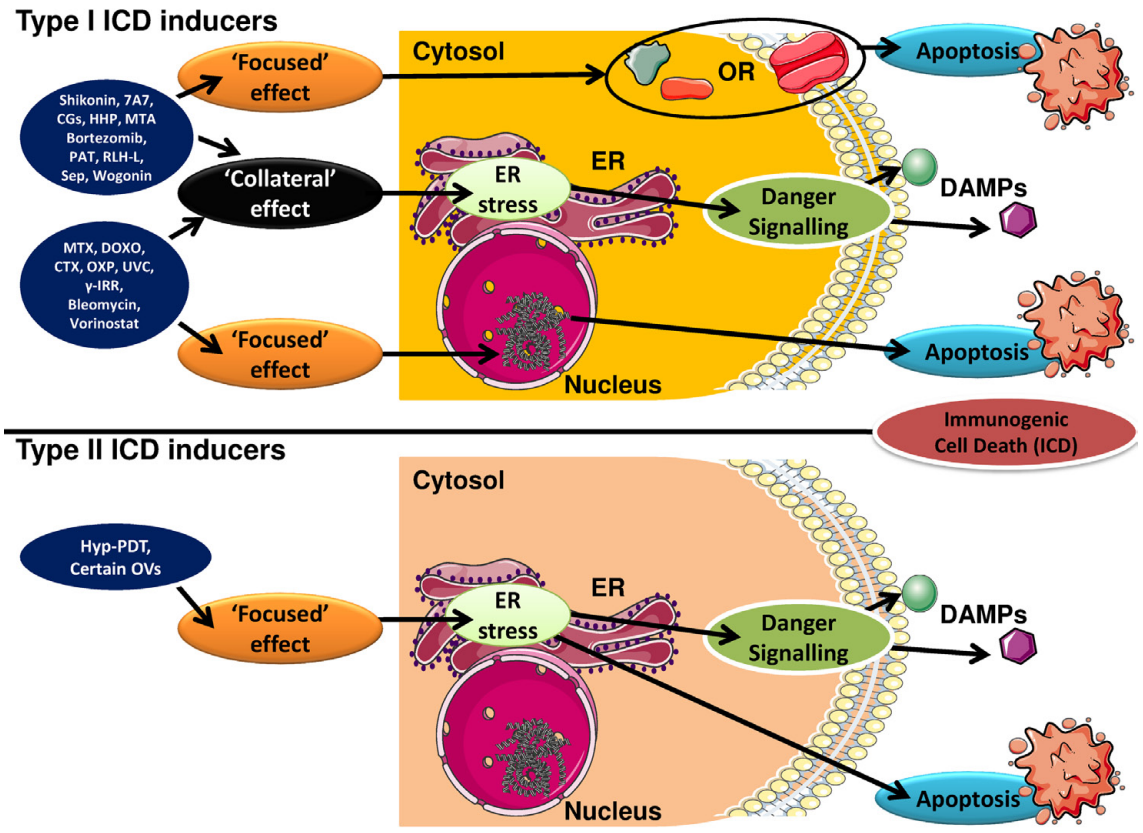

Figure 1.9: Type I ICD inducers, such as mitoxantrone (MTX), doxorubicin (DOXO) or Oxaliplatin (OXP) act on cells by inducing danger signaling via ER stress and induce cell death on targets non associate to ER stress acting for instance on mitochondria and cells nuclei. Type II ICD inducers act exclusively on ER stress-associated targets. Adapted from [58]

List of ICD-inducers.

Drug	peIF2α	DAMPs	Immune infiltrate	Vax-Mem	Ort.Valid.	References
ICD inducers						
Anthracyclines (mitoxantrone, doxorubicin, epirubin, iadarubin, daunorubicin)	Yes	CALR ATP HMGB1 ANXA1	↑: DCs, $CD8^+$, gd T 17, IL-1β, IFNγ IFN-I ↓: tregs, MDSCs	Yes	Abolished (*nu/nu* mice) depletions: $CD8^+$, IFNγ, IL-17, IL-17R	[117, 127, 136, 138, 182]
Oxaliplatin	Yes	CALR ATP HMGB1	↑: DCs, $CD8^+$, $\gamma\delta$ T 17, IL-1B, IFNγ	Yes	Abolished (*nu/nu* mice) depletions: $CD8^+$, IFNγ, IL-17, IL-17R	[127, 138, 142, 177]
Bortezomib	Yes	CALR	↑: Dcs, CD8+	Yes	Abolished (*nu/nu*, $Rag^{-/-}$, $CD8^+$ depletion)	[37]
Cyclophosphamide	nd.	CALR HMGB1 ATP	↑: DCs, $CD8^+$, IL-17, IFNγ, NK, IFN-I	↓: MDSCs, Tregs	n.d.	[30, 62, 63, 150, 184]
Bleomycin	Yes	CALR ATP HMGB1	↑: $CD8^+$, IFNγ, Tregs, TGF-β	Yes	Abolished (CD8, IFNγ depletion)	[25]
Lurbinectedin	Yes	CALR ATP HMGB1	↑: IFN-I	Partial	Abolished ($CD4^+$ and $CD8^+$ depletion)	[192]
Septacidin	nd.	CALR ATP HMGB1	n.d.	Yes	Abolished (*nu/nu* mice)	[166]
Wogonin	Yes	CALR ATP HMGB1 ANXA1	↑: DCs, lymphocytes	Yes	n.d.	[197]
Teniposide	nd.	CALR HMGB1	↑: DCs, $CD8^+$, IL2, IFNγ, IFN-I	Yes	n.d.	[186]
Bromodomain inhibitor JQ1	Yes	CALR ATP HMGB1	↑: DCs, $CD8^+$, ↓: MDSCs	Yes	Reduced (*nu/nu* mice)	[13, 146]
Cetuximab (EGFR antibody)	nd.	CALR HMGB1	↑: DCs, $CD8^+$	Yes	n.d.	[144]
7A7 (EGFR antibody)	Yes	CALR	↑: DCs, $CD8^+$, $CD4^+$, IFNγ	Yes	Abolished ($CD8^+$ depletion)	[60]
Dinaciclib (CDK inhibitor)	nd.	CALR ATP HMGB1	↑: DCs, $CD8^+$, $CD4^+$, IFNγ	Yes	Abolished ($Rag^{-/-}$ depletion)	[76]
Oncolytic peptides DTT-205,DTT-304	nd.	CALR HMGB1	↑: IFN-I	Yes	Abolished ($CD8^+$ and $CD4^+$ depletion)	[204]
Oncolytic peptide LTX-315	No	CALR ATP HMGB1	↑: DCs, macrophages, $CD8^+$, Th1, $CD4^+$, IL-1β, IL-6, IFN-I, ↓: MDSCs, Tregs	Yes	n.d.	[26, 46, 196, 203]
Oncolytic peptide LTX-401	ROS	CALR ATP HMGB1	↑: $CD3^+$, IFNγ, IFN-I	Yes	n.d.	[45, 122, 193, 203]
Radiotherapy	nd.	CALR HMGB1	↑: DCs, $CD8^+$, $\gamma\delta$ T 17, IFNγ	Yes	Abolished (*nu/nu* mice)	[4, 116, 136]
Photofrin-based PDT	nd.	CALR HMGB1	↑: monocytes, neutrophils, $CD8^+$, NK	Yes	Abolished ($CD8^+$ depletion)	[93, 94, 95, 97]

Continued on next page

Continued from previous page

Drug	peIF2α	DAMPs	Immune infiltrate	Vax-Mem	Ort.Valid.	References
Hypericin-based PDT	No (PERK and ROS)	CALR ATP	↑: DCs, IL-1β	Yes	n.d.	[59]
Redaporfin-based PDT	Yes	CALR ATP HMGB1	n.d.	Partial	n.d.	[64]
Microwave thermal ablation	nd.	CALR ATP HMGB1	↑: CD8$^+$, TNFα, IFNγ	Yes	Abolished (CD8$^+$)	[200]
8-methoxypsolaren photochemotherapy	nd.	CALR ATP HMGB1	↑: DCs, monocytes, CD8$^+$, NK, IFN-I	Yes	Abolished (CD8$^+$, CD4$^+$, spleen, NK depletion)	[175]
Electrical nanopulses	nd.	CALR ATP HMGB1	↑: CD8$^+$	Partial	n.d.	[134, 133]
UVC light	nd.	CALR*, HMGB1*	↑: DCs, CD8$^+$, IFNγ	Yes	n.d.	[136, 138, 150, 195]
Oncolytic virus T-VEC	nd.	CALR ATP HMGB1	↑: CD8$^+$, IL-1β, TNFα, IFN-I	Yes	n.d.	[21]
Newcastle diseases virus	nd.	CALR HMGB1	↑: DCs, CD8$^+$, CD4$^+$, NK, NKT, IFNγ ↓: MDSCs	Yes	Abolished (*Rag2*$^{-/-}$ mice, CD8$^+$ depletion)	[91, 201]
Clostridium difficile toxin B	ROS	CALR ATP HMGB1	n.d.	Yes	n.d.	[167]
Cardiac glycosides (digoxin and digitoxin)	nd.	CALR ATP HMGB1	↑: CD8$^+$, CD4$^+$, $\gamma\delta$ T 17, IFNγ	Yes (with CDDP or mytomicin C)	Abolished (*nu/nu* mice)	[124]
Crizotinib	Yes	CALR ATP HMGB1	↑: DCs, CD8$^+$, NKT, IL-17, IFN-I ↓: Tregs	Yes (with CDDP or mitomycin C)	Abolished (*nu/nu* mice)	[108]
Metformin	n.d.	CALR ATP HMGB1	↑: DCs, CD8$^+$, CD4$^+$	n.d.	n.d.	[33]

ICD inducers are agents that can delay tumor growth and are recognized as such only if they prompt the release of antigens along with damage-associated molecular patterns (DAMPs) during cell death. This dual action, which also contributes to a partial vaccination effect, is necessary for an agent to be classified as an ICD inducer. *Not activated in all the investigated cell lines. ANXA1, annexin A1; ATP, adenosine triphosphate; CALR, calreticulin; CTLs, cytotoxic T lymphocytes; CY-1-4 NP, nano-encapsulated tryptanthrin derivative CY-1-4; DCs, dendritic cells; IL-17, interleukin-17A–producing T cells; HMGB1, high mobility group box 1; ID, immunodeficient; IFN, interferon; IFN1, type I interferon; KP1339/IT-13, ruthenium complex sodium trans-[tetrachloridobis(1H-indazole)-ruthenate(III)]; MDSC, myeloid-derived suppressor cells; n.d., not determined; peIF2α eukaryotic initiation factor 2 phosphorylation; PDT, photodynamic therapy; rCALR, recombinant calreticulin; SCID, severe combined immunodeficiency; Th, helper T cells; Treg, regulatory T cells; T-VEC, talimogene laherparepvec; ROS, reactive oxygen species; n.d. not determined; UVC, ultraviolet C. Adapted from Humeau J. [79]

2.3.5 Platinum Salts and ICD

Platinum compounds are among the most clinically employed and investigated chemotherapy agents. CIS represents the most emblematic among the first-generation platinum-based compounds. It is used to treat various cancers, including advanced testicular, ovarian, bladder, cervix, head and neck, esophageal, small cell lung cancers, and some pediatric cancers. The second-generation compound, carboplatin, is used primarily for ovarian cancer. OXA, a third-generation compound, was FDA-approved only in 2002, and its application in the care of colon cancer has become a standard therapy line [145].

Side effects accompanying platinum salt treatments require careful follow-up and adjustments based on the patient's tolerance and response to therapy. CIS, carboplatin, and OXA commonly induce myelosuppression, which is moderate with CIS and OXA but can be dose-limiting with carboplatin (thrombocytopenia being more frequent than leukopenia and anemia). Hypersensitivity reactions can be observed with prolonged administration of carboplatin, and less frequently with OXA. Neurotoxicity is witnessed upon platinum salt treatments, with peripheral neuropathy being the most prominent side effect with CIS and OXA, especially with cumulative doses. Nephro- and oto-toxicities are recurrently reported upon carboplatin and CIS treatments. Gastrointestinal disturbances (diarrhea, nausea, and vomiting) are also observed under platinum salt [198].

Platinum-based compounds diffuse passively into cells and form lethal adducts with both nuclear and mitochondrial DNA, with a higher frequency in mitochondrial DNA. In comparison to CIS, carboplatin forms adducts more slowly, while OXA induces more double-strandbreaks in DNA adducts [84].

The efficacy of platinum agents is limited by intrinsic cellular resistance, involving multiple resistance mechanisms at each step of their action. Intracellular platinum accumulation is modulated by membrane transporters affecting influx and efflux, while platinum agents are deactivated in the cytoplasm, and adducts are increasingly repaired. DNA synthesis continues in some cells despite CIS treatment, suggesting a bypass mechanism known as translesion synthesis, which influences drug sensitivity, resistance, and mutagenicity. Pol I transcribes more DNA than Pol II, and its inhibition may cause ribosome biogenesis stress, contributing to OXA anticancer properties [23]. Classical platinum agent cytotoxicity relies on inhibiting DNA and RNA synthesis and the inability of cells to repair platinum lesions effectively.

Differences in the geometry of CIS- and OXA-induced DNA adducts affect translesion synthesis efficiency, with polymerases (η and β) bypassing OXA lesions more readily than CIS lesions. Structural characterization of OXA DNA adducts suggests hydrogen bond formation between the platinum adduct and the DNA backbone, contributing to justify the different properties of the two

drugs. CIS primary mechanism is thought to be transcription inhibition, arresting the cell cycle at G2/M. Recent experimental evidence has identified key differences in how CIS and OXA induce cell death. Unlike CIS, OXA does not trigger a DNA damage response but kills cells by causing ribosomal biogenesis stress. CIS acts as a DNA cross-linker, while OXA has a mechanism similar to transcription/translation inhibitors like rapamycin and DACT [81]. Further studies showed that OXA causes fewer double-strand DNA breaks and is less sensitive to gene silencing involved in homologous recombination and interstrand cross-link repair compared to CIS. Supporting the idea that OXA induces cell death through ribosome biogenesis stress is the observation that pre-rRNA is upregulated after treatment, while RNA Pol II transcripts remain stable [23]. Additionally, knocking down Rpl11, essential for ribosome function, makes certain cancer cells resistant to OXA. Ribosome biogenesis stress leads to the overexpression of Rpl11 subunits that bind to Mdm2, preventing its interaction with TP53, thereby reducing TP53. Epidemiological studies show that cancer types with a better response to OXA, such as colorectal cancer, have higher ribosomal gene expression than cancer types with a better response to CIS [23]. This establishes the clinical relevance of the different mechanisms by which CIS and OXA kill cancer cells.

Preclinical models showed that platinum salts harbor different immunogenic potential, that can vary depending on the type of cancer and interactions with other drugs. In the study by Martins et al., [120], both CIS and OXA induced similar mitochondrial perturbations in sarcoma and colorectal cancer cells (U2OS, MCA205, CT26). However, their ability to induce ER stress and thus to promote surface exposure of the eat-me signal CALR differed. Cancer cell immunogenicity was experienced upon CIS treatment only when co-administered with thapsigargin, an inhibitor of the Sarco/ER Ca(2+)-ATPase. This ER stressor restored exposure of CALR at the surface of CIS-treated cells; a property observed upon standalone OXA treatment. In another work by Parks et al. [139], a comparison of CIS and OXA was conducted in models of head and neck and oral cancers and found that OXA and CIS induced similar weak immunogenicity, with both failing to trigger robust release of HMGB1 and ATP. In vivo, prophylactic experiments supported the dampened potential of both platinum salts to induce antitumor immunity as a consequence of their lack of ICD promotion. Interestingly, ICD inducers can sensitize cells to immune checkpoint inhibitors [90]. Along this line, in the clinical management of gastric cancers, chemotherapy based on OXA but not CIS showed synergistic interaction with PD-1 blockade (especially in combination with 5-fluorouracil) [109].

3 System Biology in oncoimmunology

In biomedical research, Systems Biology emerges as a holistic approach that offers a broader perspective on biological phenomena, striving to comprehend the intricate interplays between organisms, tissues, and cells by scrutinizing their interconnectedness. This approach diverges from traditional reductionist biology, which dissects systems into smaller, isolated components for analysis. Thus, systems biologists employ a multifaceted workflow, harnessing theoretical knowledge, data analysis techniques, and computational modeling to formulate and test hypotheses.

Systems Biology makes extensive use of various omics datasets (such as genomics, transcriptomics, or proteomics) to elucidate the intricate molecular interactions driving tumorigenesis and metastasis.

By dissecting the signaling networks and regulatory pathways underlying cancer progression, potential therapeutic targets can be identified, unveiling mechanisms of drug resistance.

Similarly, in immunology, Systems Biology approaches aim at understanding the dynamic interplay between immune cells and pathogens, facilitating the development of novel immunotherapeutic strategies against infectious diseases and autoimmune disorders.

Systems Biology modestly contributes to advancing our understanding of complex biological processes, offering promising avenues for personalized medicine and targeted interventions in the fight against disease.

3.1 Modeling Approaches to Biology

Despite the apparent unambiguity of the word 'model,' in Biology —especially in Systems Biology— this word takes on extremely different meanings depending on the context.

To an experimental biologist, the term encompasses biological experimental settings and specific biological entities used to 'model' a certain phenomenon. This means that when an experimental biologist studies a 'model,' he/she typically refers to living organisms or biological systems that serve as representatives for studying particular biological processes. Features such as genetic simplicity, short generation times, or physiological similarities to humans make these organisms reliable tools for studying genetic, developmental, or disease-related questions.

In contrast, within the field of Systems Biology, the term 'model' often refers to a computational or mathematical representation of biological systems. Here, a 'model' is not a physical entity but rather a set of equations, algorithms, or simulations that aim to describe and predict the behavior of biological processes. These models can range from simple representations of a single biochemical pathway to highly complex simulations of entire cells or tissues. They are used to integrate vast amounts of biological data, generate hypotheses, and test the effects of different variables in silico before proceeding to experimental validation.

Thus, the word 'model' in Biology spans a spectrum from tangible organisms used in the lab to abstract mathematical constructs used to understand and predict biological behavior. This term duplicity highlights the intrinsic interdisciplinary nature of biological research, where more and more empirical data and theoretical frameworks contribute one to each other to provide deeper insights into the complexities of life.

3.1.1 Biological models

In vitro. In vitro models are a class of experimental systems that use cell cultures or tissues in a decontextualized biological setting (e.g., primary cancer cells cultivated in incubators and treated under sterile conditions). This setting excludes systemic conditioning and enhances the controllability of the process under investigation with a specific and predefined environment.

Motivated by the technical limitations of assessing a phenomenon within a living organism, in vitro models provide a viable surrogate alternative to investigate processes in fields such as cell biology, pathogenesis, disease mechanisms, and drug responses. Due to the intrinsic lack of interaction with other components of biological systems (as found in a living organism), claims based on in vitro findings still need subsequent validation steps, i.e., their application to an in vivo context. Traditional in vitro models include 2-D cell culture experiments in which the biological complexity is simplified by reducing possible cellular interactions and extracellular matrix interfaces. These beneficial properties of such a modeling approach come with a price: as anticipated above, experimental results are often difficult to translate into in vivo systems, due to substantial differences within the microenvironment and to the physical features of the artificial culture environment.

To compensate for such differences, technological advancements have been made in the field of in vitro models. 3-D models allow a more pertinent representation of tissue compared to 2-D monolayer cultures aiming to replicate the biological complexity of organized tissues. For instance, 3-D models can be used to mimic the architecture or the functioning of organs like in the case of stem cell-derived organs (organoid models). In tumor biology, 3-D models are used to better understand how tumors respond to drugs in a context that more closely resembles their natural environment.

In vivo. To gain insights into systemic responses within biological systems, in vivo models still stand as paramount tools for researchers. These models have served as indispensable means to observe and comprehend physiological as well as pathophysiological processes. Animals have served as fundamental components in modeling and studying various diseases and biological phenomena. Invertebrate models, such as zebrafish, Caenorhabditis elegans, or Drosophila melanogaster, have significantly contributed to fields like neuroscience, genetics, and cancer research. Similarly, vertebrate models encompassing species like rats, mice, or rabbits, are pivotal for translational studies in biomedical sciences.

Advancements in genetic engineering have further bridged the gap between biological reality and experimental models, facilitating the creation of animals with targeted genetic mutations that mirror human conditions. Thus, the typical trajectory of biomedical research involves initial in vitro experiments, followed by preclinical in vivo studies utilizing animal models, and ultimately, clinical validation on human subjects. Human in vivo experiments are predominantly restricted to clinical trials, representing the definitive validation phase for novel therapeutic approaches and the evaluation of new compounds' safety profiles.

Ethical considerations have shaped regulatory frameworks over time, leading to stringent guidelines — such as those enforced by the European Union (Directive 2010/63/EU) — that advocate for minimizing animal use in research and promoting the development of alternative, non-animal-based methodologies in biological studies.

3.1.2 In silico models

The objective of Systems Biology as a discipline has always been to bridge abstraction with biological context, integrating experimental data with computational simulations to comprehensively explore biological systems from molecules to organisms. This approach advances research in biomedicine and ecological sciences by providing a holistic understanding of biological processes.

In silico models encompass a diverse range of computational and mathematical approaches used to extract knowledge from abstract representations of biological processes and comprehensively simulate biological phenomena. For instance, purely data-based in silico approaches leverage large datasets to develop predictive models, such as statistical models or machine learning algorithms, that analyze biological data to uncover patterns and predict outcomes. On the other hand, mechanistic representations of biological systems allow researchers to simulate and predict outcomes based on underlying biochemical or physiological mechanisms. These models enable researchers to simulate and explore complex biological processes in a virtual environment, providing insights that inform experimental design and deepen biological understanding.

Data-based modeling. *Statistical models* encompass a wide range of methodologies, including linear models for assessing linear relationships, analysis of variance (ANOVA) for comparing group means, linear mixed-effects models to handle hierarchical data structures, and survival analysis for studying time-to-event outcomes. The intrinsic interpretability of the results and the possibility to integrate prior biological knowledge within the analytical workflows enable these models to be a reliable choice for researchers to extract meaningful insights, identify significant factors influencing biological processes, and make informed decisions in clinical and research settings.

Machine learning models utilize sophisticated algorithms to analyze extensive datasets, enabling tasks such as predicting protein structures and identifying potential drug candidates. The emergence of omics technologies, propelled by advancements in molecular biology, has facilitated the application of these models to process vast data from high-throughput technologies like single-cell analysis, thereby enhancing model performance and refinement. State-of-the-art applications span various biological research fields, with significant emphasis on predicting protein features such as structure, folding, and interactions (e.g., AlphaFold). Moreover, machine learning models are accelerating advancements in emerging technologies such as multiplexed immunohistological imaging, providing essential support for researchers in these fields.

Network models are another class of in silico data-based models used to formalize relationships within biological systems. Examples of this class include protein-protein interaction networks, gene regulatory networks, and metabolic and signaling networks. These models aim to uncover system properties by representing biological entities as nodes and their interactions as edges. Nodes and edges can get different meanings according to the biological context. For instance, protein-protein interaction networks (PPINs) are graphs used to map physical interactions, revealing protein complexes and cellular pathways. An example of such representations is available in fig. 1.10, where we present the PPI network obtained for the tumor protein 53 (TP53) using the STRING database. Gene regulatory networks (GRNs) describe gene transcription dynamics under specific conditions. Topological studies on network composition and features allow discriminating between biological elements contributing the most to a biological process and those that are marginal to the realization of a biological process.

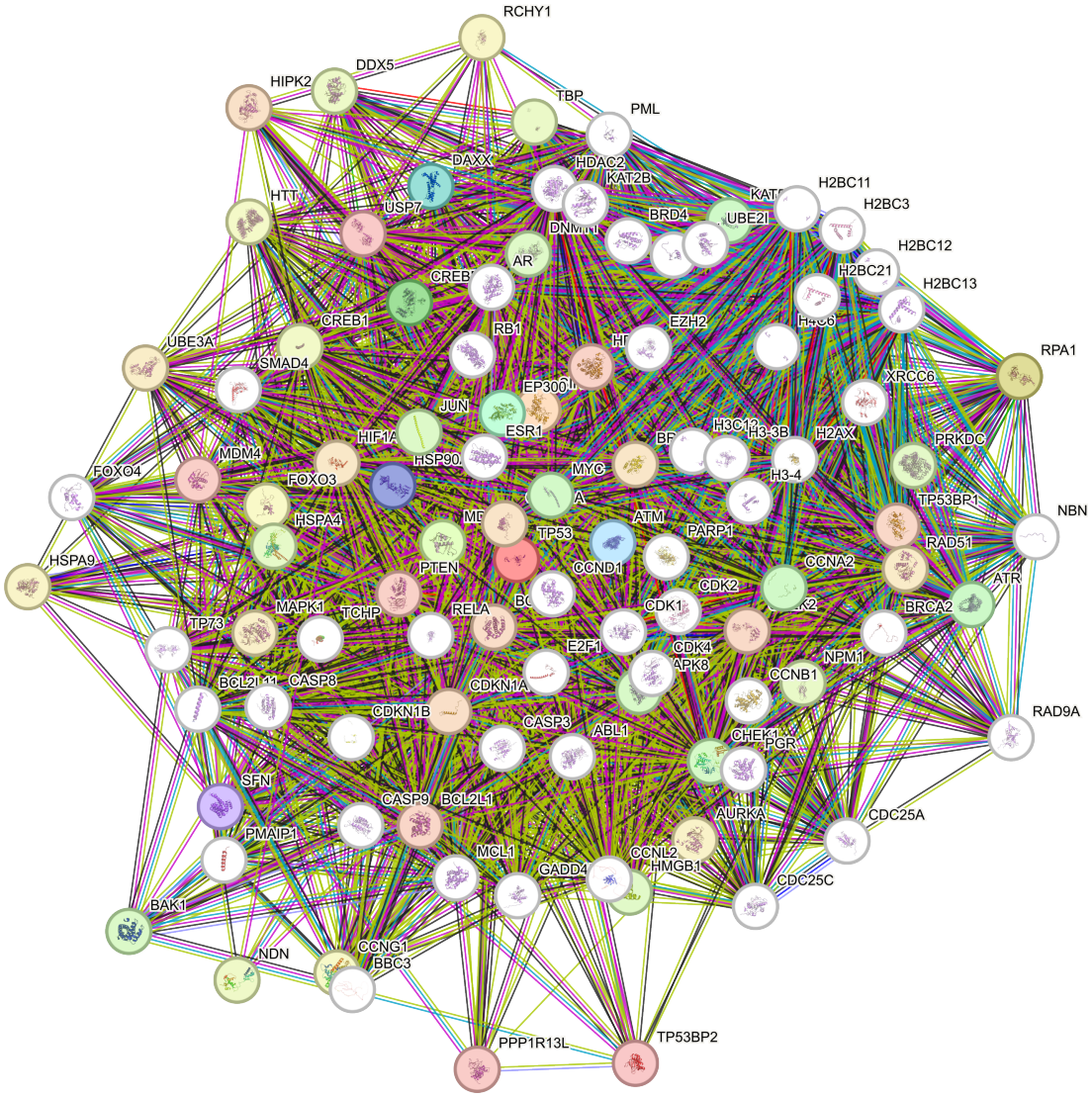

Figure 1.10: Protein-protein interactions network of tumor protein 53 (TP53). Data retrieved from STRING-db.org

Networks can be undirected, as in the case of PPINs, or directed like in the case of GRNs, where directionality is needed to establish relations of causality between the model's components. Given its relatively easy and understandable representation of biological systems, the network approach is particularly convenient in Systems Biology, and in addition to that it can also be easily translated to a mathematical model on top of which simulations can be made.

3.1.3 Network Inference

Recent reviews have explored methods to infer GRNs directly from bulk or single-cell RNAseq data [131] or from time series [119].

Networks can also be inferred from prior knowledge and a tool facilitating the construction of these

networks from a predefined list of genes will be presented in chapter 3.

3.2 Towards simulating biological systems: mathematical models for biology

These networks can be interpreted dynamically and translated into mathematical models. These mechanistic models primarily exist in two flavors: quantitative and qualitative.

Mechanistic quantitative models employ mathematical equations grounded in physical and chemical principles to describe specific biological mechanisms. These models embed biological features in mathematical representations, often utilizing ordinary or partial differential equations (ODE or PDE) to capture the system's variations through its components. That way, the concentration or activity of a protein, interacting with other proteins, can be followed over time.

To illustrate this approach, we can consider a small example of a motif widely observed in biology, a negative feedback regulation: the system is composed of a protein that inhibits its corresponding protein-coding gene by interfering with its transcription.

Let x_1 be the mRNA of a gene and x_2 the corresponding encoded protein. Let k_1 be the transcription rate of that gene into an mRNA molecule, and k_2 the translation rate of the mRNA into a protein, with γ_1 and γ_2 the corresponding degradation rates. If we indicate the negative feedback inhibition with a function $h(x_2, \theta, n)$, with θ and n as parameters of that function, the set of equations representing the feedback mechanism is given by:

$$\frac{dx_1}{dt} = k_1 h^{-}(x_2, \theta, n) - \gamma_1 x_1 \tag{1.1}$$

$$\frac{dx_2}{dt} = k_2 x_1 - \gamma_2 x_2 \tag{1.2}$$

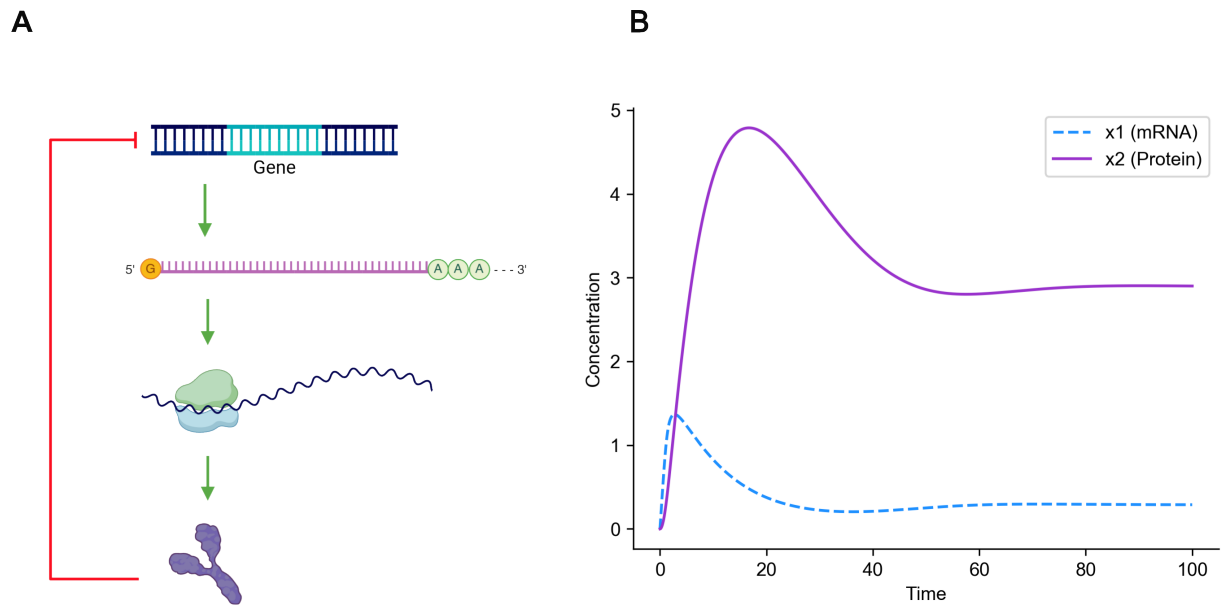

A. Graphical representation of a protein inhibiting the transcription of its corresponding protein-coding gene (negative Feedback loop). **B.** Mathematical representation of the system using 1.1 and 1.2 following the expression of each entity over time

Such a simplistic representation already holds a powerful predictive capability once the parameters characterizing the equations are well identified and assessed. Difficulties arise when trying to infer such parameters on bigger networks and more complex processes as the data for synthesis or degradation rates, or binding affinities are not easy to find and very often context-specific. Accurate parameter estimation is crucial for the model to reliably predict biological behavior. This frequently necessitates new experiments to determine the specific parameters required for precise predictions. However, in some cases, conducting these experiments to quantify certain system parameters may prove to be unfeasible.

3.3 Boolean Modeling

3.3.1 Boolean networks

Boolean models are built on networks designed to qualitatively capture the interactions among various components of the biological system being represented. These networks, grounded in biological phenomenology, can be adapted to reflect different aspects of cellular processes occurring at various scales, such as post-translational modifications or gene regulatory mechanisms, by appropriately structuring the model's components and rules.

While this framework serves as a rough approximation of biological evidence, it offers an effective representation of the qualitative dynamic behavior of biological processes. For instance, post-translational modifications can be incorporated by adding components to represent different states of a molecule, such as phosphorylated or unphosphorylated forms. Transition rules governing

these components can then capture the effects of such modifications on the molecule's activity or interactions with other components.

Similarly, gene regulatory mechanisms can be modeled by including components that represent transcription factors, promoters, and regulatory elements. Rules can then dictate how these components interact to influence gene expression levels. Biologists often adopt a binary perspective when analyzing specific system features—for example, viewing gene expression as a Boolean state representing whether a gene is "on" or "off."

The practicality of Boolean modeling is further demonstrated by its ability to approximate regulatory processes. Many of these processes involve concentration levels that can be modeled as Hill functions, which are effectively represented using step functions. This simplifies the system by restricting the set of possible values to [0,1], capturing essential dynamics without unnecessary complexity.

In this framework, the elements composing the biological system (e.g., genes, proteins, complexes) can be represented as nodes in a network. Their activity is positively or negatively influenced by other entities, simplifying the modeling of systems where molecular interaction details are not always known. This method is particularly useful for representing complex processes and signaling pathways.

Boolean networks consist of interacting nodes, where the edges represent the interactions between nodes. These edges define the logical equations governing the behavior of each node.

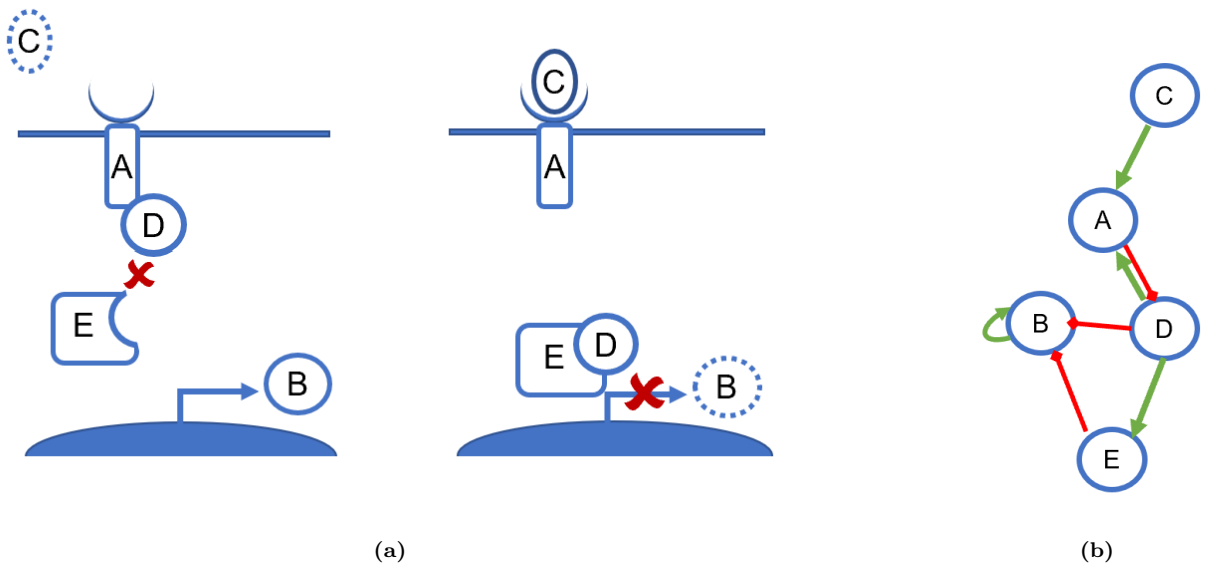

Figure 1.11: An example of a network representation of a biological system. (a) A ligand C binds to a receptor A, which is attached to a mobile subunit D. Upon binding with C, A releases D, enabling it to form a complex with protein E. The complex formed by E and D can block the transcription of gene B. (b) The biological system in (a) is adapted to a directed network of influence, where red edges and green edges indicate inhibitory and stimulatory effects, respectively.

Let $\mathcal{N}$ be a network containing n nodes. The state of the network, i.e., the collection of the states of each node, can be represented using a vector of Boolean states:

$$\mathbf{S} = \{S_i\}, \quad S_i \in \{0, 1\}, \quad i = 1, \ldots, n \tag{1.3}$$

Here, S_i represents the state of the i-th node in the network, and the entire set of S values defines the network state $\mathbf{S}$. For a given node i, consider the subset of nodes in the network that interact with i (its neighbors), denoted as $\mathcal{N}_i$. Since the logical state of i depends on the states of its neighbors, we can express the state of node i using a Boolean function f_i, which represents its incoming edges:

$$S_i(t) = f_i(S_{\mathcal{N}_i}(t)) \tag{1.4}$$

This function is formulated using logical operators such as **&** (AND), **|** (OR), and **!** (NOT). Depending on the type of updating scheme used in Boolean network simulations, the state of a node i at the time $t + 1$ can be expressed as:

$$S_i(t + 1) = f_i(S_{\mathcal{N}_i}(t)), \tag{1.5}$$

where $S_{\mathcal{N}_i}(t)$ represents the states of the neighbors of i at time t.

In Boolean modeling, the system's components are discretized into binary states, typically representing "on" (1) or "off" (0), eliminating the need for precise parameter fitting. Each node (or component of the system) has a logical equation determining its activity status: the component is active when its logical equation is satisfied (true) and inactive when not (false).

The model state is represented as a vector of Boolean variables that defines the status of all components (nodes) under specific conditions.

All possible transitions between network states form a structure known as the transition graph (or state transition graph). These transitions can be conceptualized as time steps. While they do not represent the actual timing of biological processes, they correspond to the time required to observe an event in the network, such as a change in its state.

For a Boolean network with n interacting nodes, the total number of possible network states is 2^n. Within the framework of Boolean modeling, transition graphs can be classified into two types based on the strategy used to update the network state: synchronous and asynchronous Fig. 1.12.

The synchronous transition graph arises when all nodes in the network are updated simultaneously in a single transition. In contrast, the asynchronous transition graph is generated when only one node, randomly selected from the set of all nodes, is updated during each transition.

Mathematically, the asynchronous transition between a generic pair of network states, (S, S'), is defined as follows:

$$S_{j\prime} = B_j(S) \quad \text{for a given } j, \tag{1.6}$$

$$S_{i\prime} = S_i \quad \text{for } i \neq j, \tag{1.7}$$

where $B_j(S)$ represents the Boolean function associated with the j-th node, evaluated based on the entire network state S at the given time.

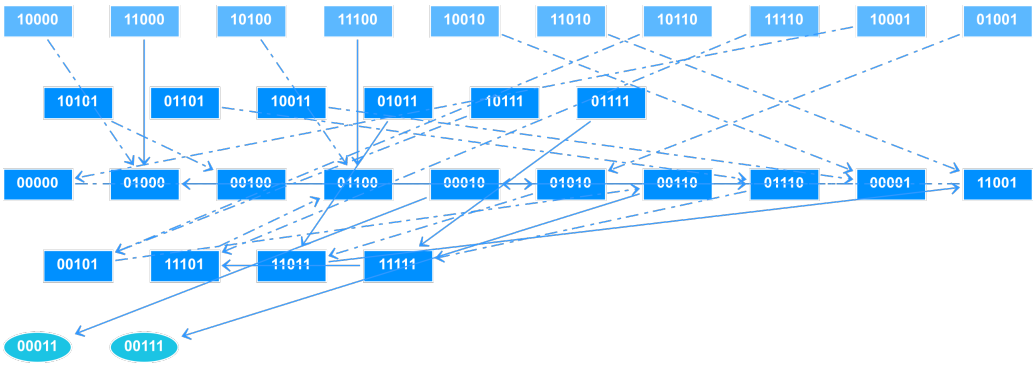

(a)

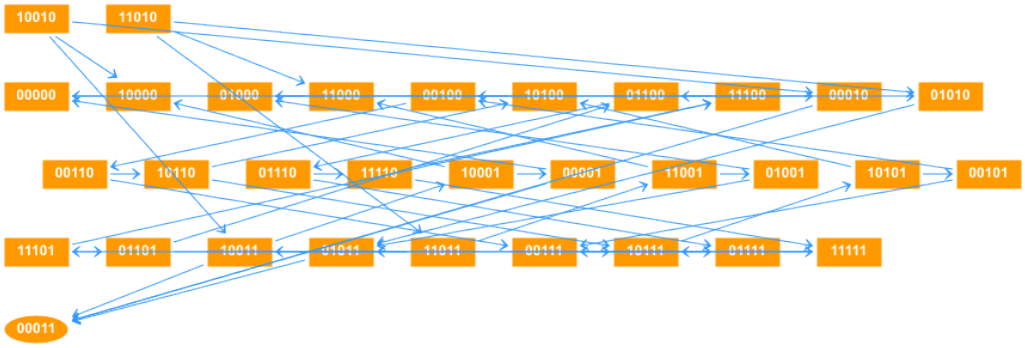

(b)

Figure 1.12: Examples of STGs realized using different updating strategies. In (a) an STG built using a synchronous, where plain arrows show one change of value in the vector of variables, and dashed arrows show more than one change, and in (b) asynchronous updating. The network used for the simulations is the same as presented in Fig. 1.11.

To complement the nomenclature of Boolean modeling, we can introduce a possible outcome of the dynamical processes occurring on the network such as the reach of stable states, also known as fixed points or attractors. These are model states that, once reached, do not transition to any other state. In other words, when the system reaches a stable state, no further changes occur, indicating that the model has reached equilibrium. These stable states are significant because they often represent steady conditions in biological systems, such as the sustained activation of a gene regulatory network responsible for a specific cellular function. In contrast, limit cycles represent a sequence of model states through which the system cycles indefinitely. Limit cycles are characterized

by a repetitive pattern of states that the model revisits in a fixed order. These cycles can represent periodic behaviors in biological systems, such as oscillations in the concentration of certain proteins or other molecular entities. The system moves through a predetermined sequence of states, returning to the starting point after completing the cycle, and then repeats this sequence continuously. Therefore, the solutions of a Boolean model are either stable states, where the system settles into a single, unchanging configuration, or limit cycles, where the system exhibits a repeating pattern of states. Both types of solutions are crucial for understanding the long-term behavior of the modeled system, with stable states representing persistent outcomes and limit cycles representing periodic dynamics. Whenever possible, these solutions are correlated with phenotypic observations, such as apoptosis, cell division, or cell cycle arrest.

This formalism is coarse-grained and provides limited predictive potential. Moreover, as stated above the number of nodes that can be handled is restricted because the size of the STG is 2^n. To address this issue, the solution of simulations of the model can be provided through a probabilistic sampling of the STG, using a stochastic approach. In the following section after having introduced the baseline concept of stochastic processes and Markov chains, I will introduce MaBoSS [163]. MaBoSS is a tool developed to simulate dynamical processes on Boolean networks using Markov processes on the STG. This feature allows the estimation of the solutions in a probabilistic manner rather than computing them in a deterministic fashion.

3.3.2 Stochastic processes on Boolean networks

This paragraph provides the essential knowledge to understand the mathematical key concepts that constitute the baseline for the approach that can be used to simulate dynamical processes on Boolean networks. I will first introduce generalities on stochastic processes and how to use this formalism to simulate a dynamic on the Boolean network.

A broad definition of the stochastic process indicates that it is essentially a collection of random variables indexed with a parameter, usually time. Alternatively, a stochastic process can be seen as a rule established to assign a value to a function of random variables [87].

$$s\colon\ t \to s(t), t \in I \subset \mathbb{R} \tag{1.8}$$

With I as an interval of real values and $S(t)$ represents a random variable assigned to each element t in I. Now, let consider that $s(t)$ can take values from possible configurations of the network and let us call this space $\mathbf{\Sigma}$. For each of the random variables, we can define their probability to assume a

specific value as:

$$\mathbf{P}[s(t) = \mathbf{S}] \in [0,1] \quad \forall \mathbf{S} \in \mathbf{\Sigma} \quad \text{and} \sum_{\mathbf{S} \in \mathbf{\Sigma}} \mathbf{P}[s(t) = \mathbf{S}] = 1 \tag{1.9}$$

A Markov process is a mathematical object that describes a stochastic process for which the probability of each event depends exclusively on the event that occurred right before it: this feature is indicated as the Markov property [88].

Markov processes are characterized by an initial condition:

$$\mathbf{P}[s(0) = \mathbf{S}] \quad \forall \mathbf{S} \in \mathbf{\Sigma} \tag{1.10}$$

It is worth noting that $s(t)$ is not independent for all t, therefore:

$$\mathbf{P}[s(t) = \mathbf{S},\ s(t') = \mathbf{S}'] \neq \mathbf{P}[s(t) = \mathbf{S}] \cdot \mathbf{P}[s(t') = \mathbf{S}']$$

and to fully describe a Markov process we also need to define the conditional probabilities:

$$\mathbf{P}[s(t) = \mathbf{S} | s(t\prime) = \mathbf{S}'] \quad \forall \mathbf{S}, \mathbf{S}' \in \mathbf{\Sigma}; \forall t,t' \in I; t < t' \tag{1.11}$$

The need for the definition of conditional probabilities derives from the fact that Markov processes are featured by the *Markov property*:

$$\mathbf{P}[s(t_i) = \mathbf{S^{(i)}} \,|\, s(t_1) = \mathbf{S^{(1)}}, s(t_2) = \mathbf{S^{(2)}}, \ldots, s(t_{i-1}) = \mathbf{S^{(i-1)}}] = \mathbf{P}[s(t_i) = \mathbf{S^{(i)}} \,|\, s(t_{i-1}) = \mathbf{S^{(i-1)}}] \tag{1.12}$$

which in other terms indicates that present events are not conditioned by either the past nor the future.

Markov processes are divided into two main categories, contextually with the definition of time used. In the case of a stochastic process for which the Markovian property holds, in which time is considered as a discrete variable ($t \in \{t_0, t_1, ..., t_n\}$), this object takes the name of *Markov chain*. In this case, the conditional probabilities are function of transition probabilities: $\mathbf{P}[s(t_i) = \mathbf{S^{(i)}} | s(t_{i-1}) = \mathbf{S^{(i-1)}}]$.

If time is considered as a continuous variable ($t \in I = [t_0, t_f]$), conditional probabilities are function of transition rates: $\rho_{\mathbf{S} \to \mathbf{S}'}$. We can also describe discrete transitions between states of a continuous-time Markov process (*jump process*): in this case, the transition probability is given by:

$$\mathbf{P}_{\mathbf{S} \to \mathbf{S}'} = \frac{\rho_{\mathbf{S} \to \mathbf{S}'}}{\sum_{\mathbf{S}\prime\prime \in \mathbf{\Sigma}} \rho_{S \to S''}}$$

In the following section, only jump processes will be considered. This kind of stochastic process and the relative formulation of the probability of transition are time-independent. In order to characterize a jump process on a Boolean Network, a deeper description of the state transition graph is needed. Let $\mathcal{S}$ a state transition graph for which all possible network states S form the network space Σ. If we assume a continuous-time Markov process, we need to take into consideration transition rates and if $\rho_{S\to S\prime} > 0$ it means there is an edge of the network $\mathbf{S}$ to $\mathbf{S\prime}$. In the case of a discrete-time Markov process, we can use transition probabilities as in 1.12. If we consider an asynchronous updating strategy on the network, we can see that this can be alternatively seen as a discrete-time Markov process. Using the formalism of the previous section, $\mathcal{N}$ is a directed network of n nodes. For the i-th node we can specify its behavior using a Boolean function as in 3.3.1. This function depends on the state of the j-th node directed to i. For a generic pair of states $(\mathbf{S}, \mathbf{S\prime}) \in \Sigma$, the asynchronous transitions are implemented as for 3.3.1.

where $B_j(S)$ represents the Boolean function associated with the j-th node, evaluated based on the entire network state S at the given time. If we want to describe the transition from a state $\mathbf{S}$ to a state $\mathbf{S\prime}$ we can take the definition of conditional probability for a Markovian process: $\mathbf{P}[s(t_i) = \mathbf{S^{(i)}} \,|\, s(t_{i-1}) = \mathbf{S^{(i-1)}}]$. Let us consider $\gamma(\mathbf{S})$ as the number of possible transitions from one network state $\mathbf{S}$ to another state $\mathbf{S\prime}$. Furthermore, we can state that:

$$\begin{aligned} &\mathbf{P}[s(t_i) = \mathbf{S}' \,|\, s(t_{i-1}) = \mathbf{S}] = \frac{1}{\gamma(\mathbf{S})} \quad \text{if} \quad \mathbf{S} \to \mathbf{S}' \quad \text{is an asynchronous transition,} \\ &\mathbf{P}[s(t_i) = \mathbf{S}' \,|\, s(t_{i-1}) = \mathbf{S}] = 0 \quad \text{if} \quad \mathbf{S} \to \mathbf{S}' \quad \text{is NOT an asynchronous transition.} \end{aligned} \tag{1.13}$$

If an initial condition is specified, the two conditions illustrated above allow us to describe the asynchronous updating of a dynamical process on a Boolean network as a discrete-time Markov process [165] (proofs available in the Appendix).

In order to deal with continuous time, we can derive the continuous-time Markov process from the discrete-time one. First, we need to consider transition rates instead of probabilities, and next in order to define a continuous-time Markov process, we need to provide an initial condition and a set of transition rates. Instant probability $\mathbf{P}[s(t) = \mathbf{S}]$ and joint probabilities are solutions of the following master equation.

$$\frac{d}{dt}\mathbf{P}[s(t) = \mathbf{S}] = \sum_{\mathbf{S\prime}} \rho_{(\mathbf{S\prime}\to\mathbf{S})}\mathbf{P}[s(t) = \mathbf{S\prime}] - \sum_{\mathbf{S}'} \rho_{(\mathbf{S}\to\mathbf{S}')}\mathbf{P}[s(t) = \mathbf{S}] \tag{1.14}$$

The generalization of asynchronous Boolean dynamics is specified by defining transition rates $\rho_{S\to S'}$ that are non-zero values only if the two network states S and S' differ by one node. Each Boolean function is replaced by two functions $R_i^{up/down}(\mathbf{S}) \in [0, \infty[$. Let be i a node in a network of n nodes

and S, $\mathbf{S}'$ two different network states; if i is the node that differs from S to S', we can define transition rates $\rho_{S\to S'}$ as:

$$\rho_{S\to S'} = R_i^{up}(\mathbf{S}) \quad if \quad S_i = 0 \rho_{S\to S'} = R_i^{down}(\mathbf{S}) \quad if \quad S_i = 1 \tag{1.15}$$

where R_i^{up} and R_i^{down} are the activation and inactivation rates of the node i. For continuous-time Markov processes, it can be proved that instantaneous probabilities always converge to a stationary distribution. In the Markovian case, the term stationary distribution refers to a set of instantaneous probabilities of a stationary Markov process that have the same transition probabilities of the given Markov process, whether its time dynamics is discrete or continuous. This means that given a stationary Markov process, for every joint probability $\mathbf{P}[s(t_1) = \mathbf{S}^(1), s(t2) = \mathbf{S}^(2), ...]$ and $\forall\tau$ it holds that:

$$\mathbf{P}[s(t_1) = \mathbf{S}^(1), s(t2) = \mathbf{S}^(1), ...] = \mathbf{P}[s(t_1 + \tau) = \mathbf{S}^(1), s(t2 + \tau) = \mathbf{S}^(1), ...] \tag{1.16}$$

where $\mathbf{P}[s(t) = \mathbf{S}]$, the instantaneous probability of a stochastic process, is time-independent. To describe continuous-time Markov process asymptotic behavior, we use indecomposable stationary distributions, i.e. stationary distributions that can not be expressed as linear combinations of other stationary distributions. A complete characterization of the asymptotic behaviors then can be given with a linear combination of indecomposable stationary distributions to which the process converges.

Periodic behavior is also possible, according to the definition of cycle and oscillation. A cycle, essentially a loop in the transition graph, does not depend on the particular value of a transition rate instead, it reflects the topology of the model. A cycle with no outgoing edges represents to all effects an indecomposable stationary distribution. In order to associate periodic behavior with instantaneous probabilities, we can only assume that such probabilities cannot be perfectly periodic. Nevertheless, they can exhibit a damped oscillatory behavior, defined as a continuous time Markov process with at least one instantaneous probability with an infinite number of possible extrema. Details are available in the Appendix. To conclude this section, we recall the necessity to compute conditional probabilities in order to solve the master equation coupled with our problem [89]. This calculation can be carried out by computing the exponential of a transition matrix :

$$\frac{d}{dt}\tilde{\boldsymbol{P}}(t) = M\tilde{\boldsymbol{P}}(t) \tag{1.17}$$

Because of the large size of the transition matrix ($2^n \times 2^n$), this calculation soon becomes unfeasible. For the purposes of modeling a biological process, interpreted as a continuous-time Markov process on a Boolean network, we will proceed by using the numerical algorithm implemented by Stoll et al. in 2012 [165], whose characterization will be illustrated in the following section.

3.3.3 Boolean Kinetic Monte Carlo algorithm

The Boolean Kinetic Monte Carlo (BKMC) algorithm is a refined version of the Kinetic Monte Carlo algorithm, commonly known as the Gillespie algorithm, first introduced in the 1940s. It was developed to model natural processes, with particular emphasis on chemical reactions. This class of algorithms is a powerful tool for exploring the probability space of a Markov process.

Specifically, the BKMC algorithm was designed to address the lack of modeling tools for phenomena represented as Boolean networks. By computing the statistically possible outcomes of a stochastic process—where activation and inactivation rates are known—the algorithm determines the time evolution of the system being investigated.

The BKMC algorithm is particularly suitable for networks fully described in terms of logical rules assigned to their nodes and transition rates that govern the activation and inactivation of these nodes. During model development, these transition rates can be assigned to align with the biological process's time evolution. Exact values are not necessary, as BKMC interprets transition rates as relative speeds of reactions within its computations.

The algorithm relies on multiple simulations, followed by a sampling of the probability space by evaluating time trajectories (or realizations) generated during these simulations. A trajectory $\hat{S}(t)$ is formally defined as:

$$\hat{\mathbf{S}}(t): \quad t \in [0, t_{max}] \longmapsto \Sigma \tag{1.18}$$

where Σ represents the set of all possible states of the system.

By using a complete set of time trajectories, the Markov process can be fully characterized, as probability computations are based on these trajectories. The algorithm generates this finite set of trajectories and calculates the associated transition probabilities. The process is iterative, beginning from an initial state $\mathbf{S}(t = t0)$, and computes a time interval δt during which a transition to a new state $\mathbf{S}'$ occurs. This state is determined by the algorithm. The time trajectory $\hat{\mathbf{S}}(t)$ is described by:

$$\mathbf{S}(t) = \hat{\mathbf{S}} \quad \text{for} \quad t \in [t_0, t_0 + \delta t] \quad \text{and} \quad \hat{\mathbf{S}}(t_0 + \delta t) = \mathbf{S}' \tag{1.19}$$

This process repeats until a predefined maximum simulation time is reached. At each step, given the current state S, two random numbers u and u' are drawn from a uniform distribution in [0,1]. The following steps are then performed:

1. Compute Total Transition Rate: All possible transitions from S are evaluated to calculate the total rate.

$$\rho_{tot} \equiv \sum_{\mathbf{S}'} \rho(\mathbf{S} \to \mathbf{S}')$$

2. Calculate Transition Time: The time until the next transition is computed as:

$$\delta t \equiv -\log(u)/\rho_{tot}$$

3. Reorder States: Possible states $\mathbf{S}'^{(j)}, j = 1, ...$ are reordered, along with their corresponding transition rates: $\rho^j = \rho(S \to S'^{(j)}$

4. Determine New State: The algorithm identifies the new state $\mathbf{S}'^{(k)}$ such that:

$$\sum_{j=0}^{k-1} \rho_j < (u'\rho_{tot}) < \sum_{j=0}^{k} \rho_j$$

The stochastic trajectories produced by the BKMC algorithm are crucial for relating continuous-time probabilities to the real-world process being modeled. To achieve this, a time window Δt is defined, allowing the derivation of a discrete stochastic process $s(\tau)$ (with $\tau \in \mathbb{N}$ from the continuous-time Markov process:

$$\mathbf{P}[s(\tau) = \mathbf{S}] \equiv \frac{1}{\Delta t} \int_{\tau\Delta t}^{(\tau+1)\Delta t} dt\, \mathbf{P}[s(\tau) = \mathbf{S}]$$

The BKMC algorithm provides estimates of $\mathbf{P}[s(\tau) = \mathbf{S}]$ through two primary steps:

1. For each trajectory j, the algorithm computes the time for which the system is in the state $\mathbf{S}$, in the time window $[\tau\Delta t, (\tau + 1)\Delta t]$.

2. This duration is divided by Δt, yielding the estimated probability for the trajectory j:

$$\hat{\mathbf{P}}_j[s(\tau) = \mathbf{S}]$$

By averaging over all trajectories j, the algorithm calculates the overall estimate $\hat{\mathbf{P}}[s(\tau) = \mathbf{S}]$ with its error:

$$\sqrt{\text{var}(\hat{\mathbf{P}}[s(\tau) = \mathbf{S}])/\text{Nr. of trajectories}}$$

In this study, we utilized MaBoSS (Markovian Boolean Stochastic Simulator), a tool based on the BKMC algorithm. Developed by the group of Stoll et al., MaBoSS is part of a suite for constructing models, running simulations, and analyzing results. Detailed information on this software is provided in the following sections.

3.3.4 The MaBoSS environment

MaBoSS (Markovian Boolean Stochastic Simulator) is a tool developed by Institut Curie that utilizes continuous-time Markov processes and implements the BKMC algorithm to estimate the activity of nodes in a Boolean network, simulating its dynamics. The tool provides a robust platform to study individual cellular dynamics [165].

MaBoSS, whose libraries are implemented in C++, operates using two essential input files: a Boolean network description file (*.bnd*) and a configuration file (*.cfg*). Every simulation based on an influence network requires these two files to proceed.

The *.bnd* defines the logical rules and transition rates for each node in the network. Nodes are represented with their logical functions and associated transition rates, as illustrated below:

```
Node A {
    logic = ( B & !C ) | D;
    rate_up = ($logic? $rate_uA : 0.0);
    rate_down = ($logic? 0.0 : $rate_dA);
}
```

In this example, the node A is governed by a logical rule based on the states of nodes B, C and D. If B is active and C is not active, or if D is active A is activated with an "up" transition rate of $rate_u A$; otherwise, it is deactivated with a "down" transition rate of $rate_d A$. Transition rates can be explicitly defined in the *.bnd* file or implicitly specified in the *.cfg* file.

This latter is a file needed to specify the initial conditions and other parameters for the simulation. Initial conditions include setting the values of certain nodes and defining which nodes are considered inputs. For input nodes, their values are fixed at the start of the simulation, while other nodes are assigned random initial values. The *.cfg* file also allows for defining global variables used to parameterize the transition rates defined in the *.bnd* file.

At the end of the simulation MaBoSS generates several types of outputs, including the stationary distribution of the network, the time-dependent probabilities of network states over a specified time window.

UPMaBoSS Conversely, for studies concerning the interactions among different cell types within multicellular systems, UPMaBoSS emerges as a valuable tool, facilitating the exploration of complex multicellular behaviors [164, 29]. UpMaBoSS, can be considered as an extension of the preexisting MaBoSS framework. The tool explicitly manages the processes of cell division (reproduction) and cell death within a population, whether the population is homogeneous or heterogeneous.

Parameter	Description
timetick	This parameter is used to evaluate estimates of the probabilities of network states. It sets the minimum time interval for nodes to change their state. Additionally, it regulates the convergence of probability estimates: a larger value for the time tick improves convergence.
max_time	The simulation generates trajectories over a specific duration determined by the value of *max_time*. If the biological timing of the process is known, this value can be explicitly defined. However, if this information is unavailable, *max_time* should be set to a value greater than the inverse of the smallest transition rate.
sample_count	This parameter specifies the number of simulations that MaBoSS executes concurrently to further evaluate the probabilities of network states.

Description of key MaBoSS parameters.

Furthermore, this framework enables the representation of the microenvironment influencing all cells in the model, as well as the activation of signaling pathways, whether direct or mediated. This approach is formalized through the concept of the *MetaCell*. The model focuses on capturing all relevant signaling pathways within a single framework. It allows us to model a mixed population of different cell types by assuming that many signaling pathways are shared across various cell types. The portion of the network corresponding to these shared pathways can be reused among the different cell types. Using this paradigm, different cell states within various populations can be represented as configurations of specific sets of nodes.

PhysiBoSS Additionally, to enhance the physical characterization of cellular environments, MaBoSS has been combined with an agent-based modeling tool, PhysiCell [61], focused on spatial cellular organization [102]. Physicell provides a modeling framework aimed to introduce a pertinent characterization of the simulation space at the physical level: this includes the introduction of chemical substrates that impact cellular behaviors and also the tuning of the physics of cells. Properties such as

Together, these tools offer a comprehensive suite for modeling and simulating biological systems, empowering researchers to unravel the complexities of cellular dynamics and multicellular interactions.

Motivation for using Boolean models Despite its simplicity, Boolean modeling can provide insights into the qualitative behavior of biological systems, detect emergent properties, and identify key regulatory mechanisms. Its intuitive nature and computational efficiency make it a powerful tool for hypothesis generation and validation in various biological contexts.

Boolean modeling has been applied for many years to study diseases and how dysregulations in signaling pathways can lead to unexpected phenotypes and undesired cellular responses [65, 129, 73]. There exist many tools that can simulate Boolean dynamics. A logical-modeling-community-based initiative, CoLoMoTo, has listed them highlighting the interoperability of the tools developed by the community. For this thesis, we will focus on two of them, MaBoSS, and its cell population version, UPMaBoSS, both based on a stochastic simulation of the Boolean network.

In this thesis, we used both approaches. MaBoSS was used to simulate what we refer to as the core model (chapter 4, section 3.3), and UPMaBoSS was applied to the ICD cycle including the interactions between cell types (chapter 4 section 3.2, [29]).

Data integration into Boolean models Models are constructed using generic biological knowledge, but to accurately predict differences between conditions—such as the downstream effects of two chemotherapeutic agents—it is crucial to integrate specific data into the Boolean model. Experimental data can be employed to manually set the initial conditions for model simulations or to use automated tools designed to configure either the initial conditions, model parameters (such as transition rates), or both.

The relevance of the type of data used depends on the biological layer being modeled. Ideally, if the model aims to represent post-translational interactions, proteomics data is the most suitable option for configuring simulations. Conversely, if the goal is to model a gene regulatory network, gene expression, and epigenetic data provide a better fit. Due to the widespread availability of transcriptomics data, gene expression profiles are frequently used as proxies to configure both the initial conditions and transition rates in simulations. Technical details regarding automatic model personalization will be provided in Chapter 3, section 3.4.

Chapter 2

Ph.D. research aims

The primary objective of this thesis was to enhance our understanding of Immunogenic Cell Death (ICD) and its potential to improve the effectiveness of chemotherapeutic treatments. By employing an interdisciplinary approach that spans experimental and computational biology, this research aims to address some key questions that represent the next steps in advancing ICD research.

Although some molecular mechanisms underlying ICD have been explored, there remain significant gaps in our knowledge that require focused investigation. This thesis endeavors to fill some gaps by identifying crucial factors and pathways involved in ICD and by developing computational models to predict and enhance the immunogenicity of chemotherapeutic drugs.

Beyond the well-established hallmarks of ICD consisting of released/surface exposed DAMPs, a major focus of this work was to determine whether a distinct molecular signature of ICD can be identified. The latter could serve as a convenient biomarker to predict the immunogenic potential of chemotherapeutic agents.

Understanding the secreted factors that contribute to the immunogenicity of chemotherapies is another key aspect of this research. The initiation of the cancer immunity cycle by ICD-inducing treatments is complex, involving the release of DAMPS, including the secretion of cytokines, that play crucial roles in recruiting and activating immune cells. By characterizing these secreted factors, my PhD work further aimed to provide insights into optimizing the immunogenic potential of chemotherapies through manipulation of the related secretome.

Additionally, this research explored the key cellular pathways that regulate the secretion and release of ICD-related DAMPs. By investigating the signaling networks and molecular mechanisms governing these processes, this study aimed to identify the pathways that influence the immunogenic potential of dying cells. This understanding could reveal new targets for boosting the immune response through ICD induction.

Building on the identification of molecular signatures and pathways, the thesis will also investigate

the feasibility of recapitulating ICD in silico. By integrating both established and newly identified hallmarks of ICD into computational models, the research aims to simulate ICD processes, predict treatment outcomes, and suggest directions for future experimental validation.

Finally, the thesis will evaluate whether the developed in silico model can effectively predict the immunogenicity of chemotherapeutic drugs. The ultimate goal is to leverage this model as a tool for optimizing drug formulations and treatment regimens, thereby enhancing their immunotherapeutic efficacy and offering a potential framework for personalized medicine.

Chapter 3

Materials and Methods

Aims

n this chapter, we detail the experimental and computational approaches used to investigate the molecular mechanisms of Immunogenic Cell Death (ICD). We describe the methodologies employed for cell culture, treatment protocols, and data collection, as well as the computational tools and analytical techniques used to interpret the results. This section provides the foundation for reproducing the experiments and analyses presented in this thesis.

1 In vitro

1.1 Cell culture

MCA205 cells, derived from 3-methylcholanthrene-induced fibrosarcoma in C57BL/6 mice, were grown in a complete cell culture medium composed of RPMI 1640 (Gibco) supplemented with 10% fetal bovine serum and 1% penicillin-streptomycin.

1.2 In vitro treatments

The drugs MTX and OXA (both from Sigma-Aldrich) were dissolved in ultrapure water prior to dilution in the cell culture medium. CIS was obtained in suspension (Mylan) from the pharmacy of Institut Gustave Roussy and diluted in the culture medium. Cells were treated with MTX at 0.5, 1, 2, and 4µM. OXA was tested at 37.5, 75, 150, and 300 µM, and CIS at 3.375, 6.75, 12.5, and 25 µM.

1.3 Cell viability assay

Viability was assessed at 12, 18, 24, 36, and 48h post-treatment by flow cytometry following staining with the cell-permeant dye DiOC6(3) (3,3'-dihexyloxacarbocyanine iodide), selective for the

mitochondria of live cells, and the cell-impermeant dye DAPI (4',6-diamidino-2-phenylindole). Data were analyzed with the software FlowJo v10.8.2.

1.4 Assessment of established ICD hallmarks

For CRT and ATP assays, cells were seeded in 96-well culture plates at 5000 cells/well. For HMGB1 assay, 24-well plates were seeded at 50000 cells/well. One day later, cells were treated with the drugs for 3, 6, 12, 18, and 24 hours before harvest of cells and culture supernatants. Exposure of CRT at the surface of cancer cells stressed/dying upon treatments was detected by flow cytometry (cytometer BD Fortessa) after staining with Live/Dead Yellow dye and an anti-CRT (ab2907, Abcam) coupled to the fluorochrome AlexaFluor 488. Extracellular ATP and HMGB1 were detected using the Enliten luciferase-based kit (Promega), and by ELISA (Tecan), respectively. Signals were measured using the microplate reader Victor Nivo (Perkin Elmer).

1.5 RNA sequencing of in vitro treated cells

10^6 MCA205 cells were plated in 10 cm-diameter Petri dishes. The day after, cells were treated with MTX at 0.5 µM, OXA at 300 µM, and CIS at 25 µM for 3, 6, 12, 18 and 24 hours. Total mRNAs were extracted using the RNeasy kit (QIAGEN). Library preparation and mRNA sequencing was performed at the Genomic Platform of IBENS by Oumi Seydi (ENS). Quality control, alignment, and quantification have been realized at Institut Curie using the automated workflow of Institut Curie's bioinformatic platform by Théo Lassalle.

1.6 Phosphoproteome analysis

Cells were plated and treated following the same procedure as for transcriptomics investigations mentioned above. Next, dry cell pellets (n=3 technical replicates per treatment condition), were shipped to Tebu Bio laboratory for analysis on an array of antibodies specific to 1300 phosphorylated and corresponding total proteins (Antibody Explorer Array, Full Moon BioSystems). Candidates identified through this screening approach as differentially phosphorylated between treatments are currently validated by western-blot.

1.7 Cytokine profiling

Cells were plated and treated following the same procedure as for transcriptomics investigations mentioned above. Next, cell culture supernatants were shipped to Tebu Bio laboratory for cytokine profiling (n=4 biological replicates per treatment condition). Samples were analyzed using an array able to detect 200 cytokines by immunofluorescence (Mouse Cytokine Array GS4000, Raybiotech)

and delivering semi-quantitative measurements. The main targets identified through this screening approach were validated by ELISA (Abcam or BioLegend) using cell culture supernatant collected from 24-well plates seeded with 50000 cells and treated as mentioned above. To get a timewise overview of the different secretomics profiles associated with the different treatments, we sampled cell culture supernatants at earlier time points for a total of 5 time points: 3, 6, 12, 18, and 24 hours. Concentrations of cytokines were measured using a microplate reader (Victor Nivo, Perkin Elmer).

2 In vivo and ex vivo experimentations

2.1 Animals

Experimentations were carried out in 8-week-old immunocompetent C57BL/6 female mice (Envigo, Gannat, France) hosted in a pathogen-free, temperature-controlled environment with 12h light/dark cycles according to the FELASA guidelines, EU Directive 63/2010, and French legislation.

2.2 Cancer vaccination-rechallenge

MCA205 cells were treated in vitro for 32 hours with MTX at 0.5µM, OXA at 300µM, and CIS at 25µM. Under these conditions, as assessed by flow cytometry following DIOC-DAPI staining, viable/dying cells represent 30-50% of the population while the remaining 50-70% correspond to dead entities. $3x10^5$ treated cells were resuspended in 100 µl of PBS and injected subcutaneously into the left flank of each mouse. To investigate the role of cytokines in ICD, some cell extracts were supplemented in cytokines prior to in vivo administration: IL6 at 4.1 ng/injection, CCL5 at 1.67 ng/injection, or CCL20 at 2.12 ng/injection. One week later, mice were rechallenged with live untreated MCA205 cells, and tumor growth was closely monitored. If cells succumbed in vitro to ICD rather than non-immunogenic cell death (e.g., necrosis, apoptosis), their challenge would work as a cancer vaccine and protect against tumor development upon rechallenge. This assay is the gold standard to validate the ICD potential of therapeutic interventions36.

2.3 In vivo treatments

$3x10^5$ syngeneic MCA205 fibrosarcoma cells were implanted subcutaneously in the right flank of the mice. Once palpable, tumors were treated by intraperitoneal injections of 200 ul of PBS (untreated control group), MTX at 5.17 mg/kg, OXA at 10 mg/kg, or CIS at 10 mg/kg. To study the role of cytokines in the efficacy of chemotherapies, some animals were administered intraperitoneally at day -1, 0, and +1 post-treatment with neutralizing antibodies targeting IL6 at 32 µg/mouse and CCL5 at 100 µg/mouse. Tumor size was measured at 2-3-day intervals using a digital caliper and mouse

survival was monitored daily.

2.4 RNA sequencing of tumors

Tumors were collected and preserved in a conserving solution RNAlater (Thermo Fisher). Portions from the external, middle, and inner rim of the tumor tissue were processed using a lysis buffer (QIAGEN) supplemented with β-mercaptoethanol) in a tube containing microbeads. Extractions were performed using RNeasy kit (QIAGEN). Library preparation and mRNA sequencing were performed at the sequencing platform of Institut Cochin (Genom'IC, Paris).

2.5 Immune cell phenotyping

MCA205 tumors were harvested at days 3, 11, and 22 post-treatment. Tumors were dissociated using a mouse tumor dissociation kit and the gentle MACS Octo dissociator following the manufacturer's instructions (Miltenyi Biotec). Single-cell suspensions were labeled with the LiveDead Yellow viability dye (ThermoFisher) and stained with purified anti-CD16/32 (BD FcBlock). Immune cells infiltrating tumor and lymphoid tissues (draining lymph node, spleen) were phenotyped by flow cytometry using two panels of fluorescent antibodies targeting the surface markers (Panel 1: CD11c, B220, CD11b, PD-L2, Live Dead Yellow, MHC-II (I-A/I-E), CD8a, PD-L1, Ly-6C, CD103, Ly-6G, F4/80, CD45, PD-1. Panel 2: CD4, CD3, Live Dead Yellow, NK1.1, CD8, CD25, Foxp3 (intranuclear), IL-4, IL-17a, CD69, IFNg, CD45).

2.6 Spatial proteomics

Samples were collected at days 3, 11, and 22 post-treatment and preserved in 4% solution of paraformaldehyde for 24 hours and then transferred in 70% ethanol for 48 hours. Samples were embedded in paraffin at the Histology, Cytometry, and Imaging Centre of Centre de Recherche des Cordeliers (CHIC, CRC, Paris). Microtome cuts and slide mounting have been realized by Floriane Arbaretaz (CHIC). Technical optimization of the assay is being finalized by Dr. Maria Perez-Lanzon, a postdoctoral fellow in our group. The run for spatial proteomics on the NanoString GeoMX device is scheduled in the coming months.

2.7 Statistical Analysis

Data analyses were conducted using Python packages (edgeR limma-voom [147], SciPy [185], lifelines [39]), R and GraphPad Prism v10.2.3. Continuous variables were compared using Dunn's test, or Kruskal-Wallis H test with Bonferroni correction. ROUT test (Q=10%) was applied to identify and exclude outliers. Randomization of mice was performed using the RandoMice software. Kaplan–Meier

survival curves were analyzed with a log-rank test. Differences were considered statistically significant when p-value (two-tailed) < 0.05.

3 In silico

3.1 Data Analysis

3.1.1 Alignements and fastq processing

`Fastq` files were processed uysing the CurieCoreTech Bioinformatics (CUBIC) pipeline for bulk RNA-seq data processing. Quality control of raw reads was assessed using `fastqc`(v0.11.9) before passing to the trimming and filtering step using `Trim Galore!` (0.6.7). Subsequently, reads were aligned to the reference murine genome (GRCm39) using `STAR` (2.7.6a) and quality of alignements was controlled using `Samtools` (1.12), `RseQC` (4.0.0) and `Qualimap` (2.2.2). Duplicates were finally removed from the aligned BAM files using `Picard` (2.25.3) and normalized coverage files was obtained using `bamCoverage` (3.5.1). Finally, raw counts table was obtained using `HTseq counts` (0.10.0).

Differential expression analysis The table of raw counts has been initially purged of genes having less than 10 counts across all conditions. The analysis of transcriptomic data was then realized using R-based software edgeR and Limma-Voom [147].

The workflow included preparing raw read count data and metadata, importing data using the edgeR package to create a `DGEList` object, and filtering out lowly expressed genes. Then we normalized data to account for technical biases. Next, we used the `voom` function to transform the count data to log-CPM with precision weights and created a design matrix for the experimental design. A linear model is fitted to the transformed data using `lmFit`, and empirical Bayes moderation was applied to improve the reliability of the statistics.

3.1.2 Proteomics

For all slides, raw data were collected on an Excel file and all values were subtracted by local background values and outliers (spots for which the signal exceeded 35% above the median value of the quadruplicate spots) were removed. The Average table provided the average values of quadruplicate spots, excluding outliers. The Normalization table presented normalized values based on POS-Ave, calculated from the equal contribution of the two positive controls. Finally, the Chart sheet generated a clustered column chart for visualizing individual markers and positive controls. Data were exported to `.csv` format for subsequent analysis. For visualization purposes, only cytokines for which statistical significativity was detected were represented for each treatment in volcano plots (for each signal in all samples, we subtracted the corresponding signal measured in the sample containing only cell culture medium) and globally in clustermap using the Python package Seaborn. Statistical analysis was realized using one-way ANOVA and Dunnett's pairwise comparison

test with the Python package Scipy [185].

3.1.3 Phospho-proteomics screening

Each signal corresponding to the protein was normalized by the median signal within each slide (remember it was one slide per sample and only one sample per condition: it means no statistical consideration but only partial speculation on this results). We filtered out undetected values and then considered that calculated the Phospho-protein / total protein for all 4 conditions. Next, we normalized to the control in order to get a relative estimate of the impact of each drug compared to the control. Results were filtered based on FC (>2.0 and < 0.5)

3.2 Transcriptomics data analysis and functional inference

In the following sections, I will detail the methods used for the development of networks and logical models of ICD.

3.2.1 Enrichment analysis

Enrichment analysis on differentially expressed genes (DEGs) has been realized using the R packages clusterprofile and enrichplot [191]. DEGs were first filtered from the table of results obtained using edgeR and Limma-Voom and genes with adjusted p-values above 0.05 were discarded. Genes were then ranked by multiplying their `"logFC"` value by their `"adj.P.Val"`. The analysis has been realized for all treatments at all timepoints separately. Gene sets considered include gene ontology (GO) molecular functions (MF), cellular components (CC), and biological processes (BP). Enrichment analysis results were filtered based on the p-value calculated during the enrichment process and the top 20 terms were ranked based on the percentage of representation of the individual term within the dataset (prop. overlap). Additionally, for the first three elements, we calculated individual enrichment scores.

3.2.2 Functional enrichment

Functional enrichment such as estimation of TFs activity analysis and pathway activity analysis was realized using the python package decoupleR [10]. For both pathways and TFs we used a univariate linear model:

$$Y = \beta_0 + \beta_1 X + \epsilon \tag{3.1}$$

Where β_1 represents the matrix with containing the activities for the TFs considered, X represents the vector containing the information relative to gene expression for each sample. Using the output

of the differential expression analysis made with limma-Voom, we took the t-statistic of each gene compared to the control, for all conditions.

The TF-target relationships needed to determine what genes to consider in 3.1 were inferred from collecTRI [130]. CollecTRI is a dataset built upon literature, text-mining and manual curation and provides the a reference network for the targets of TFs, providing references and informing if a gene is either repressed or activated by a TF.

For pathway activities, for which we used the same linear model (3.1), we used the signatures provided by PROGENy [153], a dataset containing the characterization of 13 different pathways (EGFR, Hypoxia, JAK-STAT, NFkB, VEGF, TGFb, PI3K, p53, Trail, TNFa, MAPK, Androgen, Estrogen and WNT pathway). Key features of ProgenY include constructing pathway signatures from perturbation experiments, where activators or inhibitors are used to measure gene expression changes. This approach enhances accuracy, providing more precise estimates of pathway activities compared to methods that use only static gene sets.

3.2.3 Dynamical time warping

In this study, we employed the Dynamic Time Warping (DTW) algorithm [1] to evaluate similarities between the expression profiles of genes coding for ligands, receptors, or TFs associated with some targets of interest.

DTW is an algorithm that measures the similarity between two temporal sequences by calculating the optimal alignment, thereby minimizing the cumulative distance between them. The DTW algorithm allows for shifts and distortions in time, enabling a robust comparison of sequences that may have different lengths or temporal misalignments. To implement this, we first compute the Euclidean distance between each pair of expression values from the sequences being compared. The DTW algorithm then constructs a cost matrix to accumulate these distances and determines the path that minimizes the overall distance between the sequences.

By aligning the expression patterns of TFs and their identified cytokine-encoding target genes, DTW facilitates the identification of regulatory relationships and temporal correlations.

Function DTW_DISTANCE($s1, s2$)
Input: $s1, s2$ (array-like sequences to be compared)
Output: Dynamic Time Warping distance between $s1$ and $s2$
$len\_s1 \leftarrow \text{length}(s1)$
$len\_s2 \leftarrow \text{length}(s2)$
Initialize $cost\_matrix$ with zeros of size (len_s1, len_s2)
for $i \leftarrow 0$ to $len\_s1 - 1$ **do**
  for $j \leftarrow 0$ to $len\_s2 - 1$ **do**
    $cost \leftarrow \text{abs}(s1[i] - s2[j])$
    if $i = 0$ and $j = 0$ **then**
      $cost\_matrix[i][j] \leftarrow cost$
    else if $i = 0$ **then**
      $cost\_matrix[i][j] \leftarrow cost + cost\_matrix[i][j-1]$
    else if $j = 0$ **then**
      $cost\_matrix[i][j] \leftarrow cost + cost\_matrix[i-1][j]$
    else
      $cost\_matrix[i][j] \leftarrow cost + \min(cost\_matrix[i-1][j], cost\_matrix[i][j-1], cost\_matrix[i-1][j-1])$
    end if
  end for
end for
return $cost\_matrix[len\_s1 - 1][len\_s2 - 1]$
End Function

Algorithm 1 Calculate DTW Distances for Each Row Compared to Every Other Row

Function CALCULATE_DTW_DISTANCES(df)
Input: df (dataframe containing sequences as rows)
Output: List of tuples with indexes and DTW distances
$distances \leftarrow []$
for $i \leftarrow 0$ to $\text{length}(df) - 1$ **do**
  for $j \leftarrow i + 1$ to $\text{length}(df) - 1$ **do**
    $s1 \leftarrow df[\text{iloc}[i]]$
    $s2 \leftarrow df[\text{iloc}[j]]$
    $distance \leftarrow$ DTW_DISTANCE($s1, s2$)
    $indexes \leftarrow (df[\text{index}[i]], df[\text{index}[j]])$
    Append $(indexes, distance)$ to $distances$
  end for
end for
return $distances$
End Function

The `dtw_distance` function calculates the Dynamic Time Warping (DTW) distance between two sequences s_1 and s_2. The cost matrix in this function is constructed to compute the cumulative cost of aligning two sequences s_1 and s_2 using the DTW algorithm, where the cost is calculated from the Euclidean distance between two elements of the sequences.

It begins by initializing the length of the sequences and creating an empty cost matrix filled with zeros. The function then iterates through each element of the sequences, computing the cost as

the absolute difference between the elements, and updating the cost matrix based on the minimum cumulative cost path (insertion, deletion, match). The DTW distance for the two sequences is obtained from the bottom-right cell of the matrix.

The `get_dtw_path` function is designed to find the optimal alignment path in the cost matrix that was computed during the Dynamic Time Warping (DTW) process. This path represents the best alignment between the two sequences, indicating how each element in one sequence maps to an element in the other sequence.

We checked the expression for ligands and receptors using several sources (Cytoreg [149], iCELLNET [132], CellChatdb [85]), and TF activity (regulating the expression of ligands and receptors of interest) was also estimated by using decoupleR [10]. To expand the network of possible interacting TFs, we relied on additional datasets (TRRUST [69], TFlink [105], HTFTarget [202]), and tried to establish a prioritization on the resulting regulatory network. For this task, we relied on unbiased prioritization tools, such as GENIE3 [82]. This method belongs to a class of ensemble learning algorithms and is based on decision trees to infer the regulatory relationships between genes in a given gene expression dataset.

The possibility of inferring the interactome of differentially expressed genes was also taken into account by using a novel modeling framework based on Pypath-Omnipath, developed by Dénes Türei (see section 3.3).

3.3 Network inference methods: from manual literature-based curation to NeKo

The development of the NeKo tool aiming to infer networks from a list of genes was led by Dr. Marco Ruscone from Institut Curie and in collaboration with Dr. Eirini Tsirvouli (NTNU, Trondheim), and Dr. Denés Turei (EMBL, Heidelberg, Germany).

The construction of the networks on which the Boolean models are built is a tedious task. It requires a thorough search of the literature linking genes and proteins that play a major role in the studied biological process. To facilitate this process, we created a python package that extracts knowledge from public curated pathway databases to build the first version of a network that will become the basis for the construction of the Boolean model. The network then needs manual curation but represents a first effort towards a more comprehensive model.

In 2016, an important effort was made by the group of Julio Saez Rodriguez to unify available knowledge from various databases into a single and comprehensive resource, Ominpath [181].

OmniPath allows users to infer the interactions of a biological entity by consulting the available knowledge collected in a single metadatabase. To query the database, a Python package known as Pypath was developed.

Although equipped with an enriched database, Pypath still lacks usability, and its application to network construction requires several efforts to go from a set of biological entities to a biological network.

To facilitate custom network construction, we developed a tool named NeKo. It builds networks from a list of genes provided by the user and will output a network from available knowledge in databases from Omnipath and beyond with all the annotations. Indeed, the user can manually add datasets to the available resources with an appropriate syntax and data structure.

At first, the nodes provided by the users are linked via interactions with their first neighbors via the function `connect_nodes`. The existing interactions can be of different types (e.g. binding, correlation, influence) according to the resource specified when characterizing the workspace and supported by referenced experimental evidence. Some available resources focused on signaling pathways, directly derived from OmniPath, such as SIGNOR [111], encompass transcriptional, post-transcriptional, or post-translational interactions.

The genes or proteins from the initial list are connected via different algorithms looking for the shortest paths between nodes. The method `complete_connections` aims to fully connect the disconnected network. The algorithm searches for new paths between the connected nodes via `connect_nodes`and those for which the initial search on the first neighbors did not give positive outcomes and for which an undirected path has to be inferred in the annotation databases. The user can choose what algorithm to use to complete the connections.

Available choices are 'breadth-first search' (BFS) and 'depth-first choice' (DFS) algorithms. The first one allows a faster search by exploring all neighbors at a specific graph depth before moving on to vertices at the next following depth level when the property of being connected to the previous depth layer is satisfied. By contrast, DFS percolates the tree as far as possible before backtracking the possible detected connections 3.1.

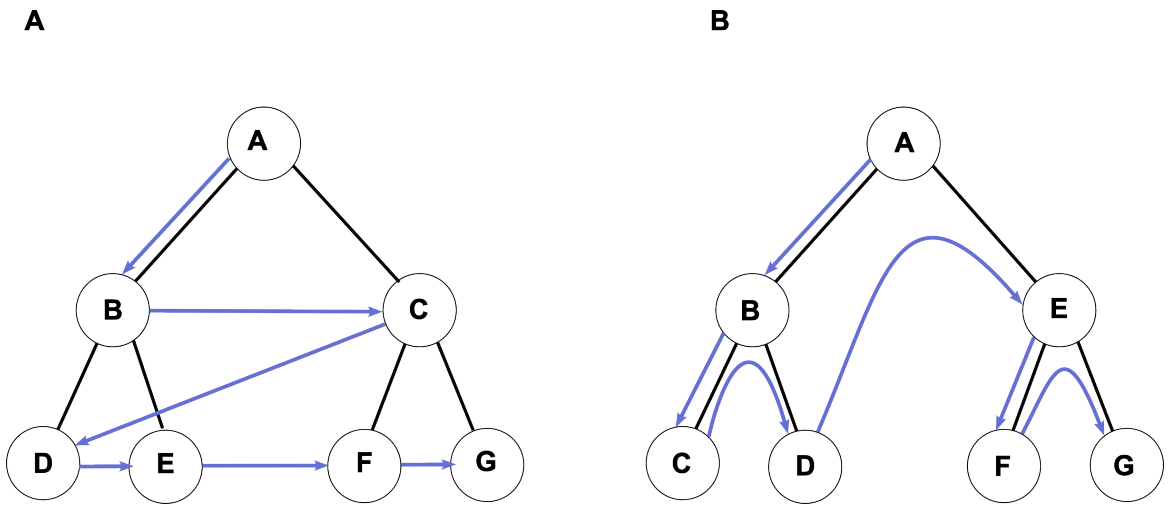

Figure 3.1: Schematic representations of network exploration algorithms available in Neko. A Breadth-first search and Depth-first search **B**

For both algorithms, non-connected nodes are used as seeds or roots for the search. In the case of the BFS, the algorithm keeps track of visited nodes during the search creating a queue. Although requiring more memory than DFS, BFS ensures finding the shortest path from the input nodes (not connected) to at least one of the output nodes (those belonging to the connected network). On the other hand, the use of DFS algorithm to complete a network does not provide a guarantee to complete it [42, 98]. In addition to that, DFS does not necessarily find the shortest path: longer paths can be found before shorter ones. According to the type of exploration one wants to realize, the two algorithms can be more or less suitable for a particular purpose.

Once the network has been created it can be visualized and exported as a `.SIF` file.

Neko also allows users to export the network into a logical model template by embedding the edges in a format compatible with logical modeling frameworks such as `.bnet` format. This feature is applicable to signed interactions, indicating whether a node or group of nodes activates or inhibits its target.

I specifically contributed to the tool with the conception, code testing and debugging, and minor code development, mainly related to network visualization.

3.4 Model Personalization with PROFILE

To build one model per patient, or one model per cell, we rely on a tool called pyPROFILE, which is a Python software derived from an original R package developed by Jonas Béal [14]. This tool integrates various types of omics data into the Boolean model to tune nodes' activity, transition rates, and initial conditions of the model, tailoring stochastic simulations on logical models to specific real-case scenarios.

Personalizing models based on experimental data involves constraining variables corresponding to

altered genes by setting model nodes to inactive (0) or active (1) states, and adjusting initial values and parameters to maintain these states during simulation.

These model modifications will modify the solution space (state transition graph, STG) and the probabilities for reaching a solution associated with a biological phenotype (e.g., cyclins' activity is used as a proxy for proliferative phenotypes and caspases' activity to apoptotic states).

PROFILE software performs both normalizations and binarization of gene expressions to personalize logical models. The process starts with evaluating gene expressions across a dataset, discarding genes that do not vary significantly. An admissibility test ensures a gene's expression falls within a sufficient range compared to others (above one-tenth of the median amplitude across all genes) and contains at least 5% non-zero values. If a gene passes this test, its distribution is evaluated for bimodality using Hartigan's dip test, the Bimodality Index, and kurtosis. Genes not following a bimodal distribution are tested for zero inflation or unimodal distribution. Unimodal distributions are transformed via a sigmoid function for normalization, while zero-inflated genes are linearly transformed to preserve their distribution density peak.

Chapter 4

Results

Aims

This chapter summarizes the key findings of my thesis, detailing various experiments conducted and their application in supporting in silico models' development.
The first section presents the main results obtained from both in vitro and in vivo experimentations. We initially assessed ICD hallmarks, followed by complementary investigations inferring the secretome and transcriptome of MCA205 cells treated with ICD inducers and non-inducers. Next, we tested in vivo the contribution of the molecular factors identified as potential contributors to cell death immunogenicity. This section highlights the differences between chemotherapies and identifies additional potential hallmarks of ICD.
In the second section of this chapter, we present a functional analysis linking experimental evidence with the construction of in silico models. We estimated pathway activity from expression data using curated databases and assessed TF activity by measuring their downstream targets. To improve accuracy, we validated this approach by applying the Dynamic Time Warping (DTW) algorithm to expression data for TF-cytokine pairs.
To conclude, the third section of the chapter illustrates the construction of three distinct in silico models, each capturing a particular aspect of ICD. These models were developed by combination prior knowledge and new experimental data. Additionally, two supplementary networks are provided as complementary results of the analyses conducted in the previous sections.

1 Experimental results

1.1 Profile of ICD-related hallmarks and immunogenicity of fibrosarcoma cells treated with cisplatin, oxaliplatin, or mitoxantrone.

MCA205 fibrosarcoma cells were treated in vitro with various dosages of CIS, OXA, and MTX before assessing viability and a series of ICD hallmarks. The objective consisted of determining their relative immunogenicity. Cell viability was evaluated using flow cytometry after staining with DiOC6(3)

and DAPI, which monitor mitochondrial membrane potential sustainability and membrane integrity, respectively (Fig. 4.1 A). Median lethal dose (LD50), referring to 50% of DiOC6(3)-negative and DAPI-positive dead cells, was achieved at 30 hours with the highest doses of the platinum salts CIS and OXA, and the lowest dose of the anthracycline MTX (Fig. 4.1A). Except for the highest concentration (2 µM) of MTX, cell death did not exceed 40% after 24 hours of chemotherapy, regardless of the chemical nature and dose of the drug tested (Fig. 4.1A, B).

Several ICD-related damage-associated molecular patterns (DAMPs), namely the release of ATP and HMGB1 in the cell culture medium, or the translocation of CALR at the surface of the plasma membrane, were monitored during the first 24 hours of drug-induced stress (Fig. 4.1C-H).

Using bioluminescence assays, an early, elevated, and acute release of ATP was observed upon MTX, peaking at 6 hours at all concentrations. By contrast, both platinum salts CIS and OXA provoked an early, moderate, and prolonged liberation of the nucleotide (Fig. 4.1 C). At 24 hours, the level of extracellular ATP remained at a significantly higher magnitude in MCA205 cells treated with the highest doses of platinum salts than untreated cells. Inversely, at that time point, the concentration of ATP detected in the culture medium of MTX-treated MCA205 cells was comparable to that of controls (Fig. 4.1 C, D).

Exposure of the ER chaperone CALR on the outer layer of the plasma membrane was significantly enhanced on live cells (i.e., LIVE/DEAD negative) stressed upon MTX and OXA, mainly at the most elevated doses, as compared to untreated (PBS) controls (Fig. 4.1 E, F). By contrast, treatment with CIS triggered marginal signal at all concentrations tested (Fig. 4.1 E, F).

To complete the assessment of the ICD hallmarks, we measured by ELISA the concentration of HMGB1 released in the supernatant of cells treated with effective doses of CIS (25 µM), OXA (300µM), and MTX (0.5 µM). Extracellular HMGB1 was detected in all conditions but with distinct dynamics. On one side, cells incubated with CIS and MTX showed leaked nuclear protein at 18 hours post-treatment, with a marked and similar increase at 24 hours (Fig. 4.1 G, H). On the other side, the detection of cell-free HMGB1 only started at 24 hours in the presence of OXA (Fig. 4.1 G, H).

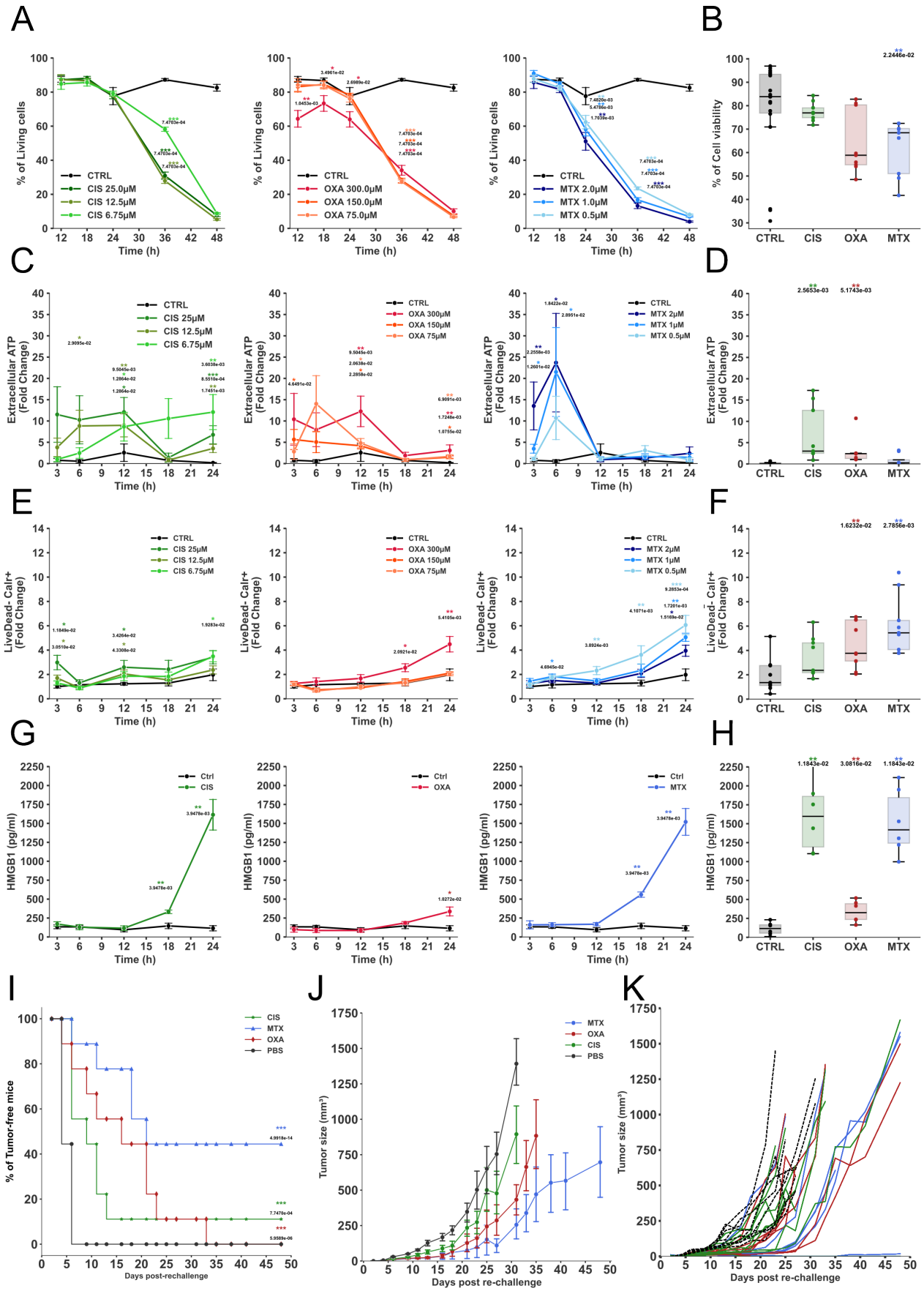

Figure 4.1: Profiles of ICD-related hallmarks upon CIS, OXA and MTX treatments of MCA205 fibrosarcoma cells in vitro. Cell viability (**A**), extracellular ATP (**B**), CALR exposure at the surface of non dead (i.e., L/D-negative) cells (n=9; pool of 3 experiments) (**E**), and extracellular HMGB1 (**G**) were measured in MCA205 fibrosarcoma cell cultures at 3, 6, 12, 18, and 24 hours of treatment with the indicated doses of CIS (green - left), OXA (red - middle), or MTX (blue - right).

Cell viability (**B**), extracellular ATP (**C**), surface-exposed CALR (**E**), and extracellular HMGB1 (**H**) are compared at 24 hours post-treatment with the doses chosen for subsequent in vitro analyses: CIS 25 µM, OXA 300 µM, and MTX 0.5 µM. (**I-K**) Assessment of ICD induction through in vivo tumor vaccination-rechallenge. Extended tumor-free survival (**I**) and mean (**J**) and individual (**K**) slowed down tumor growth are indicators of ICD induction. CIS, cisplatin; CALR, calreticulin; HMGB1, high mobility group box 1; ICD, immunogenic cell death; L/D, Live/Dead viability dye; MTX, mitoxantrone; OXA, oxaliplatin.

At last, we performed a vaccination-challenge assay to compare the overall immunogenicity of MCA205 cells succumbing to each chemotherapy. For this purpose, cells were incubated for 32 hours with either MTX at 0.5 µM, OXA at 300 µM, or CIS at 25 µM. These experimental settings resulted in comparable populations composed of 30-50% viable/dying cells, with the remaining fraction encompassing dead entities. Each of these populations was injected subcutaneously into immunocompetent C57Bl/6 mice. One week later, the animals were challenged with live MCA205 cells and tumor growth monitored; induction of ICD would translate into protection against cancer development. Median and long-term tumor-free survivals were significantly extended and tumor growth was delayed upon vaccination with MTX-treated cells, as compared to non-vaccinated controls. By contrast, CIS demonstrated much lower immunogenicity, with a short extension of tumor-free survival, whereas OXA showed an intermediate protective effect (Fig. 4.1 I-K).

Altogether, only MTX appeared to trigger bona fide ICD in fibrosarcoma cells. Intermediate immunogenicity associated with OXA could originate from a discrepancy in the kinetics of DAMP emission (prolonged ATP, late HMGB1). As reported in the literature [120], the limited immunogenicity of CIS coincided with restricted CALR exposure over time.

1.2 Transcriptomics identifies a signaling receptor activity signature associated with ICD in fibrosarcoma cells

To further characterize the premortem stress experienced upon each chemotherapy, we performed transcriptomics analyses of MCA205 cells treated in vitro with effective doses of MTX (0.5 µM), CIS (25 µM) and OXA (300 µM) for 3, 6, 12, 18 and 24 hours.

For simplicity, only the 24h timepoint data has been illustrated in the present report.

Our objective was to pinpoint molecular features of ICD by comparing the mRNA profile of cells treated with ICD versus non-ICD inducers. Out of the 16631 genes analyzed, the expression of 5728 genes was modulated ($|\log2 \text{ fold change}| > 2$; adjusted p-value < 0.05) upon chemotherapy: 4785 upon CIS, 3794 upon OXA, and 1091 upon MTX (Fig. 4.2 A, B).

Among them, 715 were shared between the three treatments whereas 2332 (1579 up-regulated, 753 down-regulated) were affected only by the two platinum salts, and 196 (115 up, 81 down) were proper to MTX treatment (Fig. 4.2 A, B).

Functional gene set enrichment analysis was performed on the list of differentially expressed genes

(DEGs) using Gene Ontology (GO) (molecular functions, biological processes) and MSigDatabase (Fig. 4.2 C). Out of the 20 most enriched GO terms, pathways related to plasma membrane receptor activity were abundant. In particular, cell-extracellular matrix (ECM) and cell-cell interactions seemed affected upon treatments, with a recurrence for immune and neuron-connected processes.

Notably, the term "signaling receptor activity" (GO:0038023) was enriched across all three chemotherapy conditions (Fig. 4.2 C). Out of the 2465 genes constitutive of this term, 240 were up-regulated while 145 were down-expressed across the different therapy conditions in comparison to untreated controls (Fig. 4.2 D). Interestingly, the expression pattern of genes associated with "signaling receptor activity" could distinguish between the platinum salts and the ICD-inducing anthracycline MTX.

More precisely, 7 genes were dysregulated (2 down- and 5 over-expressed) in MTX while remaining unaffected in both CIS and OXA. These latter encode G-coupled protein receptors (e.g., ADGRA2, GPR156), the cation channel TRPA1, the PRR MRC1 (best known as CD206), the cadherin family member CELSR1, the intranuclear receptor PPARG, and the adhesion receptor PTPRF.

In parallel, 111 genes were dysregulated (63 down- and 48 over-expressed) upon platinum salt therapy while remaining unaffected in the presence of MTX. These DEGs encode a variety of signaling molecules such as PRRs (e.g., AGER, NLRP6, NOD1/2, FPR2, TLR4/7/9, TRIM30A/D), cytokine receptors (e.g., CX3CR1, CXCR5, CSF1R, IL1R1, IL1RAP, IL17RD/RE, IL18R1, IL22RA2), immune checkpoints (e.g., FAS, LAG3, SLAMF8, TREM2), growth factor receptors (e.g., FGFR2, NRP2, PDGFRB, TGFBR2/3L), cholinergic receptors (e.g., CHRNA1/A10/B2), G-coupled protein receptors (e.g., ADGRA3, ADRA2A/2B, GPR15/35/83/85/141/152, LGR4/6, LPAR1, P2RY10B/14, PTGER1, TAS1R1/3, TAS2R108/137, TBXA2R), other adhesion-involved factors (e.g. CELSR2), ATP-binding cassette (ABC) transporters (e.g., ABCA1), and nuclear receptors (e.g., AR, NR1H3, NR2C2, NR4A3, NR6A1, RARB, RORA, RORC, ROR2) (Fig. 4.2 D - red frames).

Finally, one gene showed opposite dysregulation between treatments: *P2rx1*. The latter encodes a purinergic receptor and was overexpressed in MCA205 cells treated with the ICD inducer MTX but down-expressed upon both platinum salts.

Collectively, the transcriptomics analysis revealed a signature of DEGs related to signaling receptor activity and associated with ICD induction in fibrosarcoma cells.

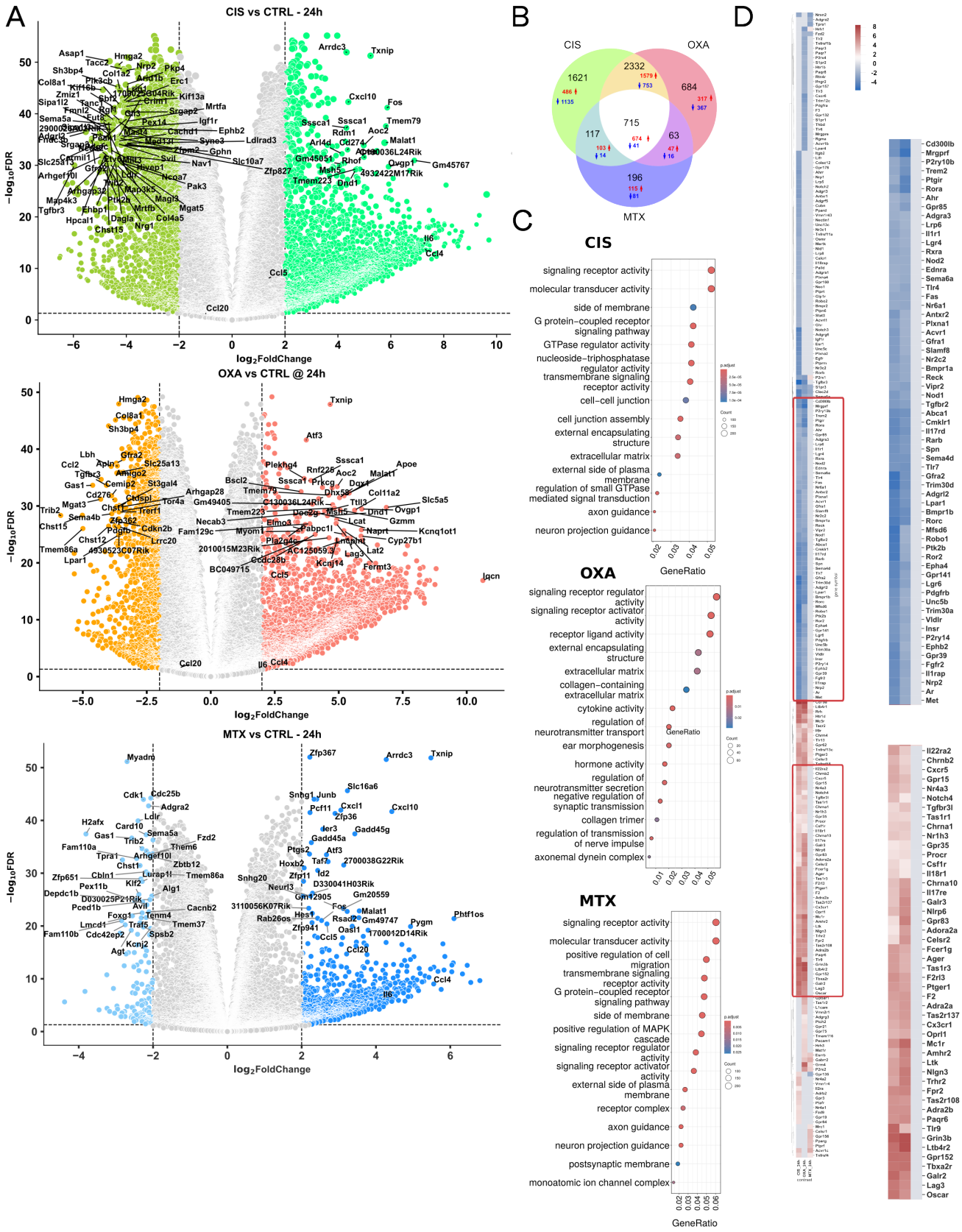

Figure 4.2: Transcirptomics profiles of MCA205 cell lines treated with ICD-inducers and non-ICD inducers highlights distinct transcriptional signature for signaling receptors. A. Volcano plot of differentially expressed genes (DEGs) at 24 hours post treatment. **B.** Venn-diagram representing the intersections between the sets of DEGs for each treatment. **C.** Enrichment analysis on DEGs at 24h post-treatment. **D.** Focus on *signaling receptor activity* ontology term.

1.3 Transcriptomics investigation reveals a secretory signature associated with cell death immunogenicity

Considering the differential expression of surface receptors between ICD and non-ICD inducers, we extended our investigations to the transcriptomic signature of proteins with autocrine, paracrine, juxtacrine and endocrine activity. A set of 255 murine genes encoding secreted factors was extracted from the literature. These latter encompassed chemokines, interleukins, interferons, growth-regulating factors, hormones (e.g., adipokines), and sculptors of the ECM. Fifty five percent of the genes (n = 141) showed detectable expression during the first 24 hours of treatment in MCA205 fibrosarcoma cells (Fig. 4.3 A). Of them, 114 genes were significantly modulated as compared to untreated controls (|log2 fold change| > 2; adjusted p-value < 0.05; Fig. 4.3B, C).

On one side, the absent/limited immunogenicity of the two platinum salts CIS and OXA coincided with altered levels of 45 mRNAs encoding secreted factors. Among them, 15 were increased and included some cytokines (IL11, IFNAB, LTA/B), factors promoting cell growth and tissue development (AMH, EFNB3, FGF17/18/20, NTN3), regulators of cell survival (FASL, PSPN) and metabolism (APOE, BGLAP3), and peptidase SERPINF2 which supports vascular co-option. The remaining 30 mRNAs exhibited decreased levels along both platinum salt treatments. They encoded other chemokines/cytokines (CCL2/7, CXCL12, IL7/15/34), some factors regulating cell proliferation, differentiation, migration (e.g., BDNF, BTC, CSF1, EDA, EFNA5, FGF7, GREM1, MET, NRG1, PDGFB/C, PTX3, SLIT2, WNT7B), adhesion (e.g., ADAMTS12), and angiogenesis (e.g., ANGPT1, CHRDL1, NTN4, VEGFC) (Fig. 4.3B-D).

On the other side, a 11-gene signature appeared specific to ICD induction, with 1 gene downexpressed (Mmp3) and 10 upregulated exclusively in MTX-treated cells (Fig. 4.3 C). In details, these latter DEGs encoded the cytokines CCL20, CXCL1, and IL33, the growth factors CCN3, CSF2 and FGF1/21, the vascular regulators ANGPTL4 and EDN1, and the hormone inactivator MME (Fig. 4.3 C).

Some similarities and discrepancies were witnessed between ICD and non-ICD-inducing treatments (Fig. 4.3 C). First, 29% of the secretome-related DEGs (n=33/114) were shared between all therapeutic interventions, thus excluding their contribution to the overall cell death immunogenicity. Surprisingly, they included *Cxcl10* whose product plays a well-acknowledged role in attracting the CXCR3+ T cell mediators of antitumor immunity, in particular following ICD induction [157]. Second, a limited number of DEGs was shared between MTX and one of the two platinum salts. The chemokine-encoding *Ccl5* gene and *Tnfsf18*, which expresses the transmembrane and soluble immune checkpoint GITRL, were activated upon both MTX and OXA treatments. The pro-angiogenic and anti-apoptotic factor ANGPT2 was upregulated upon both MTX and CIS

treatments. Inversely, *Mme* was repressed upon CIS and OXA chemotherapies, but stimulated in MTX-treated MCA205 cells (Fig. 4.3 C).

Furthermore, the longitudinal follow-up evidenced a prolonged dysregulation of most DEGs. Notably, *Ccl20*, *Cxcl1*, *Il33*, *Csf2*, and *Fgf1* experienced a sustained transcription with the ICD inducer MTX, without discontinuation starting at 6 or 12 hours of treatment (Fig. 4.3 A,C,D).

Overall, differences in immunogenicity between the platinum salts CIS and OXA and the anthracycline MTX coincided with distinct secretory signatures predisposing to immunomodulation and restructuring of the TME. More precisely, the dysregulated cytokines, growth regulators, and other ecto-enzymes, can potently attract myeloid and lymphocytic cells, and interfere with the differentiation, proliferation, adhesion, and survival of both parenchymal (epithelial, endothelial, and nerve cells) and mesenchymal (immune and fibroblastic cells) entities.

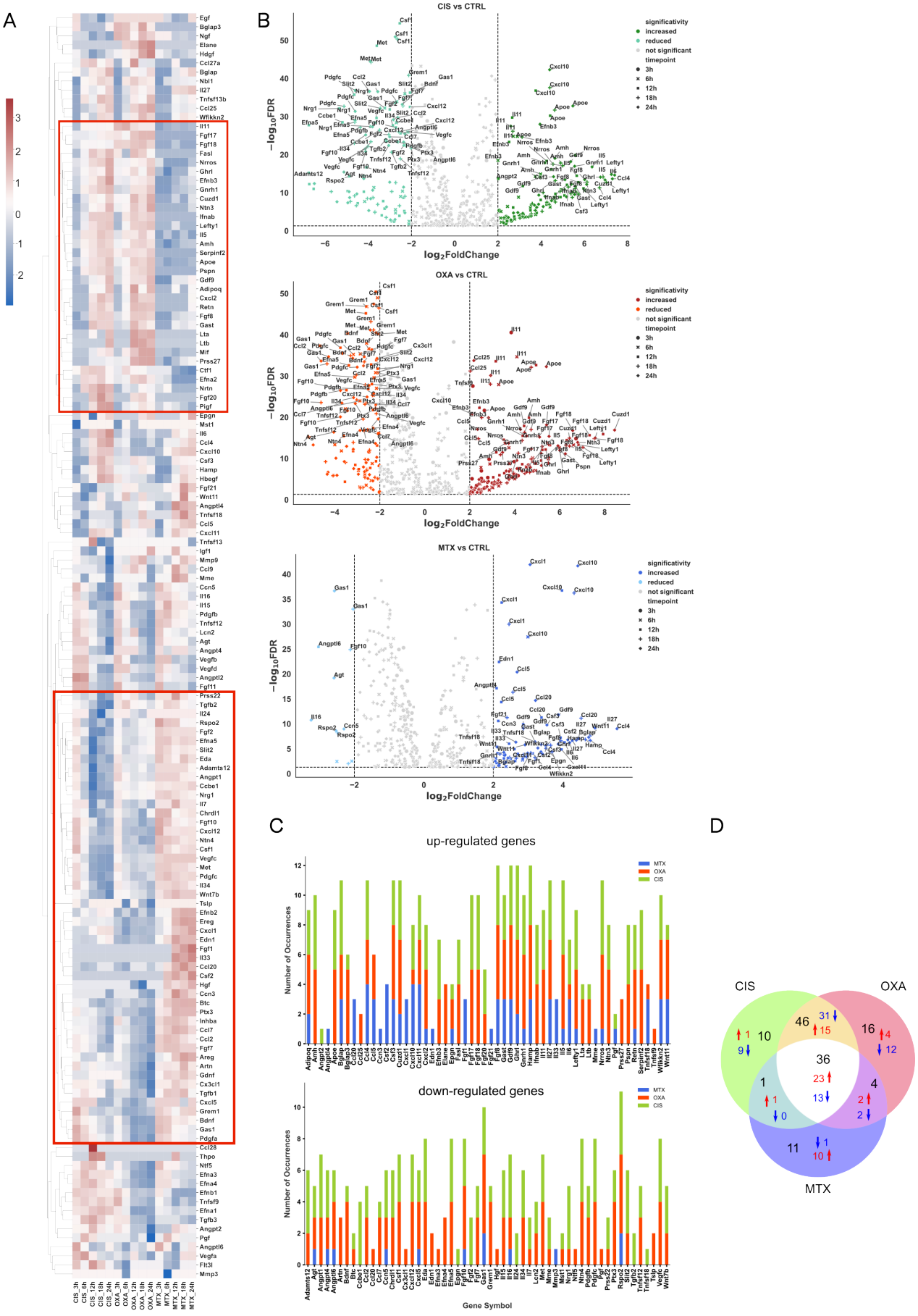

Figure 4.3: Transcriptomics profile of secreted immunomodulators distinguishes between fibrosarcoma cells treated with the ICD inducer MTX and the less immunogenic platinum salts.

A. Heatmap of the relative expression of 140 mRNAs encoding secreted immunomodulatory molecules detected within the transcriptomics dataset. Expression is displayed as relative to untreated controls.
B. Volcano plot of DEGs at all time points post treatments.
C. Stacked histograms representing the number of time points a gene was overexpressed (upper bar plot) or downregulated (lower bar plot) for each treatment.
D. Venn diagram representing the intersections between the sets of DEGs for each treatment, regardless of the time point. DEG, differentially expressed genes.

1.4 At the protein level, the secretome of fibrosarcoma cells treated with OXA, but not CIS, resembles that of their immunogenic MTX-treated counterpart.

Transcriptomics analyses highlighted differences in the secretome of fibrosarcoma cells under chemotherapy with the anthracycline MTX or the platinum salts CIS and OXA. To corroborate such findings at the protein level, we screened 200 secreted molecules in the culture supernatant of MCA205 cells treated for 24 hours. Among them, 80 proteins showed differential secretion between control and treated conditions (Fig. 4.4 A, B).

Euclidean clustering evidenced a homology between the profile of factors released upon MTX and OXA, whereas the secretome of CIS-treated cells segregated with controls (Fig. 4.4 A). As compared to controls, 24 significant modulations (20 up, 4 down) were observed upon MTX (|log2 fold change| $>$ 1.7; -log10 false discovery rate $>$ 1.3). Of them, 11 appeared specific to the ICD-inducing drug. They consisted of a non-degradation of soluble TNFSF12 provided by the culture medium and a non-production of PRL as compared to untreated controls; the latter observation being witnessed at a lesser extent upon both platinum salts. In parallel, MTX was also responsible for an extracellular enrichment of CCL19, CRP, FRZB, LGALS7, VEGFB and PSPN. Inversely, the anthracycline-treated cells demonstrated exclusive consumption of CSF2RB, SPINT1, and TNFRSF19 (Fig. 4.4 B, C).

In OXA-treated cells, the secretion of 24 molecules was affected (21 up, 3 down). Remarkably, 46% of these dysregulations (n=11) were shared with MTX but not CIS. They encompassed ADIPOQ, ARTN, CCL5, CCL20, CD36, CXCL1, CXCL7, GZMB, and TNFSF11, which all displayed enhanced levels (Fig. 4.4 B). Conversely, MTX and OXA-treated MCA205 cells harbored enhanced consumption of IL33 as compared to CIS and untreated controls.

By contrast, the secretory profile of cells exposed to CIS showed distinct characteristics. Notably, the non-ICD inducer was responsible for a potent production of IL6 and CCL4; the latter being also detected, yet to a lesser extent, in the supernatant of OXA-treated MCA205 cells (Fig. 4.4 B). Significant decrease of TGFB1, CD6, GPNMB, LCN2, METRN, and PRSS22 levels were also evidenced.

To consolidate these results, experiments were repeated and the production of selected cytokines,

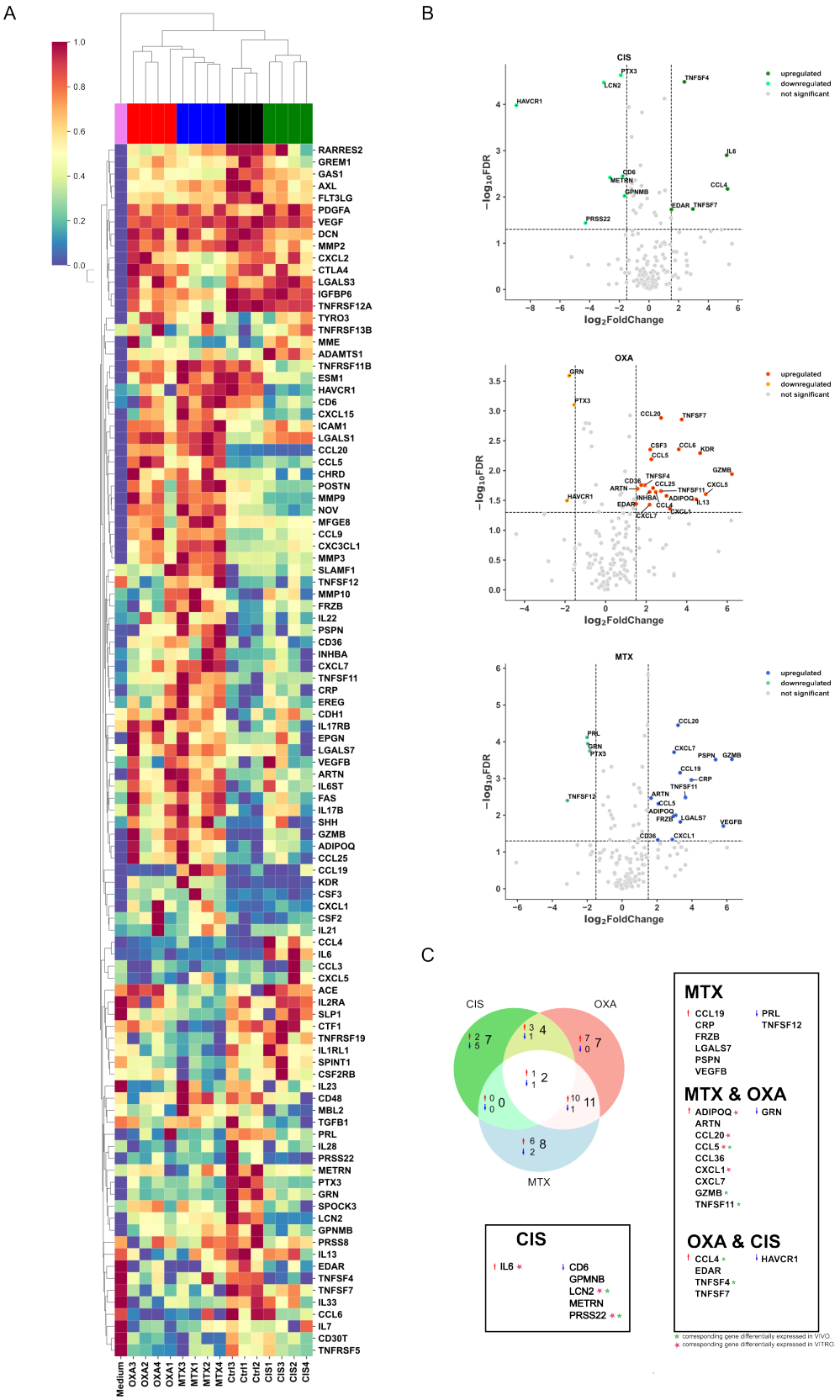

Figure 4.4: Secretomics array uncovered distinct cytokine profiles between cells treated with the ICD-inducer MTX and the non-ICD-inducer CIS. A. Heatmap representation of raw abundancies of 80 cytokines whose secretion by MCA205 cells appeared modulated upon chemotherapy as compared to untreated controls (p-value < 0.05). **B.** Volcano plot illustrating the cytokines with deregulated secretion in CIS, OXA and MTX-treated cells at 24h. Statistics have been assessed using an ANOVA model and p-values were corrected using Bonferroni correction. **C.** Venn-diagram summarizing intersections between treatment groups for up-regulated and down-regulated cytokines.

namely CCL4, CCL5, CCL20 and IL6, was monitored by ELISA, and ultimately compared with the longitudinal transcriptomics data.

Secretion of IL6 was confirmed to be specific to the non-ICD inducer CIS (Fig. 4.5 A). This robust stimulation was also detectable at the transcriptional level (Fig. 4.5 B).

ELISA and in vitro transcritpomics data comforted a major production of CCL4 by MCA205 cells treated by CIS, as opposed to lower levels in OXA and MTX-treated groups (Fig. 4.5 C, D).

Surprisingly, CCL5 secretion was witnessed at a similar magnitude upon both CIS and MTX treatments, while an apparent consumption or absence of secretion of the chemokine occurred upon OXA (Fig. 4.5 E). These ELISA results were in contradiction with the conclusions of both the cytokine array (Fig. 4.4 A, B) and transcriptomics (Fig. 4.5 F), where CCL5 production was superior in OXA and MTX-treated cells than with CIS.

Regarding CCL20, all three assays comforted a strong expression and secretion following cell exposure to the ICD inducer MTX (Fig. 4.4 A, B; Fig. 4.5 G, H). As opposed to mRNA, CCL20 protein was detected in the culture supernatants of MCA205 cells treated with platinum salts, with a trend toward superior levels in the presence of OXA than CIS (Fig. 4.4 A, B; Fig. 4.5 G, H).

Altogether, our work revealed an association between the profile of some secreted factors, like IL6 and CCL20, and the (lack of) immunogenicity of cell death. Importantly, their transcriptional level was reflecting their extracellular concentration, thus supporting our hypothesis of a transcriptomics signature of ICD induction.

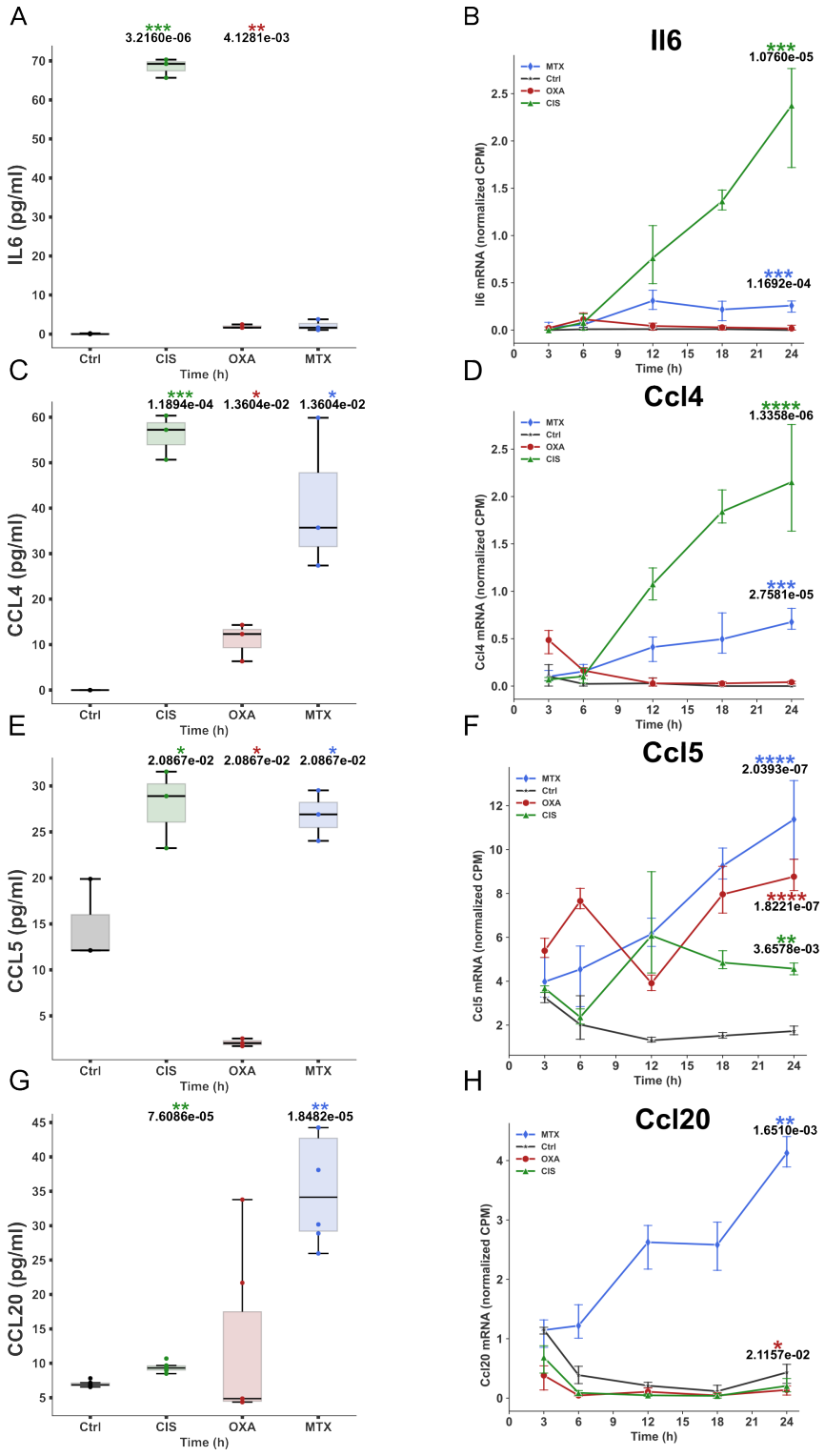

Figure 4.5: mRNA levels of IL6, CCL4, CCL5, and CCL20 mirror their secreted levels. Levels of IL6 secreted in the culture supernatant of MCA205 cells treated for 24 hours with CIS, OXA, or MTX, measured by ELISA (**A**), and corresponding longitudinal mRNA expression profile measured by RNA-seq (**B**). Same measurements for CCL4 (**C-D**), CCL5 (**E-F**), and CCL20 (**F-G**). For ELISA assay, stats were calculated using a One-way ANOVA with Benjamini-Hochberg correction. For longitudinal gene expression, a Kruskal-Wallis and Dunn's test was performed. For all assays, n=3-5 replicates per group. Ctrl, untreated control; CIS, cisplatin; MTX, mitoxantrone; OXA, oxaliplatin.

1.5 Fibrosarcoma tumors treated by MTX and platinum salts demonstrated qualitative and dynamic distinctions of their secretory profile.

By taking into consideration the critical function of secreted factors in shaping the malignant microenvironment, we extended in vivo our in vitro investigations of the secretome. Mice bearing subcutaneous MCA205 fibrosarcoma were treated with CIS, OXA, or MTX and tumors were harvested after 3, 10 or 22 days for transcriptomics analysis. At these timepoints, innate, peak and late (i.e., exhausted) adaptive immune responses are expected to occur within the TME [103, 117].

Out of the 255 genes considered for their production of secreted factors, 110 (43 %) were detected in at least one of the conditions (Fig. 4.6 A).

Among them, 104 underwent significant modulation upon chemotherapy ($|\log2 \text{ fold change}| > 0.7$; adjusted p-value < 0.05). A dichotomic imprint could be evidenced, with limited ($n = 8$) overlap between platinum salt and anthracycline-based treatments (Fig. 4.6 B, C).

On one hand, 23 genes were dysregulated upon both CIS and OXA, in their majority upregulated at day 10, and encoded chemokines (CCL3/4/5/9/17, CXCL2/3/9), interleukins (IL18/24/33), or again granzymes (e.g., GZMB) (Fig. 4.6A-D).

Thirty-three additional DEGs were specific to OXA-treated tumors at 10 days post-chemotherapy administration (Fig. 4.6A-C). Notably, they included a 6-fold increase of the mRNA encoding IFNγ, indicative of an active type-1 immunity.

On the other hand, MTX-treated tumors were characterized by a 37-DEG secretory signature, with 11 overexpressed and 26 downregulated genes. As opposed to platinum salt therapies, most of these dysregulations (92%) were documented early in the malignant tissue, 3 days post-MTX. The production of numerous chemokines (CCL11/17/22/24/27A, CXCL5/9/14), soluble/membrane-bound immune checkpoints (TNFSF10, best known as TRAIL, and TNFSF11), growth factors (e.g., EREG, IGF1, FGF10/13/23, GDF9, HGF, PDGFD, PGF), angiogenic regulators (e.g., ANGPT1/2/L4), and hormone-related factors (ADIPOQ, MME) appeared affected.

Among them, CCL17, CXCL9, FGF10, PDGFD, or again TNFSF11 experienced contrasting regulations along MTX and platinum salt treatments (Fig. 4.6 D).

Moreover, MTX shared with OXA an early (day 3) downregulation of the gene encoding the immunosuppressive cytokine IL10, together with a late upregulation (day 10) of the mitogenic factor PDGFD (Fig. 4.6 D).

Unexpectedly, the archetypal effector molecules of antitumor immune response IFNγ, GZMB, and CXCL9 were either not detected or downregulated in tumors treated by the ICD inducer MTX, in contrast to the supposedly less immunogenic CIS and/or OXA treatments. Therefore, their mRNA levels may not embody relevant in vivo markers of ICD-stimulated cancer-immunity cycle in

fibrosarcoma tumors.

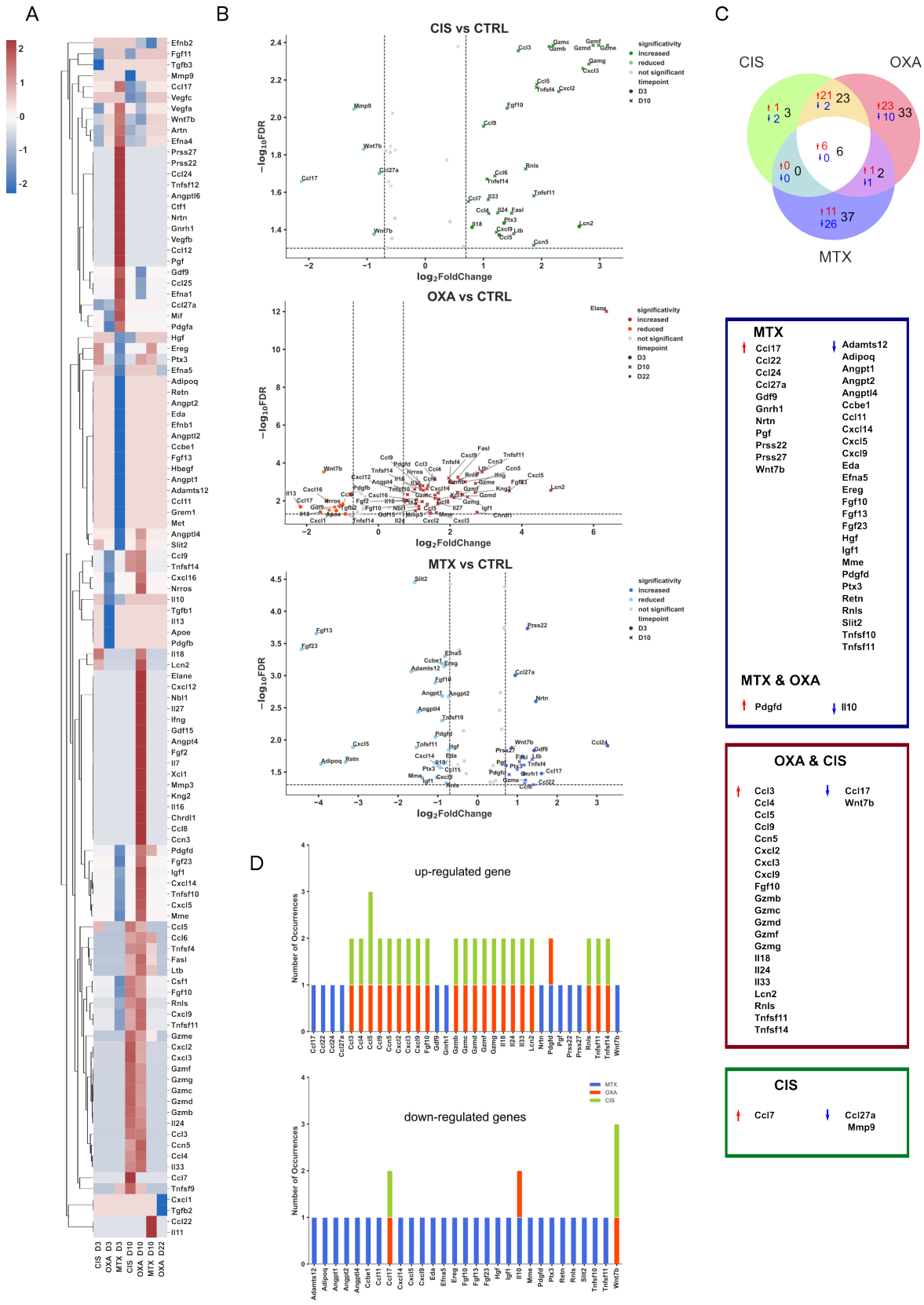

Figure 4.6: Transcriptomics profile of secreted immunomodulators of fibrosarcoma tumors treated with CIS, OXA, and MTX.

A. Heatmap displaying the expression of 110 genes encoding secreted factors with immunomodulatory function and detected in MCA205 tumors 3, 10 or 22 days post-intraperitoneal injection of CIS, OXA, or MTX. Gene expression is displayed as relative to untreated (PBS) tumor tissues. Hierarchical clustering of dysregulated mRNA based on Euclidean distance measure. **B.** Volcano plot representation, incorporating all time points within each treatment, of the transcriptomic dataset focusing on genes associated with immunomodulation. A log2FC threshold of 0.7 and an FDR of 5% were applied to highlight significant changes. **C.** Venn diagram showing the size of the intersection of differentially expressed genes within all treatments, regardless of the time point. **D.** Stacked histograms representing the number of time points a gene from the immunomodulation signature was found overexpressed (upper bar plot) or downregulated (lower bar plot) for each treatment. For all timepoints and conditions: n=4. CIS, cisplatin; OXA, oxaliplatin; MTX, mitoxantrone; CTRL, control.

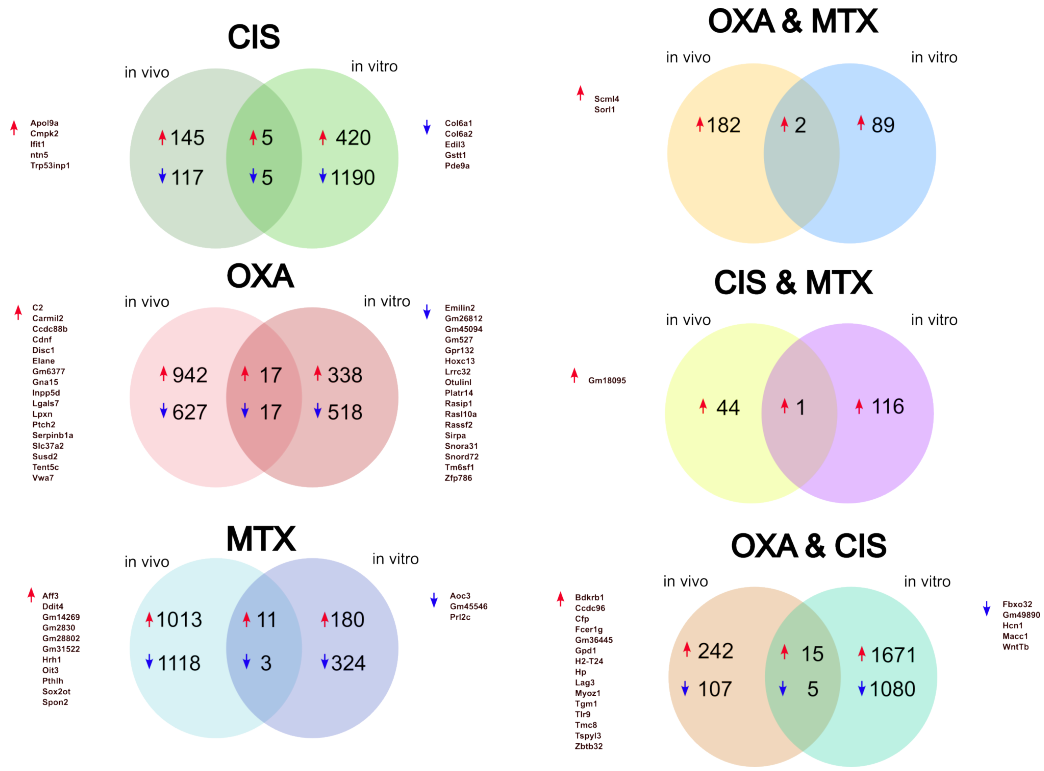

Figure 4.7: Transcriptomics overlap between fibrosarcoma cells and tumors treated with the platinum salts CIS or OXA, or the anthracycline MTX. Venn diagrams representing genesets intersections between in vivo and in vitro experiments.

Afterward, we confronted the in vitro and in vivo data (Fig. 4.3 and 4.6) to search for markers indicative of (an absence of) ICD induction at the malignant cell level and that would persist in the TME. The comparison revealed 81 genes modulated upon chemotherapies at both early (hours; in vitro) and late (days; in vivo) timepoints (Fig. 4.7). Among them, only a limited number of secreted factors showed deregulation in both MCA205 cells and tumors. They included a downregulation of *Col6a1/a2* mRNAs upon the non-ICD inducer CIS, and a downexpression of *Prl2c* upon the ICD inducer MTX (Fig. 4.7). This set of genes shows interest in predicting (lack of) immunogenicity and will be the subject of additional in silico (e.g., GO analysis, prognostic/predictive value through public database interrogation) and experimental investigations.

Furthermore, we observed an expression pattern of interest of the gene *Prss22*. Indeed, transcript

levels of *Prss22* were downregulated in vitro upon non-ICD-inducing platinum salts (Fig. 4.3 C) and upregulated in vivo upon the ICD inducer MTX (Fig. 4.6 C). Interestingly, PRSS22 controls through proteolytic cleavage the activation and extracellular availibility of the ICD hallmark ANXA1 [159, 99]. Thus, this gene may also embody a candidate of value to predict immunogenicity.

Collectively, our in vitro and in vivo analyses uncovered a set of immunomodulatory and TME-reshaping secreted factors and receptors with interest to readily define tumor immunogenicity during chemotherapeutic interventions, and thus better guide the implementation of complementary or compensatory immunotherapeutic interventions.

1.6 Estimating the expression of receptors corresponding to the cytokines released by MCA205 cells upon treatment.

To evaluate and validate the hypothesis of potential autocrine regulation occurring in MCA205 cells in response to the three different compounds, we investigated the expression levels of receptors corresponding to cytokines (see table below) identified as differentially secreted using the cytokine array assay (see the section 1.4 of this chapter).

Ligand Full Name	**Gene symbol**	**Receptor Full Name**	**Gene symbol**
Interleukin-6	Il6	Interleukin-6 Receptor	Il6ra
Interleukin-6	Il6	gp130 (IL6 Signal Transducer)	Il6st
C-C Motif Chemokine Ligand 4	Ccl4	C-C Chemokine Receptor Type 5	Ccr5
C-C Motif Chemokine Ligand 20	Ccl20	C-C Chemokine Receptor Type 6	Ccr6
Kinase Insert Domain Receptor	Kdr	Vascular Endothelial Growth Factor Receptor 1	Flt1
Colony Stimulating Factor 3	Csf3	Colony Stimulating Factor 3 Receptor	Csf3r
Granzyme B	Gzmb	Perforin 1	Prf1
C-C Motif Chemokine Ligand 5	Ccl5	C-C Chemokine Receptor Type 5	Ccr5
C-C Motif Chemokine Ligand 25	Ccl25	C-C Chemokine Receptor Type 9	Ccr9
C-X-C Motif Chemokine Ligand 1	Cxcl1	C-X-C Chemokine Receptor Type 2	Cxcr2
Adiponectin	Adipoq	Adiponectin Receptor 1	Adipor1
Adiponectin	Adipoq	Adiponectin Receptor 2	Adipor2
Tumor Necrosis Factor Ligand Superfamily Member 11	Tnfsf11	Receptor Activator of Nuclear Factor Kappa-B	Tnfrsf11a
C-C Motif Chemokine Ligand 4	Ccl4	C-C Chemokine Receptor Type 5	Ccr5
Inhibin Beta A	Inhba	Activin A Receptor Type 1B	Acvr1b
C-X-C Motif Chemokine Ligand 7	Cxcl7	C-X-C Chemokine Receptor Type 2	Cxcr2
Artemin	Artn	GDNF Family Receptor Alpha-3	Gfra3
Artemin	Artn	Rearranged During Transfection	Ret
C-C Motif Chemokine Ligand 20	Ccl20	C-C Chemokine Receptor Type 6	Ccr6
C-X-C Motif Chemokine Ligand 7	Cxcl7	C-X-C Chemokine Receptor Type 2	Cxcr2
Persephin	Pspn	GDNF Family Receptor Alpha-1	Gfra1
Persephin	Pspn	Rearranged During Transfection	Ret
Granzyme B	Gzmb	Perforin 1	Prf1
C-C Motif Chemokine Ligand 19	Ccl19	C-C Chemokine Receptor Type 7	Ccr7
C-Reactive Protein	Crp	Fc Gamma Receptors	Fcgrs
Tumor Necrosis Factor Ligand Superfamily Member 11	Tnfsf11	Receptor Activator of Nuclear Factor Kappa-B	Tnfrsf11a
Artemin	Artn	Rearranged During Transfection	Ret
Artemin	Artn	GDNF Family Receptor Alpha-3	Gfra3
C-C Motif Chemokine Ligand 5	Ccl5	C-C Chemokine Receptor Type 5	Ccr5
Adiponectin	Adipoq	Adiponectin Receptor 1	Adipor1
Galectin-7	Lgals7	Adiponectin Receptor 2	Adipor2
Vascular Endothelial Growth Factor B	Vegfb	Solute Carrier Family 2 Member 5	Slc2a5

Ligand Full Name	Gene symbol	Receptor Full Name	Gene symbol
C-X-C Motif Chemokine Ligand 1	Cxcl1	Fms-Related Tyrosine Kinase 1	Flt1
Cluster of Differentiation 36	Cd36	C-X-C Chemokine Receptor Type 2	Cxcr2
Protease Serine 22	Prss22	Cluster of Differentiation 36	Cd36
Lipocalin 2	Lcn2	Cluster of Differentiation 6	Cd6
Pentraxin 3	Ptx3	Lipocalin 2 Receptor	Lcn2r
Hepatitis A Virus Cellular Receptor 1	Havcr1	Toll-Like Receptor 4	Tlr4
Hepatitis A Virus Cellular Receptor 1	Havcr1	Complement Component 1q	C1q
Pentraxin 3	Ptx3	Fc Gamma Receptors	Fcgrs
Granulin	Grn	T-Cell Immunoglobulin and Mucin Domain 1	Timd1
Prolactin	Prl	Sortilin 1	Sort1
Granulin	Grn	Prolactin Receptor	Prlr
Pentraxin 3	Ptx3	Prolactin Receptor	Prlr
Lipocalin 2	Lcn2	Low-Density Lipoprotein Receptor-Related Protein 2	Lrp2

The table above provides an overview of the pairs ligands-receptors, and their corresponding murine gene symbols. The list include only most relevant receptors for the ligand measured using the cytokines array (see section 1.4). CIS: Cisplatin, OXA: Oxaliplatin, MTX: Mitoxantrone. Additional details available in Glossary section

Overall, the amplitude of differential expression in cells treated with different compounds segregates the three treatments into two main groups: cells treated with MTX show a weaker differential expression (both up-regulated and down-regulated) compared to the same genes in cells treated with platinum salts (Fig. 4.8).

Interestingly, although receptor expression in cells treated with platinum salts follows a similar trend to the ligands, some differences persist for specific receptors. Generally, these treatments induce a down-regulation of receptor expression, with the effect becoming more pronounced over time.

For MCA205 cells treated with OXA, we observed differential expression of *Adipor2* (Fig. 4.8 A,C,E) - the receptor for *Adipoq* - but not *Adipor1* (Fig. 4.8 B,D,F), which is up-regulated in both CIS- and MTX-treated cells, albeit with smaller amplitude for MTX (Fig. 4.8 E). Activin A receptor type I (*Acvr1b*, the receptor for Inhibin beta A *Inhba*) is down-regulated for all three treatments, except in MTX-treated cells at 3 hours post-treatment (where it is weakly up-regulated) and at 6 hours post-treatment (where no differential expression is observed).

The GDNF family receptor alpha-1 (*Gfra1*, which binds to Persephin *Pspn*) shows a similar trend for both platinum salts (Fig. 4.8 A,C) but is mildly down-regulated in MTX-treated cells at 3 and 18 hours post-treatment (Fig. 4.8 E). On the other hand, its corresponding ligand *Pspn* is strongly up-regulated in platinum salts-treated cells (Fig. 4.8 B,D) but not differentially expressed in MTX-treated cells (Fig. 4.8 F).

The two subunits of the IL-6 receptor (*Il6ra* and *Il6st*) are both down-regulated in cells treated with platinum salts (Fig. 4.8 A,C), while in cells treated with MTX (Fig. 4.8 E), the receptor subunits are consistently down-regulated. In contrast, OXA-treated cells show up-regulation of *Il6* at 6 and 24 hours post-treatment (logFC < 2.0, Fig. 4.8 D) . For CIS-treated cells, *Il6* expression is increasingly up-regulated from 12 hours onward (logFC > 6.0, Fig. 4.8 B), whereas for MTX-treated cells, the

maximal differential expression amplitude is around logFC = 4.0 (Fig. 4.8 F).

The expression of Toll-like receptor 4 (*Tlr4*) follows a trend similar to *Acvr1b*, with increasing differential expression over time for cells treated with platinum salts (Fig. 4.8 A,C). For MTX-treated cells, differential expression is weaker, showing only slight up-regulation at 3 and 6 hours post-treatment (Fig. 4.8 E), which diminishes at later time points. Similarly, tumor necrosis factor receptor superfamily member 11a (*Tnfrsf11a*) is down-regulated for platinum salts (Fig. 4.8 A, C) and exhibits a time-dependent monotonic decrease in MTX-treated cells, similar to *Tlr4* (Fig. 4.8 E). The receptor for progranulin (*Grn*), Sortilin 1 (*Sort1*), is down-regulated starting from 12 hours post-treatment in cells treated with platinum salts. This trend is observed in CIS-treated cells (Fig. 4.8 A), albeit to a lesser extent than in OXA-treated cells (Fig. 4.8 C). In cells treated with OXA, a weak up-regulation of vascular endothelial growth factor receptor 1 (*Flt1*) is detected at 18 hours after treatment (Fig. 4.8 C). Conversely, *Flt1* is down-regulated at all time points in CIS-treated cells (except at 18 hours Fig. 4.8 A) and up-regulated in MTX-treated cells (Fig. 4.8 E).

Lastly, while Low-Density Lipoprotein Receptor-Related Protein 2 (*Lrp2*, a potential receptor for Lipocalin-2 *Lcn2*) is not differentially expressed in cells treated with MTX (Fig. 4.8 E), its expression is down-regulated in cells treated with CIS at 6, 12 and 18 hours after treatment. For cells treated with OXA, it is down-regulated only at 18 hours after treatment.

Together, these observations provide a framework to hypothesize potential autocrine regulation mechanisms within MCA205 cells in response to different treatments. Based on evidence in the literature regarding receptor regulation after ligand stimulation, it is plausible that some of these receptors, corresponding to ligands measured at the proteomic level and re-assessed at the transcriptomic level, contribute to autocrine signaling. For example, the ligand-receptor pairs *Pspn-Gfra1* and *Il6-Il6ra/Il6st* illustrate scenarios where ligand overexpression is coupled with receptor down-regulation, suggesting their involvement in autocrine signaling dynamics.

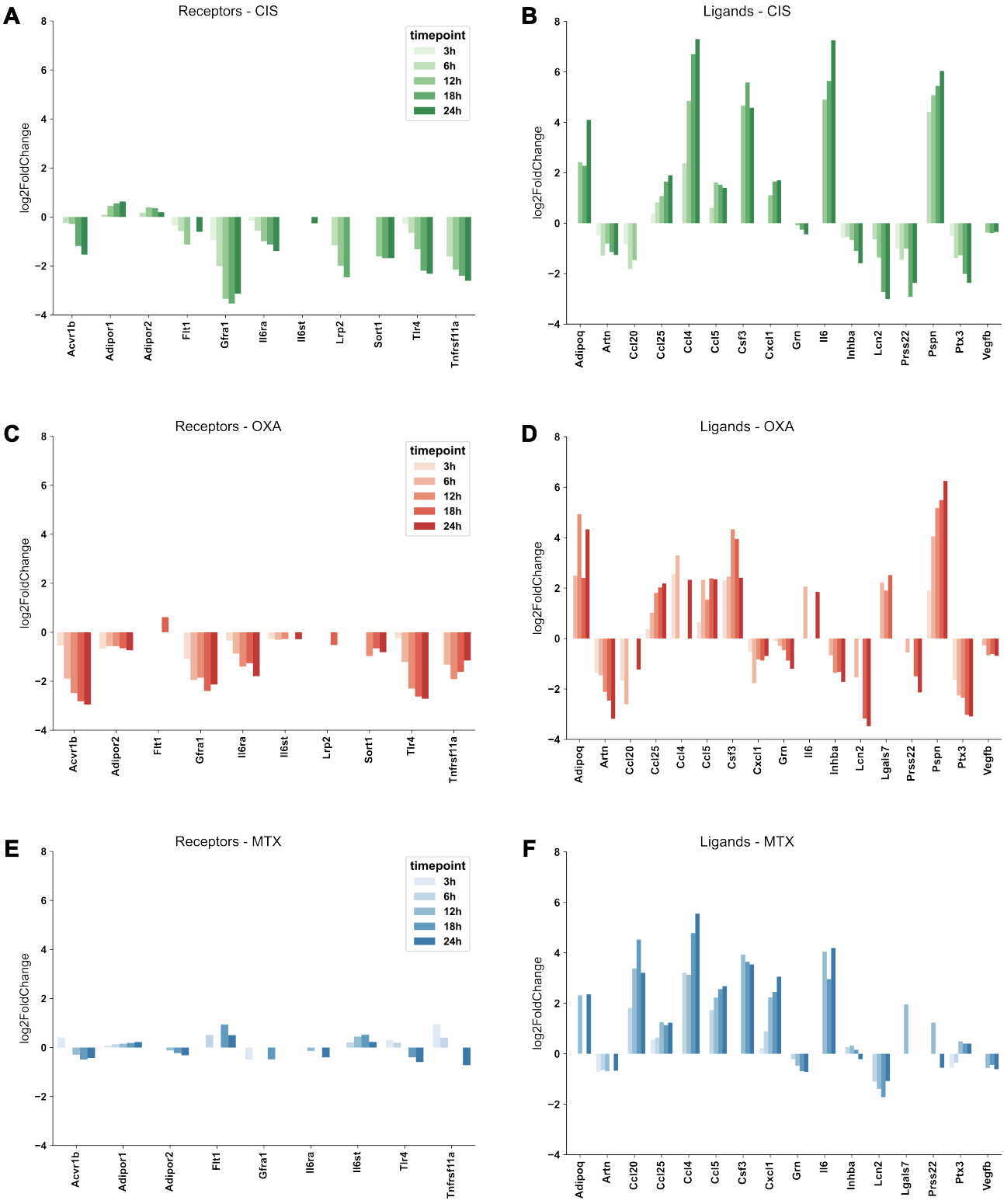

Figure 4.8: Timewise representation of differentially expressed genes associated with ligands released by MCA205 cells and their conjugate receptors. Temporal representation of differential expression patterns for ligands secreted by MCA205 cells (right) following treatment with CIS (**B**), OXA (**D**) and MTX (**F**) along with their corresponding receptor expressions (**A**,**C**,**E**) . Cytokines identified as differentially secreted at the protein level are analyzed at the transcriptional level to assess their gene expression. Simultaneously, the temporal expression profiles of their respective receptors are also evaluated.

1.7 In vivo supplementation of CCL5 and IL6, but not CCL20, seems to impede immunogenicity of chemotherapy-treated cells

To confirm or infirm the interest of some candidates evidenced by transcriptomics and secretomics as potential predictors of tumor immunogenicity upon chemotherapy, we performed additional functional investigations. These assays consisted of supplementing or neutralizing some selected secreted factors in prophylactic (i.e., vaccination with dying MCA205 cells treated in vitro followed by a challenge with live tumor cells) or therapeutic (i.e., chemotherapy of established ectopic MCA205 tumors) settings.
Our preliminary experiments were conducted with a first selection of 3 cytokines, namely CCL5, CCL20, and IL6. These latter were co-administered at low doses with the suspension of in vitro-treated MCA205 cells administered subcutaneously for tumor vaccination attempts. Then, their impact on the immunogenicity was evaluated by monitoring tumor incidence and growth (Fig. 4.9,4.10,4.11).
As previously observed, CIS and OXA-treated cells conferred poor protection against tumor development. Supplementation of CCL5 had no impact on tumor immunogenicity upon platinum salts (Fig. 4.9). Similarly, neither CCL20 nor IL6 supplementation impacted median tumor-free survival and tumor growth in hosts administered with CIS and OXA-treated MCA205 cells (Fig. 4.10,4.11).
By contrast, a reduced immunogenicity of MTX-treated MCA205 cells was witnessed when the vaccine suspension was supplemented with CCL5 (Fig. 4.9) or IL6 (Fig. 4.11), whereas CCL20 enrichment had no impact (Fig. 4.10). Thus, these preliminary data indicate that CCL5 and IL6 production seems to be detrimental to the immunogenicity of chemotherapy-induced cell death. The release of CCL20 upon ICD does not appear critical to the overall immunogenicity.
Replicates of the above-described experiments, and complementary tests in vivo involving the treatment of wild-type and cytokine-KO MCA205 tumors, in the presence or absence of systemic or local cytokine neutralization in vivo, are required prior definite conclusion about the role of these secreted markers in ICD. These assays will be extended to additional cancer types (e.g. colorectal cancer, breast cancer) and candidates (e.g., PRL, PRSS22).
Ultimately, our work will identify some hallmarks of ICD readily assessable with standard molecular techniques and that could orientate therapeutic adjustments for improved efficacy through enhanced antitumor immune response.

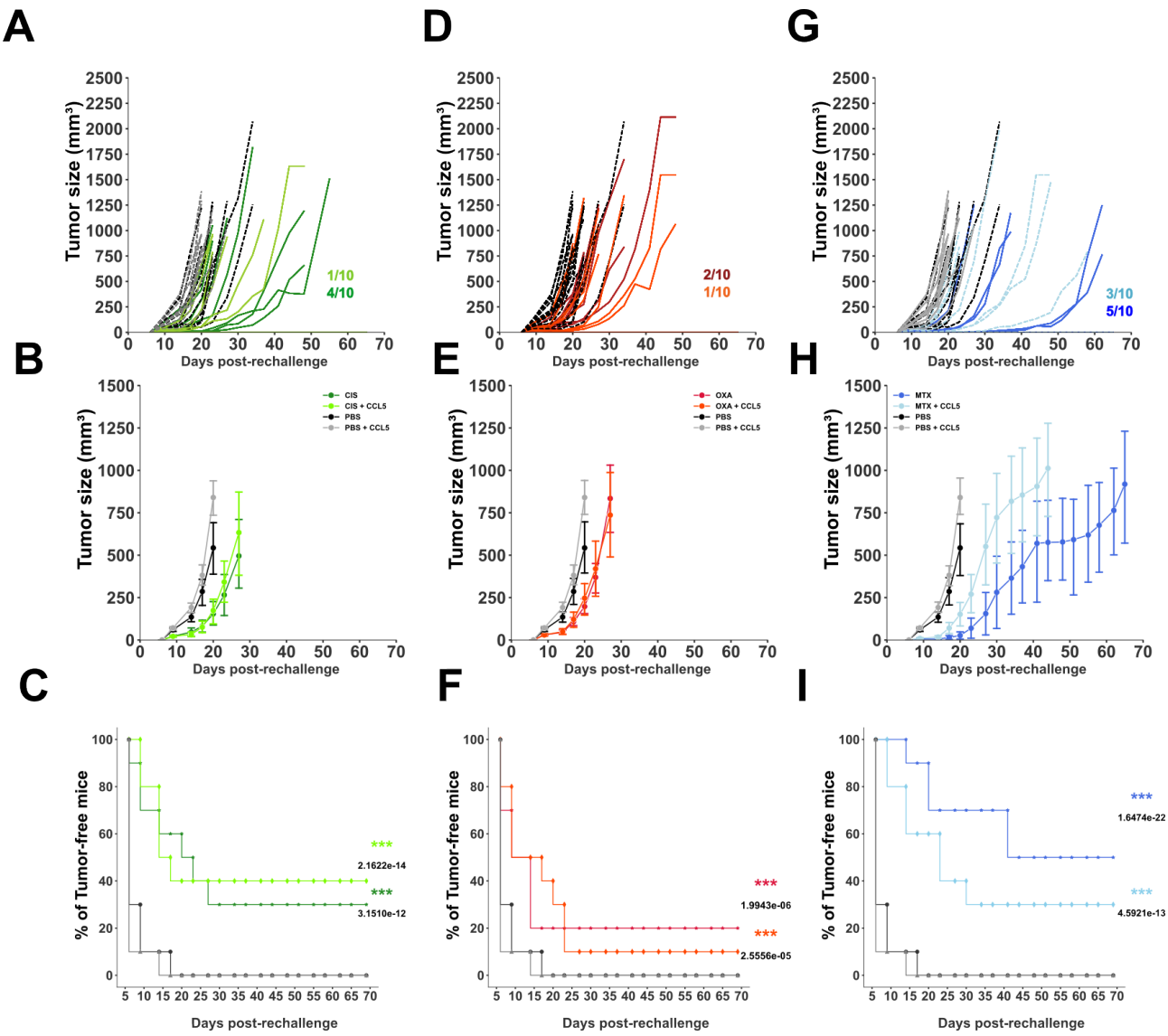

Figure 4.9: CCL5 supplementation reduces the immunogenicity of MTX-treated fibrosarcoma cells. Individual tumor growth curves (n=10) for mice under prophylactic regimen with CIS (**A**), OXA (**D**), and MTX (**G**). Following the same order, panels **B**,**E**,**H** illustrate mean tumor growth curves for the three conditions. Panels **C**, **F** and **I** illustrate the percentage of tumor-free mice. Stats have been calculated using a linear-mixed effect model in **B**, **E**, **H** and log-Rank for **C**, **F**, **I**. (*: 0.05 > p-val > 0.01, **: 0.01 > p-val > 0.001, ***:0.001 > p-val. CIS, cisplatin; OXA, oxaliplatin; MTX, mitoxantrone; CTRL, control)

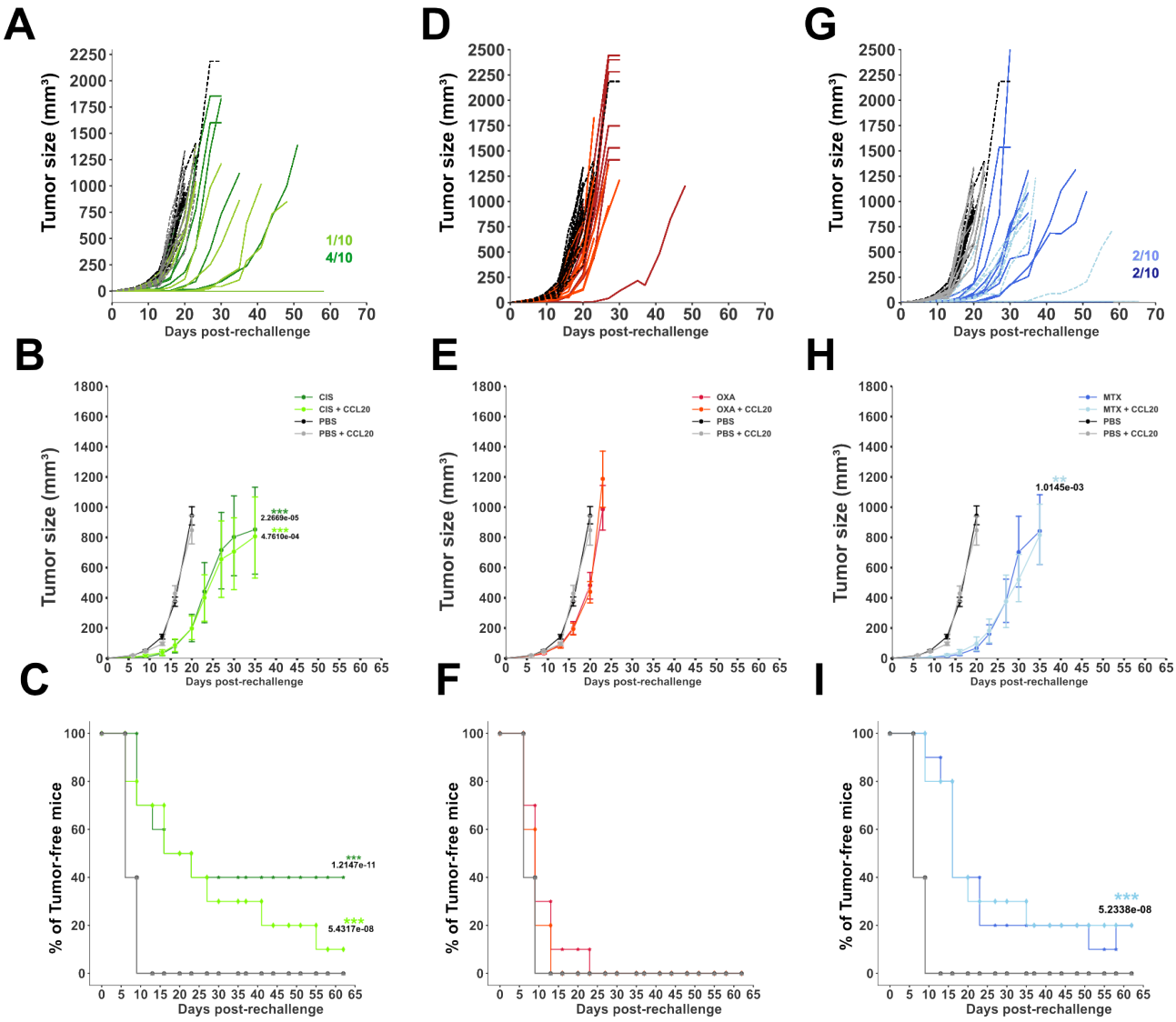

Figure 4.10: Co-supplementation of CCL20 has no impact on cell immunogenicity. Individual tumor growth curve (n=10) for CIS (**A**), OXA (**D**), and MTX (**G**). Following the same order, panels **B**,**E**,**H** illustrate mean tumor growth curves. Panels **C**, **F** and **I** illustrate the percentage of tumor-free mice in mice vaccinated with CIS, OXA, and MTX respectively. Stats have been calculated using a linear-mixed effect model **B**-**E**-**H** and log-Rank test **C**-**F**,**I** (*: 0.05 > p-val > 0.01, **: 0.01 > p-val > 0.001, ***:0.001 > p-val. CIS, cisplatin; OXA, oxaliplatin; MTX, mitoxantrone; CTRL, control)

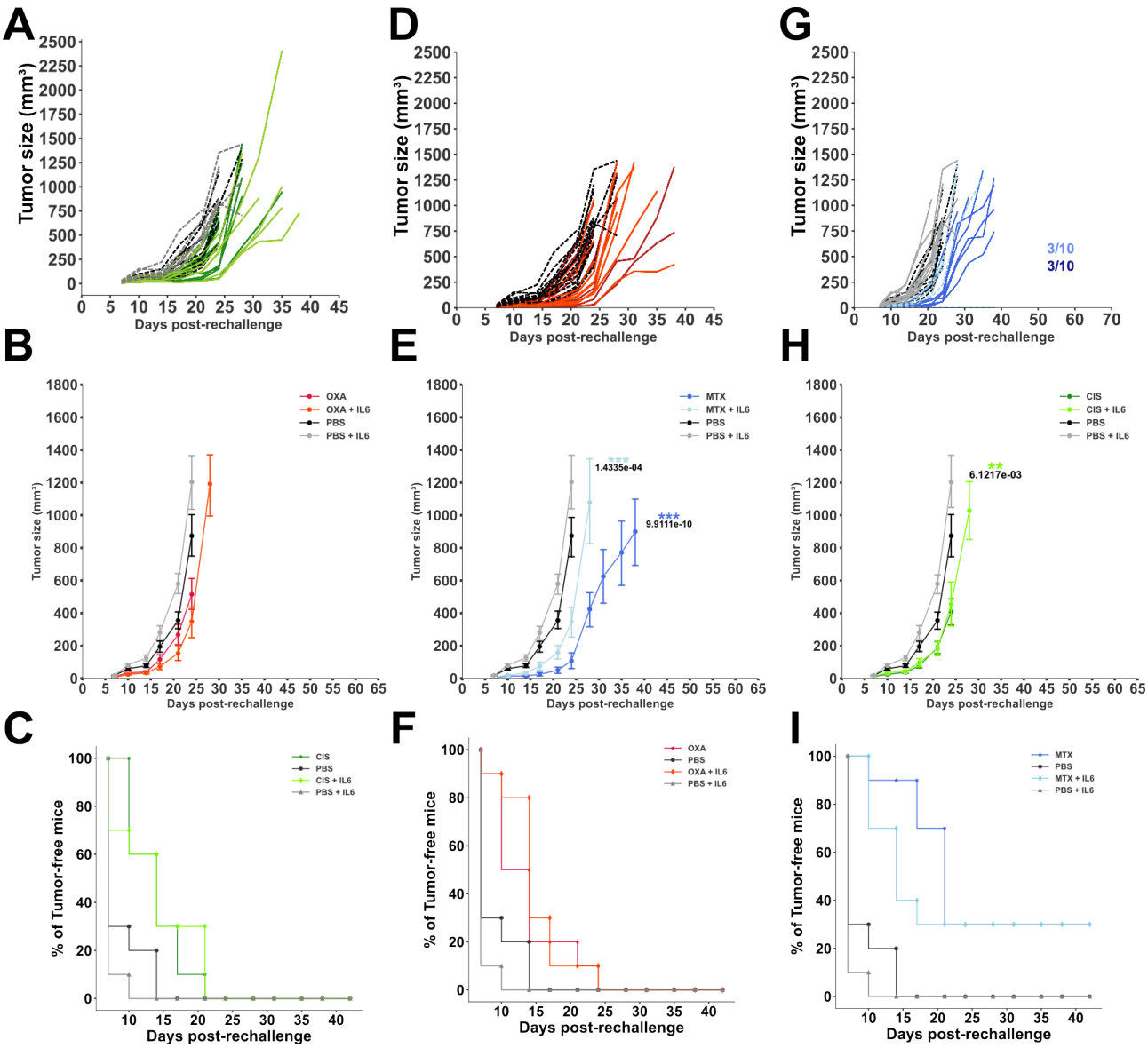

Figure 4.11: Co-supplementation of IL6 impedes immunogenicity of MTX-treated fibrosarcoma cells. Individual tumor growth curve (n=10) for CIS (**A**), OXA (**D**), MTX (**G**). Following the same order, panels **B**,**E**,**H** illustrate mean tumor growth curves. Panels **C**, **F** and **I** illustrate the percentage of tumor-free mice. Stats have been calculated using a linear-mixed effect model (*: 0.05 > p-val > 0.01, **: 0.01 > p-val > 0.001, ***:0.001 > p-val. CIS, cisplatin; OXA, oxaliplatin; MTX, mitoxantrone; CTRL, control)

2 Extrapolating pathway and TF activities from transcriptomic profiles

To select additional genes to include in the model, we performed an in-depth analysis of the transcriptomics data using dedicated algorithms.

We focused on i) longitudinal transcriptional profiling of active pathways following therapy administration and ii) measured TF activity based on the expression of their identified target genes. For both tasks, we used decoupler-py [10]. To complement the latter, we cross-validated our findings about the TF activity using a dynamical time-warping algorithm (DTW) and measured similarities between longitudinal transcriptional trajectories. This additional data analysis step is important to evaluate the pertinence of the features and components to embed in a new model recapitulating the differences between treatments and contributing to their immunogenicity.

2.1 Pathway analysis with ProgenY highlights a unique signature associated with MTX.

Direct and indirect techniques can be applied to measure the activity of cellular pathways. Direct measurement of the activation status of key proteins constituting a given pathway remains the gold standard approach, using methods like western blotting or immunofluorescence. However, considering the large set of genes of interest extracted from our transcriptomics analysis, we first inferred pathway activity indirectly using bioinformatics approaches, as a prerequisite for future direct experimental assessment.

Traditional in silico methods, like Gene Set Enrichment Analysis (GSEA), can infer the occurrence of a biological process by detecting the expression of a set of related genes. However, they disconsider post-translational modifications that determine actual pathway activity. As an intermediate alternative, we applied PROGENy, a manually curated model to infer pathway activity from key gene expression profiles. The tool consists of one of the largest pathway signature datasets available to date and allows the evaluation of the activity of 13 cellular pathways (see section 3.2.2).

For each pathway, the assessment of their activity across all conditions and time points was summarized in a cluster map (see Fig. 4.12 **A**). The clusterization segregated the MTX-treated cells from the two platinum salt treatments (Fig.4.12 B).

Across all treatments and time points, the JAK-STAT and TP53 pathways, which control cytokine production and stress response, respectively, appeared significantly stimulated, while the WNT and VEGF pathways, which regulate cell adhesion and angiogenesis, respectively, were negatively regulated (Fig.4.12 B).

The PI3K signaling, which controls the cell cycle, decreased in activity, most notably upon CIS. The pathways associated with the estrogen and androgen hormones, which impact cancer cell migration and proliferation, demonstrated a repressed activity, particularly upon MTX (Fig.4.12 B).
The NFkB signaling, which controls immunity, inflammation, and stress responses, also displayed a reduced activity at 3h before experiencing a stimulation at 6h upon each intervention, the latter stimulation being maintained over time only in the presence of MTX (Fig.4.12 B, C).
Along this line, MTX treatment harbored contrasting activities of the MAPK, TRAIL, EGFR, and TNFa pathways compared to the platinum salts. The MAPK cascades integrate stimuli regulating cell proliferation, differentiation, and death. The TRAIL pathway induces apoptosis. The EGFR signaling controls cell growth, proliferation, and survival as well as the production of pro-inflammatory cytokines. The TNFa signaling encompasses multiple pathways, including the NFkB, PI3K, and MAPK pathways. It controls cell demise (e.g., apoptosis or necroptosis), synthesis of inflammatory mediators (secreted and membrane-bound), components of intracellular signaling (including receptors and TFs), and remodeling of the extracellular matrix (Fig.4.12 B).
In detail, MCA205 cells treated with the ICD-inducing anthracycline displayed early (3-12h) and late (>=18h) stimulation of the TNFa and MAPK pathways, respectively. Conversely, these cells experienced concomitant down-regulation of the TRAIL and EGFR signaling (Fig.4.12 B, C).
These modulated pathway activities reflected the response to cell stress and death triggered by chemotherapies and provided some insights into the differential secretomes observed (Fig. 4.4, Fig. 4.3). As anticipated, differential activities of the TNFa and NFkB pathways appeared associated with the contrasting and fluctuating modulations of several secreted immunomodulators like PTX3, CXCL1, CCL20 and IL6. By contrast, the EGFR, TRAIL, and MAPK pathways seemed less involved in the secretion of immune regulators (Fig.4.12 C).
Overall, immunogenicity witnessed upon MTX might result from the singular dysregulations of the activity of signaling intermediate and transcription factors controlled by the NFkB, TNFa, MAPK, TRAIL, and EGFR pathways; the former two actively shaping the secretory signature.

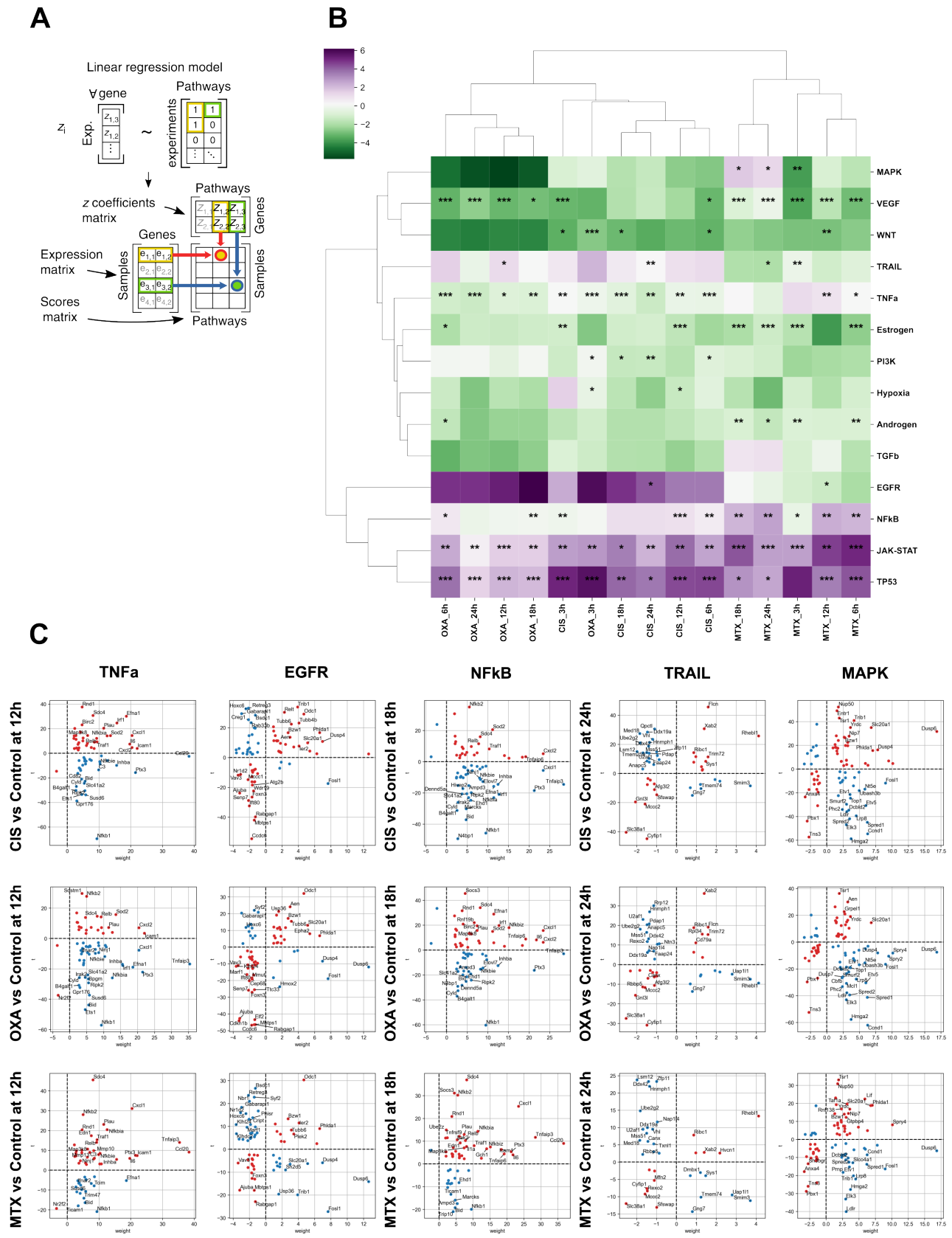

Figure 4.12: PROGENy analysis of transcriptomics data identifies a profile of pathway activity specific to the ICD inducer MTX. A. Progeny rationale: A matrix with t-statistics of all genes for all samples is multiplied by a matrix containing pathway signatures composed of genes. **B.** Clustermap summarizing the activity score associated with the pathways available in PROGENy. Statistical significance was determined by applying the survival function to the t-distribution of the coefficients from the linear model fitted using decoupleR.(*: 0.05 > p-val > 0.01, **: 0.01 > p-val > 0.001, ***:0.001 > p-val, for more detail see: [10]. **C.** Top-30 genes defining pathway signatures for TNFa and EGFR at 12 hours, NFkB at 18 hours, and TRAIL and MAPK at 24 hours post-treatments. CIS, cisplatin; OXA, oxaliplatin; MTX, mitoxantrone.

2.2 Overview of the transcriptional regulation of cytokine-coding genes

To further decipher the molecular mechanisms responsible for treatment-related differences in the secretome of MCA205, we aimed to identify some TFs that control the production of cytokines, notably CCL4, CCL5, CCL20 and IL6, whose profile could contribute to cancer cell death immunogenicity. For this purpose, we analyzed our transcriptomics data set using decoupleR [10] and CollecTRI [130] to investigate the activity of TFs based on the expression of their target genes. We applied an univariate linear model (ULM) for each sample and transcription regulator (Fig. 4.13 A).

Out of the 50 TFs harboring the strongest variation of their activity (Fig. 4.13 B), BACH2, FOXO3, KDM5D, NANOG, JUN, and STAT3 experienced an enhanced activity upon MTX while being repressed upon both platinum salts. Opposite effects were witnessed for ZNF316, KLF17, HDAC1, and MAFG.

We identified 16 that are involved in the transcriptional regulation of the *Ccl4*, *Ccl5*, *Ccl20*, and *Il6* genes (Fig. 4.13 B). For *Il6*, all 16 identified TFs play a role in its transcription, with negative regulators including FOXO3, IRF5, ATF4, BACH1, and DDIT3 (also known as CHOP), while the others act as activators. Similarly, DDIT3 is a negative regulator of *Ccl5*.

Our analysis, utilizing decoupleR for TF analysis, corroborated previous findings established with PROGENy, specifically regarding NFkB activity. For instance, the TFs NFKB1 and RELA exhibited higher activity scores in MTX-treated samples compared to platinum salts. In contrast to MTX and CIS, OXA treatment appeared to downregulate the activity of both NFKB1 and RELA at 24 hours. Both TFs are integral in regulating cytokine expression, including CCL4, CCL5, CCL20, IL6, or again CXCL10. TFs like BACH1, FOXM1, NR1D1, and FOXO3 showed distinct regulation patterns when comparing MTX to platinum salts, influencing the control of IL6. Along this line, the TFs JUN and STAT3 were remarkably differentiating the MTX and platinum salt treatments. The ICD inducers MTX and OXA showed increased activity for HOXA9, ALX1, BRCA1, ZNF316, KLF17, KLF8, and SATB2, further differentiating MTX from other treatments. Moreover, the TF activity profiles of MTX at 3h and 6h cluster together, while those at 12h and 18h form a separate subcluster distinct from 24h. Similarly, OXA and CIS cluster together at 3h and 6h post-treatment, segregating at 12h with their 18h counterparts, and at 24h, both have distinct TF activity profiles. The negative activity of E2F7 and OLIG2 for MTX at 3h highlights the differential response to treatment. Additionally, early time points of MTX treatment show increased activity for E2F family TFs, including activators E2F1, E2F2, and E2F3, and repressors E2F5 and E2F7. JUN and STAT3 exhibited higher activity for MTX at all time points, with increasing values from 6h onwards. Notably, SREBF2 is active across all treatment groups at 3h and 6h.

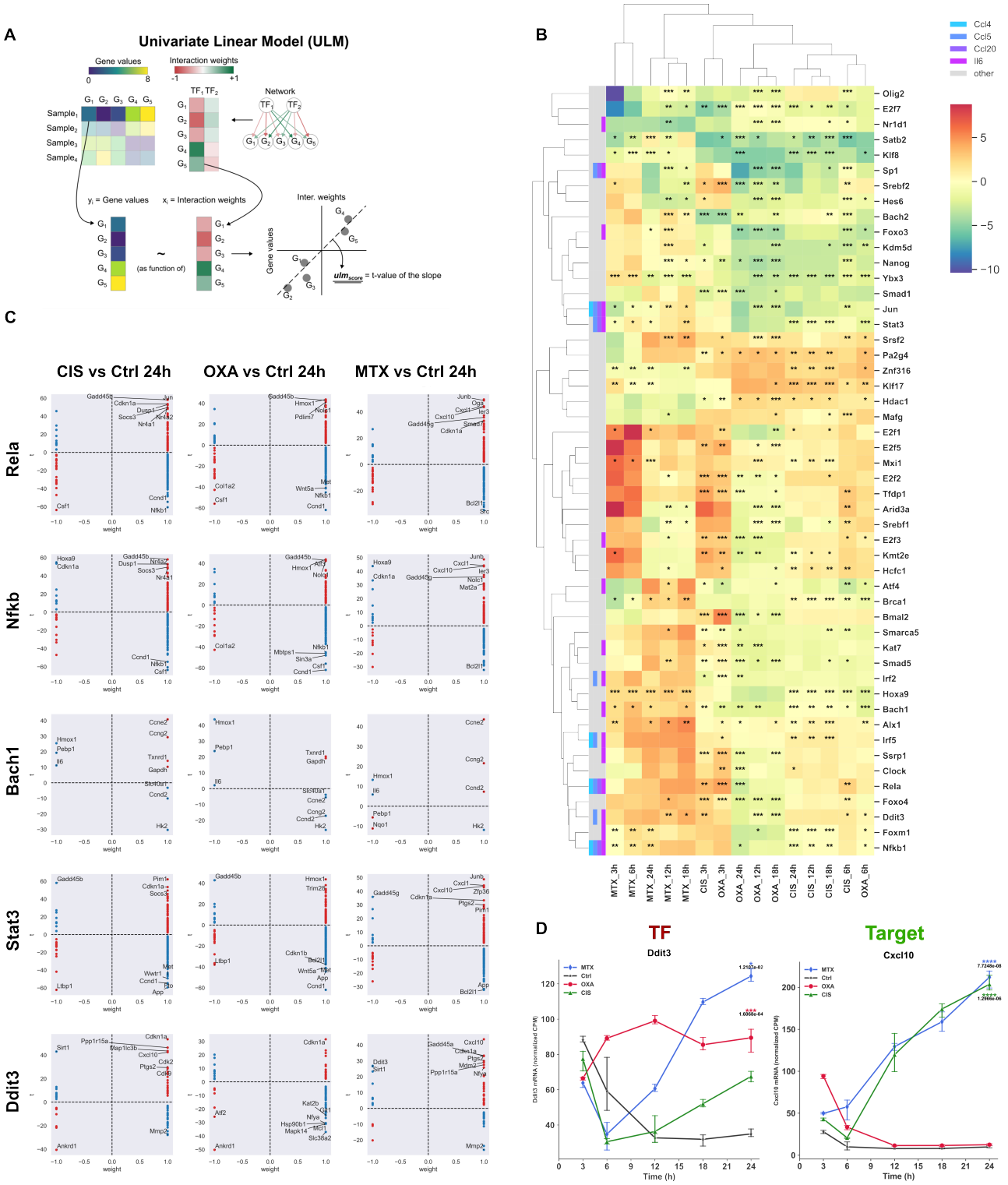

Figure 4.13: Analysis of transcription factor activity using decoupleR and CollecTRI. A operating scheme of TF-activity estimation used in decoupleR. Figure adapted from [10]. In **B**, the clustermap shows the activity score for the top-50 most variable TFs. A color code on the left side of the heatmap indicates some cytokines controlled by the TF among the list of cytokines individuated in section 1.4 (grey if no reported regulatory activity their expression). In **C**, the plots show the distribution of target genes that are repressed (left) or activated (right) by a TF. Target genes t-statistic at 24 hours for 5 TFs: RELA, NFKB1, BACH1, STAT3 and DDIT3. For every TF, the activity is calculated by estimating the slope of the best-fitting line among t-statistic values calculated from differential expression analysis of those genes that are repressed (weight = −1) and activated (weight = +1) by the TF. Statistical significance was calculated with a survival function applied to the t-distribution of the coefficients of the linear model fitted with decoupleR (*: 0.05 > p-val > 0.01, **: 0.01 > p-val > 0.001, ***:0.001 > p-val, for more detail see: [10]; TF, transcription factor; CIS, cisplatin; OXA, oxaliplatin; MTX, mitoxantrone; CTRL, control).

The expression of CCL20 is notably elevated in MTX-treated samples, although its protein is also detected in the supernatant of OXA-treated MCA205 cells at 24 hours post-treatment. In the heatmap presented in Fig. (4.13 B), *Ccl20* is regulated by five of the 16 TFs (SP1, JUN, STAT3, RELA, NFKB1), despite being regulated by at least 17 TFs within CollecTRI. *Ccl5* is regulated by eight of the 50 most active TFs, including DDDIT3, NFKB1, RELA, IRF5, IRF2, JUN, STAT3, and SP1, with 39 TFs regulating its expression overall. *Ccl4*, with 16 available regulators in CollecTRI, is influenced by four highly variable TFs: NFKB1, RELA, JUN, and IRF5. IL6, the cytokine with the highest number of regulators (128 out of 200), is influenced by 16 TFs identified with decoupleR: NFKB1, FOXM1, DDIT3, RELA, SSRP1, IRF5, BACH1, IRF2, KAT7, ATF4, E2F3, STAT3, JUN, FOXO3, SP1, and NR1D1. Notably, DDIT3 acts as a repressor for both MTX and CIS treatments.
Mapping these TFs onto the dataset containing transcriptomic signatures of pathways indicates a correspondence between TFs and pathways only in the cases of the NFkB pathway (RELA, NFKB1) and the TNFα pathway (NFKB1). Interestingly, *Ccl5* and *Il6* are regulated by a TF with opposing effects: IRF5 activates *Ccl5* expression but represses *Il6*, while literature indicates that DDDIT3 represses both cytokines. Additionally, *Ccl4*, also regulated by IRF5, shows up-regulation in CIS-treated cells. IRF5 is typically activated as an NFkB target upon TLR activation by LPS or HMGB1. A closer look at the expression of TLR-coding genes revealed constitutive expression of *Tlr2*, *Tlr3*, and *Tlr4* in MCA205 cells. For both *Tlr2* and *Tlr3*, their expressions are comparable to the control in both MTX and CIS-treated cells. This observation contrasts with their down-regulation upon OXA administration

2.3 Dynamic time warping to prioritize TFs activity based on trajectory similarities

Although CollecTRI constitutes a practical tool to infer the activity of TFs, the curated annotations composing the backbone of the transcriptional relations dataset still contain contradictory information. For instance, in the case of Il6 and Ddit3 (Fig. 4.13 C) multiple sources introduce discrepancies between the possible role of Ddit3 in regulating the expression of Il6 [56, 67].
To leverage this ambiguity, we opted for a data-driven approach. Numerous algorithms and tools have been developed to specifically assess the impact of transcription factors (TFs) on gene expression and construct gene regulatory networks from bulk RNA-seq data. Among these, ARACNE [118] estimates pairwise gene expression mutual information to infer regulatory relationships, while GENIE3 utilizes regression trees for the same purpose. Despite their intended robustness, these methods have demonstrated poor performance on both experimental and simulated data [82]. Multiple benchmarking [32, 131] of these methods revealed their inability to accurately reconstruct networks from simulated

gene expressions, highlighting the need for an alternative method that can more effectively and reliably perform this critical task. Consequently, we applied a more naive approach using the Dynamic Time Warping (DTW) algorithm, a powerful tool for measuring similarity between two temporal sequences. We assumed that a positive correlation between the expression of a TF and its corresponding target could indicate effective transcriptional regulation, where the TF is actively driving the expression of its target gene.

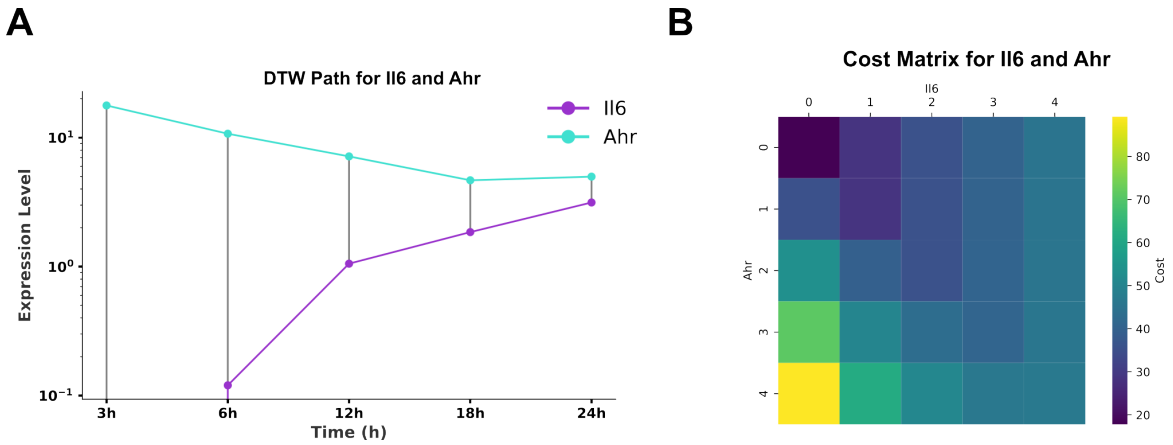

Figure 4.14: Schematization of the working principle of the DTW algorithm. A The longitudinal expression of a TF and its target cytokines are confronted and **B** the cumulative cost matrix is calculated by estimating the euclidean distance between the two trajectories at each time point.

We selected the TF pinpointed via decoupleR (Fig. 4.13 C) playing a role in the transcription of cytokines such as Ccl4, Ccl5, Il6 and CCl20 and we extended the list of regulators from other TF-target databases (Trrust [69] and CytReg [149]) (see table below). The inherent imbalance in the available information on the regulation between TFs and cytokines inevitably limits our ability to infer specific relationships for certain cytokines, such as Ccl4, which has a significantly smaller list of known regulators compared to others. In contrast, cytokines like IL6 are influenced by a much larger set of regulators, making it more critical to prioritize and analyze the activity of these regulators.

List of TFs regulating the expression of Ccl4, Ccl5, Ccl20 and Il6

Cytokines	TFs (sources: CollecTRI, TTrust, CytReg)
Ccl4	Atf3, Bcl6, Cebpb, Cebpe
Ccl5	Batf2, Ddit3, Fos, Hdac1, Irf1, Irf5, Irf8, Jun, Jund, Klf13, Nfkb1, Nfkb1, Rel, Rela, Spi1
Ccl20	Foxa2, Foxo1, Nr4a2, Nfkb1, Pias4, Rela, Relb, Stat3, Trim32
Il6	Ahr, Atf3, Atf4, Bcl6, Cebpb, Cebpd, Cebpe, Cebpg,Crebbp, Creb1, Ctr9, Elk1, Ep300, Fos, Hdac1, Jun, Ddit3, Fli1, Foxo1, Foxp1, Gbx2, Irf5, Junb, Klf4, Nfat5, Nfatc3, Nfe2l2, Nfkb1, Nr1i2, Nr4a1, Ppara, Prdm1, Rela, Relb, Smad4, Sirt1, Sp1, Sp3, Stat1, Stat3 Stat1, Zfp64

This list includes both available interactions present in the collectTRI dataset as well as available information retrieved from manually curated databases Trrust and CytReg

For each list of transcription factors (TFs) and their corresponding target genes, we applied the Dynamic Time Warping (DTW) algorithm to normalized raw count matrices, measured in transcripts per million. This approach allowed us to infer the similarity between the longitudinal transcriptomic trajectories of TFs and their corresponding target genes under different experimental conditions.

By using the DTW algorithm, we could accurately quantify and analyze the relationships between TFs and their target cytokines, even when their expression patterns were delayed or accelerated. The DTW distances served as a proxy to prioritize TFs based on their role in regulating specific cytokines according to the treatment applied.

If our hypothesis about the similarity between longitudinal expression profiles holds, then the regulation of Il6 in CIS-treated cells would primarily be influenced by the TFs Nfkb1, Irf5, Creb1, and Foxp1. In contrast, for MTX-treated cells, Il6 regulation appears to be driven by Stat1, Nr4a1, Elk1, and to a lesser extent, Creb1 and Crebbp. In OXA-treated cells, Irf5 and Foxp1 seem to play a significant role in regulating Il6 expression.

On the other hand, the regulation of Ccl5 shows less variability across conditions. The prioritization profiles indicate that Irf8 and Rel are the major contributors in all conditions. Specifically, in CIS- and OXA-treated cells, Klf13 plays a prominent role in regulating Ccl5 expression.

In CIS-treated cells, Ccl20 expression is regulated by Foxo1 and Stat3, both of which are known activators of Ccl20, with some involvement from Pias4. Interestingly, while Pias4 acts as a repressor of Ccl20 and its expression is downregulated in CIS-treated cells, the reduced signal associated with Pias4 in MTX- and OXA-treated cells suggests it may not be actively regulating Ccl20 under these treatments.

Lastly, Ccl4 expression appears to be uniquely affected by Bcl6, although in MTX-treated cells, Atf3

may also be involved in Ccl4 regulation.

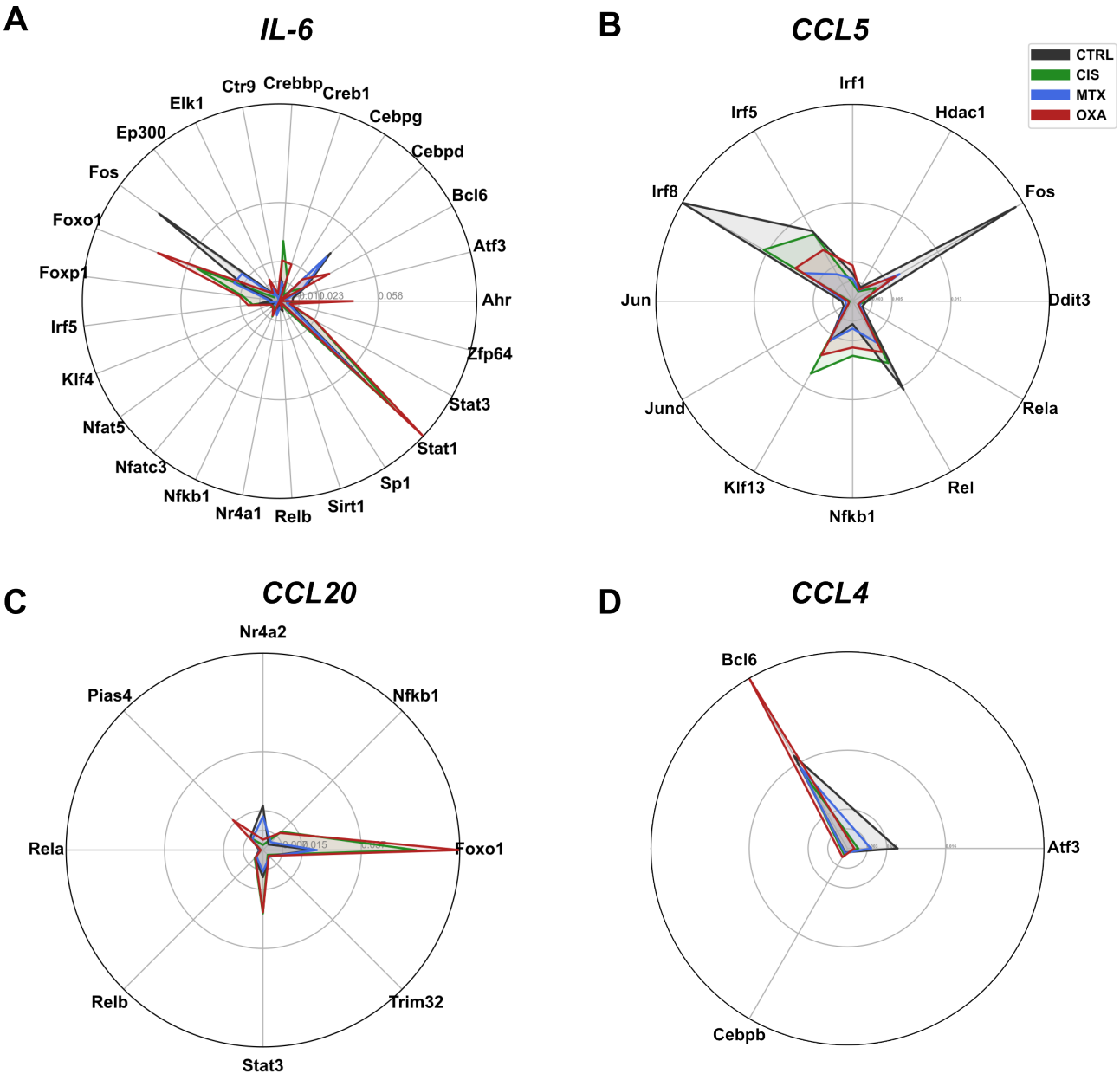

Figure 4.15: Prioritization of TF regulating cytokine expression by measuring similarity between longitudinal expression profiles. For each cytokine we evaluated the similarity between its longitudinal expression and the one of TFs that could regulate their expression. For **A** Il6, **B** Ccl5, **C** Ccl20, and **D** CCl4 we evaluated the similarity for each pair cytokine-TF in MTX, CIS, OXA, and CTRL treated samples

3 Modeling immunogenic cell death

3.1 Motivation and limitations

Models are essential for understanding the complexity of interactions within and between cells and can help explain why some treatments are more effective than others. By describing these processes

in detail, we can gain valuable insights into the underlying mechanisms. Additionally, reasoning via in silico models allows us to interpret the data obtained from experiments and propose strategies for enhancing responses, particularly for treatments that are not inducers of immunogenic cell death (ICD).

There are some limitations, though. First, it is important to note that the predictive power of these computational models is somehow limited. They rely on choices made by the modeler to abstract the knowledge that will answer the questions. These choices are related to the following questions: what are the genes, proteins, and pathways to include; how many of these pathways are needed; which cell types to consider?

Then, the type of data used to build and simulate these models may not fit exactly the description of the model itself. Indeed, the data that are often used to build or personalize these models are transcriptomics data. However, the models describe more post-transcriptional events. Thus, the transcriptomics data can only be used as proxies for the outputs of the models.

Finally, these models allow researchers to recapitulate the different cell types, pathways, and entities that need to be monitored and that could play a role. However, predicting the precise targets or drug dosage is beyond the capabilities of the models presented in this thesis. To do so, other mathematical formalisms such as ODE/PDE models for the mechanistic descriptions and pharmacokinetics/pharmacodynamics models for the drug effect could be more appropriate.

Here, we will focus on one model of population dynamics using UPMaBoSS, and on a collection of intracellular models of the tumor, for what we will refer to as the *core model*, using MaBoSS. We will also provide an example of a 3D toy model showing how dendritic cells interact with the T cells to differentiate into different Th cells using PhysiBoSS.

3.2 A population model of immunogenic cell death

A model was developed in 2020 [29] to simulate cell population dynamics following a chemotherapeutic treatment. The model describes cell-cell interactions between these cell types: Tumor cells, immature and mature dendritic cells, naive CD4, Treg, Th1, Th2, Th17, naive $CD8_+$ cytotoxic T cells (CTL), in undifferentiated (preCTL) and fully differentiated states (CTL) (Fig. 4.16A). The model encompasses 52 entities including cell types, DAMPS, and diverse ligands including cytokines such as IL1B, IL2, IL4, or IL6.

Overall, this model effectively simulates the immune response to tumor cells undergoing Immunogenic Cell Death (ICD) and the subsequent release of DAMPs. Tumor cells undergoing ICD release DAMPs, such as ATP, HMGB1, and CALR, which signal danger to the immune system. Immature dendritic cells (iDCs) recognize and respond to these DAMPs, leading to their activation and maturation, marked by increased expression of surface molecules like MHC class I and II and CD86. Activated dendritic cells (aDCs) then migrate to the lymph nodes, where they present tumor antigens to naive T cells ($CD4^+$ and $CD8^+$). This antigen presentation, along with cytokine signals, stimulates naive $CD4^+$ T cells to differentiate into various subsets (Th1, Th2, Th17, or regulatory T cells) and naive $CD8^+$ T cells to differentiate into cytotoxic T lymphocytes (CTLs). The differentiated CTLs then migrate to the tumor site, recognize tumor cells presenting the specific antigens on their MHC class I molecules, and induce apoptosis in these tumor cells through the release of perforin and granzymes, effectively killing the tumor cells.

The model was simulated with UPMaBoSS [164] and allows the computation of the population size over time in different conditions (Fig. 4.16 B-D). These simulations highlight the crucial consecutive steps of the immune response, from the initial recognition of tumor cells to the targeting and destruction of these cells by CTLs, emphasizing the role of dendritic cells in antigen presentation and T cell activation, as well as the critical functions of cytokines in directing T cell differentiation.

While this model accurately describes some processes occurring along the cancer-immunity cycle, it still lacks intracellular details. Moreover, its scope could be extended by including elements identified through recent experiments. A portrayed description of different secretomic profiles is presented in the previous section 1.5.

This population model could also be complemented by adding new cell types that participate in shaping the tumor microenvironment and are affected by immunogenic cell death (ICD). Besides dendritic cells, other immune cell populations have not been intensively studied in the context of ICD. In silico modeling could help predict or simulate possible biological scenarios involving these additional cell types.

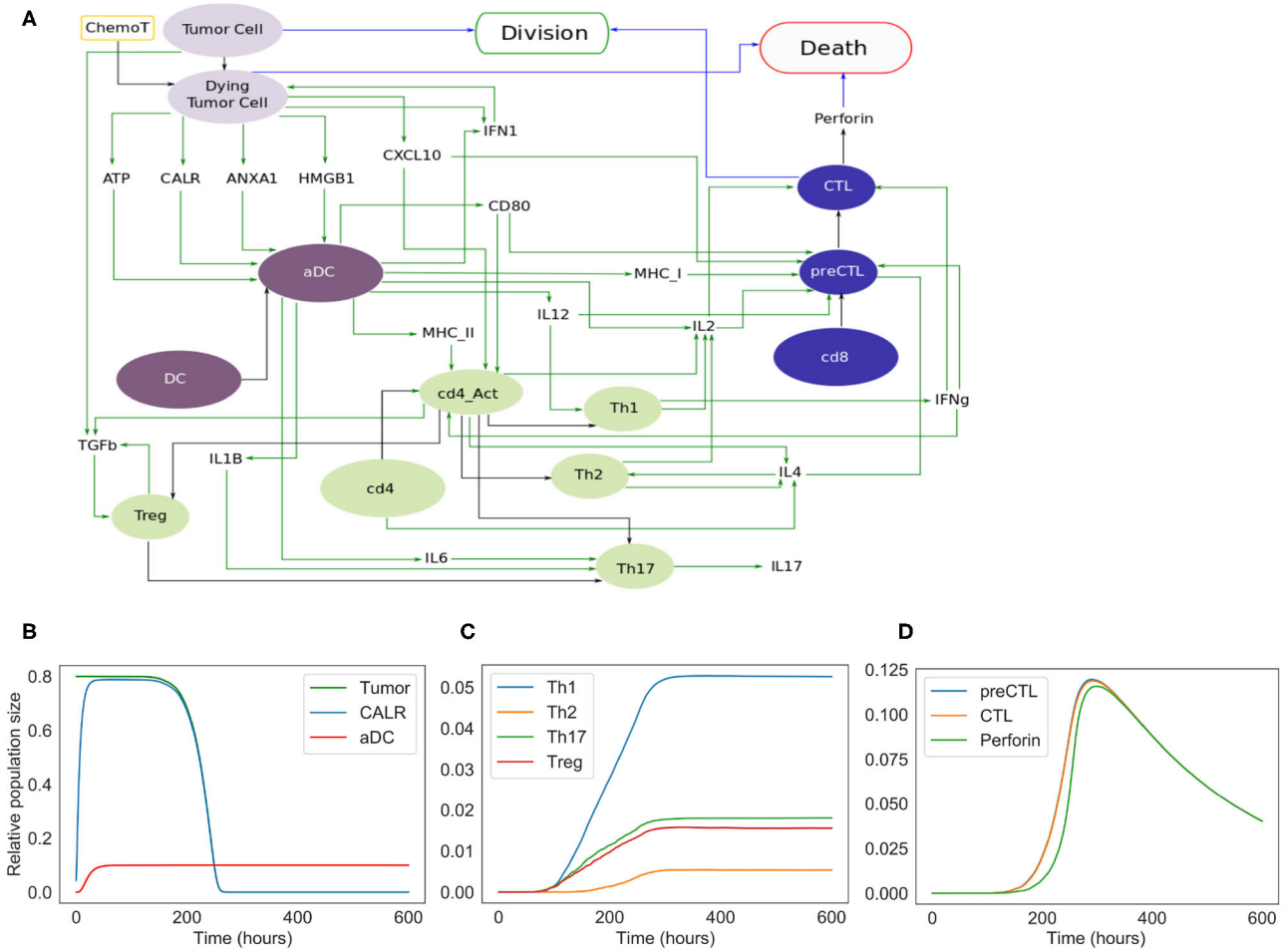

Figure 4.16: Dynamical Boolean Modeling of ICD. A model of ICD. **A**: the network representing DCs (purple nodes), T cells (in green) and tumor cells interacting through DAMPs and cytokines to drive both DCs activation and T cell differentiation. **B**,**C**,**D**: UPMABoSS simulations of the variable probability of being active over time. After an early differentiation of DCs into activated DCs, T cells start differentiating and the peak of CD8+ CTLs occurs after 200 hours (10 days). The production of perforin is directly linked to the size of the CTL population, which decreases soon after the decrease of differentiated CTLs. Moreover, tumor cells are killed when perforin is released by the CTLs.

This model provides information on the size of the cell populations, the expression of cytokines produced by the different cells, and the downstream effects of a single perturbation caused by a therapy administration. Although based on literature-based evidence, this preliminary model lacks a precise characterization of tumor intracellular behavior in response to an ICD-inducing drug.

The current model does not include some important details: the release of the DAMPs by the dying tumor cells is caused by DNA damage response pathways, ER stress, and mitochondrial stress. Additionally, our recent results (see section 1.4) revealed that MCA205 cells release some cytokines as an effect of stress induced by different compounds, even those not sharing the same mechanisms of action.

By incorporating these additional factors, the model can enhance our understanding of the complex interactions within the tumor microenvironment and potentially identify new therapeutic targets.

In the following section, I will present the advancement we made towards building a more complete

model of ICD by approaching the issue from different perspectives.

3.3 The *core* ICD model

There is no univocal consensus on the specific processes initiating ICD, although efforts in the classification of ICD-inducers provide a distinction between treatments according to the target of their mechanism of action.

As illustrated in the introduction, it is still not fully understood why some stress inducers trigger ICD while others do not or what kind of stress is necessary to trigger a specific DAMP release, and how long this stress must be maintained. Answering these questions remains complex using either experimental or in silico methods.

Previous efforts in describing the molecular features characterizing the entire pathway of exposure of specific DAMPs have revealed details on "how" DAMPs are produced or released. For instance, the pathway of CALR exposure has been well characterized in the context of ICD [138, 18, 206].

Combining experimental and in silico approaches can provide a more comprehensive understanding of ICD and its mechanisms. For this reason, during my thesis, we developed a model of the tumor, referred to as the *core* ICD model. The adjective 'core' refers to the model trying to embody the strictly necessary elements that characterize the most emblematic processes of ICD.

This model is currently composed of four distinct modules: the first module describes the exposure of CALR on the cell membrane, the second represents the translocation of nuclear HMGB1 to the cytoplasm, the third focuses on the DNA damage response, and the fourth module outlines the activation of downstream pathways that lead to the transcription, translation, and release of cytokines by the cancer cell. In the future, we plan to combine these modules into a comprehensive model of early ICD. This task is difficult and will require fine-tuning of the inputs and outputs of each module. Some pathways, such as CALR exposure and HMGB1 release, have been more extensively studied and characterized in numerous publications. However, ICD-related research has predominantly focused on the characterization of the components of the immune synapses that emerge from the interactions between DAMPs released by cancer cells and the conjugate receptors on immune cells. With the 'core' ICD model, we focus on the cancer cells, aiming to combine different sources of experimental data and integrate the extracted information into a model of the cancer cell experiencing stress induced by type 1 ICD-inducers, i.e., at both the DNA and ER levels.

CALR exposure module The submodule designed to represent CALR exposure on the cell surface of cells undergoing immunogenic cell death (ICD) is constructed based on literature evidence [206]. We first built a network based on available knowledge of CALR translocation mechanisms (Fig. 4.17 A), then translated it into a MaBoSS model and simulated the effect of an ICD-inducing therapy on

CALR exposure.

The network. We defined as input, a node named `ICD_inducer`, whose activation is impaired with a self-inhibitory loop. The rate-up for this node is set to 0.0, while the rate-down corresponds to the decay rate, which reflects the inverse of a generic compound's half-life. This self-inhibitory mechanism models the drug's natural degradation over time, allowing it to expire in a self-limiting manner.

In our simulation, we initiated the drug administration by initially activating the `ICD_inducer`, then allowed it to progressively decay over time, simulating the gradual reduction in drug efficacy. The negative interaction between the `ICD_inducer` and the `Tumor` node simplifies the process of cell death induction by the ICD-inducing treatment and also affects the induction of reactive oxygen species (ROS). The activation of the PERK pathway in response to ROS generation, or the inhibition of the PP1-GADD34 complex, induces phosphorylation of eIF2α, promoting the unfolded protein response (UPR) and the subsequent translocation of the PDIA3 (Erp57)-CALR complex.

The model. The initial conditions include all nodes set to 0 except for the nodes representing the tumor cell, the ICD inducer, the Sarco-Endoplasmic Reticulum Calcium ATPase (SERCA) that regulates calcium homeostasis, and BAP31 that regulates ER homeostasis all set to 1.

We defined the rate-down of the node representing an ICD-inducing treatment to 24 hours and simulated the behavior of the model in WT conditions. The comparison between the results of the simulation realized on WT conditions (Fig 4.17 B) and the experimental data (Fig. 4.1 E,F) demonstrates a qualitative agreement, though the model does not capture the specificity of different treatment types in the simulations.

The model analysis. To validate the model, we simulated the effect of a point mutation in eIF2α by setting both the initial condition and transition rates to 0. This mutation effectively disrupts the machinery required for CALR translocation following ICD induction [18], resulting in its failure to be exposed on the cell surface (Fig. 4.17 C).

Prior to its embedding within a core model of ICD, further developments of this module may require the personalization of simulation parameters based on experimental data and the verification of eventual cross-talking existing with the other submodules.

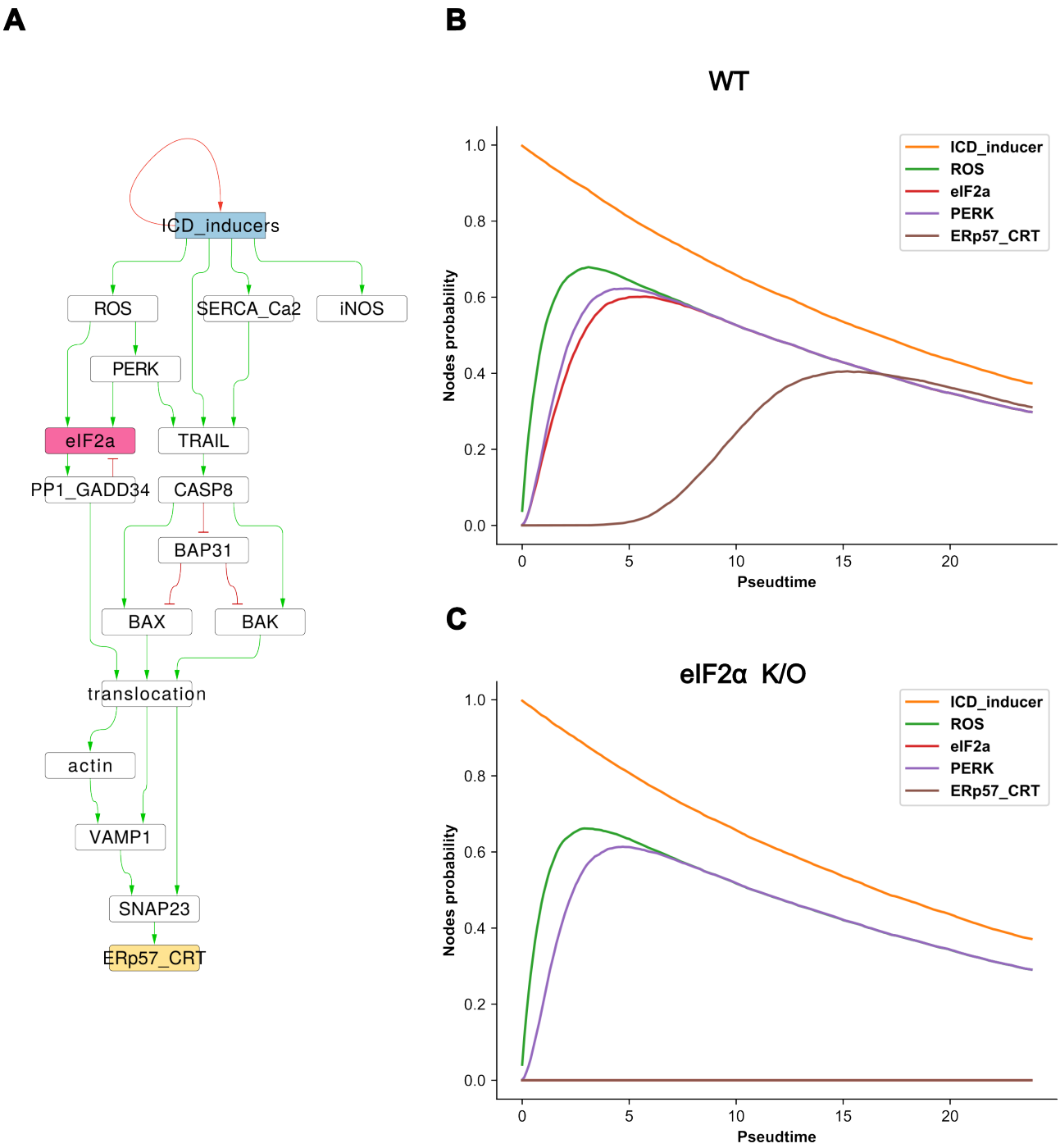

Figure 4.17: CALR exposure module. **A** The network represents the post-translational regulations determining the translocation of CALR in response to ER-stress induced by ICD-inducing treatments. **B** MaBoSS simulation on the model initialized under wild-type (WT) conditions. The generation of ROS drives the ER stress and the consequent phosphorylation of eIF2α. **C** MaBoSS simulation of the K/O on the node representing eIF2α: although the presence of ROS and the activation of PERK, the permanent inhibition of eIF2α impairs completely the exposure of CALR.

HMGB1 release module The module relative to the release of HMGB1, encompasses the description of the translocation of HMGB1 into the cytoplasm as a consequence of ICD induction. The description provided by the model focuses on the effects of both DNA damage and ER stress in promoting the deacetylation of the two NLS preventing the shuttling of HMGB1 from the nucleus to the cytoplasm.

The network. To support the construction of a MaBoSS model we initially built a network using information available on the mechanistic detail of HMGB1 mobilization [31]. Additional details have been gathered using available online post-translational interactions databases such as SIGNOR3.0 [111]. The network includes 43 nodes corresponding to elements associated with biological processes such as DNA damage recognition, induction of apoptosis, cell cycle regulation, ER stress, and nuclear protein translocation.

The model. The model does not detail the exocytosis processes occurring after HMGB1 reaches the cytoplasm. Instead, it provides a snapshot of the processes following the administration of an ICD-inducer, similar to the approach used in the CALR exposure module. Like the CALR module, this model includes components related to the induction of apoptosis (e.g., `BAX`, `BAK`, `CytC`) and nodes associated with ER stress induction (e.g., `ROS`). Additionally, this submodule includes nodes that regulate cell cycle arrest (e.g., `CDK1`, `CDK2`, `CDC25`) following DNA damage detection and response (e.g., `ATM`, `ATR`).

Assuming an ICD-inducing treatment that decays over 24 hours, the model simulates DNA damage that promotes apoptosis, generates ROS, and culminates in HMGB1 mobilization. The constitutively expressed nuclear export protein XPO1 facilitates the shuttling of HMGB1 to the cytoplasm.

The node `HMGB1` represents the fraction of HMGB1 mobilized when the two nuclear localization signals (NLS) are deacetylated, a process modeled as their deactivation due to PKC activation and SIRT1 inactivation. In this context, the NLS nodes are regulated by SIRT1 and PKC [194]. This deactivation allows HMGB1 to be "mobilized" from the nucleus. The export of HMGB1 is mediated by XPO1, which also regulates the nuclear localization of SIRT1. To limit XPO1 activity, its logical rule depends on both `NLS1` and `NLS2`.[8, 9]

The model analysis. The MaBoSS simulations for this module were conducted under both wild-type (WT) conditions and in scenarios where treatment is absent (`ICD_inducer` OFF) or nuclear export is impaired (XPO1 K/O). The initial conditions for the WT simulations include a basal level of HMGB1 (10 % ON) with the nodes representing nuclear localization signals (`NLS1` and `NLS2`) fully active. Given the homeostatic role of `XPO1` in regulating nuclear protein export, we set the initial condition of `XPO1` to be equally probable to be active or inactive (50% ON, 50% OFF). In contrast, the `ICD_inducer` node, which represents the input signal initiating downstream DNA damage activation, was set to full activation.

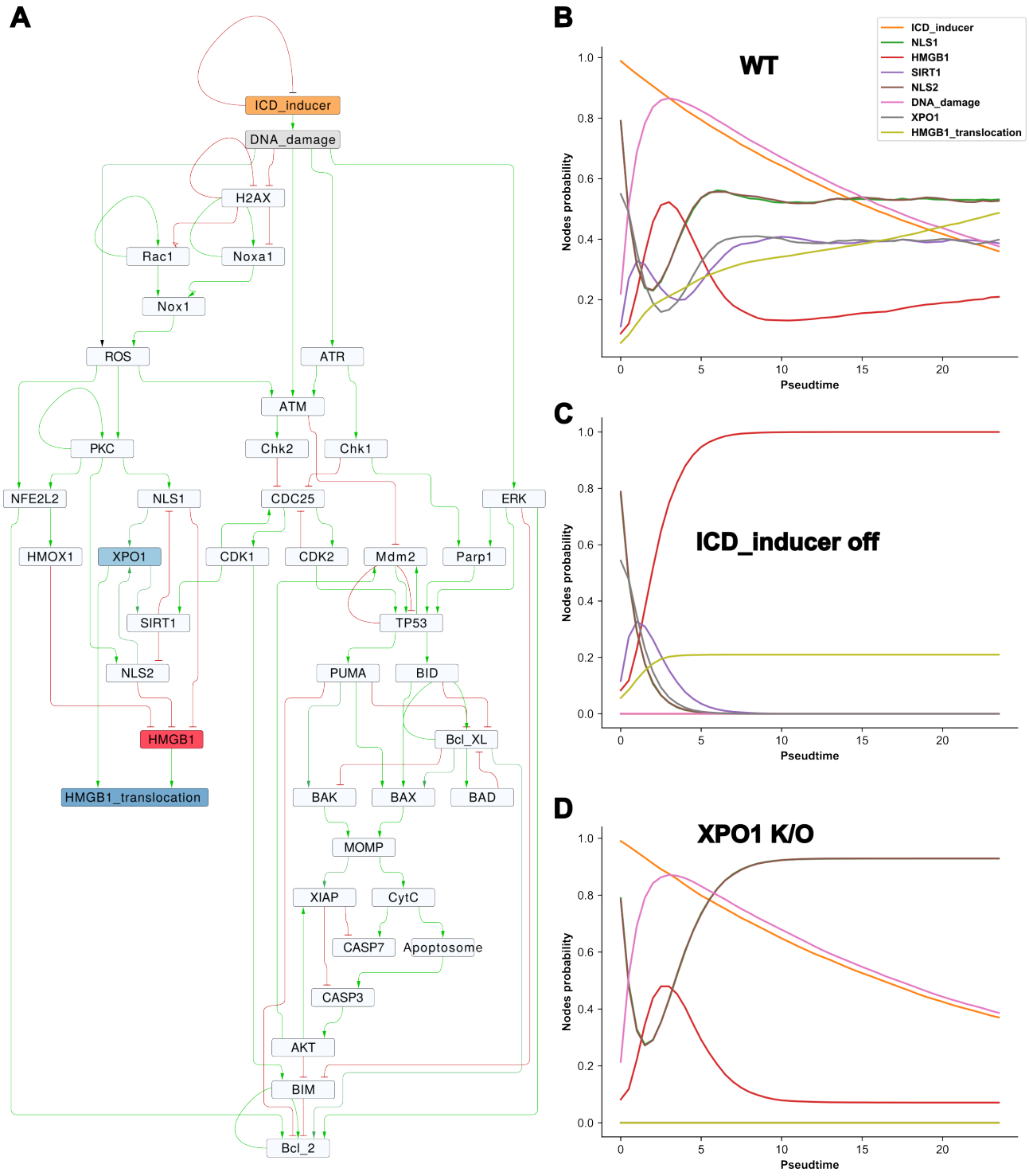

Figure 4.18: HMGB1 release module. **A** The network represents the post-translational regulations determining the mobilization of HMGB1 and its consequent shuttling to the cytoplasm in response to several stimuli including DNA damage and ER-stress induced by ICD-inducing treatments. **B** MaBoSS simulation on the model initialized under wild-type (WT) conditions. The deacetylation of the NLS anchoring HMGB1 in the nucleus following DNA damage induction, with SIRT1 driving the inhibition of these nodes allows the nuclear export of HMGB1 through the activity of XPO1. **C** MaBoSS simulation of scenario in which the generic IDC-inducing treatment is not active: a small fraction of HMGB1 appears to be translocated into the cytoplasm. **D** The simulation of the K/O of XPO1, shows that the silencing of this component prevents the translocation of HMGB1 to the cytoplasm.

As a result, the ICD-inducing treatment first triggers a rapid activation of the DNA damage node, which leads to a temporary deactivation of the two NLS nodes due to SIRT1 activation. This, in turn,

results in the activation of mobilized HMGB1 (HMGB1). The subsequent activation of XPO1 facilitates the translocation of HMGB1 to the cytoplasm.

Simulations that represent the system's behavior in the absence of an ICD-inducing treatment (Fig. 4.18 C) reveal that a small fraction of HMGB1 still translocates to the cytoplasm even in the absence of DNA damage or ROS. This observation suggests the presence of underlying regulatory mechanisms that enable HMGB1 mobilization and translocation to the cytoplasm, which requires further investigation before integration into the core ICD model.

Finally, simulations modeling the effect of a point mutation silencing XPO1 result in a complete inhibition of HMGB1 translocation to the cytoplasm (Fig. 4.18 D).

This submodule only considered the SIRT1-dependent axis activated in response to DNA damage. Future improvements should incorporate additional pathways leading to HMGB1 translocation, such as the JAK/STAT pathway [114]. Furthermore, characterizing the mechanisms responsible for the release of HMGB1 into the extracellular space will be necessary for a more comprehensive and exhaustive model of HMGB1 release.

The DNA damage module As anticipated in chapter 1 sections 2.3.4 and 2.3.5, the three compounds used in this study, share similar features in terms of mitochondrial stress but act differently when inducing ER stress [120].

OXA and MTX supposedly behave similarly as they both belong to the same class of ICD-inducers (type 1). MTX is an intercalating agent and while inducing both single-strand breaks and double-strand breaks, it is supposed to generate ribosomal stress: its impact in causing ER stress is likely due to NADPH cytochrome C reductase reacting with MTX and the consequent generation of ROS [48]. On the other hand, both platinum compounds interfere with DNA by forming DNA-platinum cross-links and eventually double-(and single) strand breaks, recruiting several branches of the molecular machinery needed for DNA repair. In addition to that, recent observations have been hypothesizing that the administration of OXA and CIS leads to different therapeutic outcomes because of the way the two compounds induce DNA damage. Remarkably, the ribosomal stress is also induced by oxaliplatin. The scope of this submodule is to describe the relationships between DNA lesion detection, DNA repair mechanism, and cell cycle regulators.

This module, in turn, is composed of two submodules related to cell cycle and DNA damage response. The construction of the backbone network has been realized using NeKo (see section 3.3), by providing a list of genes representative of the most relevant DNA damage response processes and some key components of the cell cycle.

The list of genes was mainly inspired by the work of Slyskova and colleagues [158], in which they evaluated the impact of pointwise K/O of genes contributing to DNA damage sensing and repair in

colon cancer cell lines.

NeKo provides a first draft of a connected network but requires subsequent manual curation. It contains several bimodal interactions inferred from Omnipath [181]. Subsequently, the draft of the network has been manually refined, by determining the type of interactions represented by the edges given the context using additional sources [162, 78]. Next, we removed unnecessary vertexes (i.e. dead end target nodes not having downstream interactions with other model's components) and manually added a set of nodes necessary to establish a proxy for the cell cycle (e.g. `CHEK1`, `CHEK2`, `CDC25A/C`, `CSNK1A` etc), using available information on SIGNOR3.0 [111]. We concluded by connecting the nodes relative to the cell cycle component to those involved in DNA damage repair and creating new nodes representing different types of DNA damage (e.g: `DSB`, `SSB`).

We introduced a node called `Treatment` representing a generic treatment inducing all types of DNA damage, including double-strand break (`DSB`), single-strand break `SSB`, intra-(and inter-) strand DNA-protein crosslinks (`Intra_XLINK, Inter_XLINK`). The "Treatment" node features a self-inhibitory loop, with its rate-up set to 0.00.0, while the rate-down represents the decay rate, corresponding to the inverse of the compound's half-life. This self-inhibitory mechanism models the drug's natural degradation over time, allowing it to expire in a self-limiting manner. In our simulation, we modeled the administration of the drug by activating it at the start and then allowing it to progressively decay over time, reflecting the gradual reduction in its efficacy. For the simulations of Fig. 4.20, we considered a generic compound characterized by a half-life of 24 hours.

The logical rules assigned to each node in the model have been inferred via NeKo using its default translation rules: all positive inputs are connected with an OR gate and negative inputs with an AND NOT. This formulation allows to switch off a node even if a single inhibitor is active.

The rules were then manually curated to account for some expected node behaviors. For instance, the template logical rule provided by Neko for DNA repair protein RAD51 homolog 1 (RAD51) is affected by a bimodal interaction with BRCA2 and interaction with other elements that have been either removed from the network or whose interactions have been limited to proximal interactions. In the case of RAD51, the original rule provided by Neko is:

```
RAD51 = (BRCA2 or TP53 or E2F1 or CASP3 or ABL1) & !(BRCA2 or TP53 or CASP3 or ABL1)
```

Interactions with both ABL1 and CASP3 have been suppressed, to limit the scope of the model to cell cycle and DNA damage response. To simplify the logic and preserve the biological coherence [75], the logical rule was updated and simplified in the following form:

```
RAD51 = (BRCA2)
```

To characterize the rules of nodes representing the different types of DNA damage, we considered that these nodes are conditioned by two factors contributing to their activity, i.e., the effect of a treatment,

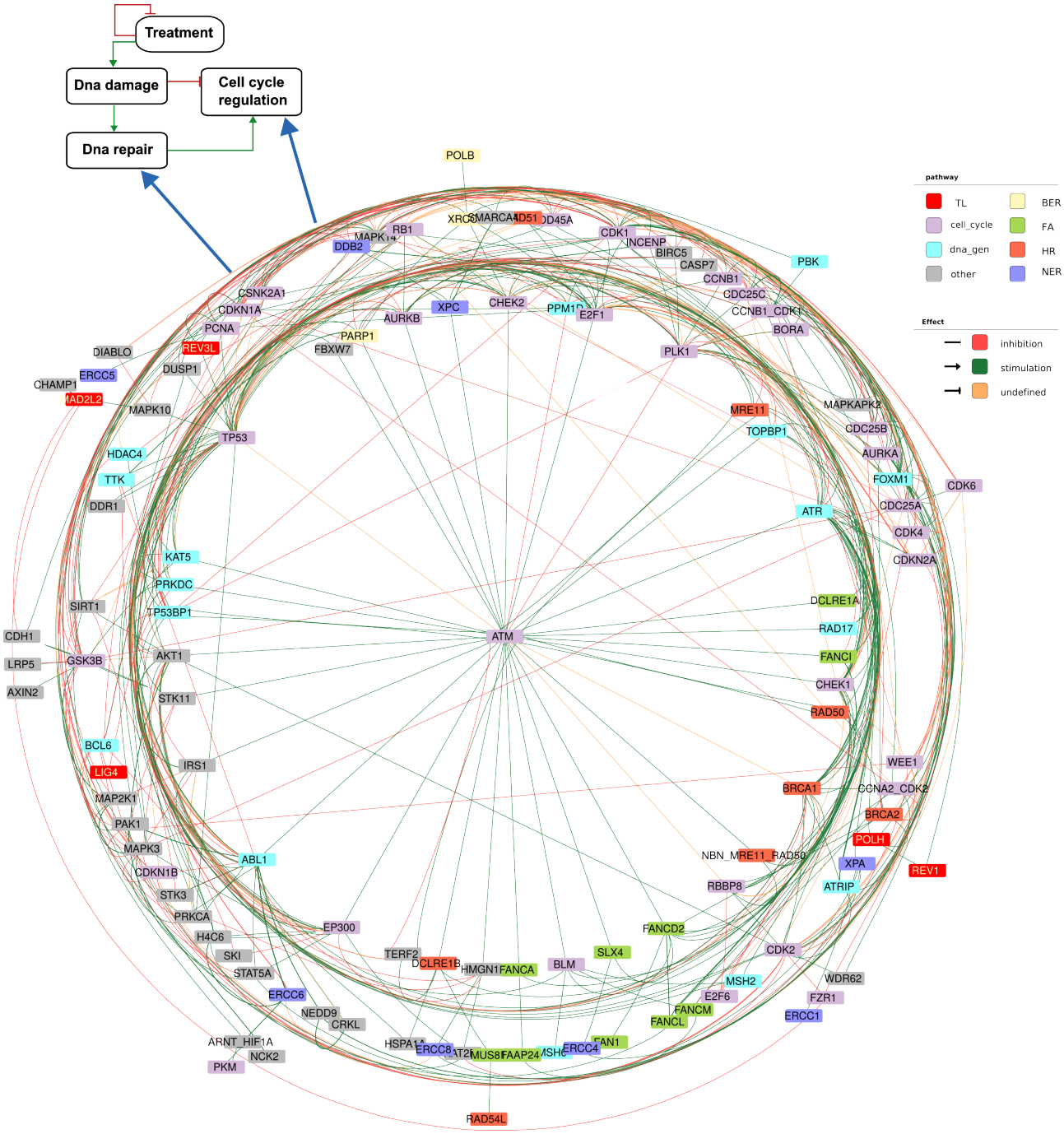

Figure 4.19: DNA damage response network inferred from prior knowledge databases with NeKo. The radial layout shows all connections inferred using Neko and the merging with the additional relations existing with nodes representing the cell's cycle. This network corresponds to the union of processes taking part to both cell cycle regulation and DNA repair (top left). Nodes are colored according to the DNA repair pathway they belong to. The edges in the network represent the signed interactions between nodes inferred using all interactions available in Omnipath: red edges represent inhibitory effects, green stimulatory/activating effects, and yellow edges correspond to bimodal interactions (i.e., interactions with dual assignment). The network visualization has been realized with Cytoscape.

represented as a "Treatment" node, and the repair mechanism that corresponds to the type of damage (e.g., `logic(DSB) = Treatment & !(DSB_repair)`).

These pathways activate downstream events that aim to repair the damage.

To validate the model and ensure that it could reproduce experimental observations, we personalized the model with PROFILE [14] using expression data of 79 colon cancer cell lines retrieved from DepMap [180]. The choice of this type of cell lines has been dictated by experimental evidence provided in Slyskova's work, where all experiments were conducted on colon cancer cell lines, among the most sensitive targets for platinum salts.

We then evaluated the model's performance by simulating the impact of individual gene knockouts on the simulation outcomes. Specifically, we tested the knockout of 36 genes associated with various DNA damage response pathways. These genes were part of a CRISPR K/O array used in Slyskova's et al. work to investigate the impairment of DNA repair mechanisms upon CIS and OXA administration [158] (see Table 4.2).

To validate our model, we utilized the findings of Slyskova et al., who conducted gene inhibition studies on 10 colon cancer cell lines. These studies employed various techniques, including the use of sgRNAs targeting specific genes and a CRISPR/SpCas9 array, to identify genes whose inhibition might impact cell viability through alterations in DNA repair mechanisms (see table below). We initially concentrated on the DLD1 cell line, where cell viability assays were performed to evaluate the effects of gene knockouts on DNA repair processes, particularly when the cells were treated with oxaliplatin (Fig. 4.21 D).

DNA damage response pathway	**Genes**
Base excision repair	PARP1, XRCC1, POLB, LIG3, RPA1
Nucleotide excision repair	XPC, XPA, DDB2, ERCC8, ERCC6, ERCC1, ERCC4, ERCC5, RAD23B
Fanconi anemia pathway	FANCD2, FAN1, MUS81, FANCI, FANCA, FAAP24, SLX4, DCLRE1A, FANCM, TOPBP1
Homologous recombination	DCLRE1B, RAD50, RAD51, RAD54L, BRCA1, BRCA2, MRE11, POLR2A, NBN
Translesion synthesis	REV3L
Non-homologous end-joining	XRCC4, LIG4

Table 4.2: Summary of DNA damage response pathways and associated genes.

The simulations ran on WT conditions indicate that models personalized on expression data of cell lines activate different DNA damage pathways.

In Fig. 4.20 A, to compactify the visualization of simulation results, we show stacked histograms representing the sum of the probability of the nodes representing the different DNA repair mechanisms,

including DSB, SSB, intra-strand and inter-strand crosslinking repair. Smaller bars indicate that DNA lesions have been recovered earlier within the simulation. We consider that if the cells proceed through the cell cycle and activate S and M phases, they have been able to recover the damage. This is true if the would have turned off the nodes representing the treatment. Alternatively, it could be possible to still go through the cell cycle and have damage maintained, which eventually would lead to mitotic catastrophe; by observing only the activity of genes associated to the cell cycle we cannot conclude anything on the possible occurrence of mitotic catastrophe. Thus, making the assumption that using cell cycle phases can be used as a proxy of cell recovery (Fig. 4.20 B), we observe that several cell lines, for which recovery from damage appears successful, have well-established cell cycle phases.
This behavior is observed in simulations personalized using expression data from C80, C84, C99, CL14, CL40 and SNU1033 cell lines. In contrast, CL11 cell line shows activity in cell cycle phases although DNA lesions are still present at the end of the simulations.
Overall, at the end of the simulations, most cell lines continue to exhibit significant DNA damage, with their cell cycles appearing to be stalled in the G1 phase. Pearson correlation analysis of the final node probabilities, across all simulations using models tailored to different cell lines (Fig. 4.20 C), suggests that the current model structure predominantly favors non-homologous end joining (NHEJ) for the repair of both interstrand crosslinks and double-strand breaks (DSBs), as well as homologous recombination (HR) for interstrand crosslink repair. Although these observations seem reasonable, they show poor concordance with experimental results from studies on colon cancer cell lines treated with platinum salts, which identify nucleotide excision repair (NER) as the most prominent repair pathway for these cells. This discrepancy underscores the need for a thorough revision and potential restructuring of the model to better align with empirical data.

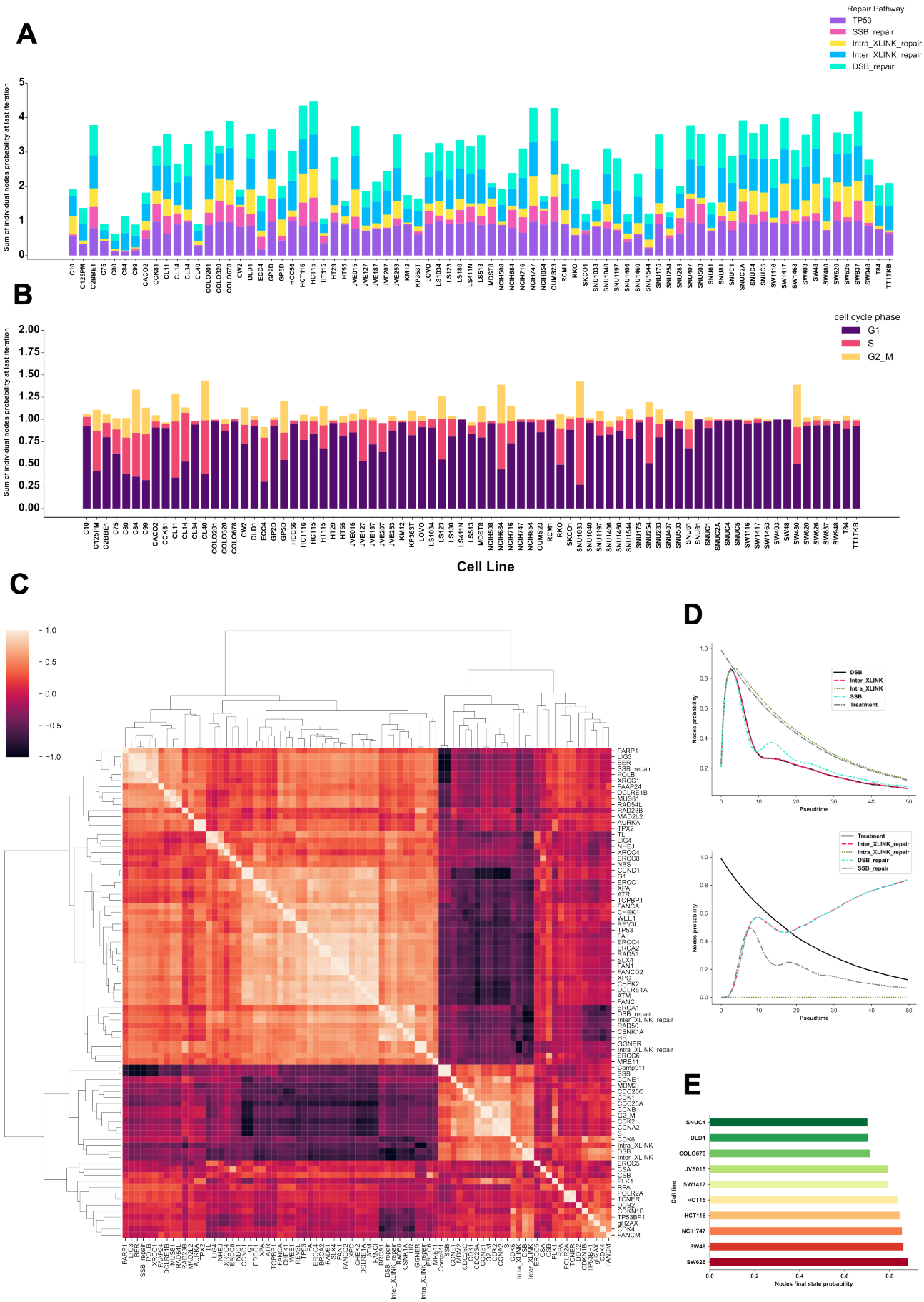

Figure 4.20: DNA damage response module. A. B. C. D. Uncalibrated models in **E.** Top 10 cell lines recovering from intra-strand crosslinking lesions.

To test how the node `Treatment` impacts the activity of downstream nodes, we first ran (fig 4.20 D) a simulation with all nodes set to 0, except for the node representing the treatment. In this setting, the simulations show that some DNA repair mechanisms (such as intra-strand crosslink repair) fail to be activated although the corresponding DNA lesion is present. Conversely, when the model's initial configuration is personalized to data, the intra-strand crosslink DNA repair pathway gets activated (fig 4.20 E).

To compare the behavior of DLD1 with a cell line that exhibits different characteristics in terms of DNA repair and cell cycle regulation, we also simulated the effects of gene knockouts using a model personalized with expression data from the C84 cell line (Fig. 4.21 A-B). The comparison between the simulations specific to each cell line reveals no significant effects on cell cycle regulation or DNA repair within models personalized to a single cell line. Distinct behaviors were only observed when comparing models based on data from different cell lines (Fig. 4.20). In the work of Slyskova et al.[158],in order to assess the impact of the K/O of genes belonging to a certain DNA repair pathway, cell viability has been assessed on mutant clones of DLD1 (Fig 4.21 D). Among mutants, variation in cell viability assed experimentally can reach even 60 % while in our simulations variations are almost neglectable.

Further analysis of transcriptomic data from in vitro experiments with MCA205 revealed highly heterogeneous behaviors even within models personalized to untreated samples from the same experimental group, despite differing time points. While wild-type simulations displayed some variation in outcomes, the knockout mutants again failed to produce significant results.

These findings indicate that the model struggles to account for differences between cell lines. The discrepancies may arise from an incomplete network structure lacking key elements, logical rules that inadequately capture component behaviors or the personalization method's reliance on transcriptomics data for post-translational events. Future work will focus on refining the model to address these limitations.

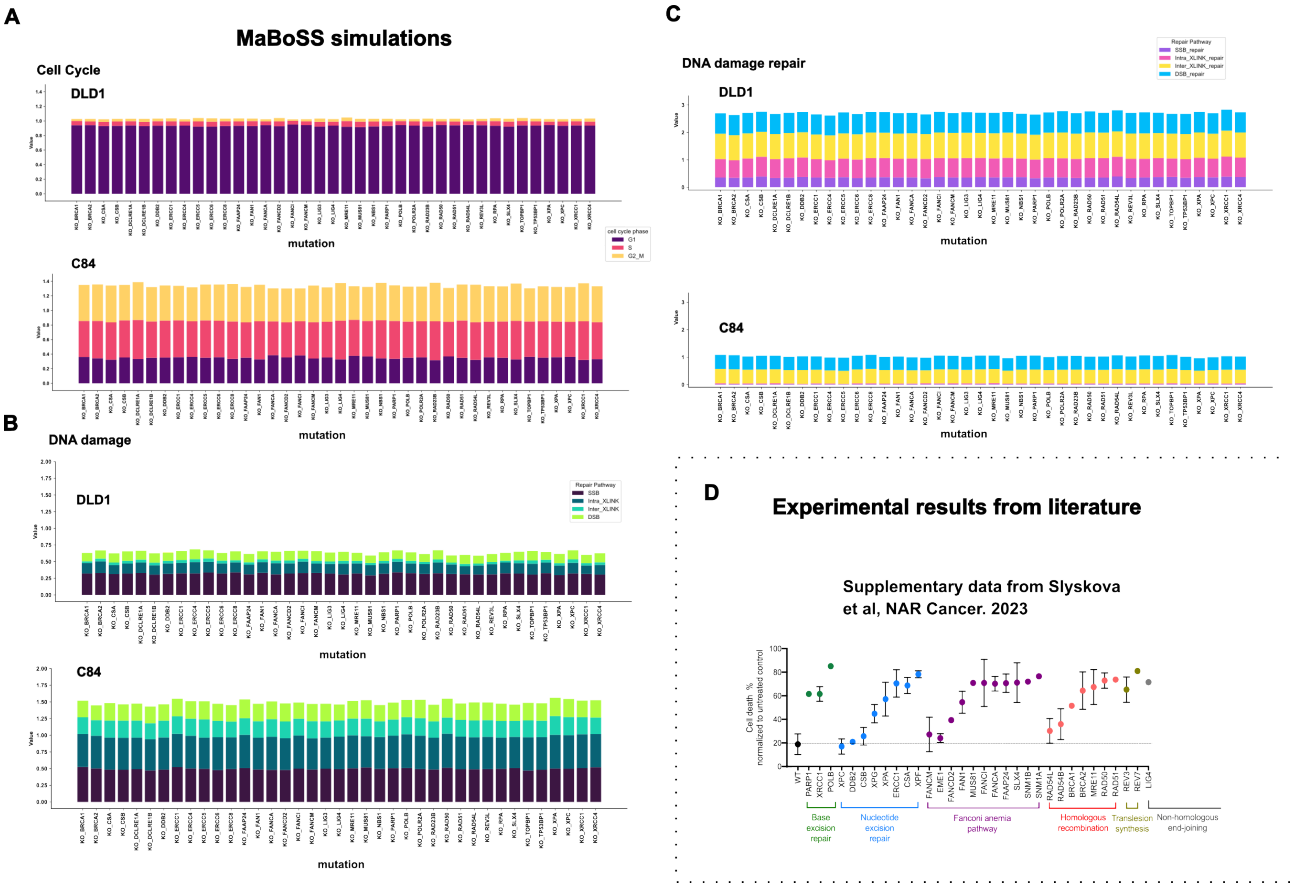

Figure 4.21: Simulations of genes' K/O on DLD1 and C84 cell lines do not reflect experimental evidence and indicate poor response of the model to DNA repair related nodes Barplot representing cumulative final states for simulations on DLD1 and C84 cell lines. In **A.** final state probability for nodes representing the cell cycle, the DNA damage **B.** and the corresponding DNA repair mechanisms **C.** Regardless of the gene silenced, models' final states are essentially the same for both models tailored with DLD1 and C84 cell lines data. **D.** The figures realized by Slyskova et al.[158], shows the impact that the K/O of a gene belonging to a certain DNA repair pathway, has on DLD1 cell line viability. Among mutants, variation in cell viability assed experimentally can reach even 60 %.

As expected, several key conclusions can be drawn. First, the model requires further refinement, either by incorporating additional genes that could account for the experimental results observed in the cell line or by adjusting the logical rules within the current version of the model. Additionally, the presence of feedback mechanisms that could influence repair processes may impact the outcomes. This aligns with challenges faced by many published Boolean models of DNA repair, where the repair process is gradual and time-sensitive—factors that Boolean models often struggle to capture effectively [6]. Furthermore, while the personalization method appears ill-suited for this type of data—given that most observations are at the protein level, whereas the data used for model personalization are transcriptomic—future improvements to the model could benefit from insights drawn from existing models already available

Transcriptional regulation of cytokines associated with ICD-inducers The results from the transcription factor (TF) activity analysis provided a foundation for constructing a network that describes the regulation of cytokine expression. The collecTRI dataset served as a reference for determining the sign of interactions and offered a baseline for estimating TF activity from transcriptional profiles. However, intrinsic biases and bimodal annotations within collecTRI prompted us to consider additional methods for prioritizing TFs in regulating cytokine expression (see Section 2.3).

References to the transcriptional roles of specific TFs were drawn from the sources used in collecTRI, and we initially constructed a network based on the 16 TFs regulating the expression of CCL4, CCL5, CCL20, and IL6 (Fig. 4.22 A). This preliminary network was derived by first identifying the top 50 highly variable TFs across all conditions and then filtering for those involved in regulating the target cytokines.

To refine this network, we incorporated results from a complementary analysis using the Dynamic Time Warping (DTW) algorithm. This approach not only expanded the set of potentially active TFs but also provided a benchmark for the observations obtained through decoupleR (see Section 2.2). We used the DTW results, focusing on the final cost—a proxy for trajectory similarity—and filtered interactions to the second percentile to capture the top hits for all cytokines across conditions.

The filtered results were then used to create individual visualizations of the network tailored to each treatment (Fig. 4.22 B-D). The edge colors represent the similarity between the trajectories of the two nodes, with lighter shades indicating higher similarity and darker shades indicating lower similarity. In the network based on similarity profiles from CIS-treated cells, IL6 is regulated by 16 TFs, with Stat1 and Foxo1 as the most prominent regulators, while Ccl5 expression is predominantly regulated by Irf8.

For CIS-treated cells, filtering to the second percentile reduced the pool of TFs regulating IL6 from 42 to 17, with Stat1, Foxo1, and Crebbp as the top three hits. Similarly, for Ccl5, only 5 out of 15 TFs remained, including Irf8, Klf13, and Irf5. Ccl4 retained only Bcl6 out of 4 TFs, while Ccl20 kept 5 out of 9 TFs, with Foxo1, Stat3, Nfkb1 as well as Pias4 among the key regulators (Fig. 4.22 B). In OXA-treated cells, filtering left 22 out of 42 TFs regulating IL6, with Stat1, Foxo1, and Ahr as the top hits. For Ccl5, 7 out of 15 TFs were retained, including Irf8, Klf13, and Irf5. Ccl4 kept only Bcl6 out of 4 TFs, while Ccl20 retained 4 out of 9 TFs, with Foxo1, Stat3, and Pias4 as key players (Fig. 4.22 C). In MTX-treated cells, filtering left 15 out of 42 TFs for IL6, with Stat1, Cebpd, and Foxo1 as the top hits. For Ccl5, 4 out of 15 TFs remained, with Irf8, Fos, and Rel standing out. As with the other treatments, Ccl4 retained only Bcl6 out of 4 TFs, while Ccl20 kept 5 out of 9 TFs, with Foxo1, Nr4a2, and Stat3 as key regulators (Fig. 4.22 D).

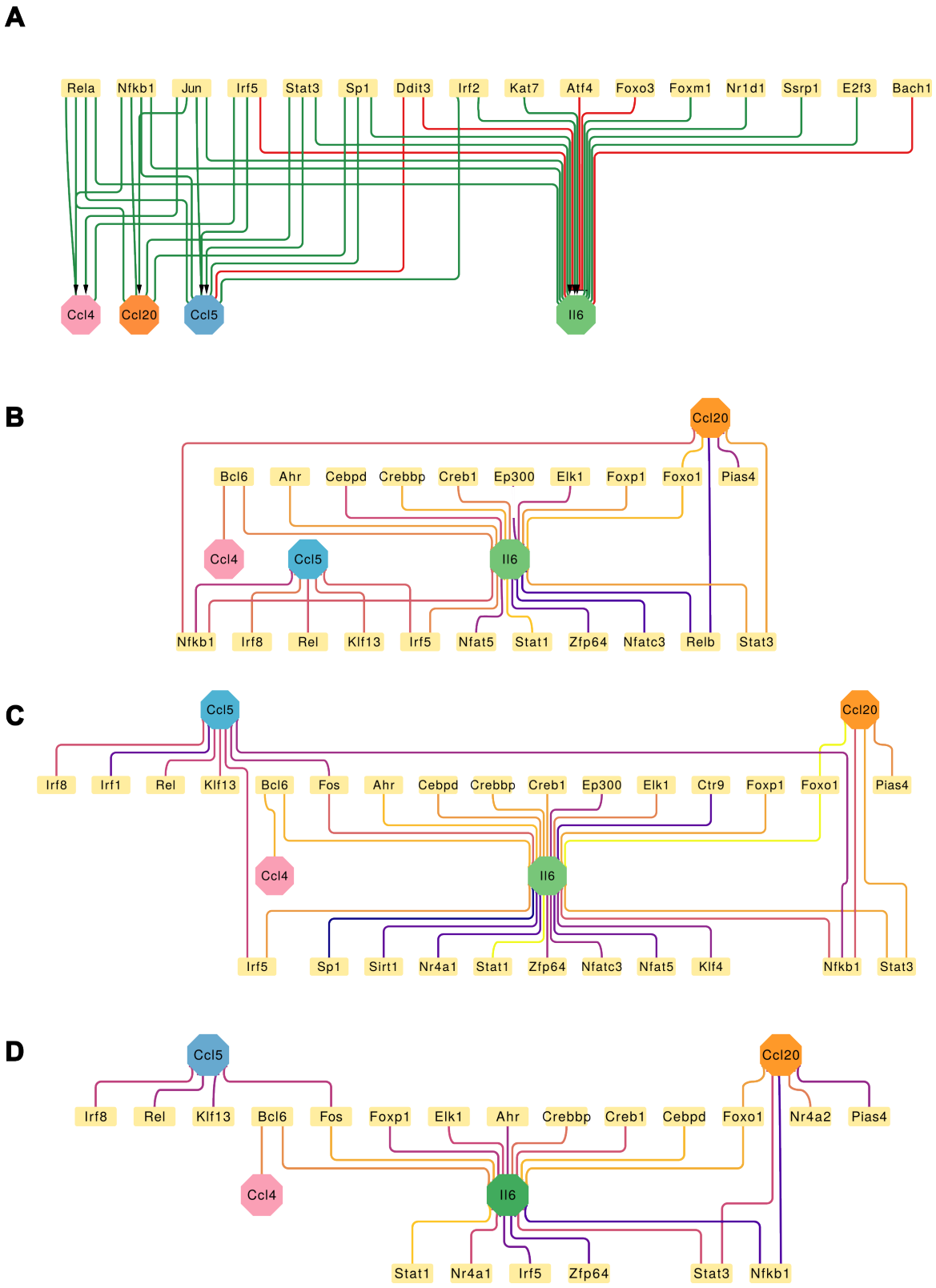

Figure 4.22: Transcriptional regulation of cytokines associated with ICD-inducers. **A** Influence network derived from CollecTRI, focusing on the top 50 most variable transcription factors (TFs) involved in regulating the expression of cytokines CCL4, CCL5, CCL20, and IL6. **B** Network customized based on the similarity between expression profiles of TFs and cytokines using data from CIS-treated samples. **C** Network for OXA-treated samples. **D** Network for MTX-treated samples. In all networks, lighter edge colors indicate higher similarity between the connected nodes, while darker edges represent lower similarity relationships. For all networks lighter edge colors correspond to higher similarity between the two ends of the edge and darker colors to relationships with lower similarity. CIS, cisplatin; OXA, oxaliplatin; MTX, mitoxantrone

To further develop this research, these networks could be integrated into a more comprehensive model that includes upstream regulators of the transcription factors, such as signaling pathways. These pathways would need to be linked to the specific initiators activated by different treatments. The resulting model, built upon these networks, could then be embedded within the core ICD model to provide deeper insights into the regulation of cytokine expression. However, it is important to note that post-transcriptional and translational regulation are still missing from this framework. Incorporating these aspects is crucial for uncovering the mechanistic details of cytokine fate, such as IL6. For example, in MTX-treated samples, IL6 expression is observed, but its release into the extracellular space is absent (see Section 1.4). This necessary upgrade could help clarify such discrepancies and provide a more complete understanding of cytokine regulation.

Building a network of post-translational interaction from phosphoproteome screening
Most of the information available in OmniPath includes post-translational interactions between proteins. Therefore, the ideal input for models built using data from interaction datasets should be estimated protein levels and phosphorylation profiles.
In this project, we conducted a phosphoproteomic screening on cell pellets treated with MTX, OXA, and CIS (see Chapter 3, section 3.1.3). The phosphoproteome was estimated using an antibody array to obtain a relative quantification of total protein and the phosphoprotein counterpart. The experiment was conducted in simplicate. For each protein within the array, we measured the fold-change with respect to the control. We applied thresholds of 0.5 and 2.0 for the fold change ratio to identify downregulated and upregulated phosphoproteins, respectively. This approach allowed us to identify a distinct set of proteins for each of the three treatments (CIS, OXA, and MTX), which we then used to reconstruct a network using Neko for each of the treatment (Fig. 3.3).
Initial results from the Phospho-explorer array indicate a similar trend for both ICD inducers OXA and MTX for tumor suppressor protien NF2 (also known as Merlin) and its phosphorylated form (Ser51) as the most prominent result of the screening. We took the opportunity to investigate Profiling results inherent to this phospho-protein show a strong signal in both ICD-inducers MTX and OXA, with the latter characterized by a bigger intensity of the signal. Our focus was on the phosphoproteins that were either significantly downregulated or upregulated in response to each treatment.
For both MTX and OXA, we identified 25 upregulated and 22 downregulated phosphoproteins. In contrast, for cell pellets treated with CIS, we observed 3 upregulated phosphoproteins and 57 downregulated ones.
Following this, we constructed networks based on the top hits from each treatment. We obtained a network for MTX composed of 167 nodes and 1179 edges, 159 nodes and 1164 edges for OXA, and 181 nodes and 1036 edges for CIS. Next we selected the network resulting from the intersection of these

individual networks to identify shared or distinct signaling pathways affected by the treatments. The resulting network contain 68 nodes and 404 edges(Fig. 4.23).

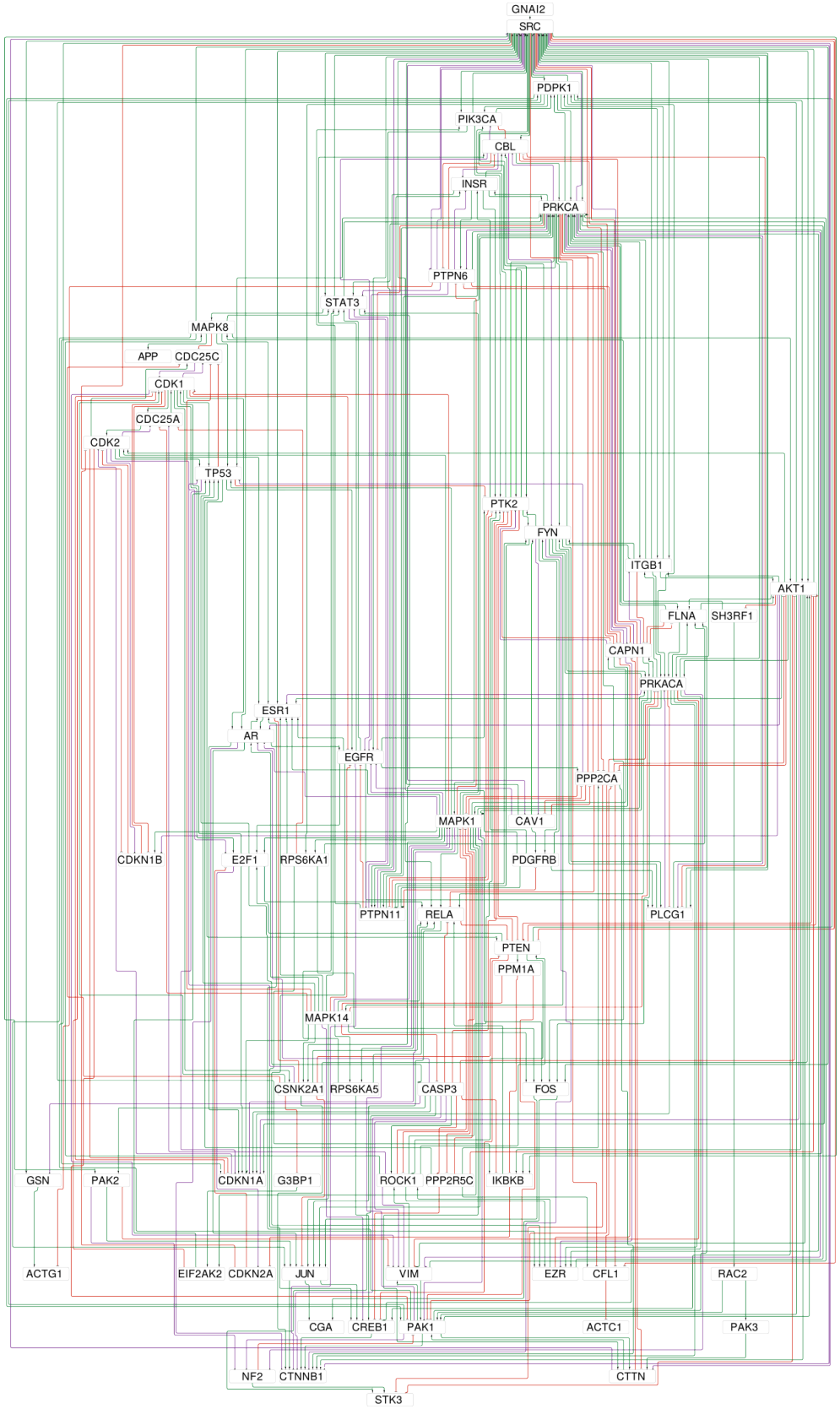

Figure 4.23: Reference network for a model based on phosphorylation-profiles. The network constitutes the backbone for a MaBoSS model and is the result of the intersection between networks obtained via NeKo, using up-regulated and down-regulated phospho-proteins measured in cell pellets treated with MTX, OXA and CIS. Green edges represent activating interactions, red inhibitory, and purple bimodal interactions.

The network inferred from a phospho-proteomic array analysis has provided a first exploration of the interactions between the identified phospho-proteins and other elements for which no role has been determined in the context of immunogenic cell death (ICD). The current objective is to refine this inferred network and develop a MaBoSS model that can be integrated into the core ICD model, thereby providing an additional layer of information related to post-translational interactions following ICD induction.

However, there are challenges at both experimental and modeling levels. One key difficulty lies in validating the phosphorylation of certain proteins. On the other hand, the large number of bimodal interactions identified using Neko requires careful adjustment and manual curation. These challenges may slow progress, as confirming specific types of interactions could necessitate individual experiments for each, an approach that is far from optimal.

To address this, once the top hits have been further validated, we can consider constructing a smaller, more focused network. This network would consist of a restricted set of nodes and aim to identify overlapping nodes with other models. Such an approach would facilitate the integration of this refined model into a broader model that details the intracellular processes of cancer cells undergoing ICD.

3.4 A toy model of cell differentiation

This model was built in the context of a tutorial for the tool PhysiBoSS [102, 143]. The tool is a multi-scale modeling framework embedding stochastic Boolean simulations on networks and physics-based cell-cell interactions. The purpose of the work was to showcase its possible applications, by implementing four different models. Among those models, we included a very simplified representation of how naive $CD4^+$ T cells differentiate into several subtypes. The model integrates some spatial considerations that may appear crucial in some contexts. In this model, we defined two different types of cells encoded as agents. Each agent can either represent a T cell, whose intracellular model encompasses signaling pathways leading to differentiated cells, or a DC that, upon contact with T cells, regulates their expression.

To do so we started by adapting an existing model of Boolean T cell differentiation developed by Corral-Jara and colleagues [38] to be suitable for PhysiBoSS simulations.

Although the model of Corral-Jara was initially meant to recapitulate the transcriptional program leading to the expression of IL-17A/F. We adapted it to describe how, upon the effect of external stimuli, a naive T cell can differentiate into either a Type 1 helper cell (Th1), a T helper 17 cell (Th17), or a regulatory T cell (Treg). Note that the model was booleanized to be simulated in MaBoSS.

We developed a toy model for DCs with a small set of nodes to describe their behavior in response to

external stimuli. This second model (4.24 A) encompasses 4 nodes: 3 inputs (Maturation, Contact, CCL21) and 1 phenotype node (Migration).

As a general assumption for this model we assumed that under the chemoattractant effect of the CC motif chemokine ligand 21 (CCL21), a cytokine constitutively expressed in secondary lymphoid organs (such as lymph nodes), a population of mature DCs (mDCs) migrates to draining lymph nodes. If the two nodes `CCL21` and `Maturation` are active, the node `Migration` will be activated.

For simplicity, we created a single endothelial cell secreting CCL21 in an area representing the lymph node. Additionally, we placed a population of T0 cells in the same area and a distant population of dendritic cells (Fig.4.25 A). The initial state of the PhysiBoSS simulation assumes that the dendritic cells are mature and expressing CCR7, a receptor that drives the migration of mature DCs (mDCs) toward secondary lymphoid structures like, in this case, the lymph nodes. We then mapped the amount of `CCL21` present in the same voxel occupied by the DC to the `CCL21` node in the DC model. Activation of the *CCL21* node within the DC network causes mDCs to move towards the CCL21 source, following its gradient combined with a random walk.

Once in the lymph node, DCs move randomly, as hypothesized in [7]. To achieve this, we created a rule where the stochasticity of chemotaxis depends on the quantity of CCL21, resulting in a saturating effect that progressively lowers migration bias as CCL21 quantity increases.

Moreover, we assumed that mDCs release a set of ligands activating the process of differentiation for the T0 population: differentiation of T0 cells into 3 different subsets of CD4+ T cells occurs when mDCs have reached the lymph nodes. This set of ligands included IL-12, IL-1β, as well as IL-6 or TGF-β. Because Corral-Jara's MaBoSS model (for T cells) already included nodes representing the above-mentioned ligands, we made the assumption that mDCs are responsible for the production of these ligands, but we chose to not include them in the model of DCs and instead chose to represent them by a single node, `Contact`. This means that when a mDC is in contact with a T0 cell, it can release these cytokines by activating the input nodes within the model of T cells. To stop the migration of mDCs once they meet a T0, the node `Contact` inhibits the node `Migration`.

The migration process restarts when a T cell has differentiated. In this model, `T0` serves as an input for the contact node. PhysiBoSS considers the spatial distribution of cells, encoding contact between cells based on the overlap of their radii. If the overlap exceeds a certain threshold, the simulator assumes the cells are in contact receptors of the MaBoSS T cell models are activated to trigger downstream pathways.

Since the activation of ligand nodes drives the differentiation of `T0`, once differentiation into other cell types occurs, the simulator detects that the input node for the DC model (`T0`) is no longer active. This triggers the resumption of migration, allowing the dendritic cell (DC) to reach other naive T cells

and initiate their differentiation program.
The T cell model in turn includes 3 master transcription factors that are assumed to be markers of differentiated T cells: RORgt (for Th17), FOXP3 (for Treg) and Tbet (for Th1). Based on these nodes, we added three phenotype nodes (`Th1`, `Treg`, and `Th17`), that became output nodes of the model, to provide a better representation of the different cell types. The activation of the phenotypes is mutually exclusive.

The model was tested with various mutants to identify potential targets influencing the differentiation probabilities of the three T cells. These mutants, introduced at the beginning of the simulation, do not immediately trigger T0 cell differentiation but instead impact the process after contact with mDCs. Among the mutants, we found that inhibiting `API`, `NFKB`, `LCK`, `TCR`, `RAS`, `ITK`, `ERK`, `cFOS`, `cJUN`, or `IKK` leads to cells differentiating exclusively into Treg. Inhibition of `IL1RAP`, `IL1R1`, `IL1R`, `FOXP3_2`, or activation of `MINA` results in a mix of Th1 and Th17. Inhibition of `STAT1`, `Tbet`, or `PLCG` produces a mix of Treg and Th17.
We also explored the impact of modifying activation rate parameters to better control Treg proportions. For example, lowering the activation rate of `NFKB` increases the proportion of Treg, while lowering the activation rate of `FOXP3_2` reduces their proportion.

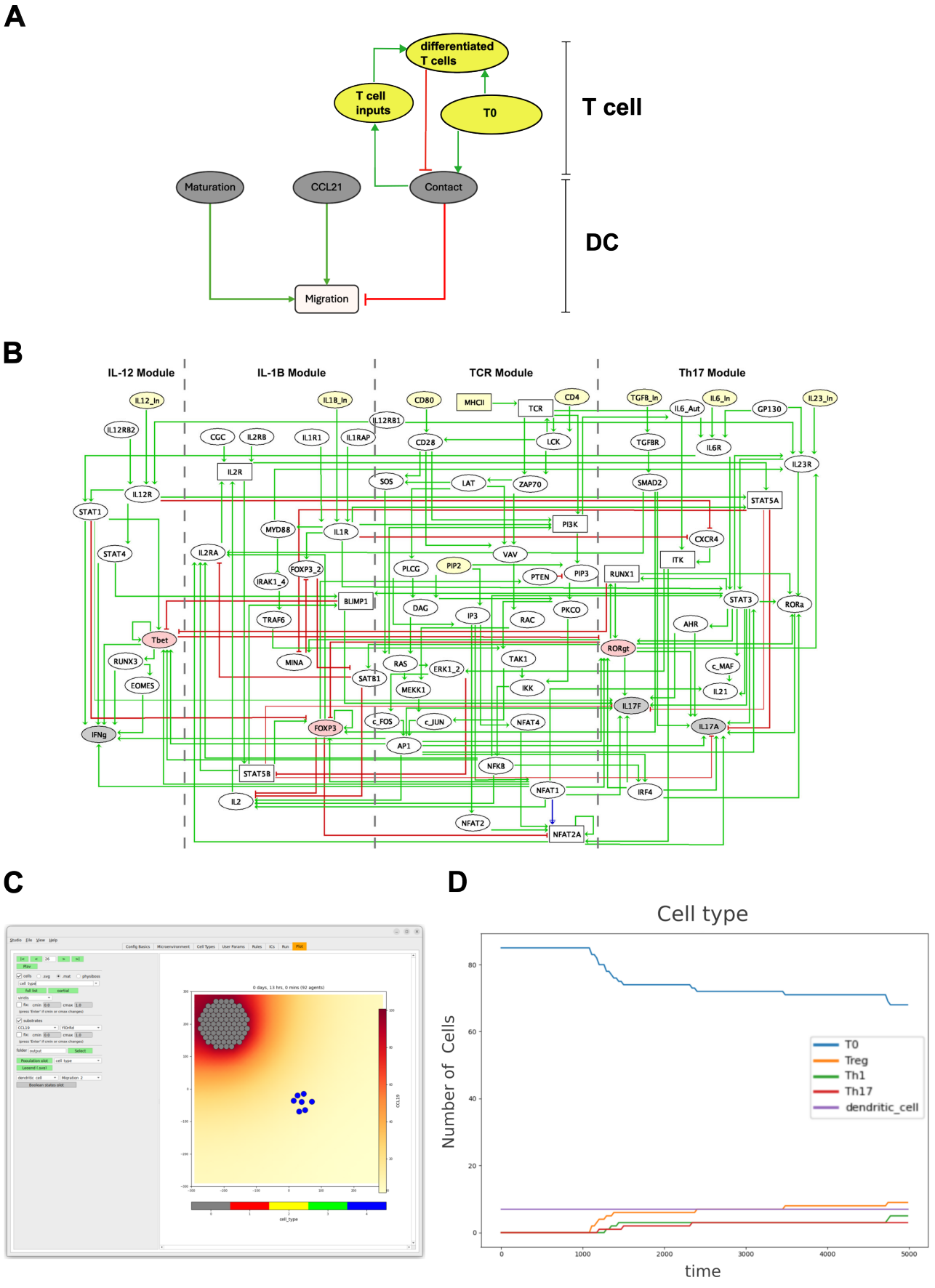

Figure 4.24: Toy model of cell differentiation: the migration of dendritic cells. **A** mDCs migrate to the lymph node under the chemoattractant effect of CCL21. **B** Network from initial published model **C** PhysiBoSS graphical interface of the model. **D.** Cell size population over time for the each cell type of the model

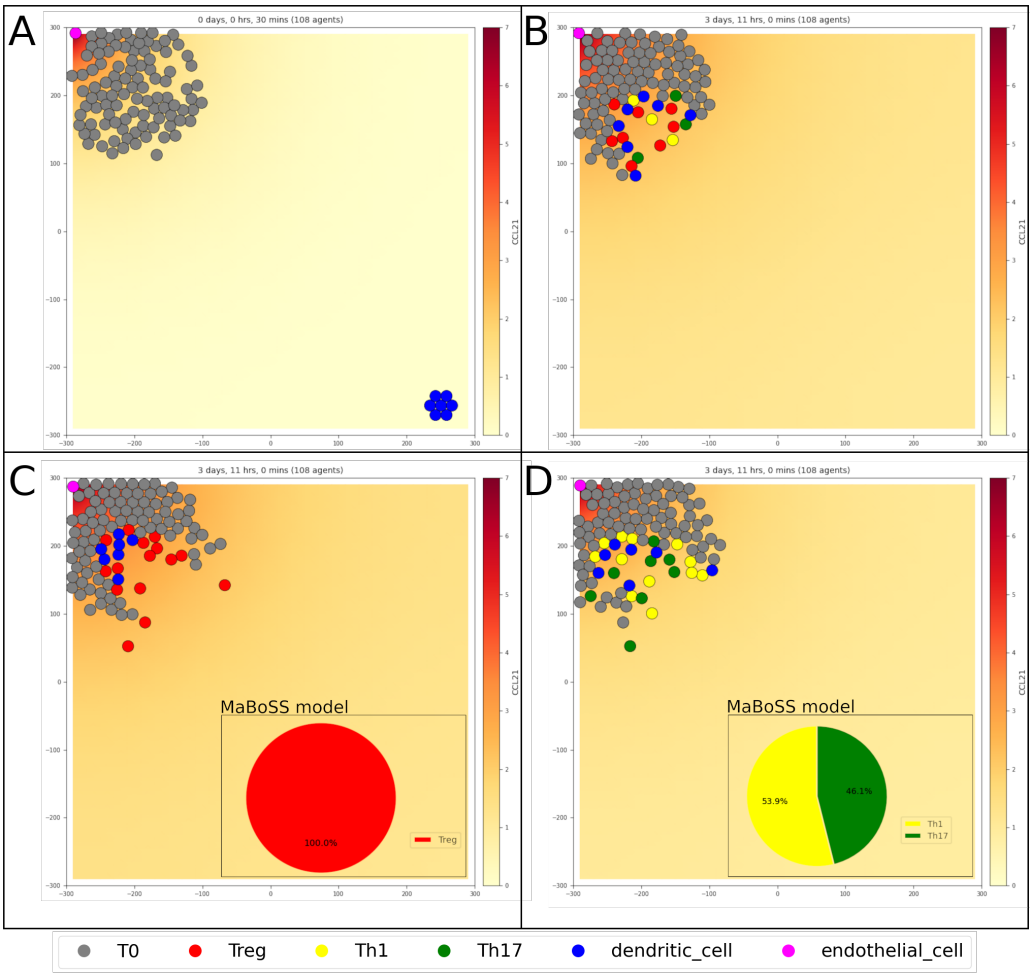

Figure 4.25: Simulation of the T cell differentiation model in 2 and 3 dimensions. **A** Initial population of T cell (gray), with an endothelial cell (pink) secreting CC21. A population of dendritic cells (blue) is attracted towards the source of CCL21. **B** Upon contact, the dendritic cells trigger the receptors of the naive T cell, which start the differentiation process according to the outputs of the intracellular model, into Treg (red), Th1 (yellow), and Th17 (green). **C** Simulation of the T cell differentiation with NFkB knock-out, resulting in only Treg. **D** Simulation of the T cell differentiation with FOXP3 knock-out, resulting in only Th1 and Th17.

This is only a toy model to showcase the possible application of PhysiBoSS, yet it demonstrates its potential in describing complex processes involving multiple cell types and their spatial interactions. While the simulation results from this model are not assumed to be realistic, they show the future possible applications of PhysiBoSS. The model incorporates spatial dimensions and intracellular details, particularly for T cells, and serves as a significant continuation of the previous work on the cancer-immunity cycle initiated upon ICD induction [29].

Given the multi-scale nature of these simulations, the most suitable data sources are multi-omics paired datasets, including spatial data such as spatial proteomics (e.g., multiplexed-histology) and spatial transcriptomics. These datasets provide essential features for configuring simulations, such as cell phenotype, position, gene expression, and protein levels. Although the high costs of these emerging technologies limit their availability for simulations, they embody the perfect candidates as data sources to configure this type of simulations.

3.5 Concluding remarks

One of the aim of this project is to develop a comprehensive model of the processes occurring following the administration of ICD-inducing treatments that integrates multiple layers of biological information, aiming to elucidate the complex interplay between these layers, from transcriptional to post-transcriptional regulation. While some components, such as the two submodules describing the manifestation of ICD hallmarks, such as CALR exposure and HMGB1 release, are nearing readiness for integration, others—like the module representing the cellular response to DNA damage—still require significant improvements and possibly simplification to achieve a more cohesive and functional model. These various modules can eventually be integrated through key biological processes, including DNA damage response, cell cycle regulation, ER stress, and apoptotic mechanisms for which overlapping nodes facilitate their integration into a single organic model.

Throughout this section, we have highlighted the inherent challenges in validating mathematical models against real-world data, like in the case of the DNA damage response module. Constructing these models is a complex and labor-intensive task that cannot be easily accomplished using existing knowledge databases alone. Although automatic network inference offers valuable support for exploring interaction spaces within a defined set of entities, it remains a multi-step process that demands substantial refinement before reaching maturity.

The initial ICD model, published in 2020 [29], was manually constructed and successfully reproduced known phenomena. Despite being based on broad assumptions and lacking detailed intracellular regulation, it provided a satisfactory framework for describing intercellular communication. The focus of the core ICD model then shifted to detailing intracellular processes, specifically aiming to capture both the manifestation of ICD-associated DAMPs and their relationship with DNA damage induction. The first two submodels, *"CALR exposure module"* and *"HMGB1 release module"*, were manually curated and produced simulations that qualitatively aligned well with experimental results.

The *"DNA damage module"* was designed to detail processes involved in the DNA damage response, including repair mechanisms and cell cycle regulation. Leveraging recent observations on DNA repair pathways activated by platinum salts, we selected hallmark genes representative of each repair pathway and used curated databases to infer networks supporting the construction of this module. However, while the inferred network demonstrated some consistency, further refinement in both structure and configuration is needed to adapt it into a MaBoSS model. This ongoing work will be discussed in more detail in an upcoming article covering the construction of the core ICD model based on our in vitro results (see Chapter 4, Section 1).

The final model presented in this section, the *"toy model of cell differentiation"*, is part of a series of models presented in an article currently under its second round of review in the journal "Briefings in

Bioinformatics." This toy model represents one of the first PhysiBoSS models to include multiple cell types. My role in this project included providing feedback on the biological coherence of the model adaptation and collaborating on its transition from a GINsim model to its MaBoSS counterpart.

Chapter 5

Conclusions and Perspectives

My PhD thesis emerged from an interdisciplinary project integrating experimental and computational approaches to model ICD. Central to this work is investigating whether ICD possesses a distinct molecular signature, alongside a secretory profile that enhances the immunogenicity of chemotherapies. Additionally, the research delves into the cellular pathways that regulate the secretion and release of ICD-related DAMPs. By integrating both known and newly identified hallmarks of ICD, this research aims to recapitulate ICD in silico, ultimately seeking to predict the immunogenicity of drugs and improve their efficacy in immunotherapy.

This thesis started with the experimental validation of established evidence, confirming that CIS and MTX treatments confer low and high immunogenicity, respectively, to dying murine fibrosarcoma cancer cells. This observation, well-documented in numerous publications, provided a solid foundation for our project. One of our initial assumptions, based on the literature, was that OXA would be an effective chemotherapy due to its strong immunogenic potential. However, contrary to previous reports in other cancer models identifying OXA as a potent ICD inducer, we observed only moderate immunogenic effects in our study.

We then evaluated the extent to which standard ICD hallmarks manifested and analyzed the differences between treatments in triggering a specific protective adaptive tumor immunity. Our findings revealed that discrepancies in treatment efficacy were linked to variations in the magnitude and timing of CALR surface exposure and HMGB1 release.

In the case of OXA, the observed reduction in immunogenicity and unexpected in vivo cytotoxicity were traced to changes in its formulation, as noted by the manufacturer. This detail proved crucial, as ICD inducers are known to exhibit a dosage effect: higher doses can lead to increased cytotoxicity while diminishing their immunogenic potential. This phenomenon was evident for OXA in our study with fibrosarcoma cells and has been similarly reported in the literature for colorectal cancer cells [177].

Given the challenges in determining the immunogenicity of therapy-induced cell death based on the extracellular release of labile DAMPs, we aimed to identify cell-intrinsic molecular determinants of ICD. By employing transcriptomics and proteomics approaches, this research identified a transcriptomic signature composed of surface receptors and secreted proteins with immunomodulatory and TME shaping activities, whose modulation correlates with the level of cancer cell immunogenicity induced by chemotherapeutic interventions. This mRNA signature has been partially confirmed at the proteomic level through protein screening via immunofluorescence and targeted ELISA-based validations.

To further explore the impact of these findings, functional studies have been initiated to assess the roles of identified markers such as IL6, CCL20, and CCL5. These investigations involved in vivo assays, including both supplementation and neutralization of these cytokines in prophylactic and therapeutic settings.

Preliminary results from the prophylactic regimen and co-supplementation assays revealed that the addition of these cytokines did not enhance the immunogenicity induced by vaccination with cells pre-treated with either ICD inducers or non-ICD inducers. Notably, in the case of CCL5, co-supplementation reduced the immunogenicity observed when cells treated with MTX were injected, suggesting a potential negative impact on the immune response in this context.

Moreover, our proposed signature has the potential to outcompete other secreted factors, namely type-I IFN and CXCL10, previously reported as indicators of immunogenicity but unvalidated in the present work in fibrosarcoma. Despite the well-acknowledged role of CXCL10 in attracting the CXCR3+ T cell mediators of antitumor immunity, especially following ICD induction [157], our analysis of transcriptomic data retrieved from in vitro experiments revealed an upregulation of Cxcl10 across all treatments. This observation suggests either that CXCL10 might be necessary but insufficient for the completion of the cancer-immunity cycle triggered by ICD, or that mRNA levels do not relate to secreted protein levels.

Additionally, we did not measure in vitro the type-I IFN response, which normally culminates into the transcription of some genes coding chemoattractant ligands like CXCL10, across treatments.

Figure 5.1 provides a comprehensive summary of our major in vitro findings, integrating various layers of information derived from direct measurements of protein abundances and transcripts, as well as indirect assessments of pathway activity and potential transcriptional circuitry. This integrated analysis suggests the presence of an autocrine loop, potentially driven by the release of factors such as ADIPOQ, GRN, INHBA, LCN2, PTX3, TNFSF11, VEGFB, and IL6.

For each cytokine, we provided a qualitative score indicating the magnitude of its release by MCA205

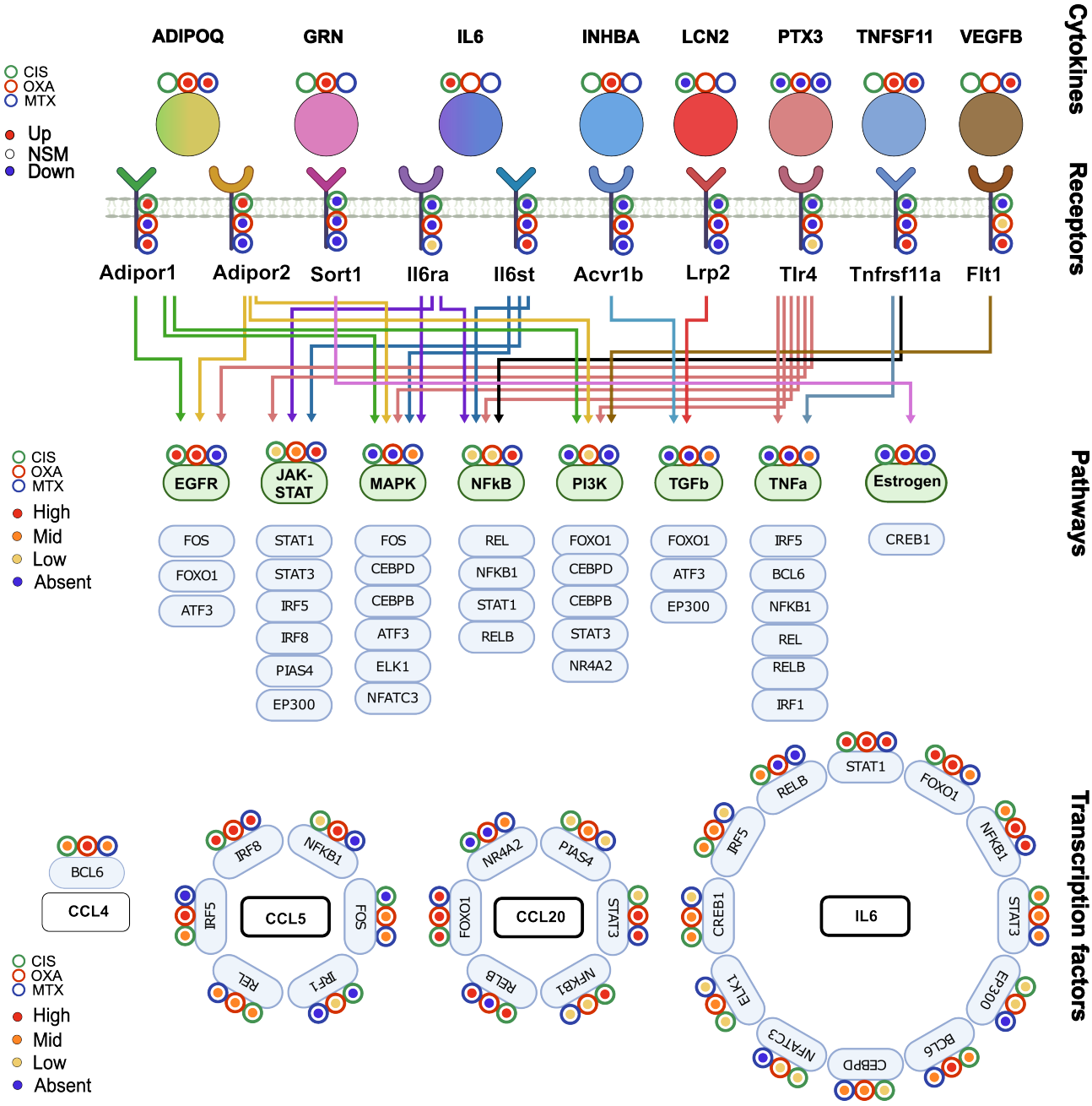

Figure 5.1: Recapitulating In Vitro Findings. The figure summarizes the results of our in vitro analyses across several layers of biological information. The top section displays the relative abundances of cytokines released by MCA205 cells following treatment with CIS, OXA, and MTX. Directly below, the expression levels of the corresponding binding receptors are shown relative to the control group. The subsequent layer depicts pathway activity, with arrows linking upstream receptors to pathways for which causal relationships have been established in the literature. Further downstream, we list transcription factors (TFs) that are potentially influenced by these pathways. The bottom layer illustrates the ranked contributions of each treatment to transcription factors regulating the expression of CCL4, CCL5, CCL20, and IL6. Both TF contributions and pathway activities are derived from indirect measurements: TF contributions are ranked using the dynamic time warping (DTW) algorithm, while pathway activities are inferred using the ULM model with Progeny enrichment analysis. For further methodological details, please refer to Chapter 4.

cells following stimulation with MTX, OXA, or CIS, compared to untreated cells. Additionally, we examined the expression of corresponding receptors to identify those capable of binding these secreted factors. These results were also contextualized against the control group, with all analyses focused on the 24-hour time point.

Pathway activities were further summarized, highlighting downstream transcription factors that could potentially be modulated by each pathway. Using dynamic time warping (DTW), we prioritized the contribution of transcription factors in regulating the expression of key cytokines analyzed in this thesis, including CCL4, CCL5, CCL20, and IL6. This enabled us to hypothesize potential contributors to pathway activation and their relationships to the autocrine signaling of the cells.

The EGFR pathway was found to be controlled by receptors such as Adipor1, Adipor2, and Tlr4. It displayed markedly higher activity in response to platinum salts, particularly CIS, which correlated with increased expression of Adipor1/2 in CIS-treated cells relative to the control group.

The JAK-STAT pathway showed the highest activity in MTX-treated cells. This aligns with the upregulation of the two subunits of the IL6 receptor (Il6st and Il6ra) and Tlr4 under these conditions. Similarly, the MAPK pathway exhibited mild activity overall, except in cells treated with MTX, where activity was elevated. Among its potential regulators, the IL6 receptors emerged as the most prominent contributors.

The NF-κB pathway was previously identified as a key discriminant between treatments (MTX vs. platinum salts). In this study, it displayed higher activity in MTX-treated cells, with upstream receptors such as Tlr4, Il6st, Il6ra, and Tnfrsf11a upregulated in MTX conditions. This provides a rationale for the observed pathway activation.

The PI3K pathway showed low activity in OXA-treated cells. However, most receptors influencing this pathway were not upregulated under these conditions, except for Vascular Endothelial Growth Factor Receptor 1 (Flt1). The TGF-β pathway demonstrated slightly increased activity in MTX-treated cells, despite the downregulation of its controlling receptors (Lrp2 and Acvr1b) across all treatments. Meanwhile, the TNF-α pathway exhibited moderate activity in MTX-treated cells, with its regulators consistently upregulated under these conditions.

To further refine these observations, we also summarized the contributions of transcription factors regulating the expression of CCL4, CCL5, CCL20, and IL6. The results of the DTW algorithm are presented qualitatively, ranking individual transcription factor contributions. While this framework provides valuable insights, validating these contributions would require extensive follow-up experiments beyond the scope of this thesis.

In conclusion, this figure provides an invaluable tool for summarizing the in vitro behavior of MCA205 cells treated with MTX, OXA, and CIS, offering hypotheses on the mechanisms underlying cytokine release and pathway regulation. This comprehensive analysis lays the groundwork for future studies to explore the intricate dynamics of autocrine signaling and its implications in therapeutic contexts.

In vivo, the archetypal effector molecules of antitumor immune response IFNγ, GZMB, and CXCL9 were unexpectedly either not detected or downregulated in tumors treated by the ICD inducer MTX,

in contrast to the supposedly less immunogenic CIS and/or OXA treatments. This observation echoed the enhanced level of Ifnab mRNA in vitro upon both platinum salts but not MTX or the dysregulated expression of Cxcl10 commented in the previous paragraph. Consequently, we hypothesize that both type-I IFN response and CXCL10 may not serve as universal markers of ICD induction.

In examining the treatment groups, we observed that chemotherapies not only vary in the extent of their ICD hallmark manifestations but also in the distinct secretome profiles they induce. Beyond the recruitment of conventional dendritic cells, other immune actors responding to ligands released by cancer cells undergoing ICD may significantly modulate the TME. While in vitro analysis of secretomes identified cytokines likely to play a major role in ICD-induced immunity upon chemotherapy, in vivo flow cytometry data will offer additional insights into the immune cell populations infiltrating the tumor in response to each treatment. A retrospective comparison of the cytokine landscape with the corresponding immune cells present at the tumor site could reveal important details about previously understudied cell types in the context of ICD.

To further investigate the role of the identified targets in cell immunogenicity induced by chemotherapeutic regimens, future studies will monitor ICD triggering upon neutralization of these targets. Along this line, MCA205 cells with targeted knockouts for selected markers have been generated. The impact of these deletions on immunogenicity will be assessed through functional in vivo assays, allowing for direct comparisons with their wild-type counterparts. The experimental framework has been expanded to include in vivo therapeutic and prophylactic regimens using these genetically modified cancer cell lines. Once the role of these targets in shaping the immunogenicity of tumor cells treated with ICD chemoinducers is confirmed, further validations in other cell lines will be necessary.

To support our preliminary in vitro findings, we plan to conduct additional validations, focusing on molecular targets identified through phospho-protein profiling assays. Previous attempts to validate these targets via Western blotting were inconclusive. To gain a more comprehensive understanding, we also intend to complete a panel of cell death assessments, including pyroptosis, necroptosis, apoptosis, and ferroptosis. Characterizing the specific forms of cell death induced by each treatment will be crucial for understanding the cellular mechanisms that drive cytokine production and release.

Furthermore, to deepen our understanding of the impact of ICD inducers on cancer cells and the TME, it is crucial to investigate the spatial distribution of tumor-infiltrating immune cells. Although this analysis was initially planned, challenges related to protocol optimization delayed our ability to explore and characterize ICD at the spatial (histological) level during this PhD. We had intended to use the Nanostring GeoMX digital spatial profiler to map cell and protein abundances and their distribution across the tumor tissue. Future investigations in this direction will add another layer of

information to the existing data.
The data gathered from this spatial analysis could also serve as a foundation for constructing and configuring agent-based models of ICD. While this approach extends beyond the scope of this thesis, it is increasingly relevant as we enter an era of spatially resolved molecular biology. Beyond generating new insights into the spatial properties of biological systems, simulation tools that incorporate spatial dimensions offer a valuable complement to experimental activities, enhancing our ability to model complex biological processes.

Although the experimental work did not fully uncover the details regulating the processes that may influence the immunogenicity of ICD-inducing treatments, the functional enrichment analysis performed on the collected data provided valuable insights into the pathways activated following treatment administration. The abundance of expression data has spurred the development of new computational tools designed to elucidate biological processes indirectly. Notably, analyses using decoupleR and pathway activity estimation through the manually curated dataset, Progeny, allowed us to identify potential contributions from the NFkB, MAPK, TRAIL, and EGFR pathways in response to ICD-inducing treatments like MTX.
While these findings have been further supported by indirect analyses, such as the estimation of TF activity, targeted experimental validations are necessary to confirm these results. This is particularly important given that the manually curated dataset used is limited to a restricted number of pathways.
The estimation of TF activity also provided a comprehensive overview of the downstream effects of different treatments, revealing the specific transcriptional programs they induce. This information proved crucial for identifying some regulators of the cytokines secreted by MCA205 cells following treatment administration. Among the 50 most variable TF activities, 16 are known regulators of the cytokines identified earlier to be associated with (lack of) immunogenicity. This observation was further strengthened by additional analyses, including the estimation of similarity between transcriptional trajectories over time using a dynamic time-warping algorithm.
Building on observations obtained directly from experiments and indirectly through functional enrichment analysis, we sought to integrate the gathered information into a comprehensive model that recapitulates our current understanding of ICD.
The initial effort in constructing a model focused on the intercellular communication between cancer cells and immune cells following the induction of ICD, leading to the development of the first in silico model of ICD [29]. However, due to my limited knowledge and time constraints, this project offered a simplified description of the molecular mechanisms driving the cancer-immunity cycle triggered by ICD.

In this thesis, we focused on delving deeper into the intracellular processes occurring within cancer cells undergoing ICD. Our goal was to build a core model of ICD that captures the intricate interplay between the various branches of molecular machinery responsible for the manifestation of ICD hallmarks in response to stress or damage.

To achieve this, we adopted a modular approach, developing distinct modules representing different aspects of ICD's classical hallmarks. One module focused on the mechanistic description of CALR translocation from the ER to the cell surface in response to ER stress, while another modeled the release of HMGB1, specifically its translocation from the nucleus to the cytoplasm. Simulations of these modules aligned well with experimental observations and existing mechanistic descriptions. Notably, these modules share several components, facilitating their integration into a future unified model.

Given the extensive literature on the mechanisms of action of the compounds used in this project—primarily the induction of DNA damage, although both MTX and OXA also induce ER stress—we further developed a module to explore the interplay between chemotherapy-induced DNA damage and downstream repair mechanisms. Driven by enthusiasm for research advancements related to these compounds, I took the opportunity to develop a model representing DNA damage induction and the subsequent activation of repair pathways. However, this module and its simulations revealed the need for further refinement. Attempts to validate the model using expression data and automated model personalization techniques were unsuccessful. Much like the myth of Icarus, my expectations were set too high, and the model failed to perform as expected. Fortunately, existing models that describe DNA repair processes for specific types of damage will be insightful for further refining this module.

As a next step in developing a comprehensive representation of the processes triggered by ICD induction, we utilized preliminary phospho-proteomics profiles (data not shown) associated with each treatment. From these profiles, we constructed a network using the top hits and further explored their interactors with the automatic network construction tool, Neko, to which I contributed to its development. Although the resulting network is currently limited by intrinsic biases and the abundance of bimodal interactions within the dataset, it holds the potential for bridging different layers of biological information, such as pathway activity and transcriptional programs. However, it is not yet ready for adaptation into a model.

Additionally, in preparation for integrating this network into the core ICD model, we focused on refining a transcriptional regulation network initially based on the cytokine signature identified as potential novel ICD-related hallmarks. By expanding the list of regulators of each cytokine, we measured the DTW distance to assess the similarity between these TFs and their target cytokines.

This approach allowed us to create networks personalized to each treatment type, which are promising candidates for adaptation into simulation-ready models.

The insights gained from our analytical work have led to the formulation of new hypotheses regarding previously unknown molecular mechanisms in the context of ICD. By measuring secreted molecules at both the proteomic and transcriptomic levels, such as IL6 and CCL5, we were able to infer the activity of the TFs regulating these molecules through indirect analysis. For example, we inferred IRF8 activity in the regulation of *Ccl5*, drawing parallels with similar processes observed in T cells [107]. Through pathway activity estimation using the PROGENy method, we identified pathways likely involved in the regulation of these TFs. Notably, NFkB activity was found to be particularly high in response to MTX and CIS treatments (see 4, section 2.1). However, to fully understand this regulatory loop, we still need to identify the molecular mediators responsible for inducing the stress that activates the NFkB pathway [156]. Given the experimental conditions — specifically, treated cell cultures —several possibilities emerge, including the activation of TLR receptors following the recognition of endogenous HMGB1, as reported in other contexts [176]. Although preliminary, these findings illustrate the potential of a systemic approach that considers all investigated features together, enabling the formulation of new scientific hypotheses for experimental verification. For instance, could blocking TLR receptors on cancer cells inhibit ICD-related cytokine secretion? And how might this impact the shaping of the TME?

This project set out with the ambitious goal of constructing a comprehensive model that captures both the phenomenology and the intricate mechanisms underlying ICD. The complexity inherent to nearly all biological processes is particularly pronounced in the case of ICD, making this endeavor both challenging and fascinating.

As I progressed through this PhD thesis project, each step forward led to the emergence of new questions about the regulation of specific processes and how to infer the full range of mechanistic details from the initiation of ICD to its conclusion. This journey highlighted the profound complexity of biological systems, challenging our ability to fully comprehend natural phenomena in their entirety. While reductionist approaches have been essential in advancing science, the desire to integrate and unify the various components of an interacting system into a cohesive framework remains a compelling and necessary goal.

ICD has been meticulously dissected into its parts by numerous dedicated researchers, each contributing valuable insights to our understanding of this process. This thesis aimed to begin the integration of this collective knowledge into a systemic framework, combining established insights with new findings derived from experiments, computational analyses, and modeling.

Looking ahead, the next objective will be to merge the refined modules into a unified model. It

is important to recognize that capturing every single process that occurs following the induction of ICD is humanly unfeasible, just as it would be for any other complex biological phenomenon. However, integrating these refined modules will bring us closer to a more comprehensive and functional representation of the key processes involved.

Transitioning from a background in physics to both experimental and computational biology was challenging, but it fueled my curiosity and passion, driving the work I have accomplished and motivating the research that lies ahead. Constant exposure to new experimental techniques, insights, and findings has sparked a continual desire to learn more and to better represent the behavior of complex systems. My background in complex systems physics has instilled in me the belief that, through the accurate description of processes at the scale of individual model components, it is possible to observe the emergence of systemic behaviors. This conviction continues to guide and inspire my work in understanding the multifaceted nature of ICD.

List of publications

Published articles

Checcoli A,, Pol JG, Naldi A, Noel V, Barillot E, Kroemer G, Thieffry D, Calzone L, Stoll G.. "*Dynamical Boolean Modeling of Immunogenic Cell Death.* ". Front Physiol. 2020 Nov 12.
DOI: doi: 10.3389/fphys.2020.590479. eCollection 2020

Paillet J, Plantureux C, Lévesque S, Le Naour J, Stoll G, Sauvat A, Caudana P, Tosello Boari J, Bloy N, Lachkar S, Martins I, Opolon P, **Checcoli A**, Delaune A, Robil N, de la Grange P, Hamroune J, Letourneur F, Autret G, Leung PSC, Gershwin ME, Zhu JS, Kurth MJ, Lekbaby B, Augustin J, Kim Y, Gujar S, Coulouarn C, Fouassier L, Zitvogel L, Piaggio E, Housset C, Soussan P, Maiuri MC, Kroemer G, Pol JG.. " *Autoimmunity affecting the biliary tract fuels the immunosurveillance of cholangiocarcinoma.*". J Exp Med. 2021 Oct 4.
DOI: doi: 10.1084/jem.20200853

Pol JG, Lizarralde-Guerrero M, **Checcoli A**, Kroemer G.. "*Targeted opening of the blood-brain barrier facilitates doxorubicin/anti-PD-1-based chemoimmunotherapy of glioblastoma.*". Oncoimmunology. 2024 Jul 27.
DOI: doi: 10.1080/2162402X.2024.2385124

Articles in preparation

- *"Profile of chemokines dictates cell death immunogenicity".*

  Content: The article shows that given their low heterogeneity when it comes to ICD-hallmarks expression, ICD-inducing drugs and non-ICD-inducing drugs may be discriminated also on top of the different secretome profiles they can induce on cancer cells. Using murine fibrosarcoma cell line MCA205, we highlighted through in vitro assays a subset of cytokines and chemokines that possibly affect tumor prognosis in pre-clinical mouse models in both therapeutic and prophylactic regimens. *Status*: The writing process is ongoing and additional experimental validations are to be completed before September. We forecast submission in November 2024.

- *"In silico modeling of cancer cell-centered effects of immunogenic cell death chemoinducers".*

  Content: The article is focused on the construction of a tumor-centered model based on our findings from in vitro assays using MCA205 cell lines. We built a model containing both the post-translational detail of ICD-hallmarks manifestation and provided mechanistic hypotheses about the transcriptional programs that link different DNA damage responses to different secretome profiles (using MTX as positive control of ICD-inducing drug and CIS as a non-ICD inducing drug).

Status: The model is currently under construction. The current version is now under in-house revision. The paper has been outlined and we forecast its submission within January 2025.

- *"Multi-scale Boolean modeling of ICD-mediated cancer immunity cycle: data-driven simulations predict immune infiltration profiles"*

  Content: This article involves the construction of a multi-cellular model based on the data gathered during both in vitro and in vivo experiments. It encompasses different cell types (cancer cells, conventional dendritic cells, T cells, and additional myeloid populations tbd) and provides a characterization of the interactions existing between these cells. Using UpMaBoSS, we simulate the effect of different chemotherapies in recruiting different cell types and how this impacts tumor prognosis.

  Status: Draft ongoing, methods and data already available, submission forecasted by Spring 2025.

- *"Building multi-scale models with PhysiBoSS, an agent-based modeling tool"*

  Content: Multi-scale models facilitate the study of complex biological processes across various spatial and temporal scales, aiming to comprehend disease mechanisms, tissue-immune system interactions, and propose therapeutic strategies. Despite their complexity, simplification through structured descriptions and graphical interfaces is essential for broader accessibility. This tutorial introduces four examples of multi-scale models, leveraging the PhysiBoSS framework—an extension of PhysiCell. It aims to empower users by simplifying model construction with PhysiCell Studio. My contribution in this article was mainly the construction of a model of cell differentiation including two cell types $CD4_+$ T cells differentiating into Th1, Th17 and Treg cells, and DCs. The model shows how mature DCs come in contact with T cell and initiate the differentiation process.

  Status: Under review in "Briefings in Bioinformatics".

Work dissemination

Posters

- PerMedCoE (EMBL-EBI) Summer School, "Modeling of Immunogenic Cell Death", 06/23, Seva (Spain)
- CRC days, "Modeling of Immunogenic Cell Death", 09/22, Centre de Recherche des Cordeliers - Paris (France)
- Inter-LabEx conference, "Modeling of Immunogenic Cell Death", 06/22, Faculty of Medicine - Paris (France)
- Computational Systems Biology of Cancer - Multi-Omics and Machine Learning Approaches, "Modeling of Immunogenic Cell Death", 09/21, Institut Curie - Paris (France)

Talks

- 3rd Interdisciplinary Signaling Workshop, 07/23, "Modeling of Immunogenic Cell Death", Visegrad (Hungary)
- Computational Systems Biology of Cancer - Multimodal Data Integration, 09/22, flash talk on "Modeling of Immunogenic Cell Death", Institut Curie - Paris (France)

Outreach

- Fête de la Science, 10/23, "Catch me if you can": workshop for general audience focused on immuno-oncology, Centre de Recherche des Cordeliers - Paris (France)

Bibliography

[1] John Aach and George M. Church. "Aligning gene expression time series with time warping algorithms". *Bioinformatics* 17.6 (2001), pp. 495–508 (cit. on p. 64).

[2] "Adenosine A2B Receptor Blockade Slows Growth of Bladder and Breast Tumors". *The Journal of Immunology* 188.5 (2011), pp. 198–205 (cit. on p. 18).

[3] Nicole M. Anderson and M. Celeste Simon. "The tumor microenvironment". *Current Biology* 30.16 (2020), R921–R925 (cit. on p. 6).

[4] L. Apetoh, F. Ghiringhelli, A. Tesniere, M. Obeid, C. Ortiz, A. Criollo, et al. "Toll-like receptor 4-dependent contribution of the immune system to anticancer chemotherapy and radiotherapy". *Nature medicine* 13 (2007), pp. 1050–1059 (cit. on pp. 22–24, 30, 32).

[5] Swathi Arur, Uche E. Uche, Karim Rezaul, Michael Fong, Victoria Scranton, Ann E. Cowan, et al. "Annexin I Is an Endogenous Ligand that Mediates Apoptotic Cell Engulfment". *Developmental Cell* 4.4 (2003), pp. 587–598 (cit. on p. 27).

[6] Cecilia Ayala-Zambrano, Mariana Yuste, Sara Frias, Benilde Garcia-de-Teresa, Luis Mendoza, Eugenio Azpeitia, et al. "A Boolean network model of the double-strand break repair pathway choice". *Journal of Theoretical Biology* 573 (2023), p. 111608 (cit. on p. 119).

[7] Ivan Azarov, Kirill Peskov, Gabriel Helmlinger, and Yuri Kosinsky. "Role of T Cell-To-Dendritic Cell Chemoattraction in T Cell Priming Initiation in the Lymph Node: An Agent-Based Modeling Study". *Frontiers in Immunology* 10 (2019), p. 1289 (cit. on p. 126).

[8] Asfar S Azmi, Yiwei Li, Irfana Muqbil, Amro Aboukameel, William Senapedis, Erkan Baloglu, et al. "Exportin 1 (XPO1) inhibition leads to restoration of tumor suppressor miR-145 and consequent suppression of pancreatic cancer cell proliferation and migration". *Oncotarget* 8.47 (2017), pp. 82144–82155 (cit. on p. 110).

[9] Asfar S. Azmi, Mohammed H. Uddin, and Ramzi M. Mohammad. "The nuclear export protein XPO1 — from biology to targeted therapy". *Nature Reviews Clinical Oncology* 18.3 (2021), pp. 152–169 (cit. on p. 110).

[10] Pau Badia-i-Mompel, Jesús Vélez Santiago, Jana Braunger, Celina Geiss, Daniel Dimitrov, Sophia Müller-Dott, et al. "decoupleR: ensemble of computational methods to infer biological activities from omics data". *Bioinformatics Advances* 2.1 (2022). Ed. by Marieke Lydia Kuijjer, vbac016 (cit. on pp. 63, 66, 95, 97–99).

[11] Elisa Elena Baracco, Gautier Stoll, Peter Van Endert, Laurence Zitvogel, Erika Vacchelli, and Guido Kroemer. "Contribution of annexin A1 to anticancer immunosurveillance". *OncoImmunology* 8.11 (2019), e1647760 (cit. on pp. 15, 27).

[12] Anja Basters, Klaus-Peter Knobeloch, and Günter Fritz. "USP18 – a multifunctional component in the interferon response". *Bioscience Reports* 38.6 (2018), BSR20180250 (cit. on p. 24).

[13] M. Bauzon, P. M. Drake, R. M. Barfield, B. M. Cornali, I. Rupniewski, and D. Rabuka. "Maytansine-bearing antibody- drug conjugates induce in vitro hallmarks of immunogenic cell death selectively in antigen-positive target cells". *Oncoimmunology* 8 (2019) (cit. on p. 32).

[14] Jonas Béal, Arnau Montagud, Pauline Traynard, Emmanuel Barillot, and Laurence Calzone. "Personalization of Logical Models With Multi-Omics Data Allows Clinical Stratification of Patients". *Frontiers in Physiology* 9 (2019), p. 1965 (cit. on pp. 68, 115).

[15] Christoph Bergmann, Hagen S Bachmann, Agnes Bankfalvi, Ramin Lotfi, Carolin Pütter, Clarissa A Wild, et al. "Toll-like receptor 4 single-nucleotide polymorphisms Asp299Gly and Thr399Ile in head and neck squamous cell carcinomas". *Journal of Translational Medicine* 9.1 (2011), p. 139 (cit. on p. 23).

[16] Pedro Berraondo, Miguel F. Sanmamed, María C Ochoa, Iñaki Etxeberria, Maria A. Aznar, José Luis Pérez-Gracia, et al. "Cytokines in clinical cancer immunotherapy". *British Journal of Cancer* 120.1 (2019), pp. 6–15 (cit. on p. 29).

[17] L. Bezu, A. Sauvat, J. Humeau, M. Leduc, O. Kepp, and G. Kroemer. “eIF2alpha phosphorylation: A hallmark of immunogenic cell death”. *Oncoimmunology* 7 (2018) (cit. on p. 16).

[18] Lucillia Bezu, Allan Sauvat, Juliette Humeau, Lígia C. Gomes-da-Silva, Kristina Iribarren, Sabrina Forveille, et al. “eIF2α phosphorylation is pathognomonic for immunogenic cell death”. *Cell Death & Differentiation* 25.8 (2018), pp. 1375–1393 (cit. on pp. 107, 108).

[19] P Bist, S C Leow, Q H Phua, S Shu, Q Zhuang, W T Loh, et al. “Annexin-1 interacts with NEMO and RIP1 to constitutively activate IKK complex and NF-ϰB: implication in breast cancer metastasis”. *Oncogene* 30.28 (2011), pp. 3174–3185 (cit. on p. 27).

[20] Philipp Blüm and Sabine Kayser. “Chimeric Antigen Receptor (CAR) T-Cell Therapy in Hematologic Malignancies: Clinical Implications and Limitations”. *Cancers* 16.8 (2024), p. 1599 (cit. on p. 30).

[21] P. K. Bommareddy, A. Zloza, S. D. Rabkin, and H. L. Kaufman. “Oncolytic virus immunotherapy induces immunogenic cell death and overcomes STING deficiency in melanoma”. *Oncoimmunology* 8 (2019) (cit. on pp. 31, 33).

[22] Cinda M Boyer, Deborah V Dawson, Sharon E Neal, Lisa F Winchell, David S Leslie, David Ring, et al. “Differential Induction by Interferons of Major Histocompatibility Complex-encoded and Non-Major Histocompatibility Complex-encoded Antigens in Human Breast and Ovarian Carcinoma Cell Lines” () (cit. on p. 24).

[23] Peter M Bruno, Yunpeng Liu, Ga Young Park, Junko Murai, Catherine E Koch, Timothy J Eisen, et al. “A subset of platinum-containing chemotherapeutic agents kills cells by inducing ribosome biogenesis stress”. *Nature Medicine* 23.4 (2017), pp. 461–471 (cit. on pp. 34, 35).

[24] Sabrina Brzostek-Racine, Chris Gordon, Sarah Van Scoy, and Nancy C. Reich. “The DNA Damage Response Induces IFN”. *The Journal of Immunology* 187.10 (2011), pp. 5336–5345 (cit. on p. 9).

[25] Hélène Bugaut, Mélanie Bruchard, Hélène Berger, Valentin Derangère, Ludivine Odoul, Romain Euvrard, et al. “Bleomycin Exerts Ambivalent Antitumor Immune Effect by Triggering Both Immunogenic Cell Death and Proliferation of Regulatory T Cells”. *PLoS ONE* 8.6 (2013). Ed. by John W. Glod, e65181 (cit. on pp. 30, 32).

[26] K. A. Camilio, O. Rekdal, and B. Sveinbjornsson. “LTX-315 (Oncopore): A short synthetic anticancer peptide and novel immunotherapeutic agent”. *Oncoimmunology* 3 (2014), e29181 (cit. on p. 32).

[27] Noelia Casares, Marie O. Pequignot, Antoine Tesniere, François Ghiringhelli, Stéphan Roux, Nathalie Chaput, et al. “Caspase-dependent immunogenicity of doxorubicin-induced tumor cell death”. *The Journal of Experimental Medicine* 202.12 (2005), pp. 1691–1701 (cit. on pp. 15, 30).

[28] C. L. Chang, Y. T. Hsu, C. C. Wu, Y. C. Yang, C. Wang, T. C. Wu, et al. “Immune mechanism of the antitumor effects generated by bortezomib”. *Journal of immunology* 189 (2012), pp. 3209–3220 (cit. on p. 30).

[29] Andrea Checcoli, Jonathan G. Pol, Aurelien Naldi, Vincent Noel, Emmanuel Barillot, Guido Kroemer, et al. “Dynamical Boolean Modeling of Immunogenic Cell Death”. *Frontiers in Physiology* 11 (2020), p. 590479 (cit. on pp. 52, 54, 105, 129, 130, 137).

[30] H. M. Chen, P. H. Wang, S. S. Chen, C. C. Wen, Y. H. Chen, W. C. Yang, et al. “Shikonin induces immunogenic cell death in tumor cells and enhances dendritic cell-based cancer vaccine”. *Cancer immunology, immunotherapy* CII.61 (2012), pp. 1989–2002 (cit. on pp. 30, 32).

[31] Ruochan Chen, Rui Kang, and Daolin Tang. “The mechanism of HMGB1 secretion and release”. *Experimental & Molecular Medicine* 54.2 (2022), pp. 91–102 (cit. on p. 110).

[32] Shuonan Chen and Jessica C. Mar. “Evaluating methods of inferring gene regulatory networks highlights their lack of performance for single cell gene expression data”. *BMC Bioinformatics* 19.1 (2018), p. 232 (cit. on p. 100).

[33] Yixiong Chen, Lufang Wang, Na Chen, and Guiju Tang. “Metformin induces tumor immunogenic cell death in ovarian cancer by activating AMPK pathway”. *Translational Oncology* 47 (2024), p. 102052 (cit. on p. 33).

[34] HyeonJoo Cheon, Ernest C. Borden, and George R. Stark. “Interferons and Their Stimulated Genes in the Tumor Microenvironment”. *Seminars in Oncology* 41.2 (2014), pp. 156–173 (cit. on p. 27).

[35] HyeonJoo Cheon, Elise G. Holvey-Bates, Daniel J. McGrail, and George R. Stark. “PD-L1 sustains chronic, cancer cell–intrinsic responses to type I interferon, enhancing resistance to DNA damage”. *Proceedings of the National Academy of Sciences* 118.47 (2021), e2112258118 (cit. on pp. 26, 27).

[36] HyeonJoo Cheon, Yuxin Wang, Samantha M. Wightman, Mark W. Jackson, and George R. Stark. “How cancer cells make and respond to interferon-I”. *Trends in Cancer* 9.1 (2023), pp. 83–92 (cit. on p. 24).

[37] M. Cirone, L. Di Renzo, L. V. Lotti, V. Conte, P. Trivedi, R. Santarelli, et al. “Primary effusion lymphoma cell death induced by bortezomib and AG 490 activates dendritic cells through CD91”. *PloS one* 7 (2012), e31732 (cit. on pp. 30, 32).

[38] Karla Fabiola Corral-Jara, Camille Chauvin, Wassim Abou-Jaoudé, Maximilien Grandclaudon, Aurélien Naldi, Vassili Soumelis, et al. “Interplay between SMAD2 and STAT5A is a critical determinant of IL-17A/IL-17F differential expression”. *Molecular Biomedicine* 2.1 (2021), p. 9 (cit. on p. 125).

[39] Cameron Davidson-Pilon. “lifelines: survival analysis in Python”. *Journal of Open Source Software* 4.40 (2019), p. 1317 (cit. on p. 60).

[40] Álvaro De Mingo Pulido, Kay Hänggi, Daiana P. Celias, Alycia Gardner, Jie Li, Bruna Batista-Bittencourt, et al. “The inhibitory receptor TIM-3 limits activation of the cGAS-STING pathway in intra-tumoral dendritic cells by suppressing extracellular DNA uptake”. *Immunity* 54.6 (2021), 1154–1167.e7 (cit. on p. 22).

[41] S. Demaria, F. R. Santori, B. Ng, L. Liebes, S. C. Formenti, and S. Vukmanovic. “Select forms of tumor cell apoptosis induce dendritic cell maturation”. *Journal of leukocyte biology* 77 (2005), pp. 361–368 (cit. on p. 30).

[42] E W Dijkstra. “A note on two problems in connexion with graphs” () (cit. on p. 68).

[43] Jennifer H. Dufour, Michelle Dziejman, Michael T. Liu, Josephine H. Leung, Thomas E. Lane, and Andrew D. Luster. “IFN-γ-Inducible Protein 10 (IP-10; CXCL10)-Deficient Mice Reveal a Role for IP-10 in Effector T Cell Generation and Trafficking1”. *The Journal of Immunology* 168.7 (2002), pp. 3195–3204 (cit. on p. 24).

[44] Linde Duprez, Nozomi Takahashi, Filip Van Hauwermeiren, Benjamin Vandendriessche, Vera Goossens, Tom Vanden Berghe, et al. “RIP Kinase-Dependent Necrosis Drives Lethal Systemic Inflammatory Response Syndrome”. *Immunity* 35.6 (2011), pp. 908–918 (cit. on p. 22).

[45] L. M. Eike, B. Mauseth, K. A. Camilio, O. Rekdal, and B. Sveinbjornsson. “The Cytolytic Amphipathic beta(2,2)-Amino Acid LTX-401 Induces DAMP Release in Melanoma Cells and Causes Complete Regression of B16 Melanoma”. *PloS one* 11 (2016) (cit. on p. 32).

[46] L. M. Eike, N. Yang, O. Rekdal, and B. Sveinbjornsson. “The oncolytic peptide LTX-315 induces cell death and DAMP release by mitochondria distortion in human melanoma cells”. *Oncotarget* 6 (2015), pp. 34910–34923 (cit. on p. 32).

[47] European Commission Joint Research Centre. *European Cancer Information System (ECIS)*. 2024 (cit. on p. 3).

[48] Benny J. Evison, Brad E. Sleebs, Keith G. Watson, Don R. Phillips, and Suzanne M. Cutts. “Mitoxantrone, More than Just Another Topoisomerase II Poison”. *Medicinal Research Reviews* 36.2 (2016), pp. 248–299 (cit. on p. 112).

[49] Marta Falcinelli, Premal H. Thaker, Susan K. Lutgendorf, Suzanne D. Conzen, Renée L. Flaherty, and Melanie S. Flint. “The Role of Psychologic Stress in Cancer Initiation: Clinical Relevance and Potential Molecular Mechanisms”. *Cancer Research* 81.20 (2021), pp. 5131–5140 (cit. on p. 9).

[50] Hanne Falk, Patrick F. Forde, Marie Lund Bay, Uma Maheswari Mangalanathan, Pernille Hojman, Declan M. Soden, et al. “Calcium electroporation induces tumor eradication, long-lasting immunity and cytokine responses in the CT26 colon cancer mouse model”. *OncoImmunology* 6.5 (2017), e1301332 (cit. on p. 21).

[51] Dean A. Fennell, Sean Dulloo, and James Harber. “Immunotherapy approaches for malignant pleural mesothelioma”. *Nature Reviews Clinical Oncology* 19.9 (2022), pp. 573–584 (cit. on p. 29).

[52] Jacques Ferlay, Mathilde Ervik, Florence Lam, Mathieu Laversanne, Mathieu Colombet, Laure Mery, et al. *Global Cancer Observatory: Cancer Today (version 1.1)*. Lyon, France: International Agency for Research on Cancer, 2024 (cit. on p. 3).

[53] S Ferrari, L Ronfani, S Calogero, and M.E. Bianchi. “The mouse gene coding for high mobility group 1 protein (HMG1).” *Journal of Biological Chemistry* 269.46 (1994), pp. 28803–28808 (cit. on p. 20).

[54] J. Fucikova, I. Moserova, I. Truxova, I. Hermanova, I. Vancurova, S. Partlova, et al. “High hydrostatic pressure induces immunogenic cell death in human tumor cells”. *International journal of cancer* 135 (2014), pp. 1165–1177 (cit. on p. 30).

[55] Lorenzo Galluzzi, Ilio Vitale, Sarah Warren, Sandy Adjemian, Patrizia Agostinis, Aitziber Buqué Martinez, et al. “Consensus guidelines for the definition, detection and interpretation of immunogenic cell death”. *Journal for ImmunoTherapy of Cancer* 8.1 (2020), e000337 (cit. on p. 15).

[56] Hongwei Gao and Richard C. Schwartz. “C/EBPζ (CHOP/Gadd153) is a negative regulator of LPS-induced IL-6 expression in B cells”. *Molecular Immunology* 47.2 (2009), pp. 390–397 (cit. on p. 100).

[57] Abhishek D. Garg, Aleksandra M. Dudek, Gabriela B. Ferreira, Tom Verfaillie, Peter Vandenabeele, Dmitri V. Krysko, et al. “ROS-induced autophagy in cancer cells assists in evasion from determinants of immunogenic cell death”. *Autophagy* 9.9 (2013), pp. 1292–1307 (cit. on p. 20).

[58] Abhishek D. Garg, Aleksandra M. Dudek-Peric, Erminia Romano, and Patrizia Agostinis. “Immunogenic cell death”. *The International Journal of Developmental Biology* 59.1-2-3 (2015), pp. 131–140 (cit. on p. 31).

[59] Abhishek D. Garg, Dmitri V. Krysko, Peter Vandenabeele, and Patrizia Agostinis. “Hypericin-based photodynamic therapy induces surface exposure of damage-associated molecular patterns like HSP70 and calreticulin”. *Cancer Immunology, Immunotherapy* 61.2 (2012), pp. 215–221 (cit. on pp. 15, 30, 33).

[60] G. Garrido, A. Rabasa, B. Sanchez, M. V. Lopez, R. Blanco, A. Lopez, et al. “Induction of immunogenic apoptosis by blockade of epidermal growth factor receptor activation with a specific antibody”. *Journal of immunology* 187 (2011), pp. 4954–4966 (cit. on pp. 30, 32).

[61] Ahmadreza Ghaffarizadeh, Randy Heiland, Samuel H. Friedman, Shannon M. Mumenthaler, and Paul Macklin. “PhysiCell: An open source physics-based cell simulator for 3-D multicellular systems”. *PLOS Computational Biology* 14.2 (2018), pp. 1–31 (cit. on p. 53).

[62] François Ghiringhelli, Lionel Apetoh, Antoine Tesniere, Laetitia Aymeric, Yuting Ma, Carla Ortiz, et al. “Activation of the NLRP3 inflammasome in dendritic cells induces IL-1β–dependent adaptive immunity against tumors”. *Nature Medicine* 15.10 (2009), pp. 1170–1178 (cit. on pp. 30, 32).

[63] Evangelos Giampazolias, Barbara Zunino, Sandeep Dhayade, Florian Bock, Catherine Cloix, Kai Cao, et al. “Mitochondrial permeabilization engages NF-ϰB-dependent anti-tumour activity under caspase deficiency”. *Nature Cell Biology* 19.9 (2017), pp. 1116–1129 (cit. on p. 32).

[64] L. C. Gomes-da-Silva, L. Zhao, L. Bezu, H. Zhou, A. Sauvat, P. Liu, et al. “Photodynamic therapy with redaporfin targets the endoplasmic reticulum and Golgi apparatus”. *The EMBO journal* 37 (2018) (cit. on pp. 30, 33).

[65] Jorge Gómez Tejeda Zañudo, Pingping Mao, Clara Alcon, Kailey Kowalski, Gabriela N. Johnson, Guotai Xu, et al. “Cell Line–Specific Network Models of ER+ Breast Cancer Identify Potential PI3Kα Inhibitor Resistance Mechanisms and Drug Combinations”. *Cancer Research* 81.17 (2021), pp. 4603–4617 (cit. on p. 54).

[66] Tao Gong, Lei Liu, Wei Jiang, and Rongbin Zhou. “DAMP-sensing receptors in sterile inflammation and inflammatory diseases”. *Nature Reviews Immunology* 20.2 (2020), pp. 95–112 (cit. on p. 15).

[67] Melker Göransson, Erik Elias, Anders Ståhlberg, Anita Olofsson, Carola Andersson, and Pierre Åman. “Myxoid liposarcoma FUS-DDIT3 fusion oncogene induces C/EBP β-mediated interleukin 6 expression”. *International Journal of Cancer* 115.4 (2005), pp. 556–560 (cit. on p. 100).

[68] John W Greiner, Patricia Horan Hand, Philip Noguchi, Paul B Fisher, Sidney Pestka, and Jeffrey Schlom. “Enhanced Expression of Surface Tumor-associated Antigens on Human Breast and Colon Tumor Cells after Recombinant Human Leukocyte a-lnterferon Treatment”. 44 (1984) (cit. on p. 24).

[69] Heonjong Han, Hongseok Shim, Donghyun Shin, Jung Eun Shim, Yunhee Ko, Junha Shin, et al. “TRRUST: a reference database of human transcriptional regulatory interactions”. *Scientific Reports* 5.1 (2015), p. 11432 (cit. on pp. 66, 101).

[70] Douglas Hanahan. “Hallmarks of Cancer: New Dimensions”. *Cancer Discovery* 12.1 (2022), pp. 31–46 (cit. on p. 5).

[71] Douglas Hanahan and Robert A Weinberg. “The Hallmarks of Cancer”. *Cell* 100.1 (2000), pp. 57–70 (cit. on p. 5).

[72] Douglas Hanahan and Robert A. Weinberg. “Hallmarks of Cancer: The Next Generation”. *Cell* 144.5 (2011), pp. 646–674 (cit. on p. 5).

[73] Ahmed Abdelmonem Hemedan, Reinhard Schneider, and Marek Ostaszewski. “Applications of Boolean modeling to study the dynamics of a complex disease and therapeutics responses”. *Frontiers in Bioinformatics* 3 (2023), p. 1189723 (cit. on p. 54).

[74] Aya Hirata, Hisayoshi Hashimoto, Chihiro Shibasaki, Kenta Narumi, and Kazunori Aoki. “Intratumoral IFN-α gene delivery reduces tumor-infiltrating regulatory T cells through the downregulation of tumor CCL17 expression”. *Cancer Gene Therapy* 26.9-10 (2019), pp. 334–343 (cit. on p. 25).

[75] William K Holloman. “Unraveling the mechanism of BRCA2 in homologous recombination”. *Nature Structural & Molecular Biology* 18.7 (2011), pp. 748–754 (cit. on p. 113).

[76] D. M. S. Hossain, S. Javaid, M. Cai, C. Zhang, A. Sawant, M. Hinton, et al. “Dinaciclib induces immunogenic cell death and enhances anti-PD1-mediated tumor suppression”. *The Journal of clinical investigation* 128 (2018), pp. 644–654 (cit. on pp. 30, 32).

[77] Eric J. Hsu, Xuezhi Cao, Benjamin Moon, Joonbeom Bae, Zhichen Sun, Zhida Liu, et al. “A cytokine receptor-masked IL2 prodrug selectively activates tumor-infiltrating lymphocytes for potent antitumor therapy”. *Nature Communications* 12.1 (2021), p. 2768 (cit. on p. 29).

[78] Ruixue Huang and Ping-Kun Zhou. “DNA damage repair: historical perspectives, mechanistic pathways and clinical translation for targeted cancer therapy”. *Signal Transduction and Targeted Therapy* 6.1 (2021), p. 254 (cit. on p. 113).

[79] Juliette Humeau. “Inhibition of Transcription by Dactinomycin Reveals a New Characteristic of Immunogenic Cell Stress”. PhD Thesis. 2019 (cit. on p. 33).

[80] Juliette Humeau, Sarah Lévesque, Guido Kroemer, and Jonathan G. Pol. “Gold Standard Assessment of Immunogenic Cell Death in Oncological Mouse Models”. *Cancer Immunosurveillance*. Ed. by Alejandro López-Soto and Alicia R. Folgueras. Vol. 1884. New York, NY: Springer New York, 2019, pp. 297–315 (cit. on p. 30).

[81] Juliette Humeau, Allan Sauvat, Giulia Cerrato, Wei Xie, Friedemann Loos, Francesca Iannantuoni, et al. "Inhibition of transcription by dactinomycin reveals a new characteristic of immunogenic cell stress". *EMBO Molecular Medicine* 12.5 (2020), e11622 (cit. on pp. 28, 35).

[82] Vân Anh Huynh-Thu, Alexandre Irrthum, Louis Wehenkel, and Pierre Geurts. "Inferring Regulatory Networks from Expression Data Using Tree-Based Methods". *PLoS ONE* 5.9 (2010). Ed. by Mark Isalan, e12776 (cit. on pp. 66, 100).

[83] Takashi Inozume. "Adoptive cell transfer therapy for melanoma". *Experimental Dermatology* 32.3 (2023), pp. 250–255 (cit. on p. 29).

[84] E. R. Jamieson and S. J. Lippard. "Structure, Recognition, and Processing of Cisplatin-DNA Adducts". *Chem. Rev.* 99.9 (1999), pp. 2467–2498 (cit. on p. 34).

[85] Suoqin Jin, Christian F. Guerrero-Juarez, Lihua Zhang, Ivan Chang, Raul Ramos, Chen-Hsiang Kuan, et al. "Inference and analysis of cell-cell communication using CellChat". *Nature Communications* 12.1 (2021), p. 1088 (cit. on p. 66).

[86] Douglas B. Johnson, Caroline A. Nebhan, Javid J. Moslehi, and Justin M. Balko. "Immune-checkpoint inhibitors: long-term implications of toxicity". *Nature Reviews Clinical Oncology* 19.4 (2022), pp. 254–267 (cit. on p. 29).

[87] N. G. VAN KAMPEN. "Chapter III - STOCHASTIC PROCESSES". *Stochastic Processes in Physics and Chemistry (Third Edition)*. Ed. by N. G. VAN KAMPEN. Third Edition. North-Holland Personal Library. Amsterdam: Elsevier, 2007, pp. 52–72 (cit. on p. 46).

[88] N. G. VAN KAMPEN. "Chapter IV - MARKOV PROCESSES". *Stochastic Processes in Physics and Chemistry (Third Edition)*. Ed. by N. G. VAN KAMPEN. Third Edition. North-Holland Personal Library. Amsterdam: Elsevier, 2007, pp. 73–95 (cit. on p. 47).

[89] N. G. VAN KAMPEN. "Chapter V - THE MASTER EQUATION". *Stochastic Processes in Physics and Chemistry (Third Edition)*. Ed. by N. G. VAN KAMPEN. Third Edition. North-Holland Personal Library. Amsterdam: Elsevier, 2007, pp. 96–133 (cit. on p. 49).

[90] Oliver Kepp, Laurence Zitvogel, and Guido Kroemer. "Clinical evidence that immunogenic cell death sensitizes to PD-1/PD-L1 blockade". *OncoImmunology* 8.10 (2019), e1637188 (cit. on p. 35).

[91] C. A. Koks, A. D. Garg, M. Ehrhardt, M. Riva, L. Vandenberk, L. Boon, et al. "Newcastle disease virotherapy induces long-term survival and tumor-specific immune memory in orthotopic glioma through the induction of immunogenic cell death". *International journal of cancer* 136 (2015), E313–325 (cit. on pp. 31, 33).

[92] Qian Kong, Yunyao Li, Qixiang Liang, Jianwei Xie, Xinyu Li, and Jianpei Fang. "SIRT6-PARP1 is involved in HMGB1 polyADP-ribosylation and acetylation and promotes chemotherapy-induced autophagy in leukemia". *Cancer Biology & Therapy* 21.4 (2020), pp. 320–331 (cit. on p. 21).

[93] M. Korbelik and G. J. Dougherty. "Photodynamic therapy-mediated immune response against subcutaneous mouse tumors". *Cancer research* 59 (1999), pp. 1941–1946 (cit. on pp. 30, 32).

[94] M. Korbelik, B. Stott, and J. Sun. "Photodynamic therapy-generated vaccines: relevance of tumour cell death expression". *British journal of cancer* 97 (2007), pp. 1381–1387 (cit. on pp. 30, 32).

[95] M. Korbelik, W. Zhang, and S. Merchant. "Involvement of damage-associated molecular patterns in tumor response to photodynamic therapy: surface expression of calreticulin and high-mobility group box-1 release". *Cancer immunology, immunotherapy* CII.60 (2011), pp. 1431–1437 (cit. on pp. 30, 32).

[96] Guido Kroemer, Claudia Galassi, Laurence Zitvogel, and Lorenzo Galluzzi. "Immunogenic cell stress and death". *Nature Immunology* 23.4 (2022), pp. 487–500 (cit. on p. 14).

[97] G. Krosl, M. Korbelik, and G. J. Dougherty. "Induction of immune cell infiltration into murine SCCVII tumour by photofrin-based photodynamic therapy". *British journal of cancer* 71 (1995), pp. 549–555 (cit. on pp. 30, 32).

[98] Joseph B Kruskal, Laurent Beauguitte, and Marion Maisonobe. "Joseph B. Kruskal, Jr., 1956, On the Shortest Spanning Subtree of a Graph and the Traveling Salesman Problem. Version bilingue et commentée" () (cit. on p. 68).

[99] Julie Le Naour, Peng Liu, Liwei Zhao, Sandy Adjemian, Zsofia Sztupinszki, Julien Taieb, et al. "A TLR3 Ligand Reestablishes Chemotherapeutic Responses in the Context of FPR1 Deficiency". *Cancer Discovery* 11.2 (2021), pp. 408–423 (cit. on p. 87).

[100] Weiss Leonard. "Early Concepts of Cancer". *Cancer and Metastasis Reviews* 19.3 (2000), pp. 205–217 (cit. on p. 2).

[101] Katerina I. Leonova, Leonid Brodsky, Brittany Lipchick, Mahadeb Pal, Liliya Novototskaya, Alex A. Chenchik, et al. "p53 cooperates with DNA methylation and a suicidal interferon response to maintain epigenetic silencing of repeats and noncoding RNAs". *Proceedings of the National Academy of Sciences* 110.1 (2013) (cit. on p. 27).

[102] Gaelle Letort, Arnau Montagud, Gautier Stoll, Randy Heiland, Emmanuel Barillot, Paul Macklin, et al. "PhysiBoSS: a multi-scale agent-based modelling framework integrating physical dimension and cell signalling". *Bioinformatics* 35.7 (2019). Ed. by Jonathan Wren, pp. 1188–1196 (cit. on pp. 53, 125).

[103] Sarah Lévesque, Julie Le Naour, Federico Pietrocola, Juliette Paillet, Margerie Kremer, Francesca Castoldi, et al. "A synergistic triad of chemotherapy, immune checkpoint inhibitors, and caloric restriction mimetics eradicates tumors in mice". *OncoImmunology* 8.11 (2019), e1657375 (cit. on p. 83).

[104] Changfeng Li, Ying Zhang, Xing Cheng, Hua Yuan, Shan Zhu, Jiao Liu, et al. "PINK1 and PARK2 Suppress Pancreatic Tumorigenesis through Control of Mitochondrial Iron-Mediated Immunometabolism". *Developmental Cell* 46.4 (2018), 441–455.e8 (cit. on p. 22).

[105] Orsolya Liska, Balázs Bohár, András Hidas, Tamás Korcsmáros, Balázs Papp, Dávid Fazekas, et al. "TFLink: an integrated gateway to access transcription factor–target gene interactions for multiple species". *Database* 2022 (2022), baac083 (cit. on p. 66).

[106] Huayang Liu, Javad Golji, Lauren K. Brodeur, Franklin S. Chung, Julie T. Chen, Rosalie S. deBeaumont, et al. "Tumor-derived IFN triggers chronic pathway agonism and sensitivity to ADAR loss". *Nature Medicine* 25.1 (2019), pp. 95–102 (cit. on p. 24).

[107] Jian Liu and Xin Ma. "Interferon regulatory factor 8 regulates RANTES gene transcription in cooperation with interferon regulatory factor-1, NF-kappaB, and PU.1". *Journal of Biological Chemistry* 281.28 (2006), pp. 19188–19195 (cit. on p. 139).

[108] P. Liu, L. Zhao, J. Pol, S. Levesque, A. Petrazzuolo, C. Pfirschke, et al. "Crizotinib-induced immunogenic cell death in non-small cell lung cancer". *Nature communications* 10 (2019), p. 1486 (cit. on pp. 31, 33).

[109] Peng Liu, Jianzhou Chen, Liwei Zhao, Antoine Hollebecque, Oliver Kepp, Laurence Zitvogel, et al. "PD-1 blockade synergizes with oxaliplatin-based, but not cisplatin-based, chemotherapy of gastric cancer". *OncoImmunology* 11.1 (2022), p. 2093518 (cit. on p. 35).

[110] Kristen M. Livesey, Rui Kang, Philip Vernon, William Buchser, Patricia Loughran, Simon C. Watkins, et al. "p53/HMGB1 Complexes Regulate Autophagy and Apoptosis". *Cancer Research* 72.8 (2012), pp. 1996–2005 (cit. on p. 21).

[111] Prisca Lo Surdo, Marta Iannuccelli, Silvia Contino, Luisa Castagnoli, Luana Licata, Gianni Cesareni, et al. "SIGNOR 3.0, the SIGnaling network open resource 3.0: 2022 update". *Nucleic Acids Research* 51.D1 (2023), pp. D631–D637 (cit. on pp. 67, 110, 113).

[112] Carlos López-Otín, Maria A. Blasco, Linda Partridge, Manuel Serrano, and Guido Kroemer. "The Hallmarks of Aging". *Cell* 153.6 (2013), pp. 1194–1217 (cit. on p. 3).

[113] Fiorenza Lotti, Awad M. Jarrar, Rish K. Pai, Masahiro Hitomi, Justin Lathia, Adam Mace, et al. "Chemotherapy activates cancer-associated fibroblasts to maintain colorectal cancer-initiating cells by IL-17A". *Journal of Experimental Medicine* 210.13 (2013), pp. 2851–2872 (cit. on p. 9).

[114] Ben Lu, Daniel J. Antoine, Kevin Kwan, Peter Lundbäck, Heidi Wähämaa, Hanna Schierbeck, et al. "JAK/STAT1 signaling promotes HMGB1 hyperacetylation and nuclear translocation". *Proceedings of the National Academy of Sciences* 111.8 (2014), pp. 3068–3073 (cit. on pp. 20, 112).

[115] Jing Ma, Mohanraj Ramachandran, Chuan Jin, Clara Quijano-Rubio, Miika Martikainen, Di Yu, et al. "Characterization of virus-mediated immunogenic cancer cell death and the consequences for oncolytic virus-based immunotherapy of cancer". *Cell Death & Disease* 11.1 (2020), p. 48 (cit. on p. 15).

[116] Y. Ma, L. Aymeric, C. Locher, S. R. Mattarollo, N. F. Delahaye, P. Pereira, et al. "Contribution of IL-17-producing gamma delta T cells to the efficacy of anticancer chemotherapy". *The Journal of experimental medicine* 208 (2011), pp. 491–503 (cit. on pp. 30, 32).

[117] Yuting Ma, Sandy Adjemian, Stephen R. Mattarollo, Takahiro Yamazaki, Laetitia Aymeric, Heng Yang, et al. "Anticancer Chemotherapy-Induced Intratumoral Recruitment and Differentiation of Antigen-Presenting Cells". *Immunity* 38.4 (2013), pp. 729–741 (cit. on pp. 32, 83).

[118] Adam A Margolin, Ilya Nemenman, Katia Basso, Chris Wiggins, Gustavo Stolovitzky, Riccardo Dalla Favera, et al. "ARACNE: An Algorithm for the Reconstruction of Gene Regulatory Networks in a Mammalian Cellular Context". *BMC Bioinformatics* 7.S1 (2006), S7 (cit. on p. 100).

[119] Malvina Marku and Vera Pancaldi. "From time-series transcriptomics to gene regulatory networks: A review on inference methods". *PLOS Computational Biology* 19.8 (2023). Ed. by Qing Nie, e1011254 (cit. on p. 40).

[120] I Martins, O Kepp, F Schlemmer, S Adjemian, M Tailler, S Shen, et al. "Restoration of the immunogenicity of cisplatin-induced cancer cell death by endoplasmic reticulum stress". *Oncogene* 30.10 (2011), pp. 1147–1158 (cit. on pp. 31, 35, 73, 112).

[121] Polly Matzinger. "The Danger Model: A Renewed Sense of Self". *Science* 296.5566 (2002), pp. 301–305 (cit. on p. 15).

[122] B. Mauseth, K. A. Camilio, J. Shi, C. L. Hammarstrom, O. Rekdal, B. Sveinbjornsson, et al. “The Novel Oncolytic Compound LTX-401 Induces Antitumor Immune Responses in Experimental Hepatocellular Carcinoma”. *Molecular therapy oncolytics* 14 (2019), pp. 139–148 (cit. on p. 32).

[123] Finlay McNab, Katrin Mayer-Barber, Alan Sher, Andreas Wack, and Anne O’Garra. “Type I interferons in infectious disease”. *Nature Reviews Immunology* 15.2 (2015), pp. 87–103 (cit. on p. 24).

[124] L. Menger, E. Vacchelli, S. Adjemian, I. Martins, Y. Ma, S. Shen, et al. “Cardiac glycosides exert anticancer effects by inducing immunogenic cell death”. *Science translational medicine* 4.143ra (2012), p. 199 (cit. on pp. 31, 33).

[125] Davorka Messmer, Huan Yang, Gloria Telusma, Faye Knoll, Jianhua Li, Bradley Messmer, et al. “High Mobility Group Box Protein 1: An Endogenous Signal for Dendritic Cell Maturation and Th1 Polarization”. *The Journal of Immunology* 173.1 (2004), pp. 307–313 (cit. on p. 22).

[126] Marek Michalak. “Calreticulin: Endoplasmic reticulum Ca $^{2+}$ gatekeeper”. *Journal of Cellular and Molecular Medicine* 28.5 (2024), e17839 (cit. on p. 15).

[127] Mickaël Michaud, Isabelle Martins, Abdul Qader Sukkurwala, Sandy Adjemian, Yuting Ma, Patrizia Pellegatti, et al. “Autophagy-Dependent Anticancer Immune Responses Induced by Chemotherapeutic Agents in Mice”. *Science* 334.6062 (2011), pp. 1573–1577 (cit. on pp. 20, 32).

[128] H.J. Min, J-H Kim, J.E. Yoo, J-H Oh, K.S. Kim, J-H Yoon, et al. “ROS-dependent HMGB1 secretion upregulates IL-8 in upper airway epithelial cells under hypoxic condition”. *Mucosal Immunology* 10.3 (2017), pp. 685–694 (cit. on p. 21).

[129] Arnau Montagud, Jonas Béal, Luis Tobalina, Pauline Traynard, Vigneshwari Subramanian, Bence Szalai, et al. “Patient-specific Boolean models of signalling networks guide personalised treatments”. *eLife* 11 (2022), e72626 (cit. on p. 54).

[130] Sophia Müller-Dott, Eirini Tsirvouli, Miguel Vazquez, Ricardo O Ramirez Flores, Pau Badia-i-Mompel, Robin Fallegger, et al. “Expanding the coverage of regulons from high-confidence prior knowledge for accurate estimation of transcription factor activities”. *Nucleic Acids Research* 51.20 (2023), pp. 10934–10949 (cit. on pp. 64, 98).

[131] Hung Nguyen, Duc Tran, Bang Tran, Bahadir Pehlivan, and Tin Nguyen. “A comprehensive survey of regulatory network inference methods using single cell RNA sequencing data”. *Briefings in Bioinformatics* 22.3 (2021), bbaa190 (cit. on pp. 40, 100).

[132] Floriane Noël, Lucile Massenet-Regad, Irit Carmi-Levy, Antonio Cappuccio, Maximilien Grandclaudon, Coline Trichot, et al. “Dissection of intercellular communication using the transcriptome-based framework ICELLNET”. *Nature Communications* 12.1 (2021), p. 1089 (cit. on p. 66).

[133] R. Nuccitelli, J. C. Berridge, Z. Mallon, M. Kreis, B. Athos, and P. Nuccitelli. “Nanoelectroablation of Murine Tumors Triggers a CD8-Dependent Inhibition of Secondary Tumor Growth”. *PloS one* 10 (2015) (cit. on pp. 30, 33).

[134] R. Nuccitelli, A. McDaniel, S. Anand, J. Cha, Z. Mallon, J. C. Berridge, et al. “Nano-Pulse Stimulation is a physical modality that can trigger immunogenic tumor cell death”. *Journal for immunotherapy of cancer* 5 (2017), p. 32 (cit. on pp. 30, 33).

[135] M Obeid, T Panaretakis, N Joza, R Tufi, A Tesniere, P van Endert, et al. “Calreticulin exposure is required for the immunogenicity of c-irradiation and UVC light-induced apoptosis”. *2007* 14 (2007), pp. 1848–1850 (cit. on p. 30).

[136] Michel Obeid, Antoine Tesniere, François Ghiringhelli, Gian Maria Fimia, Lionel Apetoh, Jean-Luc Perfettini, et al. “Calreticulin exposure dictates the immunogenicity of cancer cell death”. *Nature Medicine* 13.1 (2007), pp. 54–61 (cit. on pp. 15, 30–33).

[137] Young Joo Oh, Ju Ho Youn, Yeounjung Ji, Sang Eun Lee, Kook Jin Lim, Ji Eun Choi, et al. “HMGB1 Is Phosphorylated by Classical Protein Kinase C and Is Secreted by a Calcium-Dependent Mechanism”. *The Journal of Immunology* 182.9 (2009), pp. 5800–5809 (cit. on p. 20).

[138] Theocharis Panaretakis, Oliver Kepp, Ulf Brockmeier, Antoine Tesniere, Ann-Charlotte Bjorklund, Daniel C Chapman, et al. “Mechanisms of pre-apoptotic calreticulin exposure in immunogenic cell death”. *The EMBO Journal* 28.5 (2009), pp. 578–590 (cit. on pp. 30, 32, 33, 107).

[139] So-Jin Park, Wenda Ye, Roy Xiao, Christopher Silvin, Michelle Padget, James W. Hodge, et al. “Cisplatin and oxaliplatin induce similar immunogenic changes in preclinical models of head and neck cancer”. *Oral Oncology* 95 (2019), pp. 127–135 (cit. on p. 35).

[140] Christopher Paustian, Patricia Taylor, Terrence Johnson, Min Xu, Nancy Ramirez, Kenneth S. Rosenthal, et al. “Extracellular ATP and Toll-Like Receptor 2 Agonists Trigger in Human Monocytes an Activation Program That Favors T Helper 17”. *PLoS ONE* 8.1 (2013). Ed. by Georg Häcker, e54804 (cit. on p. 18).

[141] Mauro Perretti and Fulvio D'Acquisto. "Annexin A1 and glucocorticoids as effectors of the resolution of inflammation". *Nature Reviews Immunology* 9.1 (2009), pp. 62–70 (cit. on p. 27).

[142] Federico Pietrocola, Jonathan Pol, Erika Vacchelli, Shuan Rao, David P. Enot, Elisa E. Baracco, et al. "Caloric Restriction Mimetics Enhance Anticancer Immunosurveillance". *Cancer Cell* 30.1 (2016), pp. 147–160 (cit. on p. 32).

[143] Miguel Ponce-de-Leon, Arnau Montagud, Vincent Noël, Annika Meert, Gerard Pradas, Emmanuel Barillot, et al. "PhysiBoSS 2.0: a sustainable integration of stochastic Boolean and agent-based modelling frameworks". *npj Systems Biology and Applications* 9.1 (2023), p. 54 (cit. on p. 125).

[144] C. Pozzi, A. Cuomo, I. Spadoni, E. Magni, A. Silvola, A. Conte, et al. "The EGFR-specific antibody cetuximab combined with chemotherapy triggers immunogenic cell death". *Nature medicine* 22 (2016), pp. 624–631 (cit. on pp. 30, 32).

[145] Ian A. Riddell. "Cisplatin and Oxaliplatin: Our Current Understanding of Their Actions". *Met Ions Life Sci* 18 (2018), /books/9783110470734/9783110470734–007/9783110470734–007.xml (cit. on p. 34).

[146] C. Riganti, M. F. Lingua, I. C. Salaroglio, C. Falcomata, L. Righi, D. Morena, et al. "Bromodomain inhibition exerts its therapeutic potential in malignant pleural mesothelioma by promoting immunogenic cell death and changing the tumor immune-environment". *Oncoimmunology* 7 (2018) (cit. on pp. 30, 32).

[147] Mark D. Robinson, Davis J. McCarthy, and Gordon K. Smyth. "edgeR : a Bioconductor package for differential expression analysis of digital gene expression data". *Bioinformatics* 26.1 (2010), pp. 139–140 (cit. on pp. 60, 62).

[148] Anna Sandström Gerdtsson, Mattis Knulst, Johan Botling, Artur Mezheyeuski, Patrick Micke, and Sara Ek. "Phenotypic characterization of spatial immune infiltration niches in non-small cell lung cancer". *OncoImmunology* 12.1 (2023), p. 2206725 (cit. on p. 6).

[149] Clarissa S Santoso, Zhaorong Li, Sneha Lal, Samson Yuan, Kok Ann Gan, Luis M Agosto, et al. "Comprehensive mapping of the human cytokine gene regulatory network". *Nucleic Acids Research* 48.21 (2020), pp. 12055–12073 (cit. on pp. 66, 101).

[150] G. Schiavoni, A. Sistigu, M. Valentini, F. Mattei, P. Sestili, F. Spadaro, et al. "Cyclophosphamide synergizes with type I interferons through systemic dendritic cell reactivation and induction of immunogenic tumor apoptosis". *Cancer research* 71 (2011), pp. 768–778 (cit. on pp. 30, 32, 33).

[151] M. Schiraldi, A. Raucci, L. M. Munoz, E. Livoti, B. Celona, E. Venereau, et al. "HMGB1 promotes recruitment of inflammatory cells to damaged tissues by forming a complex with CXCL12 and signaling via CXCR4". *The Journal of experimental medicine* 209 (2012), pp. 551–563 (cit. on p. 22).

[152] William M. Schneider, Meike Dittmann Chevillotte, and Charles M. Rice. "Interferon-Stimulated Genes: A Complex Web of Host Defenses". *Annual Review of Immunology* 32.1 (2014), pp. 513–545 (cit. on p. 24).

[153] Michael Schubert, Bertram Klinger, Martina Klünemann, Anja Sieber, Florian Uhlitz, Sascha Sauer, et al. "Perturbation-response genes reveal signaling footprints in cancer gene expression". *Nature Communications* 9.1 (2018), p. 20 (cit. on p. 64).

[154] Ronald H. Schwartz. "T Cell Anergy". *Annual Review of Immunology* 21.1 (2003), pp. 305–334 (cit. on p. 15).

[155] Vijay Shankaran, Hiroaki Ikeda, Allen T Bruce, J Michael White, Paul E Swanson, Lloyd J Old, et al. "IFNg and lymphocytes prevent primary tumour development and shape tumour immunogenicity". 410 (2001) (cit. on p. 11).

[156] Bhesh Raj Sharma and Thirumala-Devi Kanneganti. "NLRP3 inflammasome in cancer and metabolic diseases". *Nature Immunology* 22.5 (2021), pp. 550–559 (cit. on p. 139).

[157] A. Sistigu, T. Yamazaki, E. Vacchelli, K. Chaba, D. P. Enot, J. Adam, et al. "Cancer cell-autonomous contribution of type I interferon signaling to the efficacy of chemotherapy". *Nature medicine* 20 (2014), pp. 1301–1309 (cit. on pp. 27, 76, 133).

[158] Jana Slyskova, Alba Muniesa-Vargas, Israel Tojal da Silva, Rodrigo Drummond, Jiyeong Park, David Häckes, et al. "Detection of oxaliplatin- and cisplatin-DNA lesions requires different global genome repair mechanisms that affect their clinical efficacy". *NAR Cancer* 5.4 (2023), zcad057 (cit. on pp. 112, 115, 118, 119).

[159] Lin Song, Hui Li, Ran-Ran Ma, Sen Liu, Guo-Hao Zhang, Xiang-Yu Guo, et al. "E2F1-initiated transcription of PRSS22 promotes breast cancer metastasis by cleaving ANXA1 and activating FPR2/ERK signaling pathway". *Cell Death & Disease* 13.11 (2022), p. 982 (cit. on pp. 28, 87).

[160] Radek Spisek, Anna Charalambous, Amitabha Mazumder, David H. Vesole, Sundar Jagannath, and Madhav V. Dhodapkar. "Bortezomib enhances dendritic cell (DC)–mediated induction of immunity to human myeloma via exposure of cell surface heat shock protein 90 on dying tumor cells: therapeutic implications". *Blood* 109.11 (2007), pp. 4839–4845 (cit. on p. 30).

[161] J Stagg and M J Smyth. "Extracellular adenosine triphosphate and adenosine in cancer". *Oncogene* 29.39 (2010), pp. 5346–5358 (cit. on pp. 17, 18).

[162] Julian Stingele, Roberto Bellelli, and Simon J. Boulton. "Mechanisms of DNA–protein crosslink repair". *Nature Reviews Molecular Cell Biology* 18.9 (2017), pp. 563–573 (cit. on p. 113).

[163] Gautier Stoll, Barthélémy Caron, Eric Viara, Aurélien Dugourd, Andrei Zinovyev, Aurélien Naldi, et al. "MaBoSS 2.0: an environment for stochastic Boolean modeling". *Bioinformatics* 33.14 (2017). Ed. by Jonathan Wren, pp. 2226–2228 (cit. on p. 46).

[164] Gautier Stoll, Aurélien Naldi, Vincent Noël, Eric Viara, Emmanuel Barillot, Guido Kroemer, et al. "UPMaBoSS: A Novel Framework for Dynamic Cell Population Modeling". *Frontiers in Molecular Biosciences* 9 (2022), p. 800152 (cit. on pp. 52, 105).

[165] Gautier Stoll, Eric Viara, Emmanuel Barillot, and Laurence Calzone. "Continuous time boolean modeling for biological signaling: application of Gillespie algorithm". *BMC Systems Biology* 6.1 (2012), p. 116 (cit. on pp. 48, 49, 52).

[166] A Q Sukkurwala, I Martins, Y Wang, F Schlemmer, C Ruckenstuhl, M Durchschlag, et al. "Immunogenic calreticulin exposure occurs through a phylogenetically conserved stress pathway involving the chemokine CXCL8". *Cell Death & Differentiation* 21.1 (2014), pp. 59–68 (cit. on pp. 30, 32).

[167] Chunli Sun, Haiying Wang, Shuang Mao, Ji Liu, Shan Li, and Jufang Wang. "Reactive oxygen species involved in CT26 immunogenic cell death induced by Clostridium difficile toxin B". *Immunology Letters* 164.2 (2015), pp. 65–71 (cit. on pp. 31, 33).

[168] Qian Sun, Zhenya Hong, Cong Zhang, Liangliang Wang, Zhiqiang Han, and Ding Ma. "Immune checkpoint therapy for solid tumours: clinical dilemmas and future trends". *Signal Transduction and Targeted Therapy* 8.1 (2023), p. 320 (cit. on p. 29).

[169] Jeremy B. Swann, Yoshihiro Hayakawa, Nadeen Zerafa, Kathleen C. F. Sheehan, Bernadette Scott, Robert D. Schreiber, et al. "Type I IFN Contributes to NK Cell Homeostasis, Activation, and Antitumor Function". *The Journal of Immunology* 178.12 (2007), pp. 7540–7549 (cit. on p. 24).

[170] Charles Swanton, Elsa Bernard, Chris Abbosh, Fabrice André, Johan Auwerx, Allan Balmain, et al. "Embracing cancer complexity: Hallmarks of systemic disease". *Cell* 187.7 (2024), pp. 1589–1616 (cit. on p. 5).

[171] Daolin Tang, Rui Kang, Tom Vanden Berghe, Peter Vandenabeele, and Guido Kroemer. "The molecular machinery of regulated cell death". *Cell Research* 29.5 (2019), pp. 347–364 (cit. on p. 13).

[172] Daolin Tang, Rui Kang, Kristen M. Livesey, Chun-Wei Cheh, Adam Farkas, Patricia Loughran, et al. "Endogenous HMGB1 regulates autophagy". *Journal of Cell Biology* 190.5 (2010), pp. 881–892 (cit. on p. 21).

[173] Daolin Tang, Rui Kang, Herbert J. Zeh, and Michael T. Lotze. "The multifunctional protein HMGB1: 50 years of discovery". *Nature Reviews Immunology* 23.12 (2023), pp. 824–841 (cit. on p. 23).

[174] Yiting Tang, Xin Zhao, Daniel Antoine, Xianzhong Xiao, Haichao Wang, Ulf Andersson, et al. "Regulation of Posttranslational Modifications of HMGB1 During Immune Responses". *Antioxidants & Redox Signaling* 24.12 (2016), pp. 620–634 (cit. on p. 20).

[175] Kazuki Tatsuno, Takahiro Yamazaki, Douglas Hanlon, Patrick Han, Eve Robinson, Olga Sobolev, et al. "Extracorporeal photochemotherapy induces bona fide immunogenic cell death". *Cell Death & Disease* 10.8 (2019), p. 578 (cit. on pp. 30, 33).

[176] Asger Teo Hansen Selnø, Stephanie Schlichtner, Inna M. Yasinska, Svitlana S. Sakhnevych, Walter Fiedler, Jan Wellbrock, et al. "High Mobility Group Box 1 (HMGB1) Induces Toll-Like Receptor 4-Mediated Production of the Immunosuppressive Protein Galectin-9 in Human Cancer Cells". *Frontiers in Immunology* 12 (2021), p. 675731 (cit. on p. 139).

[177] A Tesniere, F Schlemmer, V Boige, O Kepp, I Martins, F Ghiringhelli, et al. "Immunogenic death of colon cancer cells treated with oxaliplatin". *Oncogene* 29.4 (2010), pp. 482–491 (cit. on pp. 23, 32, 132).

[178] Remy Thomas, Ghaneya Al-Khadairi, Jessica Roelands, Wouter Hendrickx, Said Dermime, Davide Bedognetti, et al. "NY-ESO-1 Based Immunotherapy of Cancer: Current Perspectives". *Frontiers in Immunology* 9 (2018), p. 947 (cit. on p. 11).

[179] Andrés Tittarelli, Fermín E. González, Cristián Pereda, Gabriela Mora, Leonel Muñoz, Carlos Saffie, et al. "Toll-like receptor 4 gene polymorphism influences dendritic cell in vitro function and clinical outcomes in vaccinated melanoma patients". *Cancer Immunology, Immunotherapy* 61.11 (2012), pp. 2067–2077 (cit. on p. 23).

[180] Aviad Tsherniak, Francisca Vazquez, Phil G. Montgomery, Barbara A. Weir, Gregory Kryukov, Glenn S. Cowley, et al. "Defining a Cancer Dependency Map". *Cell* 170.3 (2017), 564–576.e16 (cit. on p. 115).

[181] Dénes Türei, Tamás Korcsmáros, and Julio Saez-Rodriguez. "OmniPath: guidelines and gateway for literature-curated signaling pathway resources". *Nature Methods* 13.12 (2016), pp. 966–967 (cit. on pp. 66, 113).

[182] Erika Vacchelli, Yuting Ma, Elisa E. Baracco, Antonella Sistigu, David P. Enot, Federico Pietrocola, et al. "Chemotherapy-induced antitumor immunity requires formyl peptide receptor 1". *Science* 350.6263 (2015), pp. 972–978 (cit. on pp. 23, 28, 32).

[183] Erika Vacchelli, Antonella Sistigu, Takahiro Yamazaki, Ilio Vitale, Laurence Zitvogel, and Guido Kroemer. "Autocrine signaling of type 1 interferons in successful anticancer chemotherapy" () (cit. on p. 15).

[184] Sophie Viaud, Caroline Flament, Mustapha Zoubir, Patricia Pautier, Axel LeCesne, Vincent Ribrag, et al. "Cyclophosphamide Induces Differentiation of Th17 Cells in Cancer Patients". *Cancer Research* 71.3 (2011), pp. 661–665 (cit. on p. 32).

[185] Pauli Virtanen, Ralf Gommers, Travis E. Oliphant, Matt Haberland, Tyler Reddy, David Cournapeau, et al. "SciPy 1.0: fundamental algorithms for scientific computing in Python". *Nature Methods* 17.3 (2020), pp. 261–272 (cit. on pp. 60, 63).

[186] Amy Y. Wang and Hongtao Liu. "The past, present, and future of CRM1/XPO1 inhibitors". *Stem Cell Investigation* 6 (2019), pp. 6–6 (cit. on pp. 21, 32).

[187] Haichao Wang, Ona Bloom, Minghuang Zhang, Jaideep M. Vishnubhakat, Michael Ombrellino, Jiantu Che, et al. "HMG-1 as a Late Mediator of Endotoxin Lethality in Mice". *Science* 285.5425 (1999), pp. 248–251 (cit. on p. 20).

[188] Zining Wang, Jiemin Chen, Jie Hu, Hongxia Zhang, Feifei Xu, Wenzhuo He, et al. "cGAS/STING axis mediates a topoisomerase II inhibitor–induced tumor immunogenicity". *Journal of Clinical Investigation* 129.11 (2019), pp. 4850–4862 (cit. on p. 30).

[189] Ralph R. Weichselbaum, Hemant Ishwaran, Taewon Yoon, Dimitry S. A. Nuyten, Samuel W. Baker, Nikolai Khodarev, et al. "An interferon-related gene signature for DNA damage resistance is a predictive marker for chemotherapy and radiation for breast cancer". *Proceedings of the National Academy of Sciences* 105.47 (2008), pp. 18490–18495 (cit. on p. 27).

[190] World Health Organization. *Cancer*. 2020 (cit. on p. 2).

[191] Tianzhi Wu, Erqiang Hu, Shuangbin Xu, Meijun Chen, Pingfan Guo, Zehan Dai, et al. "clusterProfiler 4.0: A universal enrichment tool for interpreting omics data". *The Innovation* 2.3 (2021), p. 100141 (cit. on p. 63).

[192] Wei Xie, Sabrina Forveille, Kristina Iribarren, Allan Sauvat, Laura Senovilla, Yan Wang, et al. "Lurbinectedin synergizes with immune checkpoint blockade to generate anticancer immunity". *OncoImmunology* 8.11 (2019), e1656502 (cit. on pp. 30, 32).

[193] Wei Xie, Laura Mondragón, Brynjar Mauseth, Yan Wang, Jonathan Pol, Sarah Lévesque, et al. "Tumor lysis with LTX-401 creates anticancer immunity". *OncoImmunology* 8.7 (2019), e1594555 (cit. on p. 32).

[194] Siqi Xu, Zhenhua Zeng, Ming Zhao, Qiaobing Huang, Youguang Gao, Xingui Dai, et al. "Evidence for SIRT1 Mediated HMGB1 Release From Kidney Cells in the Early Stages of Hemorrhagic Shock". *Frontiers in Physiology* 10 (2019), p. 854 (cit. on pp. 20, 110).

[195] Yoshiyuki Yamamura, Takahiro Tsuchikawa, Kengo Miyauchi, Shintaro Takeuchi, Masataka Wada, Toshihiko Kuwatani, et al. "The key role of calreticulin in immunomodulation induced by chemotherapeutic agents". *International Journal of Clinical Oncology* 20.2 (2015), pp. 386–394 (cit. on pp. 30, 33).

[196] T Yamazaki, J M Pitt, M Vétizou, A Marabelle, C Flores, Ø Rekdal, et al. "The oncolytic peptide LTX-315 overcomes resistance of cancers to immunotherapy with CTLA4 checkpoint blockade". *Cell Death & Differentiation* 23.6 (2016), pp. 1004–1015 (cit. on p. 32).

[197] Yong Yang, Xian-Jing Li, Zhen Chen, Xuan-Xuan Zhu, Jing Wang, Lin-bo Zhang, et al. "Wogonin Induced Calreticulin/Annexin A1 Exposure Dictates the Immunogenicity of Cancer Cells in a PERK/AKT Dependent Manner". *PLoS ONE* 7.12 (2012). Ed. by Marc Tjwa, e50811 (cit. on pp. 30, 32).

[198] Atsushi Yonezawa and Ken-ichi Inui. "Organic cation transporter OCT/SLC22A and H+/organic cation antiporter MATE/SLC47A are key molecules for nephrotoxicity of platinum agents". *Biochemical Pharmacology* 81.5 (2011), pp. 563–568 (cit. on p. 34).

[199] Renren Yu, Bo Zhu, and Degao Chen. "Type I interferon-mediated tumor immunity and its role in immunotherapy". *Cellular and Molecular Life Sciences* 79.3 (2022), p. 191 (cit. on p. 26).

[200] Zhe Yu, Jie Geng, Minghua Zhang, Yong Zhou, Qingyu Fan, and Jingyuan Chen. "Treatment of osteosarcoma with microwave thermal ablation to induce immunogenic cell death". *Oncotarget* 5.15 (2014), pp. 6526–6539 (cit. on pp. 30, 33).

[201] Dmitriy Zamarin, Rikke B. Holmgaard, Sumit K. Subudhi, Joon Seok Park, Mena Mansour, Peter Palese, et al. "Localized Oncolytic Virotherapy Overcomes Systemic Tumor Resistance to Immune Checkpoint Blockade Immunotherapy". *Science Translational Medicine* 6.226 (2014) (cit. on pp. 31, 33).

[202] Qiong Zhang, Wei Liu, Hong-Mei Zhang, Gui-Yan Xie, Ya-Ru Miao, Mengxuan Xia, et al. "hTFtarget: A Comprehensive Database for Regulations of Human Transcription Factors and Their Targets". *Genomics, Proteomics & Bioinformatics* 18.2 (2020), pp. 120–128 (cit. on p. 66).

[203] H Zhou, S Forveille, A Sauvat, T Yamazaki, L Senovilla, Y Ma, et al. "The oncolytic peptide LTX-315 triggers immunogenic cell death". *Cell Death & Disease* 7.3 (2016), e2134–e2134 (cit. on pp. 31, 32).

[204] Heng Zhou, Laura Mondragón, Wei Xie, Brynjar Mauseth, Marion Leduc, Allan Sauvat, et al. "Oncolysis with DTT-205 and DTT-304 generates immunological memory in cured animals". *Cell Death & Disease* 9.11 (2018), p. 1086 (cit. on p. 32).

[205] Yixuan Zhou, Ingmar Niels Bastian, Mark D. Long, Michelle Dow, Weihua Li, Tao Liu, et al. "Activation of NF-ϰB and p300/CBP potentiates cancer chemoimmunotherapy through induction of MHC-I antigen presentation". *Proceedings of the National Academy of Sciences* 118.8 (2021), e2025840118 (cit. on p. 14).

[206] Laurence Zitvogel, Oliver Kepp, Laura Senovilla, Laurie Menger, Nathalie Chaput, and Guido Kroemer. "Immunogenic Tumor Cell Death for Optimal Anticancer Therapy: The Calreticulin Exposure Pathway". *Clinical Cancer Research* 16.12 (2010), pp. 3100–3104 (cit. on p. 107).

Annexes

DNA damage response *.bnd* file

```
Node Treatment {
    logic = (!Treatment);
    rate_up = @logic ? $u_Treatment : 0;
    rate_down = @logic ? 0 : $d_Treatment;
}
Node DSB {
    logic = (Treatment & !DSB_repair);
    rate_up = @logic ? $u_DSB : 0;
    rate_down = @logic ? 0 : $d_DSB;
}
Node SSB {
    logic = (Treatment & !SSB_repair);
    rate_up = @logic ? $u_SSB : 0;
    rate_down = @logic ? 0 : $d_SSB;
}
Node Inter_XLINK {
    logic = (Treatment & !Inter_XLINK_repair);
    rate_up = @logic ? $u_Inter_XLINK : 0;
    rate_down = @logic ? 0 : $d_Inter_XLINK;
}
Node Intra_XLINK {
    logic = (Treatment & !Intra_XLINK_repair);
    rate_up = @logic ? $u_Intra_XLINK : 0;
    rate_down = @logic ? 0 : $d_Intra_XLINK;
}
Node Inter_XLINK_repair {
    logic = (!NHEJ & !GGNER & !TCNER & HR) | (!NHEJ & !GGNER & TCNER) | (!NHEJ &
        GGNER) | (NHEJ);
    rate_up = @logic ? $u_Inter_XLINK_repair : 0;
    rate_down = @logic ? 0 : $d_Inter_XLINK_repair;
}
Node Intra_XLINK_repair {
    logic = (!GGNER & TCNER) | (GGNER);
```

```
    rate_up = @logic ? $u_Intra_XLINK_repair : 0;
    rate_down = @logic ? 0 : $d_Intra_XLINK_repair;
}
Node DSB_repair {
    logic = (!NHEJ & HR) | (NHEJ);
    rate_up = @logic ? $u_DSB_repair : 0;
    rate_down = @logic ? 0 : $d_DSB_repair;
}
Node SSB_repair {
    logic = (BER);
    rate_up = @logic ? $u_SSB_repair : 0;
    rate_down = @logic ? 0 : $d_SSB_repair;
}
Node RPA {
    logic = (Intra_XLINK);
    rate_up = @logic ? $u_RPA : 0;
    rate_down = @logic ? 0 : $d_RPA;
}
Node CSA {
    logic = (Intra_XLINK);
    rate_up = @logic ? $u_CSA : 0;
    rate_down = @logic ? 0 : $d_CSA;
}
Node CSB {
    logic = (Intra_XLINK);
    rate_up = @logic ? $u_CSB : 0;
    rate_down = @logic ? 0 : $d_CSB;
}
Node POLR2A {
    logic = (Intra_XLINK & POLR2A);
    rate_up = @logic ? $u_POLR2A : 0;
    rate_down = @logic ? 0 : $d_POLR2A;
}
Node Comp911 {
    logic = (SSB);
    rate_up = @logic ? $u_Comp911 : 0;
    rate_down = @logic ? 0 : $d_Comp911;
}
Node TOPBP1 {
    logic = (SSB);
    rate_up = @logic ? $u_TOPBP1 : 0;
    rate_down = @logic ? 0 : $d_TOPBP1;
}
Node PARP1 {
    logic = (SSB);
    rate_up = @logic ? $u_PARP1 : 0;
    rate_down = @logic ? 0 : $d_PARP1;
```

```
}
Node gH2AX {
    logic = (DSB);
    rate_up = @logic ? $u_gH2AX : 0;
    rate_down = @logic ? 0 : $d_gH2AX;
}
Node TP53BP1 {
    logic = (DSB);
    rate_up = @logic ? $u_TP53BP1 : 0;
    rate_down = @logic ? 0 : $d_TP53BP1;
}
Node FANCM {
    logic = (Inter_XLINK & FAAP24);
    rate_up = @logic ? $u_FANCM : 0;
    rate_down = @logic ? 0 : $d_FANCM;
}
Node MRE11 {
    logic = (MRE11);
    rate_up = @logic ? $u_MRE11 : 0;
    rate_down = @logic ? 0 : $d_MRE11;
}
Node RAD50 {
    logic = (RAD50);
    rate_up = @logic ? $u_RAD50 : 0;
    rate_down = @logic ? 0 : $d_RAD50;
}
Node NBS1 {
    logic = (NBS1);
    rate_up = @logic ? $u_NBS1 : 0;
    rate_down = @logic ? 0 : $d_NBS1;
}
Node ATM {
    logic = (!gH2AX & !TP53BP1 & !MRE11 & !ATR & XPC) | (!gH2AX & !TP53BP1 & !MRE11 &
        ATR) |
 (!gH2AX & !TP53BP1 & MRE11 & !RAD50 & !ATR & XPC) | (!gH2AX & !TP53BP1 & MRE11 & !
     RAD50 & ATR) |
 (!gH2AX & !TP53BP1 & MRE11 & RAD50 & !NBS1 & !ATR & XPC) |
 (!gH2AX & !TP53BP1 & MRE11 & RAD50 & !NBS1 & ATR) |
 (!gH2AX & !TP53BP1 & MRE11 & RAD50 & NBS1) |
 (!gH2AX & TP53BP1) | (gH2AX);
    rate_up = @logic ? $u_ATM : 0;
    rate_down = @logic ? 0 : $d_ATM;
}
Node ATR {
    logic = (!RPA & !POLR2A & !Comp911 & !TOPBP1 & DDB2) | (!RPA & !POLR2A & !Comp911
        & TOPBP1) | (!RPA & !POLR2A & Comp911) | (!RPA & POLR2A) | (RPA);
    rate_up = @logic ? $u_ATR : 0;
```

```
    rate_down = @logic ? 0 : $d_ATR;
}
Node CHEK1 {
    logic = (!RPA & !Comp911 & !TOPBP1 & ATR) | (!RPA & !Comp911 & TOPBP1) | (!RPA &
        Comp911) | (RPA);
    rate_up = @logic ? $u_CHEK1 : 0;
    rate_down = @logic ? 0 : $d_CHEK1;
}
Node CHEK2 {
    logic = (ATM);
    rate_up = @logic ? $u_CHEK2 : 0;
    rate_down = @logic ? 0 : $d_CHEK2;
}
Node CDC25A {
    logic = (!CHEK2);
    rate_up = @logic ? $u_CDC25A : 0;
    rate_down = @logic ? 0 : $d_CDC25A;
}
Node CDC25C {
    logic = (!CHEK1);
    rate_up = @logic ? $u_CDC25C : 0;
    rate_down = @logic ? 0 : $d_CDC25C;
}
Node TP53 {
    logic = (!ATM & !CHEK2 & !MDM2 & CDK2) | (!ATM & CHEK2 & !MDM2) | (ATM & !MDM2);
    rate_up = @logic ? $u_TP53 : 0;
    rate_down = @logic ? 0 : $d_TP53;
}
Node MDM2 {
    logic = (!ATM & !ATR & TP53);
    rate_up = @logic ? $u_MDM2 : 0;
    rate_down = @logic ? 0 : $d_MDM2;
}
Node CSNK1A {
    logic = (TP53 & !CSNK1A);
    rate_up = @logic ? $u_CSNK1A : 0;
    rate_down = @logic ? 0 : $d_CSNK1A;
}
Node CDKN1B {
    logic = (CDK6 & !CDK2);
    rate_up = @logic ? $u_CDKN1B : 0;
    rate_down = @logic ? 0 : $d_CDKN1B;
}
Node CDK4 {
    logic = (!CSNK1A & CCND1);
    rate_up = @logic ? $u_CDK4 : 0;
    rate_down = @logic ? 0 : $d_CDK4;
```

```
}
Node CDK6 {
    logic = (!CSNK1A);
    rate_up = @logic ? $u_CDK6 : 0;
    rate_down = @logic ? 0 : $d_CDK6;
}
Node CDK1 {
    logic = (CDC25C & !CSNK1A & !WEE1);
    rate_up = @logic ? $u_CDK1 : 0;
    rate_down = @logic ? 0 : $d_CDK1;
}
Node CDK2 {
    logic = (!CDC25A & !WEE1 & CCNE1) | (CDC25A & !WEE1);
    rate_up = @logic ? $u_CDK2 : 0;
    rate_down = @logic ? 0 : $d_CDK2;
}
Node AURKA {
    logic = (TPX2);
    rate_up = @logic ? $u_AURKA : 0;
    rate_down = @logic ? 0 : $d_AURKA;
}
Node TPX2 {
    logic = (AURKA);
    rate_up = @logic ? $u_TPX2 : 0;
    rate_down = @logic ? 0 : $d_TPX2;
}
Node PLK1 {
    logic = (CDK1 & CDK2 & AURKA & CCNA2);
    rate_up = @logic ? $u_PLK1 : 0;
    rate_down = @logic ? 0 : $d_PLK1;
}
Node WEE1 {
    logic = (CHEK1 & !PLK1);
    rate_up = @logic ? $u_WEE1 : 0;
    rate_down = @logic ? 0 : $d_WEE1;
}
Node G1 {
    logic = (CCND1 & !CCNA2);
    rate_up = @logic ? $u_G1 : 0;
    rate_down = @logic ? 0 : $d_G1;
}
Node S {
    logic = (!CCNA2 & CCNE1) | (CCNA2);
    rate_up = @logic ? $u_S : 0;
    rate_down = @logic ? 0 : $d_S;
}
Node G2_M {
```

```
    logic = (CCNB1);
    rate_up = @logic ? $u_G2_M : 0;
    rate_down = @logic ? 0 : $d_G2_M;
}
Node CCND1 {
    logic = (!CCNA2 & !CCNB1 & !CCNE1);
    rate_up = @logic ? $u_CCND1 : 0;
    rate_down = @logic ? 0 : $d_CCND1;
}
Node CCNA2 {
    logic = (CDK2);
    rate_up = @logic ? $u_CCNA2 : 0;
    rate_down = @logic ? 0 : $d_CCNA2;
}
Node CCNB1 {
    logic = (!CDC25A & CDC25C & !CSNK1A & CCNA2) | (CDC25A & !CSNK1A & CCNA2);
    rate_up = @logic ? $u_CCNB1 : 0;
    rate_down = @logic ? 0 : $d_CCNB1;
}
Node CCNE1 {
    logic = (CDK2 & !CCNB1);
    rate_up = @logic ? $u_CCNE1 : 0;
    rate_down = @logic ? 0 : $d_CCNE1;
}
Node XRCC1 {
    logic = (PARP1);
    rate_up = @logic ? $u_XRCC1 : 0;
    rate_down = @logic ? 0 : $d_XRCC1;
}
Node POLB {
    logic = (XRCC1);
    rate_up = @logic ? $u_POLB : 0;
    rate_down = @logic ? 0 : $d_POLB;
}
Node XPC {
    logic = (!ATR & DDB2) | (ATR);
    rate_up = @logic ? $u_XPC : 0;
    rate_down = @logic ? 0 : $d_XPC;
}
Node DDB2 {
    logic = (Inter_XLINK & TP53 & DDB2);
    rate_up = @logic ? $u_DDB2 : 0;
    rate_down = @logic ? 0 : $d_DDB2;
}
Node ERCC6 {
    logic = (ERCC6);
    rate_up = @logic ? $u_ERCC6 : 0;
```

```
    rate_down = @logic ? 0 : $d_ERCC6;
}
Node ERCC5 {
    logic = (ERCC5);
    rate_up = @logic ? $u_ERCC5 : 0;
    rate_down = @logic ? 0 : $d_ERCC5;
}
Node XPA {
    logic = (!ATR & ERCC8) | (ATR);
    rate_up = @logic ? $u_XPA : 0;
    rate_down = @logic ? 0 : $d_XPA;
}
Node ERCC1 {
    logic = (XPA);
    rate_up = @logic ? $u_ERCC1 : 0;
    rate_down = @logic ? 0 : $d_ERCC1;
}
Node ERCC8 {
    logic = (ERCC8);
    rate_up = @logic ? $u_ERCC8 : 0;
    rate_down = @logic ? 0 : $d_ERCC8;
}
Node ERCC4 {
    logic = (!XPA & SLX4) | (XPA);
    rate_up = @logic ? $u_ERCC4 : 0;
    rate_down = @logic ? 0 : $d_ERCC4;
}
Node FANCD2 {
    logic = (!ATM & !ATR & BRCA1) | (!ATM & ATR) | (ATM);
    rate_up = @logic ? $u_FANCD2 : 0;
    rate_down = @logic ? 0 : $d_FANCD2;
}
Node FAN1 {
    logic = (FANCD2);
    rate_up = @logic ? $u_FAN1 : 0;
    rate_down = @logic ? 0 : $d_FAN1;
}
Node MUS81 {
    logic = (!DCLRE1B & RAD54L) | (DCLRE1B);
    rate_up = @logic ? $u_MUS81 : 0;
    rate_down = @logic ? 0 : $d_MUS81;
}
Node FANCI {
    logic = (!ATM & ATR) | (ATM);
    rate_up = @logic ? $u_FANCI : 0;
    rate_down = @logic ? 0 : $d_FANCI;
}
```

```
Node FANCA {
    logic = (!ATM & !ATR & FAAP24) | (!ATM & ATR) | (ATM);
    rate_up = @logic ? $u_FANCA : 0;
    rate_down = @logic ? 0 : $d_FANCA;
}
Node FAAP24 {
    logic = (FAAP24);
    rate_up = @logic ? $u_FAAP24 : 0;
    rate_down = @logic ? 0 : $d_FAAP24;
}
Node SLX4 {
    logic = (!ATM & FANCD2) | (ATM);
    rate_up = @logic ? $u_SLX4 : 0;
    rate_down = @logic ? 0 : $d_SLX4;
}
Node DCLRE1B {
    logic = (DCLRE1B);
    rate_up = @logic ? $u_DCLRE1B : 0;
    rate_down = @logic ? 0 : $d_DCLRE1B;
}
Node DCLRE1A {
    logic = (!ATM & ATR) | (ATM);
    rate_up = @logic ? $u_DCLRE1A : 0;
    rate_down = @logic ? 0 : $d_DCLRE1A;
}
Node RAD54L {
    logic = (RAD54L);
    rate_up = @logic ? $u_RAD54L : 0;
    rate_down = @logic ? 0 : $d_RAD54L;
}
Node BRCA1 {
    logic = (!RAD50 & !ATM & !ATR & !CDK4 & !CDK1 & CDK2) | (!RAD50 & !ATM & !ATR & !
        CDK4 & CDK1) | (!RAD50 & !ATM & ATR & !CDK4) | (!RAD50 & ATM & !CDK4) | (
        RAD50 & !CDK4);
    rate_up = @logic ? $u_BRCA1 : 0;
    rate_down = @logic ? 0 : $d_BRCA1;
}
Node BRCA2 {
    logic = (!ATR & FANCD2) | (ATR);
    rate_up = @logic ? $u_BRCA2 : 0;
    rate_down = @logic ? 0 : $d_BRCA2;
}
Node RAD51 {
    logic = (BRCA2);
    rate_up = @logic ? $u_RAD51 : 0;
    rate_down = @logic ? 0 : $d_RAD51;
}
```

```
356 Node REV3L {
357     logic = (TP53);
358     rate_up = @logic ? $u_REV3L : 0;
359     rate_down = @logic ? 0 : $d_REV3L;
360 }
361 Node MAD2L2 {
362     logic = (MAD2L2);
363     rate_up = @logic ? $u_MAD2L2 : 0;
364     rate_down = @logic ? 0 : $d_MAD2L2;
365 }
366 Node LIG4 {
367     logic = (LIG4);
368     rate_up = @logic ? $u_LIG4 : 0;
369     rate_down = @logic ? 0 : $d_LIG4;
370 }
371 Node LIG3 {
372     logic = (PARP1 & XRCC1);
373     rate_up = @logic ? $u_LIG3 : 0;
374     rate_down = @logic ? 0 : $d_LIG3;
375 }
376 Node XRCC4 {
377     logic = (XRCC4);
378     rate_up = @logic ? $u_XRCC4 : 0;
379     rate_down = @logic ? 0 : $d_XRCC4;
380 }
381 Node NHEJ {
382     logic = (LIG4 & XRCC4);
383     rate_up = @logic ? $u_NHEJ : 0;
384     rate_down = @logic ? 0 : $d_NHEJ;
385 }
386 Node GGNER {
387     logic = (XPC & RAD23B);
388     rate_up = @logic ? $u_GGNER : 0;
389     rate_down = @logic ? 0 : $d_GGNER;
390 }
391 Node TCNER {
392     logic = (CSA & CSB & POLR2A);
393     rate_up = @logic ? $u_TCNER : 0;
394     rate_down = @logic ? 0 : $d_TCNER;
395 }
396 Node BER {
397     logic = (XRCC1 & POLB & LIG3);
398     rate_up = @logic ? $u_BER : 0;
399     rate_down = @logic ? 0 : $d_BER;
400 }
401 Node HR {
402     logic = (BRCA1 & BRCA2 & RAD51);
```

```
    rate_up = @logic ? $u_HR : 0;
    rate_down = @logic ? 0 : $d_HR;
}
Node TL {
    logic = (REV3L & LIG4);
    rate_up = @logic ? $u_TL : 0;
    rate_down = @logic ? 0 : $d_TL;
}
Node FA {
    logic = (ERCC1 & FANCD2 & FAN1 & SLX4);
    rate_up = @logic ? $u_FA : 0;
    rate_down = @logic ? 0 : $d_FA;
}
Node RAD23B {
    logic = (RAD23B);
    rate_up = @logic ? $u_RAD23B : 0;
    rate_down = @logic ? 0 : $d_RAD23B;
}
```

Listing 7.1: Node Definitions

CALR exposure module *.bnd* file

```

Node ICD_inducer {
  logic = !ICD_inducer;
  rate_up = @logic? $u_ICD_inducer : 0.0;
  rate_down = @logic? 0.0 : 1/24;
}

Node ROS {
  logic = (ICD_inducer);
  rate_up = @logic ? $u_ROS : 0;
  rate_down = @logic ? 0 : $d_ROS;
}

Node iNOS {
  logic = (ICD_inducer);
  rate_up = @logic ? $u_iNOS : 0;
  rate_down = @logic ? 0 : $d_iNOS;
}

Node eIF2a {
  logic = (ROS & (PERK | !PP1_GADD34));
  rate_up = @logic ? $u_eIF2a : 0;
  rate_down = @logic ? 0 : $d_eIF2a;
}
```

```
25
26 Node PERK {
27   logic = (ROS);
28   rate_up = @logic ? $u_PERK : 0;
29   rate_down = @logic ? 0 : $d_PERK;
30 }
31
32 Node PP1_GADD34 {
33   logic = (eIF2a);
34   rate_up = @logic ? $u_PP1_GADD34 : 0;
35   rate_down = @logic ? 0 : $d_PP1_GADD34;
36 }
37
38 Node SERCA_Ca2 {
39   logic = (ICD_inducer);
40   rate_up = @logic ? $u_SERCA_Ca2 : 0;
41   rate_down = @logic ? 0 : $d_SERCA_Ca2;
42 }
43
44 Node TRAIL {
45   logic = ICD_inducer & SERCA_Ca2 & PERK;
46   rate_up = @logic ? $u_TRAIL : 0.0;
47   rate_down = @logic ? 0.0 : $d_TRAIL;
48   }
49
50 Node CASP8 {
51   logic = (TRAIL);
52   rate_up = @logic ? $u_CASP8 : 0;
53   rate_down = @logic ? 0 : $d_CASP8;
54 }
55
56 Node BAP31 {
57   logic = (!CASP8);
58   rate_up = @logic ? $u_BAP31 : 0;
59   rate_down = @logic ? 0 : $d_BAP31;
60 }
61
62 Node BAX {
63   logic = (!BAP31 & CASP8);
64   rate_up = @logic ? $u_BAX : 0;
65   rate_down = @logic ? 0 : $d_BAX;
66 }
67
68
69 Node BAK {
70   logic = (!BAP31 & CASP8);
71   rate_up = @logic ? $u_BAK : 0;
```

```
  rate_down = @logic ? 0 : $d_BAK;
}

Node translocation {
  logic = (BAX & BAK & PP1_GADD34);
  rate_up = @logic ? $u_translocation : 0;
  rate_down = @logic ? 0 : $d_translocation;
}

Node actin {
  logic = (translocation);
  rate_up = @logic ? $u_actin : 0;
  rate_down = @logic ? 0 : $d_actin ;
}

Node VAMP1 {
  logic = (translocation & actin);
  rate_up = @logic ? $u_VAMP1 : 0;
  rate_down = @logic ? 0 : $d_VAMP1;
}

Node SNAP23 {
  logic = (VAMP1 & translocation);
  rate_up = @logic ? $u_SNAP23 : 0;
  rate_down = @logic ? 0 : $d_SNAP23;
}

Node ERp57_CRT {
  logic = (SNAP23);
  rate_up = @logic ? $u_ERp57_CRT : 0;
  rate_down = @logic ? 0 : $d_ERp57_CRT;
}
```

Listing 7.2: Node Definitions

HMGB1 release module *.bnd* file

```

Node ICD_inducer {
  logic = !ICD_inducer;
  rate_up = @logic? $u_ICD_inducer : 0.0;
  rate_down = @logic? 0.0 : 1/24;
}

Node NLS1 {
    logic = (PKC & !SIRT1);
  rate_up = @logic? $u_NLS1 : 0.0;
```

```
  rate_down = @logic? 0.0 : $d_NLS1 ;
}

Node HMGB1 {
    logic = (!NLS2 & !NLS1 & !HMOX1);
  rate_up = @logic? $u_HMGB1 : 0.0;
  rate_down = @logic? 0.0 : $d_HMGB1 ;
}

Node SIRT1 {
    logic = XPO1;
  rate_up = @logic? $u_SIRT1 : 0.0;
  rate_down = @logic? 0.0 : $d_SIRT1 ;
}

Node NLS2 {
    logic = (PKC & !SIRT1);
  rate_up = @logic? $u_NLS2 : 0.0;
  rate_down = @logic? 0.0 : $d_NLS2 ;
}

Node PKC {
    logic = PKC | ROS ;
  rate_up = @logic? $u_PKC : 0.0;
  rate_down = @logic? 0.0 : $d_PKC ;
}

Node Parp1 {
    logic = Chk1 | ERK;
  rate_up = @logic? $u_Parp1 : 0.0;
  rate_down = @logic? 0.0 : $d_Parp1 ;
}

Node DNA_damage {
  logic = ICD_inducer;
  rate_up =  @logic? $u_DNA_damage : 0.0;
  rate_down = @logic? 0.0 : $d_DNA_damage;
}

Node CASP3 {
    logic = Apoptosome & !XIAP;
  rate_up = @logic? $u_CASP3 : 0.0;
  rate_down = @logic? 0.0 : $d_CASP3 ;
}

Node CASP7 {
    logic = CytC & !XIAP;
```

```
  rate_up = @logic? $u_CASP7 : 0.0;
  rate_down = @logic? 0.0 : $d_CASP7 ;
}

Node XIAP {
  logic = AKT & MOMP;
  rate_up = @logic? $u_XIAP : 0.0;
  rate_down = @logic? 0.0 : $d_XIAP ;
}

Node TP53 {
    logic = (ERK & !TP53 & Mdm2) | (Parp1 & !TP53 & Mdm2) | CDK2 ;
  rate_up = @logic? $u_TP53 : 0.0;
  rate_down = @logic? 0.0 : $d_TP53 ;
}

Node ROS {
    logic = Nox1 | DNA_damage;
  rate_up = @logic? $u_ROS : 0.0;
  rate_down = @logic? 0.0 : $d_ROS ;
}

Node H2AX {
    logic = !DNA_damage & !H2AX;
  rate_up = @logic? $u_H2AX : 0.0;
  rate_down = @logic? 0.0 : $d_H2AX ;
}

Node Rac1 {
    logic = Rac1 & !H2AX;
  rate_up = @logic? $u_Rac1 : 0.0;
  rate_down = @logic? 0.0 : $d_Rac1 ;
}

Node Noxa1 {
    logic = Noxa1 & !H2AX;
  rate_up = @logic? $u_H2AX : 0.0;
  rate_down = @logic? 0.0 : $d_H2AX ;
}

Node Nox1 {
    logic = Noxa1 & Rac1;
  rate_up = @logic? $u_Nox1 : 0.0;
  rate_down = @logic? 0.0 : $d_Nox1 ;
}

Node Mdm2 {
```

```
105     logic = (TP53 & !ATM) | (AKT & !ATM) | (AKT & !ATM & TP53);
106   rate_up = @logic? $u_Mdm2 : 0.0;
107   rate_down = @logic? 0.0 : $d_Mdm2 ;
108 }
109
110 Node Chk1 {
111     logic = ATR;
112   rate_up = @logic? $u_Chk1 : 0.0;
113   rate_down = @logic? 0.0 : $d_Chk1 ;
114 }
115
116 Node ATM {
117     logic = (DNA_damage | ATR) | (ROS & ATR);
118   rate_up = @logic? $u_ATM : 0.0;
119   rate_down = @logic? 0.0 : $d_ATM ;
120 }
121
122 Node ATR {
123     logic = DNA_damage;
124   rate_up = @logic? $u_ATR : 0.0;
125   rate_down = @logic? 0.0 : $d_ATR ;
126 }
127
128 Node AKT {
129   logic = CASP3;
130   rate_up = @logic? $u_AKT : 0.0;
131   rate_down = @logic? 0.0 : $d_AKT ;
132 }
133
134 Node Chk2 {
135     logic = ATM;
136   rate_up = @logic? $u_Chk2 : 0.0;
137   rate_down = @logic? 0.0 : $d_Chk2 ;
138 }
139
140 Node BIM {
141     logic = CDK1 & !AKT | !ERK;
142   rate_up = @logic? $u_BIM : 0.0;
143   rate_down = @logic? 0.0 : $d_BIM ;
144 }
145
146 Node PUMA {
147     logic = TP53;
148   rate_up = @logic? $u_PUMA : 0.0;
149   rate_down = @logic? 0.0 : $d_PUMA ;
150 }
151
```

```
Node ERK {
    logic = DNA_damage;
  rate_up = @logic? $u_ERK : 0.0;
  rate_down = @logic? 0.0 : $d_ERK ;
}

Node Bcl_2 {
    logic = (!PUMA & !BIM) | Bcl_2 | Bcl_XL | ERK;
  rate_up = @logic? $u_Bcl_2 : 0.0;
  rate_down = @logic? 0.0 : $d_Bcl_2 ;
}

Node Bcl_XL {
    logic = (!PUMA & Bcl_XL & !BAD & !BID) | (!BAD & !PUMA & !BID);
  rate_up = @logic? $u_Bcl_XL : 0.0;
  rate_down = @logic? 0.0 : $d_Bcl_XL ;
}

Node BAK {
    logic = PUMA & !Bcl_XL;
  rate_up = @logic? $u_BAK : 0.0;
  rate_down = @logic? 0.0 : $d_BAK ;
}

Node BAD {
  logic = Bcl_XL;
  rate_up = @logic? $u_BAD : 0.0;
  rate_down = @logic? 0.0 : $d_BAD ;
}

Node BAX {
    logic = PUMA & BID & Bcl_XL;
  rate_up = @logic? $u_BAX : 0.0;
  rate_down = @logic? 0.0 : $d_BAX ;
}

Node MOMP {
    logic = BAX | BAK;
  rate_up = @logic? $u_MOMP : 0.0;
  rate_down = @logic? 0.0 : $d_MOMP ;
}

Node CytC {
    logic = MOMP;
  rate_up = @logic? $u_CytC : 0.0;
  rate_down = @logic? 0.0 : $d_CytC ;
}
```

```
199
200 Node BID {
201   logic = TP53;
202   rate_up = @logic? $u_BID : 0.0;
203   rate_down = @logic? 0.0 : $d_BID ;
204 }
205
206 Node Apoptosome {
207     logic = CytC;
208   rate_up = @logic? $u_Apoptosome : 0.0;
209   rate_down = @logic? 0.0 : $d_Apoptosome ;
210 }
211
212 Node CDC25 {
213     logic = !CDK2 & (!Chk1 | !Chk2) & CDK1;
214   rate_up = @logic? $u_CDC25 : 0.0;
215   rate_down = @logic? 0.0 : $d_CDC25 ;
216 }
217
218 Node CDK2 {
219     logic = CDC25;
220   rate_up = @logic? $u_CDK2 : 0.0;
221   rate_down = @logic? 0.0 : $d_CDK2 ;
222 }
223
224 Node CDK1 {
225     logic = CDC25;
226   rate_up = @logic? $u_CDK1 : 0.0;
227   rate_down = @logic? 0.0 : $d_CDK1 ;
228 }
229
230 Node NFE2L2 {
231     logic = PKC & ROS;
232   rate_up = @logic? $u_NFE2L2 : 0.0;
233   rate_down = @logic? 0.0 : $d_NFE2L2 ;
234 }
235
236 Node HMOX1 {
237     logic = NFE2L2;
238   rate_up = @logic? $u_HMOX1 : 0.0;
239   rate_down = @logic? 0.0 : $d_HMOX1 ;
240 }
241
242 Node XPO1 {
243     logic =  (NLS1 & NLS2);
244   rate_up = @logic? $u_XPO1 : 0.0;
245   rate_down = @logic? 0.0 : $d_XPO1 ;
```

```
}

Node HMGB1_translocation {
    logic = XPO1 & HMGB1;
  rate_up = @logic? $u_HMGB1_translocation : 0.0;
  rate_down = @logic? 0.0 : $d_HMGB1_translocation ;
}
```

Listing 7.3: Node Definitions

Mathematical proofs of MaBoSS

Lemma 1. *Consider a stationary continuous time Markov process $s(t)$. Let $G(\Sigma, E)$ the graph associated with the transition rates (transition graph). Let $H(V, F) \subset G$ a sub-graph without outgoing edges. Let ∂V the set of nodes with an edge to H. $\forall \mathbf{S} \in \partial V, \quad \mathbf{P}[s(t) = \mathbf{S}] = 0$.*

Proof. Consider the master equation applied to the sum of probabilities on V. Using the definition of V and ∂V and the fact that the markov process is stationary:

$$\begin{aligned} 0 &= \sum_{\mathbf{S} \in V} \frac{d}{dt} \mathbf{P}[s(t) = \mathbf{S}] \\ &= \sum_{\mathbf{S} \in V, \mathbf{S}' \in (V \cup \partial V)} (\rho_{\mathbf{S}' \to \mathbf{S}} P[s(t) = \mathbf{S}'] - \rho_{\mathbf{S} \to \mathbf{S}'} P[s(t) = \mathbf{S}]) \\ &= \sum_{\mathbf{S} \in V, \mathbf{S}' \in \partial V} \rho_{\mathbf{S}' \to \mathbf{S}} \mathbf{P}[s(t) = \mathbf{S}'] \end{aligned}$$

align*
By definition of V and ∂V, $\forall \mathbf{S}' \in \partial V, \quad \exists \mathbf{S} \in V$ such that $\rho_{\mathbf{S}' \to \mathbf{S}}$ is non-zero. The equation above implies that $\mathbf{P}[s(t) = \mathbf{S}'] = 0$. □

Theorem 0.1. *Consider a continuous time Markov process $s(t)$ that is stationary. Let $G(\Sigma, E)$ the graph associated with the transition rates (transition grpah). Let $\mathcal{F}_G = \{\mathbf{\Phi}_k(\phi_k, e_k), k = 1, ..., s\}$ be the set of connected component with no outcoming edges. The set $\{\mathbf{S}$ s.th. $\mathbf{P}[s(t) = \mathbf{S}] > 0\}$ is the union of some of the ϕ_k .*

Proof. If a state $\mathbf{S}$ has a zero instantaneous probability $\mathbf{P}[s(t) = \mathbf{S}]$, all states $\mathbf{S}'$ that have a connection $\mathbf{S}' \to \mathbf{S}$ in G have also zero instantaneous probability. Demonstrable by applying the master equation to $\mathbf{P}[s(t) = \mathbf{S}]$. Consider all states with a connection with on of the ϕ_k, according to lemma 1 they have zero instantaneous probability. By applying this argument iteratively all states that are not in ϕ_k have zero instantaneous probability.
If a state that belongs to one of the ϕ_k has a non-zero instantaneous probability, all states in ϕ_k have non-zero probability.
Suppose this is not true, which means $\exists \mathbf{S}, \mathbf{S}' \in \phi_k$ such that $\mathbf{P}[s(t) = \mathbf{S}] = 0$ and $\mathbf{P}[s(t) = \mathbf{S}'] > 0$. Because of the definition of strongly connected component, there exists a path in Φ_k from $\mathbf{S}'$ to $\mathbf{S}$. With this argument applied iteratively to statements at the beginning of the proof, we have a contradiction. □

Corollary 0.1. *Consider a set of transition rates. Let $G(\Sigma, E)$ be the graph associated with the transition rates (transition graph). Let $\mathcal{F} = \{\Phi_k(\phi_k, e_k), k = 1, ..., s\}$ be the set of connected components with no outcoming edges- Any stationary continuous time Markov process that is indecomposable has a support in $\mathcal{F}_G$*

Proof. Use results of previous theorem (0.1). □

Theorem 0.2. *Assume two different stationary Markov processes with the same transition rates and same support (states with non-zero instant probabilities). If both stationary distributions are indecomposable (i.e. associated to the same strongly connected component), they are identical.*

Proof. In vector notation, let M be the transition matrix, $\tilde{\mathbf{P}}$ and $\tilde{\vec{\mathbf{P}}}$ are such that

$$M\vec{\mathbf{P}} = \tilde{\vec{\mathbf{P}}} = 0 \text{ and } \sum_\mu \mathbf{P}_\mu = \sum_\mu \widetilde{\mathbf{P}}_\mu = 1$$

Let $\vec{\mathbf{P}}^{(\alpha)} = \alpha\vec{\mathbf{P}} + (1-\alpha)\tilde{\vec{\mathbf{P}}}$ with $\alpha \in [0,1]$, $\vec{\mathbf{P}}^{(\alpha)}$. For such α, $\vec{\mathbf{P}}^{(\alpha)}$ is a stationary distribution according to M.
If $\alpha \notin [0,1]$, $\vec{\mathbf{P}}^{(\alpha)}$ may not be a stationary distribution. Let's consider α_m for which it holds that:

$$\alpha_m = max_\alpha\{\alpha < 0 \text{ s.t. } \exists\mu \text{ for which } \vec{\mathbf{P}}^{(\alpha)}_\mu = 0\}$$

We know that at least there is one μ such that $\mathbf{P}_\mu \neq \widetilde{\mathbf{P}}$. Moreover, since the sum of their components always sum up to 1 by definition, there exists a ν such that $\mathbf{P}_\nu > \widetilde{\mathbf{P}}_\nu$. If so it is, $\mathbf{P}^{(\alpha)}_\nu$ is a linear function of α, with positive slope and can be set to zero by negative values of α. This set of α values exists and is finite, hence α_m exists. With this definition of α_m, $\vec{\mathbf{P}}^{(\alpha_m)}$ is a stationary distribution for M that has all positive components except one.
The support of $\vec{\mathbf{P}}^{(\alpha_m)}$ is smaller than $\vec{\mathbf{P}}$ and $\tilde{\vec{\mathbf{P}}}$, causing contradiction with the previous theorem (0.1). □

Theorem 0.3. *Consider a continuous time Markov process s(t) whose initial condition has its support in a strongly connected component with no outgoing edges ϕ. The infinite time average of instantaneous probabilities converges to the stationary distribution associated to the same transition rates with support in ϕ.*

Proof. The average on finite time of a probability is: $\mathbf{P}_T(\mathbf{S}) \equiv \frac{1}{T}\int_0^T dt\mathbf{P}[s(t) = \mathbf{S}]$. In vector notation, let M be the transition matrix, $\tilde{\mathbf{P}}(t)$ be $\mathbf{P}[s(t) = \mathbf{S}]$ and $\tilde{\mathbf{P}}_\mathbf{T}$ as $\mathbf{P}_\mathbf{T}(\mathbf{S})$. By definition the components $\tilde{\mathbf{P}}(t)$ are non-negative and their sum is equal to 1.
We apply M to $\vec{\mathbf{P}}_T$, therefore:

$$M\vec{\mathbf{P}}_T = \frac{1}{T}\int_0^T dt\frac{d}{dt}\vec{\mathbf{P}}_T = \frac{1}{T}[\vec{\mathbf{P}}_T(T) - \vec{\mathbf{P}}(0)]$$

We see that because every component of $\vec{\mathbf{P}}(t)$ is bounded, $\lim_{T\to\infty} M\vec{\mathbf{P}_\mathbf{T}} = 0$. Moreover, the space of $\vec{\mathbf{P}_\mathbf{T}}$ is compact there exists a converging sub-sequence $\vec{\mathbf{P}_{\mathbf{T_i}}}, i = 1, ...$
$\vec{\mathbf{P}} \equiv \lim_{i\to\infty}\vec{\mathbf{P}}_T$, is therefore a stationary distribution associated to M. Choosing an initial condition, instantaneous probabilities are zero for states outside ϕ: this means the support of $\vec{\mathbf{P}}$ is in ϕ. Because of previous theorem it exists only one stationary distribution with these features, each converging sub-sequence of $\vec{\mathbf{P}}_T$ has the same limit. $\vec{\mathbf{P}}_T$ converges to the unique indecomposable stationary distribution with its support in ϕ. □

Theorem 0.4. *Let s(t) a continuous time Markov process whose initial condition has its support in a strongly connected component with no outgoing edges ϕ. The limit $t \to \infty$ of instantaneous probabilities converges to the indecomposable stationary distribution associated to ϕ.*

Proof. Using a vector notation and considering only strongly connected component ϕ of the state space Σ, the master equation is: $\frac{d}{dt}\vec{\mathbf{P}}(t) = M\vec{\mathbf{P}}(t)$. With statements of 0.3 we know that $\exists!\vec{\mathbf{P}}^{(0)}$ such that: $M\vec{\mathbf{P}}^{(0)} = 0$ and where $\mathbf{P}^{(0)}_i \in]0,1[\quad \forall i = 1, ...$ and $\sum_i \mathbf{P}_i(0) = 1$.
On top of that, any solution with an initial condition satisfying the following, $\mathbf{P}_i(0) \in [0,1] \quad \forall i = 1, ...$ and $\sum_i \mathbf{P}_i(0) = 1$ holds the property that: $\mathbf{P}_i(t) \in]0,1[\quad \forall i = 1, ... \quad \forall t > 0$.
Assume now the converse. Because solutions to the master equation are continuous, consider the smallest $\widetilde{t} > 0$ such that $\exists\widetilde{\mathbf{S}}$ with $\mathbf{P}[s(t) = \widetilde{\mathbf{S}}] = 0$. However we have the resulting:

$$\frac{d}{dt}\mathbf{P}[s(t) = \widetilde{\mathbf{S}}] = \sum_{\mathbf{S}'} \rho_{\mathbf{S}'\to\widetilde{\mathbf{S}}}\mathbf{P}[s(\widetilde{t}) = \widetilde{\mathbf{S}}'] \geq 0$$

The case $\frac{d}{dt}\mathbf{P}[s(t) = \widetilde{\mathbf{S}}] \geq 0$ is impossible: before $\widetilde{t}$ all instantaneous probabilities are non-negative, by definition, and because the master equation solutions are continuous. $\frac{d}{dt}\mathbf{P}[s(t) = \widetilde{\mathbf{S}}] = 0$ at $t = \widetilde{t}$ and

all states mapped to $\widetilde{\mathbf{S}}$ have also a zero probability.
If we apply the statement iteratively, since the system is restricted to strongly connected component, all states have zero probability at time $\widetilde{t}$, which is a contradiction. For $t > 0$, all states have non-zero positive probability. Because the sum of probabilities is equal to one, $\mathbf{P}_i(t) \in]0,1[\quad \forall i = 1, ... \quad \forall t > 0$.
Moreover, let's consider the spectral decomposition of M: $\{\lambda_i, \vec{v}^{(i)}\}$, $\vec{\mathbf{P}}^{(0)} = \vec{v}^{(i)}$ for $\lambda_i = 0$.
Any solution can be expressed as $\sum_i \beta_i \exp(t\lambda_i)\vec{v}_i$ (if M not-diagonalizable, the exp can be multiplied by a polynomial in t). In order to have $\sum_i \mathbf{P}_i(t) = \text{const}$, one should have $\sum_j v_j^i = 0$ for i such that $\lambda_i \neq 0$. Any solution with $\sum_i \mathbf{P}_i(t) = 1$ is the linear combination of $\vec{\mathbf{P}}^{(0)}$ and any other time varying solution. The constant coefficient in front of time varying solutions can be set as small as possible, such that the initial conditions of probabilities are in [0,1]. In that case, the property $\mathbf{P}_i(t) \in]0,1[\quad \forall i = 1, ... \quad \forall t > 0$ implies that $\Re\lambda_i \leq 0 \quad \forall \lambda_i$.
To show that an oscillatory solution is impossible, (*i.e.* $\Re\lambda_i < 0 \forall \lambda_i \neq 0$) we assume it is possible. Let $\vec{\mathbf{P}} = \alpha\vec{\mathbf{P}}^{(0)} + \beta\vec{\mathbf{P}}^{(s)}(t)$ be a solution of the master equation, with $\vec{\mathbf{P}}^{(s)}(t)$ an oscillatory solution. For particular choices of α and β such that $\sum_i \mathbf{P}_i(t) = 1$ and $\mathbf{P}_i(t) \in]0,1[\quad \forall i = 1, ... \quad \forall t > 0$. It is possible to choose β_m such that $\exists (j, \widetilde{t} > 0)$ with $\mathbf{P}_j(\widetilde{t}) = 0$ and $\mathbf{P}_i(t) \in [0,1] \quad \forall i = 1, ... \quad \forall t > 0^{\dagger}$. But we proved before that it is impossible, thus $\Re\lambda_i < 0$ for $\lambda_i \neq 0$ and any time varying solution converges to the stationary solution $\vec{\mathbf{P}}^{(0)}$.

□

Corollary 0.2. *For a continuous time Markov process to a finite state space, the limit $t \to \infty$ of instantaneous probabilities converges to a stationary distribution.*

Proof. With the usual notation, we consider the spectrum of M, i.e. $\lambda_i, \vec{v}^{(i)}$. Because for every solution $\sum_i \mathbf{P}_i(t) = \text{const}$, $\sum_j v_j^{(i)} = 0$ for i such that: $\lambda_i \neq 0$. With the same arguments of previous theorem $\Re\lambda_i < 0 \forall \lambda_i$.
Take $\vec{\mathbf{P}} = \alpha\vec{\mathbf{P}}^{(0)} + \beta\vec{\mathbf{P}}^{(s)}(t)$ where $\vec{\mathbf{P}}^{(s)}(t)$ is an oscillatory solution. Like we did before, we can tune α and β such that $\mathbf{P}_j(\widetilde{t}) = 0$ for given j and $\widetilde{t}$. Again all states that have non-zero transition rate to state j have also zero probability at time $\widetilde{t}$.
The smallest sub-graph $H \subset G(\Sigma, E)$, containing the state j and without any incoming edges, has nodes with zero probability at time $\widetilde{t}$. Because there are no incoming edges, nodes probability is zero also when $t > \widetilde{t}$. Because of uniqueness of solutions for any system of linear differential equations, this result can be extended to $t > 0$. With this argument, applying it to a state outside H, $\vec{\mathbf{P}^{(s)}}(t)$=0 everywhere. We can conclude that $\Re\lambda_i < 0$ if $\lambda_i \neq 0$ and any time varying solution converges to a stationary one. □

Theorem 0.5. *Consider a continuous time Markov process to a discrete state space Σ. Time average along a single trajectory converges to a stationary distribution.*

Proof. As before, consider the Markov process as a stationary one, restricting it in a single strongly connected component with no outcoming edges: there is a finite time τ after which the trajectory belongs to a strongly connected component with no outcoming edges. For $t > \tau$, the trajectory also belongs to the stationary Markov process associated with this strongly connected component with no outcoming edges. If time average starting at τ converges, then time average starting at any time converges to the same value.
Formally the set of trajectories represents the set of elementary events $\omega \in \Omega$, with the right definition of the probability measure $\mathbf{P}$ on a given σ-algebra $\mathcal{F}$. The stationary sequence is given by the instantaneous probabilities $\mathbf{P}[s(t_i) = \mathbf{S}]$ defined on equidistant discrete time $t_i = v * i, i = 1, ...,$. In fact the stationaritu of continuous time Markov process and definition of t_i implies that the discrete process is stationary and Markovian.
Formally a trajectory ω is a function $\mathbb{R} \to \Sigma, t \mapsto \omega_t$ and the stationary sequence is a set of random variables $\mathbb{N} \times \Omega \to \Sigma, (\omega, i) \mapsto \omega_{t_i}$. An invariant set $A \in \mathcal{F}$ is such that there exists $B = B_1 \times B_2 \times ...$ with $B_i \subset \Sigma$, such that for all $n \geq 1$, $A = \{\omega \text{ s.th. } (\omega_{t_n}, \omega_{t_{n+1}}, ...) \in B\}$.
If $B = \Sigma \times \Sigma \times ...$, then $A = \Omega$ and $\mathbf{P}(A) = 1$. Consider the biggest set B that is smaller than $\Sigma \times \Sigma \times ....$ It consists of removing one element in one of the B_i. With no loss of generality, let us consider that $B_1 = \Sigma \setminus \{\mathbf{S}\}$. In that case $A = \{\omega \text{s.th} \omega_{t_n} \neq \mathbf{S}, \forall n \geq 1\}$ and using Markovianity:

$$\begin{aligned}
\mathbf{P}(A) &= \mathbf{P}[s(t_1) \neq \mathbf{S}, s(t_2) \neq \mathbf{S}, ...] \\
&= \lim_{x \to \infty} \sum_{\mathbf{S^{(1)}} ... \mathbf{S^{(n)}} \neq \mathbf{S}} \mathbf{P}[s(t_1) = \mathbf{S^{(1)}}] \times \\
&\times \mathbf{P}[s(t_2) = \mathbf{S^{(2)}} | s(t_1) = \mathbf{S^{(1)}}] \times \mathbf{P}[s(t_n) = \mathbf{S^{(n)}} | s(t_{n-1}) = \mathbf{S^{(n-1)}}]
\end{aligned}$$

Using theorem (0.4), any solution of master equation has non-zero probabilities (except for the initial condition). Because transition probabilities are computed by using solutions of the master equation,

$$\sum_{\mathbf{S}'\neq\mathbf{S}} \mathbf{P}[s(t_1)=\mathbf{S}'|s(t_1)=\mathbf{S}''] \leq k \leq 1$$

because $\mathbf{P}[s(t_1)=\mathbf{S}'|s(t_1)=\mathbf{S}''] \geq 0$. So, $\mathbf{P}(A) \leq \lim_{n\to\infty} \sum_{\mathbf{S}^{(1)}\neq\mathbf{S}} \mathbf{P}[s(t_1)=\mathbf{S}^{(1)}]k^{n-1} = 0$ If A has zero probability, any sub-set has also zero probability. The stationary sequence is ergodic. Applying the ergodic theorem, time average of the stationary sequence converges to instantaneous probability distribution. If any discrete average converges to the same distribution, continuous time average converges also to the stationary distribution. □

Theorem 0.6. *Consider a set of transition rates. It is possible to construct a damped oscillatory Markov process with these transition rates if and only if the transition matrix has at least a non-real eigenvalue*

Theorem 0.7. *A transition matrix, whose transition graph has no cycle, has only real eigenvalue.*

Proof. Consider a master equation:

$$\frac{d}{dt}\mathbf{P}[s(t)=\mathbf{S}] = \sum_{\mathbf{S}'}\{\rho_{(\mathbf{S}'\to\mathbf{S})}\mathbf{P}[s(t)=\mathbf{S}'] - \rho_{(\mathbf{S}\to\mathbf{S}')}\mathbf{P}[s(t)=\mathbf{S}]\}$$

it can be expressed as:

$$\frac{d}{dt}\mathbf{P}[s(t)=\mathbf{S}] + \sum_{\mathbf{S}'}\rho_{(\mathbf{S}\to\mathbf{S}')}\mathbf{P}[s(t)=\mathbf{S}] = \sum_{\mathbf{S}'}\rho_{(\mathbf{S}'\to\mathbf{S})}\mathbf{P}[s(t)=\mathbf{S}']$$

or eventually:

$$\frac{d}{dt}\mathbf{P}[s(t)=\mathbf{S}] + K\mathbf{P}[s(t)=\mathbf{S}] = F(t)$$

Then $\mathbf{P}[s(t)=\mathbf{S}] = e^{-Kt} + \int_0^t F(s)e^{K(s-t)}ds$. $F(t)$ depends only on instantaneous probabilities of upstream states (in the transition graph). Because the transition graph has no cycle, probabilities of upstream states do not depend on $\mathbf{P}[s(t)=\mathbf{S}]$. Therefore, every $\mathbf{P}[s(t)=\mathbf{S}]$ can be obtained iteratively by computing it starting at states that have no in-coming edges in the transition graphs. Because the iterative procedure consists in integrating exponential, it will never produce oscillatory function. The transition matrix has only real eigenvalues. □

Theorem 0.8. *Consider a transition matrix ($m \times m$), whose transition graph is a unique cycle with identical transition rates. If the matrix dimension is bigger than 2×2, the matrix has at least one non-real eigenvalue.*

Proof. Assume we order states along the cycle, the transition matrix becomes:

$$M|_{\mu,\nu} = \delta_{\mu,\nu}(-\rho) + \delta_{\mu,\nu+1}\rho \quad \text{for}\mu < m$$
$$M|_{\mu,m} = \delta_{\mu,m}(-\rho) + \delta_{\mu,1}\rho$$

where ρ is the transition rate. The characteristic polynomial of M is $pM(\lambda) = (\lambda+\rho)^m - \rho m$. Because of the definition of determinant of M, the eigenvalues of M are

$$\lambda_k = \rho e^{i2\pi k/m} - 1 \text{ with } k = 1, .., m$$

Therefore if $m > 2$ there is at least on λ_k that is non-real, producing a damped oscillatory process. □

Corollary 0.3. *Consider a graph with at least one cycle. There exists a set of transition rates associated with this graph, whose transition matrix has at least one non-real valued eigenvalue.*

Proof. Let M_0 be a transition matrix whose transition rates are identical to those associated with the cycle of the transition graph, and all other are set to zero. According to theorem (0.8), M_0 has one non-zero eigenvalue and so has damped oscillatory solution. Consider now M_p, a perturbation of M_0, which consists in adding small transition rates associated with other links in the graph. Because any solution of the master equation is analytic in the transition rates, a small perturbation of damped oscillatory solution will remain 'qualitatively' the same. Therefore M_p has also a damped oscillatory behavior if the new transition rates are small enough. It follows that M_p has at least one non-real eigenvalue. □

Glossary

ABC - ATP-Binding Cassette: A family of transporters that utilize ATP to translocate substrates across cellular membranes.

ABCA1 - ATP-Binding Cassette Subfamily A Member 1: A protein involved in the regulation of cellular cholesterol and phospholipid efflux.

ABL1 - ABL Proto-Oncogene 1: A tyrosine kinase involved in cell differentiation, division, adhesion, and stress responses.

ADAMTS12 - A Disintegrin And Metalloprotease With Thrombospondin Motifs 12: An enzyme involved in tissue remodeling and inflammatory processes.

ADAR - Adenosine Deaminase Acting on RNA: An enzyme that modifies RNA molecules through adenosine-to-inosine editing.

ADGRA2 - Adhesion G Protein-Coupled Receptor A2: Involved in cellular adhesion and signaling.

ADGRA3 - Adhesion G Protein-Coupled Receptor A3: Similar to ADGRA2, plays a role in cellular communication.

ADIPOQ - Adiponectin: A hormone secreted by adipose tissue, involved in regulating glucose levels and fatty acid breakdown.

ADO - Adenosine Deaminase Deficiency (ADO): A genetic condition leading to severe combined immunodeficiency.

ADP - Adenosine Diphosphate: A key molecule in cellular energy metabolism and signaling.

ADRA2A - Adrenergic Receptor Alpha 2A: A receptor involved in norepinephrine signaling and the autonomic nervous system.

AGER - Advanced Glycation End-Product Receptor: Plays a role in inflammatory and oxidative stress responses.

AGER8 - Variant of the AGER gene involved in similar pathways.

AKT - AKT Serine/Threonine Kinase: A critical regulator of cell survival, metabolism, and proliferation.

ALX1 - ALX Homeobox 1: A transcription factor involved in craniofacial development.

AMPK - AMP-Activated Protein Kinase: A cellular energy sensor regulating metabolism.

ANGPT1 - Angiopoietin 1: A protein involved in angiogenesis and vascular stability.

ANGPT2 - Angiopoietin 2: Functions in vascular remodeling and inflammation.

ANGPTL4 - Angiopoietin Like 4: Regulates lipid metabolism and angiogenesis.

ANOVA - Analysis of Variance: A statistical method for comparing means across groups.

ANXA1 - Annexin A1: Involved in anti-inflammatory responses and membrane repair.

APOE - Apolipoprotein E: Involved in lipid transport and metabolism, with links to Alzheimer's disease.

ARACNE - Algorithm for the Reconstruction of Accurate Cellular Networks: Computational tool for inferring regulatory networks.

ARTN - Artemin: A growth factor in the GDNF family that supports neuronal survival.

ATF4 - Activating Transcription Factor 4: Regulates stress responses and amino acid metabolism.

ATF6 - Activating Transcription Factor 6: A key regulator in the unfolded protein response.

ATG10 - Autophagy Related 10: Involved in the autophagy process, particularly in the formation of autophagosomes.

ATG12 - Autophagy Related 12: Plays a role in autophagosome elongation and autophagy regulation.

ATG5 - Autophagy Related 5: Essential for the formation of autophagosomes.

ATG7 - Autophagy Related 7: An E1-like enzyme required for autophagy regulation.

ATM - Ataxia Telangiectasia Mutated: A kinase involved in DNA damage response and repair.

ATR - Ataxia Telangiectasia and Rad3 Related: Works with ATM to repair damaged DNA.

AURKA - Aurora Kinase A: Involved in cell cycle regulation, particularly in mitotic spindle formation.

BACH1 - BTB And CNC Homology 1: A transcription factor that regulates oxidative stress responses.

BACH2 - BTB And CNC Homology 2: Plays a role in immune regulation and B cell differentiation.

BAK - BCL2 Antagonist/Killer: A pro-apoptotic protein involved in mitochondrial apoptosis.

BAP31 - B-Cell Receptor Associated Protein 31: A protein involved in apoptosis and endoplasmic

reticulum function.

BAX - BCL2 Associated X Protein: Promotes apoptosis by facilitating cytochrome c release from mitochondria.

BDNF - Brain-Derived Neurotrophic Factor: A neurotrophin essential for neuronal survival and synaptic plasticity.

BECN1 - Beclin 1: A key regulator of autophagy and apoptosis.

BFS - Biochemical Failure-Free Survival: A metric used in oncology to measure treatment success.

BGLAP3 - Bone Gamma-Carboxyglutamate Protein 3 (Osteocalcin): Involved in bone formation.

BID - BH3 Interacting Domain Death Agonist: A pro-apoptotic member of the BCL2 family.

BIM - BCL2 Interacting Mediator Of Cell Death: Promotes apoptosis by activating BAX and BAK.

BKMC - Boolean-kinetic Monte Carlo algorithm.

BRCA1 - Breast Cancer 1: A tumor suppressor gene involved in DNA repair.

BRCA2 - Breast Cancer 2: Works with BRCA1 in homologous recombination to repair DNA.

BROS - May refer to bioinformatics tools or unpublished terms (context required).

BSR20180250 - Likely refers to a specific research or dataset identifier (context-dependent).

BTC - Betacellulin: A growth factor involved in epithelial cell growth and wound healing.

CALR - Calreticulin: A calcium-binding protein involved in cellular calcium signaling and folding.

CAR - Chimeric Antigen Receptor: A synthetic receptor designed for engineered T cells in cancer immunotherapy.

CASP3 - Caspase 3: A critical executioner caspase in the apoptosis pathway.

CASP7 - Caspase 7: Another effector caspase involved in apoptosis.

CASP8 - Caspase 8: Initiates apoptosis through the extrinsic death receptor pathway.

CASP9 - Caspase 9: Initiator caspase of the intrinsic mitochondrial apoptosis pathway.

CBP - CREB Binding Protein: A transcriptional coactivator and histone acetyltransferase.

CCL11 - Chemokine (C-C Motif) Ligand 11: Involved in eosinophil recruitment during inflammation.

CCL17 - Chemokine (C-C Motif) Ligand 17: Attracts T-helper 2 cells and plays a role in immune response.

CCL19 - Chemokine (C-C Motif) Ligand 19: Involved in T cell and dendritic cell migration.

CCL2 - Chemokine (C-C Motif) Ligand 2: Also known as MCP-1, recruits monocytes to sites of inflammation.

CCL20 - Chemokine (C-C Motif) Ligand 20: Attracts lymphocytes and dendritic cells to inflammation sites.

CCL21 - Chemokine (C-C Motif) Ligand 21: Attracts naive T cells to secondary lymphoid tissues.

CCL3 - Chemokine (C-C Motif) Ligand 3: Plays a role in inflammation and immune responses.

CCL4 - Chemokine (C-C Motif) Ligand 4: Involved in the recruitment of immune cells during inflammatory responses.

CCL5 - Chemokine (C-C Motif) Ligand 5: Also known as RANTES, involved in recruiting immune cells to inflammation sites.

CCN3 - Cellular Communication Network Factor 3: Regulates cell adhesion, migration, and growth.

CCNA2 - Cyclin A2: A cyclin protein that regulates the cell cycle during S phase.

CCNB1 - Cyclin B1: Essential for the control of mitosis in the cell cycle.

CCND1 - Cyclin D1: Regulates cell cycle progression through the G1/S checkpoint.

CCNE1 - Cyclin E1: Promotes the transition from G1 to S phase in the cell cycle.

CCR7 - C-C Motif Chemokine Receptor 7: Regulates T cell migration to lymph nodes.

CDC25 - Cell Division Cycle 25: A family of phosphatases involved in cell cycle progression.

CDC25A - A subtype of CDC25 phosphatase that regulates G1/S transition.

CDC25C - A subtype of CDC25 phosphatase that regulates the G2/M transition in the cell cycle.

CDDP - Cisplatin: A chemotherapy drug used to treat various cancers.

CDK - Cyclin-Dependent Kinase: A family of protein kinases that regulate the cell cycle.

CDK1 - Cyclin-Dependent Kinase 1: Critical for the G2/M transition in the cell cycle.

CDK2 - Cyclin-Dependent Kinase 2: Regulates cell cycle progression during S phase.

CDK4 - Cyclin-Dependent Kinase 4: Works with Cyclin D in the G1 phase.

CDK6 - Cyclin-Dependent Kinase 6: Similar to CDK4, involved in regulating G1 phase progression.

CDKN1B - Cyclin-Dependent Kinase Inhibitor 1B (p27): Inhibits CDK2 activity to control cell cycle progression.

CELSR1 - Cadherin EGF LAG Seven-Pass G-Type Receptor 1: A protein involved in planar cell polarity and neural development.

CELSR2 - Cadherin EGF LAG Seven-Pass G-Type Receptor 2: Plays a role in cell adhesion and

signaling.

CHEK1 - Checkpoint Kinase 1: Key player in the DNA damage response and cell cycle arrest.

CHEK2 - Checkpoint Kinase 2: Works alongside CHEK1 to regulate DNA damage repair.

CHIC - Could refer to CHIC Family Proteins: Known for cell signaling roles (context-dependent).

CHOP - C/EBP Homologous Protein: A transcription factor that promotes apoptosis under stress.

CHRDL1 - Chordin-Like 1: Inhibits BMP signaling and is involved in neural development.

CHRNA1 - Cholinergic Receptor Nicotinic Alpha 1 Subunit: Involved in synaptic transmission at neuromuscular junctions.

CII - Collagen Type II Alpha 1 Chain: Found in cartilage tissue.

CIS - Cisplatin.

CNRS - National Center for Scientific Research (France).

CPM - Counts per milion.

CRC - Colorectal Cancer: A term used to describe cancers of the colon and rectum / Centre de Recherche des Cordeliers.

CREB - cAMP Response Element Binding Protein: A transcription factor involved in memory and neuronal plasticity.

CREBBP - CREB Binding Protein: A co-activator with acetyltransferase activity, critical for transcriptional regulation.

CRISPR - Clustered Regularly Interspaced Short Palindromic Repeats: A genome-editing tool used for precise DNA modifications.

CRM1 - Chromosome Region Maintenance 1: A nuclear export receptor involved in protein trafficking.

CRP - C-Reactive Protein: A marker of inflammation produced by the liver.

CRT - Calreticulin: A multifunctional protein involved in calcium homeostasis and quality control in the ER.

CSA - Cockayne Syndrome A: A gene involved in DNA repair and transcription-coupled repair processes.

CSB - Cockayne Syndrome B: Works with CSA in DNA repair mechanisms.

CSF1 - Colony Stimulating Factor 1: Promotes the differentiation and proliferation of monocytes/macrophages.

CSF1R - Colony Stimulating Factor 1 Receptor: Receptor for CSF1, involved in macrophage development.

CSF2 - Colony Stimulating Factor 2: Also known as GM-CSF, stimulates growth of white blood cells.

CSF2RB - Colony Stimulating Factor 2 Receptor Beta: Mediates the action of GM-CSF, IL-3, and IL-5.

CSNK1A - Casein Kinase 1 Alpha: Involved in various signaling pathways, including Wnt and circadian rhythms.

CTL - Cytotoxic T Lymphocytes: Immune cells that destroy virus-infected cells and tumors.

CTLA - Cytotoxic T Lymphocyte Antigen: Plays a role in regulating immune responses.

CTLA4 - Cytotoxic T Lymphocyte Antigen 4: An inhibitory receptor that downregulates immune responses.

CTRL - Control.

CXCL1 - Chemokine (C-X-C Motif) Ligand 1: Attracts neutrophils to sites of inflammation.

CXCL10 - Chemokine (C-X-C Motif) Ligand 10: Plays a role in immune cell trafficking and inflammation.

CXCL12 - Chemokine (C-X-C Motif) Ligand 12: Also known as SDF-1, it plays a role in stem cell trafficking and cancer metastasis.

CXCL2 - Chemokine (C-X-C Motif) Ligand 2: Involved in neutrophil recruitment during inflammatory responses.

CXCL5 - Chemokine (C-X-C Motif) Ligand 5: Mediates neutrophil migration and activation.

CXCL7 - Chemokine (C-X-C Motif) Ligand 7: Plays a role in platelet activation and inflammation.

CXCL8 - Chemokine (C-X-C Motif) Ligand 8: Also known as IL-8, a key mediator in neutrophil recruitment and inflammation.

CXCL9 - Chemokine (C-X-C Motif) Ligand 9: Attracts T cells to inflamed tissues.

CXCR3 - C-X-C Motif Chemokine Receptor 3: Binds CXCL9, CXCL10, and CXCL11 to mediate immune responses.

CXCR4 - C-X-C Motif Chemokine Receptor 4: Critical for hematopoiesis, immune cell trafficking, and cancer metastasis.

CXCR5 - C-X-C Motif Chemokine Receptor 5: Guides the movement of B cells in lymphoid tissues.

DACT - Actinomycin D.
Chemotherapeutic agent.

DAMPS - Damage-Associated Molecular Patterns: Molecules released by stressed cells to trigger immune responses.

DAPI - 4',6-Diamidino-2-Phenylindole: A fluorescent stain used to label DNA in cells.

DCLRE1A - DNA Cross-Link Repair 1A: A protein involved in DNA repair processes.

DCLRE1B - DNA Cross-Link Repair 1B: Also

plays a role in DNA repair mechanisms.

DDB2 - Damage Specific DNA Binding Protein 2: Involved in nucleotide excision repair.

DDDIT3 - DNA Damage Inducible Transcript 3 (CHOP): A stress-induced transcription factor promoting apoptosis.

DDIT3 - Another name for CHOP (duplicate term in some contexts).

DDX58 - DExD/H-Box Helicase 58: Also known as RIG-I, recognizes viral RNA and activates immune responses.

DEAD - DEAD-Box Helicases: Enzymes involved in unwinding RNA during cellular processes.

DEAH - DEAH-Box Helicases: Related to DEAD, but distinct in substrate specificity and function.

DEG - Differentially Expressed Genes: Genes showing differences in expression between conditions.

DFS - Disease-Free Survival: A clinical endpoint indicating the length of time without disease recurrence.

DIOC - DiOC6: A fluorescent dye used to assess mitochondrial membrane potential.

DLD1 - A Human Colorectal Cancer Cell Line: Frequently used in cancer research.

DNA - Deoxyribonucleic Acid: The molecule carrying genetic information.

DOX - Doxorubicin: A chemotherapy drug used to treat various cancers.

DOXO - Abbreviation for Doxorubicin (alternative notation).

DSB - Double-Strand Break: A severe type of DNA damage that can lead to genome instability.

DTT - Dithiothreitol: A reducing agent used in molecular biology to stabilize proteins.

DTW - Dynamic Time Warping: An algorithm used for pattern recognition and time series analysis.

EBI - European Bioinformatics Institute: A major center for biological data analysis and storage.

EBP - Endothelial Binding Protein: Involved in interactions with endothelial cells (specific context needed).

ECIS - Electric Cell-Substrate Impedance Sensing: A technique to measure cell adhesion and behavior.

ECM - Extracellular Matrix: A network of proteins and carbohydrates providing structural support to cells.

EDA - Ectodysplasin A: A protein involved in ectodermal development.

EDN1 - Endothelin 1: A vasoconstrictor involved in blood pressure regulation.

EFNA5 - Ephrin A5: Plays a role in axon guidance and cell-cell communication.

EFNB3 - Ephrin B3: Involved in neuronal development and synaptic plasticity.

EGFR - Epidermal Growth Factor Receptor: A receptor tyrosine kinase involved in cell proliferation and cancer.

EIF2 - Eukaryotic Translation Initiation Factor 2: Regulates protein synthesis during stress.

EIF2AK2 - Eukaryotic Translation Initiation Factor 2 Alpha Kinase 2: Activates EIF2 in response to stress signals.

EIF2AK3 - Eukaryotic Translation Initiation Factor 2 Alpha Kinase 3: Another regulator of EIF2 under stress.

EIF2AK4 - Eukaryotic Translation Initiation Factor 2 Alpha Kinase 4: Similar function as EIF2AK2 and EIF2AK3.

ELISA - Enzyme-Linked Immunosorbent Assay: A lab technique for detecting and quantifying substances.

EMBL - European Molecular Biology Laboratory: A research institution focusing on molecular biology.

EMBO - European Molecular Biology Organization: Promotes excellence in life sciences.

EMY - Emycin (context-dependent): Possibly referring to erythromycin, an antibiotic.

ENS - Ensembl: A genomic database providing information on genes, transcripts, and proteins.

ENTPD1 - Ectonucleoside Triphosphate Diphosphohydrolase 1: Involved in purinergic signaling by hydrolyzing nucleotides.

ERAD - Endoplasmic Reticulum-Associated Degradation: A quality control mechanism for protein degradation.

ERBB2 - Erb-B2 Receptor Tyrosine Kinase 2: Also known as HER2, a receptor involved in cell growth and cancer.

ERCC1 - Excision Repair Cross-Complementation Group 1: Plays a role in DNA nucleotide excision repair.

ERCC4 - Excision Repair Cross-Complementation Group 4: Functions in the nucleotide excision repair pathway.

ERCC5 - Excision Repair Cross-Complementation Group 5: Also involved in DNA repair processes.

ERCC6 - Excision Repair Cross-Complementation Group 6: Plays a role in transcription-coupled DNA repair.

ERCC8 - Excision Repair Cross-Complementation Group 8: Another key player in nucleotide excision repair.

EREG - Epiregulin: A growth factor involved in cell proliferation and differentiation.

ERK - Extracellular Signal-Regulated Kinase:

Part of the MAP kinase pathway involved in cell signaling.

ESO - Early Somatic Embryogenesis: A process in plant and animal development.

ESO1 - Context-dependent, possibly referring to embryonic stem cells (needs clarification).

FAAP24 - Fanconi Anemia Associated Protein 24: Involved in DNA repair within the Fanconi anemia pathway.

FAN1 - Fanconi Associated Nuclease 1: Functions in DNA interstrand crosslink repair.

FANCA - Fanconi Anemia Complementation Group A: Critical for DNA repair in Fanconi anemia patients.

FANCD2 - Fanconi Anemia Complementation Group D2: A central player in the Fanconi anemia repair pathway.

FANCI - Fanconi Anemia Complementation Group I: Functions alongside FANCD2 in DNA repair.

FANCM - Fanconi Anemia Complementation Group M: A DNA repair protein that recognizes damaged DNA.

FAS - Fas Cell Surface Death Receptor: Induces apoptosis through the extrinsic pathway.

FASL - Fas Ligand: Binds to FAS receptor to trigger apoptosis.

FDA - Food and Drug Administration: U.
S.
regulatory agency for food, drugs, and medical devices.

FDR - False Discovery Rate: A statistical method to control errors in multiple hypothesis testing.

FGF1 - Fibroblast Growth Factor 1: Involved in angiogenesis and wound healing.

FGF10 - Fibroblast Growth Factor 10: Plays a role in embryonic development and tissue repair.

FGF17 - Fibroblast Growth Factor 17: Important in brain development and signaling.

FGF7 - Fibroblast Growth Factor 7: Also known as keratinocyte growth factor, regulates epithelial cell growth.

FGFR2 - Fibroblast Growth Factor Receptor 2: A receptor for FGFs, involved in cell signaling and growth.

FIRE - Functional Interpretation of Regulatory Elements: A computational tool for genomic analysis.

FOXM1 - Forkhead Box M1: A transcription factor regulating cell cycle progression and proliferation.

FOXO3 - Forkhead Box O3: A transcription factor involved in cell cycle regulation and stress responses.

FOXP3 - Forkhead Box P3: A key regulator of Treg (regulatory T cell) function and immune homeostasis.

FPR1 - Formyl Peptide Receptor 1: Involved in immune cell chemotaxis.

FPR2 - Formyl Peptide Receptor 2: Plays roles in inflammation and immune responses.

FRZB - Frizzled-Related Protein: A modulator of Wnt signaling pathways.

FUS - Fused In Sarcoma: A RNA-binding protein involved in gene regulation and DNA repair.

GADD34 - Growth Arrest And DNA Damage-Inducible Protein 34: Plays a role in stress response and apoptosis.

GDF9 - Growth Differentiation Factor 9: Important for ovarian follicle development.

GENIE3 - Gene Network Inference with Ensemble of Trees: A computational tool for inferring gene regulatory networks.

GGNER - Global Genomic Nucleotide Excision Repair: A pathway for repairing DNA damage across the genome.

GITRL - Glucocorticoid-Induced TNF Receptor Ligand: A costimulatory molecule for T cell activation.

GPNMB - Glycoprotein Non-Metastatic Melanoma Protein B: Involved in cell migration and repair.

GPR15 - G Protein-Coupled Receptor 15: A receptor involved in immune cell trafficking.

GPR156 - G Protein-Coupled Receptor 156: Functions are not fully elucidated but likely involved in signaling.

GREM1 - Gremlin 1: A BMP antagonist that plays a role in development and disease processes.

GRP78 - Glucose-Regulated Protein 78: A chaperone protein involved in protein folding and ER stress.

GSEA - Gene Set Enrichment Analysis: A computational method for analyzing gene expression data.

GZMB - Granzyme B: A serine protease that induces apoptosis in target cells.

HAVCR2 - Hepatitis A Virus Cellular Receptor 2: Also known as TIM3, regulates immune responses.

HDAC1 - Histone Deacetylase 1: Involved in chromatin remodeling and gene expression regulation.

HGF - Hepatocyte Growth Factor: Promotes cell growth, motility, and morphogenesis in various tissues.

HIF1A - Hypoxia-Inducible Factor 1 Alpha: Regulates cellular responses to low oxygen levels.

HMGB1 - High-Mobility Group Box 1: A chromatin-associated protein with roles in transcription and inflammation.

HMOX1 - Heme Oxygenase 1: Enzyme involved in heme degradation and protection against oxidative stress.

HOXA9 - Homeobox A9: A transcription factor involved in embryonic development and hematopoiesis.

HPV - Human Papillomavirus: A virus associated with cervical cancer and other malignancies.

HSP70 - Heat Shock Protein 70: A molecular chaperone involved in protein folding and stress response.

HSP90 - Heat Shock Protein 90: A chaperone protein critical for stabilizing and activating other proteins.

HSPA1A - Heat Shock Protein Family A Member 1A: Part of the HSP70 family involved in protein quality control.

IARC - International Agency for Research on Cancer: A specialized agency of WHO focusing on cancer research.

IBENS - Institute of Biology of the ENS (École Normale Supérieure).

ICD - Immunogenic Cell Death: A form of cell death that activates the immune system.

ICELLNET - Integrated Cell Network: A bioinformatics tool for studying cell-cell communication.

ICI - Immune Checkpoint Inhibitors: Drugs that block immune checkpoint proteins to enhance immune responses against cancer.

IDC - Invasive Ductal Carcinoma: The most common type of breast cancer.

IFIH1 - Interferon Induced With Helicase C Domain 1: Also known as MDA5, recognizes viral RNA to induce immune responses.

IFN - Interferon: A group of signaling proteins involved in antiviral and immune responses.

IFN1 - Type I Interferon: Includes IFN-alpha and IFN-beta, involved in antiviral defense.

IFNA - Interferon Alpha: A cytokine involved in immune responses, particularly against viral infections.

IFNAB - Type I Interferons Alpha and Beta: Subtypes of interferons involved in antiviral immunity.

IFNAR - Interferon Alpha/Beta Receptor: Mediates the biological effects of type I interferons.

IFNB - Interferon Beta: A cytokine with roles in antiviral responses and immune modulation.

IFNG - Interferon Gamma: A type II interferon that activates macrophages and enhances antigen presentation.

IGF1 - Insulin-Like Growth Factor 1: A hormone involved in growth and development.

IKK - IκB Kinase: A kinase involved in activating NF-κB, a transcription factor regulating immune responses.

INED - Institut National d'Études Démographiques (French Demographic Institute).

INSERM - Institut National de la Santé et de la Recherche Médicale: French National Institute of Health and Medical Research.

IRDS - Interferon-Related DNA Damage Signature: A set of genes upregulated in response to DNA damage and interferon signaling.

IRE1 - Inositol-Requiring Enzyme 1: A sensor of ER stress that activates the unfolded protein response.

IRF2 - Interferon Regulatory Factor 2: A transcription factor regulating type I interferons and other genes.

IRF3 - Interferon Regulatory Factor 3: Activates type I interferon genes in response to viral infections.

IRF5 - Interferon Regulatory Factor 5: Plays a role in antiviral immunity and inflammatory responses.

IRF7 - Interferon Regulatory Factor 7: Essential for the induction of type I interferons during viral infections.

IRF8 - Interferon Regulatory Factor 8: Regulates macrophage and dendritic cell differentiation.

IRF9 - Interferon Regulatory Factor 9: Forms a complex with STAT1 and STAT2 to activate interferon-stimulated genes.

ISGF3 - Interferon-Stimulated Gene Factor 3: A transcription complex activated by type I interferons.

ITK - IL-2-Inducible T-Cell Kinase: A tyrosine kinase involved in T-cell receptor signaling

JAK - Janus Kinase: A family of tyrosine kinases involved in cytokine signaling pathways.

JAK1 - Janus Kinase 1: Plays a key role in signaling for cytokines and growth factors.

JUN - Jun Proto-Oncogene: A component of the AP-1 transcription factor complex involved in cellular proliferation.

KAT2B - Lysine Acetyltransferase 2B: Involved in chromatin remodeling and transcriptional regulation.

KAT3A - Lysine Acetyltransferase 3A (CBP): Functions as a transcriptional coactivator.

KAT7 - Lysine Acetyltransferase 7: Regulates chromatin dynamics and gene expression.

KDM5D - Lysine Demethylase 5D: A histone demethylase involved in gene expression regulation.

KLF17 - Kruppel-Like Factor 17: A transcription factor involved in regulating epithelial-mesenchymal transition.

KLF8 - Kruppel-Like Factor 8: Regulates cell cycle and DNA repair processes.

LAG3 - Lymphocyte Activation Gene 3: An immune checkpoint receptor involved in T-cell

regulation.

LAMP1 - Lysosomal Associated Membrane Protein 1: Involved in lysosome function and autophagy.

LCK - Lymphocyte-Specific Protein Tyrosine Kinase: Critical for T-cell receptor signaling.

LCN2 - Lipocalin 2: Plays a role in immune responses and iron metabolism.

LGALS7 - Galectin 7: A protein involved in cell-cell and cell-matrix interactions.

LGR4 - Leucine-Rich Repeat Containing G Protein-Coupled Receptor 4: Functions in Wnt signaling.

LIG3 - DNA Ligase 3: Involved in base excision repair and other DNA repair processes.

LIG4 - DNA Ligase 4: Essential for non-homologous end joining in DNA double-strand break repair.

LIVE - Likely refers to viability in assays or live imaging (context-dependent).

LPAR1 - Lysophosphatidic Acid Receptor 1: Involved in cell signaling and migration.

LPS - Lipopolysaccharide: A component of bacterial cell walls that triggers immune responses.

LRP1 - LDL Receptor-Related Protein 1: Involved in lipid metabolism and endocytosis.

LTA - Lymphotoxin Alpha: A cytokine involved in inflammation and lymphoid organ development.

MACS - Magnetic-Activated Cell Sorting: A technique for separating cell populations.

MAD2L2 - Mitotic Arrest Deficient 2 Like 2: Plays a role in DNA repair and cell cycle regulation.

MAFG - MAF BZIP Transcription Factor G: Regulates oxidative stress responses and cell differentiation.

MAPK - Mitogen-Activated Protein Kinase: A family of kinases involved in cell signaling pathways.

MATE - Multi-Antimicrobial Extrusion Protein: Involved in drug and toxin efflux.

MCA205 - A murine fibrosarcoma cancer cell line.

MDM2 - Mouse Double Minute 2: A negative regulator of the p53 tumor suppressor protein.

MDSC - Myeloid-Derived Suppressor Cells: Immune cells that suppress T-cell activity and promote tumor growth.

MET - MET Proto-Oncogene: Encodes the hepatocyte growth factor receptor, involved in cell growth and migration.

METRN - Meteorin: A protein involved in neurogenesis and tissue repair.

MHC - Major Histocompatibility Complex: A set of cell surface proteins essential for immune recognition.

MME - Membrane Metalloendopeptidase: Involved in degrading peptide hormones and signaling molecules.

MMP9 - Matrix Metallopeptidase 9: Enzyme involved in degrading extracellular matrix components.

MOMP - Mitochondrial Outer Membrane Permeabilization: A process central to apoptosis regulation.

MRC1 - Mannose Receptor C-Type 1: Plays a role in immune response and endocytosis.

MRE11 - Meiotic Recombination 11: A key component of the MRN complex involved in DNA repair.

MTX - Mitoxantrone.
Chemotherapy agent acting on DNA through intercalation.

MUS81 - MUS81 Structure-Specific Endonuclease Subunit: Involved in DNA damage repair and genome stability.

MYD88 - Myeloid Differentiation Primary Response 88: A key adapter protein in Toll-like receptor signaling.

NAD - Nicotinamide Adenine Dinucleotide: A coenzyme involved in redox reactions and metabolism.

NADPH - Nicotinamide Adenine Dinucleotide Phosphate: A coenzyme used in anabolic reactions and oxidative stress response.

NANOG - Homeobox Protein NANOG: A transcription factor critical for maintaining pluripotency in stem cells.

NAR - Nucleic Acids Research: A scientific journal (context-dependent term).

NBN - Nibrin: A DNA repair protein involved in maintaining genome stability.

NBS1 - Nijmegen Breakage Syndrome 1: A protein involved in DNA double-strand break repair.

NEMO - NF-κB Essential Modulator: A regulatory subunit of the IKK complex that activates NF-κB signaling.

NER - Nucleotide Excision Repair: A DNA repair mechanism that removes bulky DNA lesions.

NES - Nuclear Export Signal: A sequence that facilitates protein export from the nucleus.

NFE2 - Nuclear Factor, Erythroid 2: A transcription factor involved in erythroid and megakaryocyte development.

NFE2L2 - Nuclear Factor, Erythroid 2 Like 2 (NRF2): Regulates antioxidant response and detoxification pathways.

NFKB - Nuclear Factor Kappa B: A transcription factor regulating immune and inflammatory responses.

NFKB1 - Nuclear Factor Kappa B Subunit 1 (p50): A subunit of the NF-κB complex.

NHEJ - Non-Homologous End Joining: A DNA repair pathway for double-strand breaks.

NIH - National Institutes of Health: A U.
S.
agency for medical research.

NKT - Natural Killer T Cells: A subset of T cells with both innate and adaptive immune functions.

NLRP3 - NOD-Like Receptor Family Pyrin Domain Containing 3: A component of the inflammasome involved in inflammatory responses.

NLRP6 - NOD-Like Receptor Family Pyrin Domain Containing 6: Regulates gut microbiota and inflammation.

NLS - Nuclear Localization Signal: A sequence directing proteins to the nucleus.

NOD - Nucleotide-Binding Oligomerization Domain: Intracellular proteins involved in detecting pathogens.

NOD1 - Nucleotide-Binding Oligomerization Domain Containing 1: Recognizes bacterial peptidoglycans.

NOD2 - Nucleotide-Binding Oligomerization Domain Containing 2: Involved in immune responses to bacterial components.

NRF2 - Nuclear Factor Erythroid 2-Related Factor 2: Activates antioxidant and cytoprotective responses.

NRG1 - Neuregulin 1: A growth factor involved in nervous system development and function.

NRP2 - Neuropilin 2: A receptor involved in axonal guidance and vascular development.

NTN3 - Netrin 3: A guidance molecule for neuronal migration and axon growth.

NTN4 - Netrin 4: Similar to NTN3, plays roles in cell adhesion and migration.

OCT - Octamer-Binding Transcription Factor: Refers to a family of transcription factors, including OCT4, involved in stem cell pluripotency.

OXA - Oxaliplatin.

OXP - Oxaliplatin.

PANX1 - Pannexin 1: A channel protein involved in ATP release and purinergic signaling.

PARK2 - Parkin RBR E3 Ubiquitin Protein Ligase: A gene mutated in Parkinson's disease, involved in mitophagy.

PARP1 - Poly (ADP-Ribose) Polymerase 1: A DNA repair enzyme involved in base excision repair.

PBS - Phosphate-Buffered Saline: A buffer solution commonly used in biological research.

PDE - Phosphodiesterase: Enzymes that degrade cyclic nucleotides like cAMP and cGMP.

PDGF - Platelet-Derived Growth Factor: A growth factor involved in angiogenesis and wound healing.

PDGFB - Platelet-Derived Growth Factor Subunit B: A component of the PDGF signaling pathway.

PDGFD - Platelet-Derived Growth Factor Subunit D: Another subtype involved in cell growth and development.

PDGFRB - Platelet-Derived Growth Factor Receptor Beta: A receptor for PDGFB and PDGFD, mediates cell signaling.

PDIA3 - Protein Disulfide Isomerase Family A Member 3: Involved in protein folding in the endoplasmic reticulum.

PDL1 - Programmed Death-Ligand 1: A protein that suppresses immune responses, targeted in cancer immunotherapy.

PDT - Photodynamic Therapy: A treatment method using light and photosensitizing agents to kill cancer cells.

PERK - Protein Kinase R (PKR)-Like Endoplasmic Reticulum Kinase: Activates the unfolded protein response under stress.

PGF - Placental Growth Factor: Regulates angiogenesis and vascular development.

PINK1 - PTEN-Induced Kinase 1: Involved in mitochondrial quality control and mitophagy.

PKC - Protein Kinase C: A family of enzymes regulating various cellular processes, including cell growth and differentiation.

PLK1 - Polo-Like Kinase 1: Regulates mitosis and cell cycle progression.

PLOS - Public Library of Science: A nonprofit publisher of open-access scientific journals.

POLB - DNA Polymerase Beta: Involved in base excision repair.

POLR2A - RNA Polymerase II Subunit A: A component of the transcription machinery for mRNA synthesis.

POS - Position: Often used in genomic contexts to indicate a specific nucleotide position.

PPARG - Peroxisome Proliferator-Activated Receptor Gamma: Regulates lipid metabolism and glucose homeostasis.

PRL - Prolactin: A hormone involved in lactation and reproductive functions.

PROFILE - Software developed at Institut Curie to deal with Boolean model personalization.

PRR - Pattern Recognition Receptor: Recognizes pathogens and triggers immune responses.

PRSS22 - Serine Protease 22: Involved in tissue-specific proteolytic processes.

PSC - Pluripotent Stem Cells: Cells capable of differentiating into various cell types.

PSL - Université Paris Sciences et Lettres.

PSPN - Persephin: A growth factor in the GDNF

family involved in neuronal survival.

PTGER1 - Prostaglandin E Receptor 1: Mediates the action of prostaglandin E2 in various tissues.

PTPRF - Protein Tyrosine Phosphatase Receptor Type F: Regulates cell signaling and adhesion.

PTX3 - Pentraxin 3: An acute-phase protein involved in immune responses.

PUMA - p53 Upregulated Modulator of Apoptosis: A pro-apoptotic protein in the BCL2 family.

RAD23B - RAD23 Homolog B: Involved in nucleotide excision repair.

RAD50 - RAD50 Double Strand Break Repair Protein: Part of the MRN complex for DNA repair.

RAD51 - RAD51 Recombinase: Promotes homologous recombination for DNA repair.

RAD54L - RAD54 Like: Involved in DNA strand exchange and homologous recombination.

RAGE - Receptor for Advanced Glycation End Products: Triggers inflammation and oxidative stress.

RANTES - Regulated upon Activation, Normal T Cell Expressed and Secreted: Also known as CCL5, involved in immune cell recruitment.

RARB - Retinoic Acid Receptor Beta: Regulates gene transcription in response to retinoic acid.

RAS - Rat Sarcoma Viral Oncogene Homolog: A family of GTPases involved in cell growth signaling.

RCD - Regulated Cell Death: A term for programmed cell death mechanisms.

RELA - RELA Proto-Oncogene: A subunit of NF-$\varkappa$B, involved in transcriptional regulation of immune responses.

REV3L - DNA Polymerase Zeta Catalytic Subunit: Functions in translesion DNA synthesis.

RIG - Retinoic Acid-Inducible Gene: Typically refers to RIG-I, involved in antiviral responses.

RIP - Receptor-Interacting Protein Kinase: A family of kinases involved in necroptosis and inflammation.

RIP1 - Receptor-Interacting Serine/Threonine-Protein Kinase 1: A key player in necroptosis.

RIPK - Receptor-Interacting Protein Kinase: Another notation for RIP family kinases.

RIPK3 - Receptor-Interacting Protein Kinase 3: Central to necroptosis and inflammation.

RNA - Ribonucleic Acid: Molecule involved in coding, decoding, regulation, and expression of genes.

ROR2 - Receptor Tyrosine Kinase-Like Orphan Receptor 2: Plays a role in Wnt signaling.

RORA - RAR-Related Orphan Receptor Alpha: Regulates circadian rhythms and lipid metabolism.

RORC - RAR-Related Orphan Receptor C: Involved in T cell differentiation and immune responses.

ROS - Reactive Oxygen Species: Molecules involved in oxidative stress and cellular signaling.

ROUT - Statistical method to remove experimental outliers.

RPA - Replication Protein A: Binds single-stranded DNA during replication and repair.

RPA1 - Replication Protein A1: A subunit of the RPA complex, critical for DNA metabolism.

RPMI - Roswell Park Memorial Institute Medium: A culture medium used in cell biology.

SATB2 - Special AT-Rich Sequence-Binding Protein 2: A transcription factor important for craniofacial development.

SCCVII - A squamous cell carcinoma cell line used in cancer research.

SCID - Severe Combined Immunodeficiency: A condition of severe immune deficiency.

SERCA - Sarco/Endoplasmic Reticulum Ca2+-ATPase: Regulates calcium levels in cells.

SERPINF2 - Serpin Family F Member 2: Involved in inhibiting fibrinolysis.

SIGNOR - Signaling Network Open Resource: A database for signal transduction pathways.

SIRT1 - Sirtuin 1: A protein involved in cellular stress responses and metabolism.

SIRT6 - Sirtuin 6: Regulates genome stability and metabolism.

SLAMF8 - SLAM Family Member 8: Plays a role in immune responses.

SLC22A - Solute Carrier Family 22: A family of transport proteins for organic ions.

SLC47A - Solute Carrier Family 47 Member A: Functions as a multidrug transporter.

SLIT2 - Slit Guidance Ligand 2: Involved in neural development and angiogenesis.

SLX4 - Structure-Specific Endonuclease Subunit SLX4: Plays a role in DNA repair.

SMAD2 - SMAD Family Member 2: A key mediator of TGF-beta signaling.

SNAP23 - Synaptosome-Associated Protein 23: Involved in vesicle trafficking and exocytosis.

SNARE - Soluble NSF Attachment Protein Receptor: A family of proteins mediating vesicle fusion.

SNP - Single Nucleotide Polymorphism: A variation in a single nucleotide in the genome.

SNU1033 - A human gastric cancer cell line used in research.

SPINT1 - Serine Peptidase Inhibitor, Kunitz Type 1: Regulates protease activity in tissue

remodeling.

SREBF2 - Sterol Regulatory Element-Binding Protein 2: Regulates cholesterol metabolism.

SSB - Single-Strand Binding Protein: Protects single-stranded DNA during replication and repair.

SSRP1 - Structure-Specific Recognition Protein 1: Involved in chromatin remodeling and transcriptional regulation.

STAR - Steroidogenic Acute Regulatory Protein: Regulates steroid hormone biosynthesis.

STAT - Signal Transducer and Activator of Transcription: A family of transcription factors in cytokine signaling.

STAT1 - Signal Transducer and Activator of Transcription 1: Mediates interferon signaling.

STAT2 - Signal Transducer and Activator of Transcription 2: Works with STAT1 in type I interferon responses.

STAT3 - Signal Transducer and Activator of Transcription 3: Involved in cell growth and survival signaling.

STAT5A - Signal Transducer and Activator of Transcription 5A: Regulates growth hormone signaling.

STG - State transition graph.

STING - Stimulator of Interferon Genes: Activates immune responses upon detecting cytosolic DNA.

STING1 - Another name for STING, emphasizing its gene form.

STRING - Search Tool for the Retrieval of Interacting Genes/Proteins: A database of protein-protein interactions.

TAA - Tumor-Associated Antigen: Antigens expressed by tumor cells, recognized by the immune system.

TAS1R1 - Taste Receptor Type 1 Member 1: Involved in taste perception.

TAS2R108 - Taste Receptor Type 2 Member 108: A bitter taste receptor.

TBK1 - TANK-Binding Kinase 1: Plays a role in antiviral responses and NF-$\varkappa$B activation.

TBXA2R - Thromboxane A2 Receptor: Mediates the effects of thromboxane in blood clotting and inflammation.

TCNER - Transcription-Coupled Nucleotide Excision Repair: A sub-pathway of nucleotide excision repair.

TCR - T Cell Receptor: A molecule on T cells that recognizes antigens presented by MHC.

TGF - Transforming Growth Factor: A family of proteins involved in cell growth and differentiation.

TGFB1 - Transforming Growth Factor Beta 1: A cytokine regulating immune responses and tissue repair.

TGFBR2 - Transforming Growth Factor Beta Receptor 2: Mediates TGF-beta signaling.

TIM - T Cell Immunoglobulin Mucin: A family of proteins involved in immune regulation.

TIM3 - T Cell Immunoglobulin and Mucin Domain-Containing Protein 3: An inhibitory receptor on T cells.

TIR - Toll/Interleukin-1 Receptor: A signaling domain found in immune receptors.

TLR - Toll-Like Receptor: A family of receptors involved in pathogen recognition.

TLR3 - Toll-Like Receptor 3: Recognizes double-stranded RNA, a marker of viral infections.

TLR4 - Toll-Like Receptor 4: Recognizes lipopolysaccharides on Gram-negative bacteria.

TME - Tumor Microenvironment: The environment around a tumor, including immune and stromal cells.

TNF - Tumor Necrosis Factor: A cytokine involved in inflammation and apoptosis.

TNFRSF19 - Tumor Necrosis Factor Receptor Superfamily Member 19: Involved in apoptosis and cell signaling.

TNFSF10 - Tumor Necrosis Factor Superfamily Member 10 (TRAIL): Induces apoptosis in tumor cells.

TNFSF11 - Tumor Necrosis Factor Superfamily Member 11 (RANKL): Regulates bone metabolism.

TNFSF12 - Tumor Necrosis Factor Superfamily Member 12 (TWEAK): Promotes inflammation and apoptosis.

TOPBP1 - Topoisomerase Binding Protein 1: Involved in DNA damage response and replication.

TPX2 - Targeting Protein for Xklp2: Regulates spindle assembly during mitosis.

TRAIL - TNF-Related Apoptosis-Inducing Ligand: Promotes apoptosis in cancer cells.

TREM2 - Triggering Receptor Expressed on Myeloid Cells 2: Regulates microglial function in the brain.

TRIF - TIR-Domain-Containing Adapter-Inducing Interferon-Beta: A key adapter in TLR signaling.

TRIM30A - Tripartite Motif Containing 30A: Involved in immune regulation and inflammatory responses.

TRPA1 - Transient Receptor Potential Ankyrin 1: A sensor for pain and noxious stimuli.

TRRUST - Transcriptional Regulatory Relationships Unraveled by Sentence-Based Text Mining: A database of transcriptional networks.

TSA - Trichostatin A: An inhibitor of histone deacetylases, affecting gene expression.

TYK2 - Tyrosine Kinase 2: Mediates signaling for several cytokines, including type I interferons.

ULM - Univariate linear model.

UPR - Unfolded Protein Response: A cellular stress response triggered by misfolded proteins in the ER.

USP18 - Ubiquitin Specific Peptidase 18: Regulates type I interferon signaling.

UVC - Ultraviolet C: A type of UV radiation used in sterilization processes.

VAMP1 - Vesicle-Associated Membrane Protein 1: A SNARE protein involved in vesicle fusion.

VEC - Vascular Endothelial Cadherin: Mediates cell-cell adhesion in blood vessels.

VEGF - Vascular Endothelial Growth Factor: Promotes angiogenesis and vascular permeability.

VEGFB - Vascular Endothelial Growth Factor B: Involved in vascular development and energy metabolism.

VEGFC - Vascular Endothelial Growth Factor C: Regulates lymphangiogenesis.

WEE1 - WEE1 G2 Checkpoint Kinase: Regulates entry into mitosis by inhibiting CDKs.

WHO - World Health Organization: A specialized agency of the United Nations for global health.

WNT - Wnt Signaling Pathway: Regulates cell fate, proliferation, and migration.

WNT7B - Wnt Family Member 7B: Plays a role in developmental signaling pathways.

XBP1 - X-Box Binding Protein 1: Regulates the unfolded protein response.

XIAP - X-Linked Inhibitor of Apoptosis Protein: Inhibits caspases to prevent apoptosis.

XPA - Xeroderma Pigmentosum Group A: Involved in nucleotide excision repair.

XPC - Xeroderma Pigmentosum Group C: Plays a role in DNA damage recognition.

XPO1 - Exportin 1: Mediates nuclear export of proteins and RNAs.

XRCC1 - X-Ray Repair Cross-Complementing Protein 1: Involved in base excision repair.

XRCC4 - X-Ray Repair Cross-Complementing Protein 4: Essential for DNA double-strand break repair.

ZBP1 - Z-DNA Binding Protein 1: Recognizes viral DNA and triggers immune responses.

ZIP - ZRT/IRT-Like Protein: A family of zinc transporters.

ZNF316 - Zinc Finger Protein 316: A transcription factor involved in gene regulation.

RÉSUMÉ

Cette thèse vise à approfondir notre compréhension de la Mort Cellulaire Immunogène (ICD) et de son potentiel à améliorer l'efficacité des traitements chimiothérapeutiques. En adoptant une approche multidisciplinaire qui intègre la biologie expérimentale et computationnelle, cette recherche aborde des questions clés essentielles à l'avancement des études sur l'ICD.

Malgré les progrès réalisés dans le décryptage des mécanismes moléculaires de l'ICD, des lacunes importantes subsistent dans notre compréhension. Cette thèse s'efforce de combler ces lacunes en identifiant les facteurs et les voies critiques impliqués dans l'ICD et en développant des modèles computationnels pour prédire et renforcer l'immunogénicité des agents chimiothérapeutiques.

Un axe central de ce travail a été l'identification d'une signature moléculaire distincte de l'ICD, au-delà des marqueurs traditionnels tels que les DAMPs libérés et exposés à la surface. Une telle signature pourrait servir de biomarqueur fiable pour prédire le potentiel immunogène des chimiothérapies. De plus, la recherche a exploré les facteurs sécrétés, en particulier les cytokines, qui jouent un rôle crucial dans l'initiation du cycle immunitaire anticancéreux en recrutant et activant les cellules immunitaires. Comprendre ces facteurs est essentiel pour optimiser le potentiel immunogène des régimes chimiothérapeutiques.

En outre, la thèse s'est penchée sur les voies cellulaires qui régulent la sécrétion et la libération des DAMPs liés à l'ICD. En explorant les réseaux de signalisation et les mécanismes moléculaires impliqués, l'étude visait à découvrir des voies influençant l'immunogénicité des cellules mourantes, avec l'objectif potentiel d'identifier de nouvelles cibles pour amplifier la réponse immunitaire via l'induction de l'ICD.

Sur la base de ces résultats, la recherche a également exploré la possibilité de recréer l'ICD in silico. En intégrant à la fois les marqueurs établis et nouvellement identifiés dans des modèles computationnels, la thèse visait à simuler les processus de l'ICD, prédire les résultats des traitements et orienter les futures expérimentations.

Enfin, la thèse a évalué la capacité prédictive des modèles in silico développés pour évaluer l'immunogénicité des médicaments chimiothérapeutiques. L'objectif ultime était d'utiliser ces modèles pour optimiser les formulations médicamenteuses et les protocoles de traitement, renforçant ainsi leur efficacité immunothérapeutique et contribuant au développement de stratégies de médecine personnalisée.

En conclusion, cette thèse apporte des contributions significatives au domaine de l'ICD en combinant validation expérimentale et modélisation computationnelle innovante. Elle établit une base pour une compréhension plus intégrée de la manière dont les thérapies anticancéreuses peuvent être optimisées pour exploiter pleinement le potentiel du système immunitaire dans la lutte contre le cancer.

MOTS CLÉS

Mort Cellulaire Immunogène, Biologie des Systèmes, Cytokines, Modelisation en Silico

ABSTRACT

This thesis aims to advance our understanding of Immunogenic Cell Death (ICD) and its potential to enhance the efficacy of chemotherapeutic treatments. By employing a multidisciplinary approach that integrates experimental and computational biology, this research addresses key questions essential for the progression of ICD research.

Despite the progress made in unraveling the molecular mechanisms of ICD, significant gaps in our knowledge remain. This thesis seeks to bridge these gaps by identifying critical factors and pathways involved in ICD and by developing computational models to predict and enhance the immunogenicity of chemotherapeutic agents.

A central focus of this work was the identification of a distinct molecular signature of ICD beyond the traditional hallmarks, such as released and surface-exposed DAMPs. Such a signature could serve as a reliable biomarker for predicting the immunogenic potential of chemotherapies. Additionally, the research investigated the secreted factors, particularly cytokines, that play a crucial role in initiating the cancer immunity cycle by recruiting and activating immune cells. Understanding these factors is key to optimizing the immunogenic potential of chemotherapeutic regimens.

Furthermore, the thesis delved into the cellular pathways that regulate the secretion and release of ICD-related DAMPs. By exploring the signaling networks and molecular mechanisms involved, the study aimed to uncover pathways that influence the immunogenicity of dying cells, potentially identifying new targets to amplify the immune response through ICD induction.

Building on these findings, the research also explored the feasibility of recapitulating ICD in silico. By integrating both established and newly identified hallmarks into computational models, the thesis aimed to simulate ICD processes, predict treatment outcomes, and guide future experimental efforts.

Finally, the thesis evaluated the predictive power of the developed in silico models in assessing the immunogenicity of chemotherapeutic drugs. The ultimate goal was to use these models to optimize drug formulations and treatment protocols, thereby enhancing their immunotherapeutic efficacy and contributing to the development of personalized medicine strategies.

In conclusion, this thesis makes significant contributions to the field of ICD by combining experimental validation with innovative computational modeling. It establishes a foundation for a more integrated understanding of how cancer therapies can be optimized to fully exploit the immune system's potential in combating cancer.

KEYWORDS

Immunogenic Cell Death, Systems Biology, Cytokines, In silico Modeling